JAEA-Conf 2014-002
INDC(JPN)-199

JAEA-Conf

Proceedings of the 2013 Symposium on Nuclear Data
November 14-15, 2013, Research Institute of Nuclear Engineering
University of Fukui, Tsuruga, Fukui, Japan

(Eds.) Naoki YAMANO , Osamu IWAMOTO, Shoji NAKAMURA
Satoshi KUNIEDA, Wilfred van ROOIJEN and Hiroyuki KOURA

Nuclear Science and Engineering Center
Sector of Nuclear Science Research

February 2015
Japan Atomic Energy Agency

日本原子力研究開発機構

JAEA-Conf 2014-002
INDC(JPN)-199

Proceedings of the 2013 Symposium on Nuclear Data
November 14-15, 2013, Research Institute of Nuclear Engineering
University of Fukui, Tsuruga, Fukui, Japan

(Eds.) Naoki YAMANO*, Osamu IWAMOTO, Shoji NAKAMURA, Satoshi KUNIEDA,
Wilfred van ROOIJEN* and Hiroyuki KOURA+

Nuclear Science and Engineering Center
Sector of Nuclear Science Research
Japan Atomic Energy Agency
Tokai-mura, Naka-gun, Ibaraki-ken

(Received November 21, 2014)

The 2013 Symposium on Nuclear Data was held at Research Institute of Nuclear Engineering, University of Fukui, on November 14 and 15, 2013. The Nuclear Data Division of the Atomic Energy Society of Japan and Research Institute of Nuclear Engineering, University of Fukui organize this symposium in cooperation with Nuclear Science and Engineering Directorate of Japan Atomic Energy Agency and the Chubu Branch of Atomic Energy Society of Japan. In the oral sessions, papers were presented on topics of progress in neutron cross-section measurement and analysis, application of nuclear data, recent topics on nuclear data measurement and theory, and progress in studies of high-energy nuclear reactions. In the poster session, papers were presented concerning experiments, evaluations, benchmark tests and applications. Two tutorials for evaluation of nuclear decay data and fission physics were also presented. Talks as well as posters presented at the symposium aroused lively discussions among 64 participants. This report consists of total 35 papers including 14 oral presentations and 21 poster presentations.

Keywords: Nuclear Data, Symposium, Abstract, Nuclear Reaction, JENDL, Experiment, Evaluation, Benchmark Test, Cross Section, Nuclear Reactor, Nuclear Fuel Cycle, Accelerator

---

+ Advanced Science Research Center
* Research Institute of Nuclear Engineering, University of Fukui
Organizers: N. Yamano (Univ. of Fukui, Chair), O. Iwamoto (JAEA, Vice-Chair), K. Kato (Hokkaido U.), T. Yoshii (TEPSYS), J. Hori (Kyoto U.), I. Murata (Osaka U.), K. Nakajima (Kyoto U.), T. Hazama (JAEA), S. Kunieda (JAEA), H. Koura (JAEA), S. Chiba (Tokyo Institute of Technology), S. Nakamura (JAEA)

JAEA-Conf 2014-002
INDC(JPN)-199

2013 年度核データ研究会報告集

2013 年 11 月 14 日～11 月 15 日

福井大学附属国際原子力工学研究所、福井県敦賀市

日本原子力研究開発機構 原子力科学研究部門　原子力基礎工学研究センター
（編）山野　直樹*、岩本　修、中村　詔司、国枝　賢、Wilfred van Rooijin*、小浦　寛之+

（2014 年 11 月 21 日　受理）

2013 年核データ研究会は、2013 年 11 月 14 日から 15 日にかけて、福井県敦賀市の福井大学附属国際原子力工学研究所にて開催された。本研究会は日本原子力学会核データ部会と福井大学附属国際原子力工学研究所の主催、日本原子力研究開発機構原子力基礎工学研究センターおよび日本原子力学会中部支部の共催の下、4 つのトピックス：「中性子断面積測定と解析」、「核データの応用」、「核データ測定と理論における最近のトピックス」、「高エネルギー核反応研究の進展」に関する講演・議論が行われるとともに、実験、評価、ベンチマークテスト、応用に至る幅広い分野のポスター発表が行われた。さらに、崩壊データ評価と核分裂の物理に係る 2 件のチュートリアルも実施された。参加総数は 64 名で、盛況のうちに全日程を終えた。本報告書は、同研究会における口頭発表 14 件とポスター発表 21 件を含む 35 件の全論文を纏めたものである。

原子力科学研究所：〒319-1195 茨城県那珂郡東海村白方白根 2-4
+ 先端基礎研究センター
* 福井大学附属国際原子力工学研究所
2013 年核データ研究会実行委員会：山野　直樹（委員長、福井大学）、岩本　修（副委員長、原子力機構）、加藤　幾芳（北海道大学）、吉井　貴（テプコシステムズ）、堀　順一（京都大学）、村田　勲（大阪大学）、中島　健（京都大学）、羽様　平（原子力機構）、国枝　賢（原子力機構）、小浦　寛之（原子力機構）、千葉　敏（東京工業大学）、中村　詔司（原子力機構）

Contents

Papers presented at a Poster Session

目　次

ポスター発表論文

1. Program of the 2013 Symposium on Nuclear Data

Date: November 14-15, 2013
Venue: Research Institute of Nuclear Engineering
University of Fukui, Tsuruga, Fukui, Japan
Host: The Nuclear Data Division of the Atomic Energy Society of Japan
& Research Institute of Nuclear Engineering, University of Fukui
Co-Host: Nuclear Science and Engineering Center of Japan Atomic Energy Agency
& the Chubu Branch of Atomic Energy Society of Japan.

<u>November 14 (Thu), 2013 at primary lecture room</u>

12:00 ~ 13:00 Registration

13:00 ~ 13:15 **Opening Session** N. Yamano (Fukui U.)
Opening Address S. Chiba (Tokyo Tech)

13:15 ~15:15
Session 1: **Progress in Neutron Cross-section Measurement and Analysis** 【Chair: J. Hori (Kyoto U.)】
1.1 Measurements of Neutron Capture Cross Sections for MAs [30] S. Nakamura (JAEA)
1.2 Neutron Cross Section Measurement for Long-Lived Fission Products [30] T. Katabuchi (Tokyo Tech)
1.3 Cross-sections and Uncertainty Estimation through the R-matrix Analysis [30] S. Kunieda (JAEA)
1.4 Cross-section Measurement in Pohang Neutron Experimental Facility [30] A. Makinaga (Hokkaido U.)

15:15 ~ 15:35 Conference Photo and Coffee Break [20]

15:35 ~ 17:20 Poster Presentations

17:30 ~ 20:00 Social Gathering (at primary lecture room)

<u>November 15 (Fri), 2013 at primary lecture room</u>

09:00 ~10:30
Session 2: **Application of Nuclear Data** 【Chair: I. Murata (Osaka U.)】
2.1 Nuclear Data Application in Monju [30] T. Hazama (JAEA)
2.2 Development of a Neutronic Analysis Code using Data from Monju [30] W.F.G. van Rooijen (Fukui U.)
2.3 Research Progress on Accelerator-Driven System in Kyoto University Research Reactor Institute [30]
C.H. Pyeon (Kyoto U.)

10:30 ~ 10:40 Coffee Break [10]

Tutorials 【Chair: N. Yamano (Fukui U.)】

10:40 ~ 11:40 Tutorial 1: Evaluation of Nuclear Decay Data for Science and Engineering [60]
J. Katakura (Nagaoka U. of Tech.)

11:40 ~ 13:00 Lunch [80]

13:00 ~ 14:00 Tutorial 2: Introduction to Fission Physics: Back to Basics [60] T. Ohsawa (Kinki U.)

14:00 ~ 14:05 Coffee Break [5]

14:05 ~ 15:05

Session 3 Recent topics 【Chair: S. Chiba (Tokyo Tech)】

3.1 Study of Deuteron-induced Reactions for Engineering Design of Accelerator-driven Neutron Sources
[20] Y. Watanabe (Kyusyu U.)

3.2 Application of CDCC Theory to Nuclear Data Evaluation for Nucleon-induced Reactions on ^{6,7}Li
[20] H. Guo (Kyushu U.)

3.3 Cross Section Measurement for Photo Nuclear Reaction using Laser Compton-scattering γ-ray [20]
F. Kitatani (JAEA)

15:05 ~ 15:15 Coffee Break [10]

15:15 ~ 16:55

Session 4: Progress in Studies of High-energy Nuclear Reaction 【Chair: Y. Watanabe (Kyushu U.】

4.1 Recent Progress in Experimental and Theoretical Studies of Proton-induced Fragment Production Cross Section at Intermediate Energies [25] M. Hagiwara (KEK)

4.2 Overview of Particle and Heavy Ion Transport Code System PHITS [25] Y. Iwamoto (JAEA)

4.3 Recent Developments in Intranuclear Cascade Model at Kyushu University [25]
Y. Uozumi (Kyushu U.)

4.4 Measurement of Neutron Production Cross-sections from Heavy-ion Induced Reaction [25]
N. Shigyo (Kyusyu U.)

16:55 ~ 17:15 **Closing Session**

Poster Awards Nuclear Data Division, AESJ

Closing Address N. Yamano (Fukui U.)

Poster Presentation

Date: November 14 (Thu) 2013, 15:35 ~ 17:20

P1 Response Function for the Measurement of (n,γ) Reactions with the ANNRI-Cluster Ge Detectors at J-PARC — K.Y. Hara (JAEA)

P2 Study of the γ-ray Strength Function in a ^{80}Se(γ,γ') Experiment at ELBE — A. Makinaga (Hokkaido U.)

P3 Analysis of Tritium Production from Nucleon-induced Reactions on ^{7}Li and its Application to Nuclear Data Evaluation — K. Nagaoka (Kyushu U.)

P4 Theoretical Study of Beta Decay for Delayed Neutron and Decay Heat — H. Koura (JAEA)

P5 Evaluation of Neutron Induced Reaction Cross Sections on Rh Isotopes — N. Iwamoto (JAEA)

P6 Measurement of Neutron Capture Cross Section of ^{241}Am using NaI(Tl) Spectrometer at J-PARC — T. Arai (Tokyo Tech)

P7 Neutron Capture Cross section Measurements on ^{232}Th with a Total Absorption BGO Spectrometer at KURRI-LINAC — J. Hori (Kyoto U.)

P8 Measurement of Proton, Deuteron, and Triton Production Double Differential Cross Sections on Carbon by 290 MeV/nucleon Ar ions — T. Kajimoto (Hiroshima U.)

P9 Measurement of Cross Section and Yields of Neutron Produced by 100 MeV/u C(C,xn) Reaction — Y. Imahayashi (Kyushu U.)

P10 Light Mass Fragment Production DDXs of 70 MeV Proton, Helium and Carbon Induced Reactions — T. Sanami (KEK)

P11 Feasibility Study on High-dynamic-range Neutron Spectrometer with Continuously Thick-adjustable Moderator/Absorber — S. Tamaki (Osaka U.)

P12 Scattering Problems in Complex Scaling Method — M. Odsuren (Hokkaido U.)

P13 Recent Activity of Central Asian Nuclear Reaction Data Base and Asian Collaboration on Nuclear Reaction Data Compilation — M. Takibayeva (CANRDB)

P14 FENDL-3.0 Benchmark Test with Shielding Experiments at JAEA/TIARA — C. Konno (JAEA)

P15 Analysis of Integral Experiment for Th-232(n,γ) Reaction Cross Section at KUCA — T. Sano (Kyoto U.)

P16 Neutron Spectrum Measurement of Am-Be source by Multi-activation-foil Method — R. Nakamura (Osaka U.)

P17 Design Calculation of Epi-thermal Neutron Field with DT Neutron Source for Low Energy Neutron Spectrometer Developed for BNCT — K. Tsubouchi (Osaka U.)

P18 Feasibility Study on Polonium-209 as Radioisotope Fuel for Space Nuclear Power — J. Nishiyama (Tokyo Tech)

P19 Study on Fluid Temperature Measurement using an AmBe Neutron — H. Ito (Osaka U.)

P20 Present Status of BNCT-SPECT Development with CdTe Detector — M. Manabe (Osaka U.)

P21 Study on the Validity of Thorium-232 Cross-section in JENDL-4.0 — T. Mishiro (Osaka U.)

2. Measurements of Neutron Capture Cross Sections for MAs

S.Nakamura[1)], A.Kimura[1)], K.Hirose[1)], M.Ohta[1)], S.Goko[1)], T.Fujii[2)], S.Fukutani[2)], K.Furutaka[1)], K.Y.Hara[1,4)], H.Harada[1)], J.Hori[2)], M.Igashira[3)], T.Kamiyama[4)], T.Katabuchi[3)], T.Kin[1)], K.Kino[4)], F.Kitatani[1)], Y.Kiyanagi[4)†], M.Koizumi[1)], M.Mizumoto[3)], M.Oshima[1)‡], K.Takamiya[2)] andY.Toh[1)]

1) Japan Atomic Energy Agency, 2-4 Shirane, Shirakata, Tokai-mura, Naka-gun, Ibaraki 319-1195
2) Research Reactor Institute, Kyoto University, 2-1010 Asashiro Nishi, Kumatori-cho, Sennan-gun, Osaka 590-0494
3) Research Laboratory for Nuclear Reactors, Tokyo Institute of Technology, O-okayama, Meguro, Tokyo 152-8550, Japan
4) Faculty of Engineering, Hokkaido University, Kita 13, Nishi 8, Kita-ku, Sapporo, 060-8628, Japan
† Present address: Nagoya University, Furo-cho, Chikusa-ku, Nagoya, 464-8601, Japan
‡ Present address: Japan Chemical Analysis Center, 295-3 Sannou-cho, Inage-ku, Chiba-city, Chiba263-0002, Japan

E-mail: shoji.nakamura@jaea.go.jp

To evaluate the feasibility of development of nuclear transmutation technology and advanced nuclear system, precise nuclear data of neutron capture cross sections for long-lived fission products (LLFPs) and minor actinides (MAs) are indispensable. In this paper, our research activities, particularly for cross-section measurements of minor actinides by the activation and the TOF methods, will be presented together with the details of experiments and the obtained data.

1. Introduction

The social acceptability of nuclear power reactors is related to the waste management of long-lived fission products (FPs) and minor actinides (MAs) existing in spent nuclear fuels. The FPs (*ex*., ^{137}Cs, ^{90}Sr, ^{99}Tc, ^{129}I, ^{107}Pd, ^{93}Zr, and so on) and MAs (*ex*., ^{237}Np, ^{241}Am, ^{243}Am, and ^{244}Cm isotopes) are important in the nuclear waste management, because the presence of these nuclides induces long-term radiotoxicity because of their extremely long half-lives. The transmutation is one of the solutions to reduce the radiotoxicity of nuclear wastes. To evaluate the feasibility of development of nuclear transmutation technology, precise nuclear data of neutron capture cross-sections for LLFPs and minor actinides MAs are indispensable. However, there are discrepancies among the reported data for the thermal-neutron capture cross-sections for those nuclides. The discrepancies reach to 10-20%. Therefore, our concern was focused to re-measure the cross-sections of those FPs and MAs.

This paper presents joint research activities by JAEA and Universities for the measurements of the neutron capture cross sections of MAs by a neutron time-of-flight (TOF) method at J-PARC.

2. Present Status of MA Data

Although the accurate data of neutron capture cross sections are necessary to evaluate reaction rates and burn-up study, there are discrepancies among the reported data for the thermal neutron capture cross sections for MAs. As an example for MA, **Figure 1** shows the trend of the thermal neutron capture cross section for ^{237}Np and the evaluated nuclear data from JENDL-4.0[1]. The discrepancies reached to 10% or so. The discrepancies between experimental and evaluated data are still remained. This is why our concern was focused to re-measure the neutron capture cross sections of MAs.

a) b)

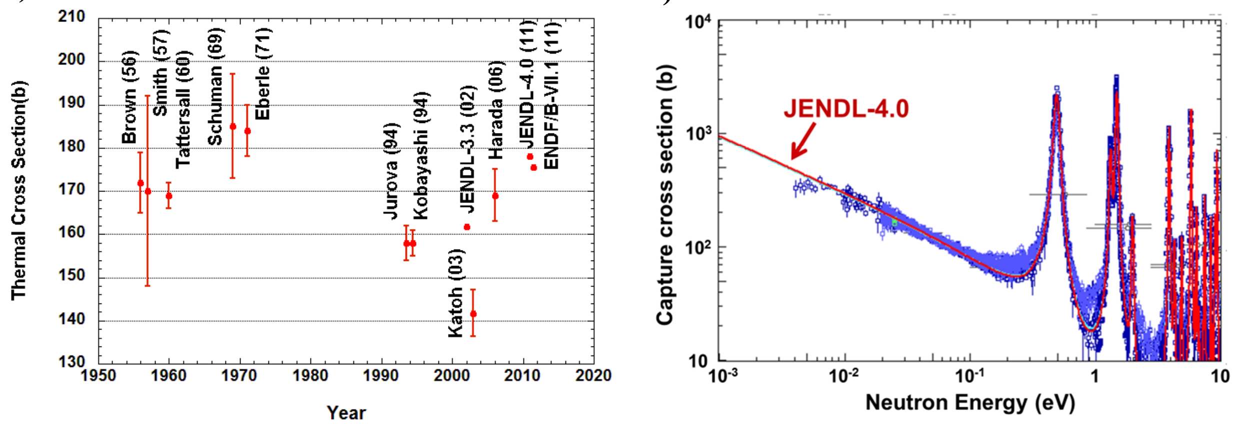

Fig. 1 **a)** The trend of the thermal neutron capture cross section of ^{237}Np from 1950s,
b) JENDL-4.0 [1] evaluated nuclear data of ^{237}Np

3. J-PARC/MLF/BL04, "ANNRI"

A new experimental apparatus called "Accurate Neutron Nucleus Reaction measurement Instrument (ANNRI)" has been constructed on the Beam Line No.4 (BL04) of the MLF in the J-PARC. The ANNRI has two detector systems. One is a large Ge detectors array, which consists of two cluster-Ge detectors, eight coaxial-shaped Ge detectors and BGO Compton suppression detectors, and another is a large NaI(Tl) spectrometer as shown in **Figure 2**. The ANNRI has an advantage for the neutron cross-section measurements because the MLF facility can provide the highest pulsed neutron intensity in the world when the 1-MW operation would be achieved [2]. The pulsed neutron beam intensities are listed in **Table 1**.

a) b)

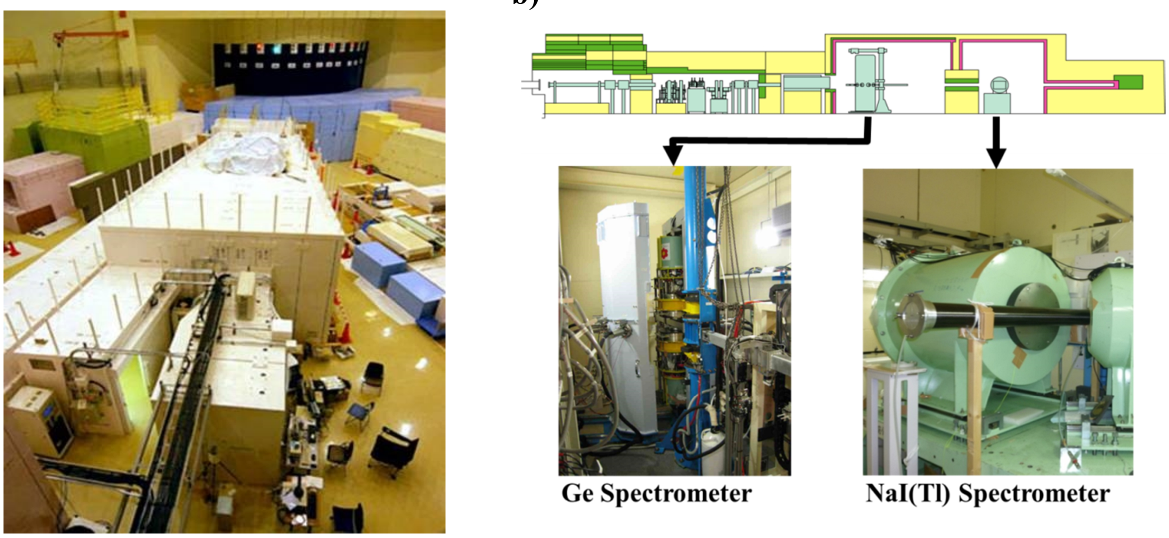

Fig. 2 **a)** A new experimental apparatus called "Accurate Neutron Nucleus Reaction measurement Instrument (ANNRI)" **b)** The cross sectional view of ANNRI is shown in upper side, the spectrometer in left side, and the NaI(Tl) spectrometer in right side.

Table 1 Pulsed neutron beam intensities in 1-MW and 120-kW operations at J-PARC/MLF/ANNRI

energy-integrated intensities	1MW (Future)	120 kW
1.5-25 meV	4.3×10^{7} n/s/cm^2	4.5×10^{6} n/s/cm^2
0.9-1.1 keV	6.3×10^{6} n/s/cm^2	6.6×10^{5} n/s/cm^2

In addition of the highest pulsed neutron intensity, ANRRI has another advantage by introducing High speed data acquisition system [3]. ANNRI is applicable both for Radio Isotope samples with half-lives shorter than 90 years and for small amount of samples.

Our Ge spectrometer has 2 cluster Ge detectors, 8 coaxial-Ge detectors, and Compton suppressing BGO detectors. Its energy resolutions for 1.33-MeV γ-ray s are 5.8 keV in on-beam and 2.4 keV in off- beam conditions. Its peak efficiency for 1.33-MeV γ-ray is 3.64±0.11%[4]. To reduce neutron scattering by air, the air in the beam duct is replaced with Helium gas.

The NaI(Tl) spectrometer at ANNRI consists of two NaI(Tl) scintillators each of which is surrounded by an annular shaped plastic scintillator. This spectrometer has been used for experiments of the fast neutron capture reaction. The cylindrical NaI(Tl) scintillators, 13” mm in diameter and 8” mm in length, and 8” in diameter and 8” in length, are located at the angles of 90^{O} and 125^{O} with respect to the neutron-beam line, respectively. These spectrometers are shielded from background γ rays and scattered neutrons by using the lead layers, cadmium, borated polyethylene and lithium (^{6}Li) hydride.

An analog-to-digital converter (ADC) module (Fast ComTec 7072 Dual ADC) was used for the pulse-height measurements. The signals from the NaI(Tl) scintillator were amplified, and then input to a multi-stop time-to-digital converter (TDC) module. The resolution of TDC was 1 μsec/channel. Signals from TDC and ADC were handled with a data acquisition system (Fast ComTech MPA-3).

4. Some Highlight Data

The neutron capture cross sections of ^{241}Am, ^{244,246}Cm and ^{237}Np have been measured relative to the ^{10}B(n, αγ) standard cross section by the Time-Of-Flight method. Some of highlight results obtained in our research activities are presented as follows.

4.1 ^{241}Am neutron capture cross section

A sample of ^{241}Am (952 MBq in activity, 7.5 mg in weight and 10 mm in diameter) in chemical form of AmO_2 covered with an Al case was used for the measurement. The ^{241}Am(n,γ)^{242}Am cross sections have been measured using the Ge spectrometer installed in ANNRI. **Figure 3** shows the neutron capture cross section of ^{241}Am for neutron energies ranging from 0.01 to 10 eV [5]. The absolute value of the experimental cross section was normalized to the thermal-neutron capture cross section of JENDL-4.0 in the energy range between 20.3 meV and 30.3 meV; the averaged cross section in this energy range of the JENDL-4.0[1] is 688.3 [b]. The Westcott neutron capture factor [6] is obtained as 1.02±0.01, which is consistent with that of JENDL-4.0 but about 3 % smaller than Mughabghab's evaluation.

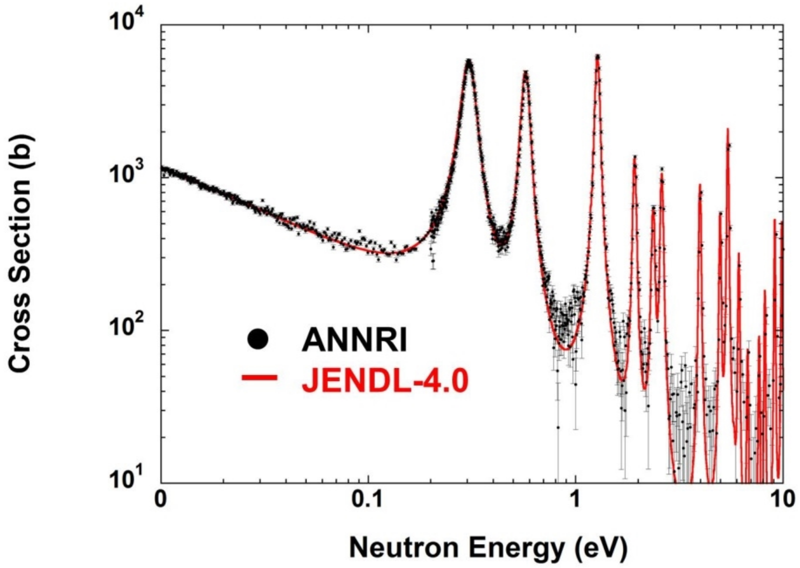

Fig. 3 ^{241}Am(n,γ)^{242}Am cross section obtained using the ANNRI

4.2 ^{244}Cm neutron capture cross section

Curium-244 (half-life: 18.1 years) is among the most important MAs, and contributes nearly 50% of the total actinide decay-heat in spent nuclear fuels after three years of cooling. However, there is only one of experimental data for the neutron capture cross section of ^{244}Cm [7] in the resonance region, and its uncertainties of the data are larger than the required ones from 4.1 to 25.7 %.

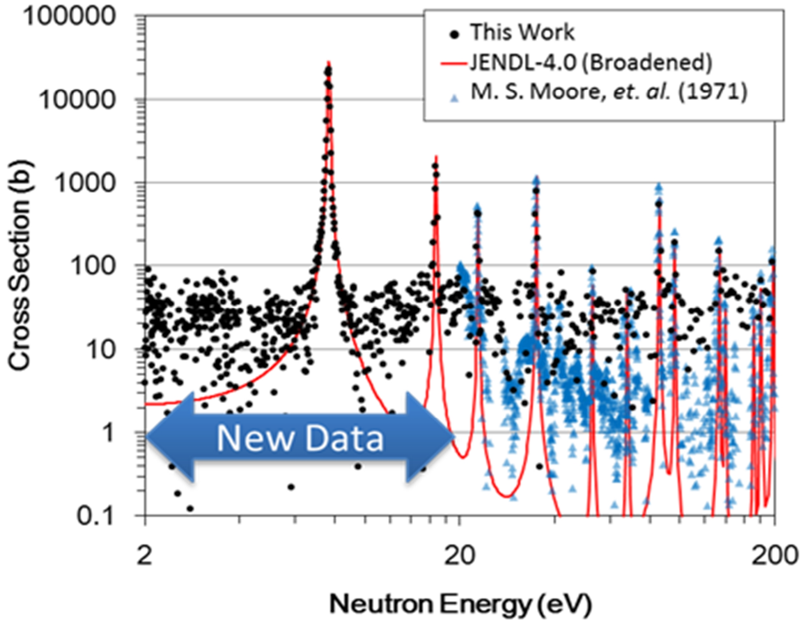

Fig. 4 Neutron-capture cross section of ^{244}Cm in comparison with that by Moore and broadened values from JENDL-4.0.

The ^{244}Cm sample was 0.6 mg of curium oxide. Its isotopic enrichment was 90.1 mole%, and its activity was 1.8 GBq due to ^{244}Cm. The neutron capture cross section of ^{244}Cm was measured in the neutron energy ranging from 1 eV to 300 eV with the Ge spectrometer in the ANNRI at J-PARC/MLF as shown in Figure 4. The ^{244}Cm resonance at around 7.7 and 16.8 eV was observed in the neutron capture reaction for the first time [8]. The uncertainty of the obtained cross section was 5.8 % at the top of the first resonance of ^{244}Cm.

4.3 ^{237}Np neutron capture cross section

The cross section of the ^{237}Np(n,γ) reaction has been measured in an energy range from 10 meV to 1 keV [9,10]. The NaI(Tl) spectrometer installed in ANNRI was used for the measurement. The relative cross section was obtained using the neutron spectrum measured by the ^{10}B(n,αγ) reaction. The absolute value of the cross section was deduced by normalizing the relative cross section to the evaluated value in JENDL-4.0[1] at the first resonance. **Figure 5** shows the result of the neutron capture cross section of ^{237}Np in the neutron energy ranging from 10 meV to 12 eV. The result is compared to the previously reported data by Weston [11] and Esch [12]. As seen in Fig.5, the results obtained at ANNRI are good agreement with the data reported by Weston. The data by Esch are discrepant with this.

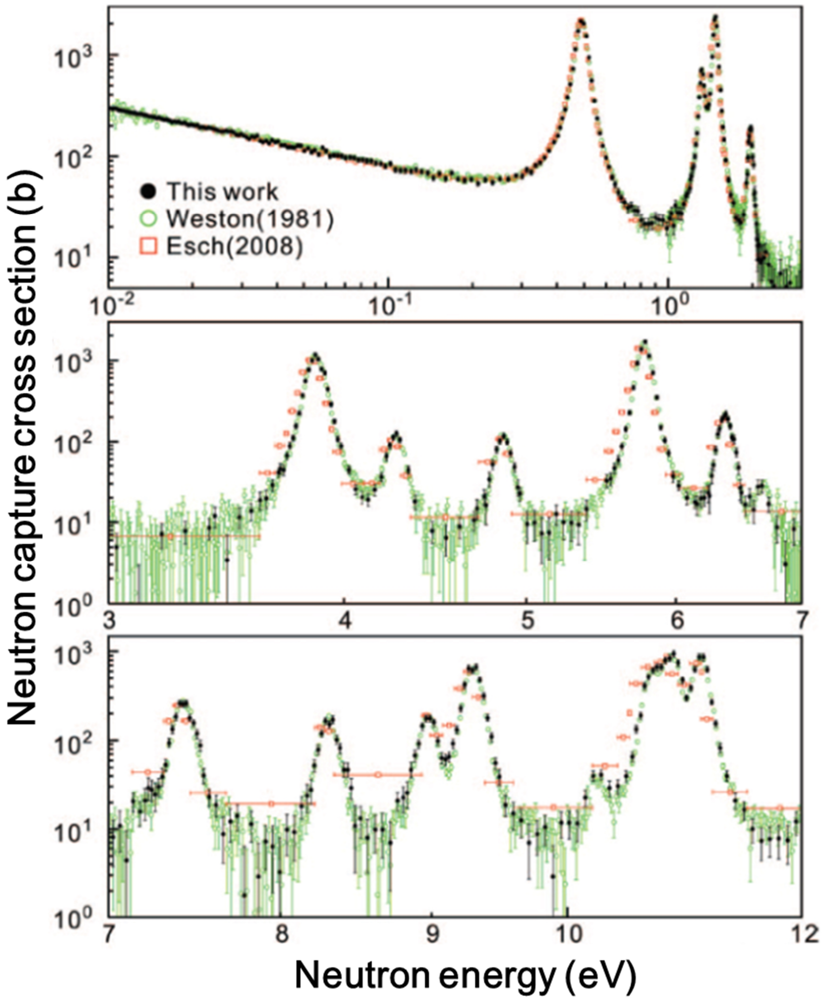

Fig. 5 The result of the ^{237}Np(n,γ) cross sections obtained by the ANNRI NaI(Tl) spectrometer compared with those by Weston and Esch *et al*.

5. Summary

This paper described the JAEA's research activities for the measurements of the neutron capture cross sections for MAs by the neutron time-of-flight (TOF) method.

The operation of a new experimental apparatus called "Accurate Neutron-Nucleus Reaction measurement Instrument (ANNRI)" in the MLF at J-PARC has been started for neutron capture cross section measurements of MAs and LLFPs. As a part of our measurement activities for MAs, some of highlight results were shown for ^{241}Am, ^{244}Cm and ^{237}Np.

Acknowledgment

The authors would like to appreciate the accelerator staff of J-PARC for their operation of the accelerator. This work is supported by JSPS KAKENHI (22226016).

References

[1] K. Shibata *et al.*, "JENDL-4.0: A New Library for Nuclear Science and Engineering," *J.Nucl.Sci. Technol.*, **48** (1), pp.1-30 (2011).
[2] K. Kino *et al.*, *NIM-A*, **626**, pp.58 -66 (2011).
[3] A. Kimura *et. al.*, *Conf. Rec. of IEEE NSS/MIC/RTDS 2008*, N30-68, (2008).
[4] T. Kin *et. al.*, *the 2009 NSS-MIC Conf. Rec.*, N24-2, (2009).
[5] H. Harada, *et al.*, *International Conference on Nuclear Data For Science and Technology (ND2013), New York NY USA*, March 4-8, 2013, *Nuclear Data sheets,* **119**, pp.143-146 (2014).
[6] C.H. Westcott, *Ann. Nucl. Energy*, **2**, p.59 (1955).
[7] M.S.Moore, G.A.Keyworth, *Physical Review* C**3**, p.1656 (1971).
[8] A. Kimura *et al.*, *J. Nucl. Sci. Technol.*, **49**, pp.708-724 (2012).
[9] K. Hirose *et al.*, *International Conference on Nuclear Data For Science and Technology (ND2013), New York NY USA*, March 4-8, 2013, *Nuclear Data sheets,* **119**, pp.48-51 (2014).
[10] K. Hirose *et al.*, *J. Nucl. Sci. Technol.*, **50**, pp.188-200 (2013).
[11]L.W.Weston, J.H.Todd, *Nucli. Sci. Eng*., **79**, p.184 (1981).
[12]E-I, Esch *et al.*, *Phys. Rev*. C**77**, 034309 (2008).

3. Neutron Cross Section Measurement of Long Lived Fission Products

Tatsuya Katabuchi

Research Laboratory for Nuclear Reactors, Tokyo Institute of Technology,
2-12-1 Ookayama, Meguro-ku, Tokyo 152-8550, Japan
e-mail: buchi@nr.titech.ac.jp

Nuclear data on long-live fission products (LLFP) are important for developing nuclear transmutation systems. This short review summarizes the current experimental data of the neutron capture cross sections of LLFPs and briefly reports the recent progress on neutron capture cross section measurements in J-PARC.

1. Introduction

Management of high level radioactive waste from nuclear power plants is a serious issue in nuclear energy production. Long-lived fission products (LLFP) and minor actinides (MA) in nuclear waste remain for long time. Deep geological disposal and long-term management are required. Partition and nuclear transmutation have been suggested as an option for reducing the potential toxicity of high level nuclear waste and downsizing the disposal site. In the suggested transmutation system, LLFP and MA nuclides are transmuted into shorter lived or stable nuclides through the neutron capture reaction or the neutron-induced fission. To design a nuclear transmutation system, reliable nuclear data of LLFP and MA are necessary. This short review briefly summarizes the existing experimental data of LLFP, mainly focusing on the neutron capture cross sections, and then reports the recent progress of neutron capture cross section measurement at the Japan Proton Accelerator Research Complex (J-PARC).

2. Experimental data of LLFPs

There are seven LLFP nuclides, whose life times are longer than 100,000 years. These LLFPs are summarized in **Table 1**. The half-life, the cumulative fission yield, the annual limit on intake (ALI) and the hazard index are also shown. ^{99}Tc, ^{129}I and ^{135}Cs have high hazard indexes.

Table 1. Long-lived fission products. ALI: annual limit of intake.

Nuclide	$T_{1/2}$ [year]	Fission yield [%]	ALI [%]	Hazard index
^{79}Se	0.295 M	4.53×10^{-2}	21 – 160	0.04 – 0.3
^{93}Zr	15.3 M	6.39	54 – 110	0.35 – 0.71
^{99}Tc	0.211 M	6.11	140	1.9
^{107}Pd	6.50 M	0.14	1000 – 1300	$(1.5 – 1.9) \times 10^{-4}$
^{126}Sn	0.100 M	5.49×10^{-2}	10	0.5
^{129}I	15.7 M	15.7 M	0.2 – 0.67	0.63 – 2.1
^{135}Cs	2.30 M	2.30 M	260	1

Sample availability and preparation are important keys to achieving reliable measurements. Pure ^{99}Tc samples are unavailable because of existence of no stable isotopes. However other LLFP samples normally include a substantial amount of isotopic impurities unless isotope separation is performed. To derive the cross sections, background subtraction for coexisting isotopes is required. In addition to stable isotopes, radioactive isotopes sometimes cause problems. For ^{135}Cs, strong radioactivities of chemically unseparated isotopes ^{134}Cs and ^{137}Cs limit the sample amount of ^{135}Cs and the quality of measurement. In addition, for ^{79}Se, ^{107}Pd and ^{126}Sn, their nuclear properties make sample preparation very difficult. They are pure β-decay nuclides that emit no γ-rays. Simple γ-ray detection technique cannot be used to monitor chemical separation process of these nuclides from other fission products and quantify the final sample amount. For these sample preparation difficulties, measurements for LLFPs are generally carried out under poorer experimental conditions due to a less amount of sample and larger background from radioactivities and impurities than measurements for stable nuclides using a highly isotopically enriched sample.

Recent technological developments are improving the quality of measurement for LLFPs. Spallation neutron sources provide high intensity pulsed neutron beams, allowing for measurements with less amount samples. Three spallation neutron source facilities, CERN/n_TOF [1], LANSCE [2] and J-PARC [3], are currently used for nuclear data measurements. In addition to the intense neutron beams, large detector arrays are utilized in these new experimental facilities. The large detector arrays achieved high detection efficiencies and elaborate data analysis.

Table 2 summarizes the number of existing experimental data categorized in thermal neutron capture cross section, resolved resonance parameters and keV-neutron capture cross section. The resonance parameter measurements are categorized into three experimental types: transmission, capture, and both transmission and capture. Except for ^{99}Tc and ^{129}I, measurements for LLFPs have not been carried out extensively. Several experiments updated the LLFP cross section data in the past ten years. Noguere et al. performed high-resolution transmission and capture time-of-flight experiments using a pulsed neutron source at the Geel electron linear accelerator facility [30]. They determined the resolved resonance parameters of individual resonances up to 10 keV. Belgya et al. measured the thermal neutron capture cross section of ^{129}I using a chopped cold neutron beam from the Budapest Research Reactor [26]. Patronis et al. measured the averaged neutron capture cross section of ^{135}Cs at 30 keV and 500 keV using a ^{7}Li(p,n)^{7}Be neutron source at the Karlsruhe Van de Graaff accelerator [37]. The ^{135}Cs sample was made by implanting magnetically separated ^{135}Cs ions into a graphite disk. Tagiliente et al. measured the neutron capture reaction of ^{93}Zr up to 8 keV at the CERN n_TOF facility [42]. Resonance analysis was applied for observed 64 resonances.

Table 2. Number of experimental data of LLFPs. The numbers in the parentheses are the reference numbers.

	Thermal capture	Resolved resonance parameters			keV-neutron capture
		Transmission	Capture	Trans. & Cap.	
^{99}Tc	8 (4-11)	3 (12-14)	5 (15-19)	0	5 (16-17, 19-21)
^{129}I	5 (22-26)	1 (27)	2 (28-29)	1 (30)	3 (28-30)
^{135}Cs	3 (31-33)	2 (34-35)	0	0	2 (36-37)
^{93}Zr	2 (38-39)	1 (40)	2 (41-42)	0	0
^{107}Pd	1 (43)	0	1 (44-45)	1 (46)	1 (46)
^{126}Sn	1 (47)	0	0	0	0
^{79}Se	0	0	0	0	0

3. Measurements at J-PARC/ANNRI

The Accurate Neutron-Nucleus Reaction Measurement Instrument (ANNRI) was built for nuclear data measurements using a neutron beam from the spallation neutron source in J-PARC [48,49]. Two types of γ-ray detectors were installed in ANNRI. In the upstream experimental area, a large Ge detector array was placed. The Ge detector array consists of two cluster Ge detectors and eight coaxial-type Ge detectors. BGO detectors for anti-Compton suppression were also implemented. This is the first time to use a large Ge detector array in neutron capture experiments with a spallation neutron source. High energy resolution of Ge detectors allows for detailed study on the neutron capture reaction. In the downstream experimental area, NaI(Tl) detectors were placed. Although NaI(Tl) detectors have a poor energy resolution comparing with Ge detectors, NaI(Tl) detectors have faster time response. It enables to measure capture cross sections in higher energy region than Ge detectors.

Moreover, independent measurements using the different types of detectors reduce systematic uncertainties.

Neutron capture cross section measurements for LLFPs are ongoing with ANNRI. Recent progress was reported in Refs. 50-52. These experiments demonstrated that the Ge detector array is a considerably powerful tool to remove impurity background and study the transition pattern of the neutron capture state. Nakamura et al. measured the neutron capture reaction of ^{107}Pd with the Ge detector array. They found previously misassigned resonances from prompt γ-ray energies. For ^{107}Pd, measurements with the NaI(Tl) detector were also performed and data analysis is ongoing. Kino et al. studied the prompt γ-ray spectra of ^{99}Tc with the Ge detector array [52]. It is found that the transition pattern at the first resonance was similar to that of the thermal capture but they were very different at higher energy resonances. Measurements and data analysis of ^{93}Zr and ^{129}I with ANNRI are also ongoing.

4. Summary

Experimental data of the neutron capture cross sections of LLFPs were briefly reviewed. Except for ^{99}Tc and ^{129}I, measurements for LLFPs were not performed extensively. Reliable experimental data of LLFPs are necessary to improve the nuclear data. Measurements and data analysis of the capture cross sections of LLFPs with the spallation neutron source in J-PARC are ongoing. Some of the recent progress has been already published. Further results of the J-PARC measurements will improve the nuclear data of LLFPs.

References

[1] N. Colonna et al., Nuclear Instruments and Methods in Physics Research B, 269, 3251 (2011).
[2] P. W. Lisowski and K. F. Schoenberg, Nuclear Instruments and Methods in Physics Research A, 562, 910 (2006).
[3] F. Maekawa et al., Nuclear Instruments and Methods in Physics Research A, 620, 159 (2010).
[4] N. J. Pattenden, Proceedings of 2nd International Conference on Peaceful Uses of Atomic Energy, Geneva, Vol. 16, p. 44 (1958).
[5] R. B. Tattersall et al., Journal of Nuclear Energy 12 A, 16 (1960).
[6] H. Pomerance, Technical Report ORNL-1975, 31, 5509, Oak Ridge National Laboratory (1975).
[7] V. V. Ovechkin et al., Proceedings of Conference on Neutron Physics, Kiev 1973, Vol. 2, p. 131 (1974).
[8] M. Lucas et al., IAEA-TC-119/14, p. 407 (1977).

[9] H. Harada et al., Journal of Nuclear Science and Technology, 32, 395 (1995).
[10] G. L. Molnar et al., Radiochimica Acta, 90, 479 (2002).
[11] K. Furutaka et al., Journal of Nuclear Science and Technology, 41, 1033 (2004).
[12] T. Watanabe and S. D. Reder, Journal of Nuclear Science and Engineering, 41, 188 (1970).
[13] F. Gunsing et al., Proceedings of Conference on Nuclear Data for Science and Technology, Trieste, Vol. 2, p. 1293 (1997).
[14] F. Gunsing et al., Physical Review C, 61, 054608 (2000).
[15] Yu. V. Adamchuk et al., Yaderno-Fizicheskie Issledovaniya Rports, 18, 12 (1974).
[16] R. C. Little and R. C. Block, Transactions of the American Nuclear Society, 26, 574 (1977).
[17] R. L. Macklin and R. R. Winters, Nuclear Science and Engineering, 81, 520 (1982).
[18] Raepsaet et al., Proceedings of Conference on Nuclear Data for Science and Technology, Trieste, Vol. 2, p. 1289 (1997).
[19] K. Kobayashi et al., Nuclear Science and Engineering, 146, 209 (2004).
[20] J. C. Chou et al., Journal of Nuclear Energy, 27, 811 (1973).
[21] T. Matsumoto et al., Journal of Nuclear Science and Technology, 40, 61 (2003).
[22] J. Roy and D. Wuschke, Canadian Journal of Chemistry, 36, 1424 (1958).
[23] N. J. Pattenden, Nuclear Science and Engineering, 17, 371 (1963).
[24] S. Nakamura et al., Journal of Nuclear Science and Technology, 33, 283 (1996).
[25] M. I. Krivopustov et al., Int. Sem. on Interaction of Neutrons with Nuclei, 5, 390 (1997).
[26] T. Belgya et al, International Conference on Nuclear Data for Science and Technology, Vol. 1, 631 (2007).
[27] J. A. Harvey et al., Proceedings of the Second International Atomic Energy Conference, Geneva, Vol. 16, 150 (1958).
[28] R. L. Macklin, Journal of Nuclear Science and Engineering, 85, 350 (1983).
[29] G. Noguere et al., Journal of Nuclear Science and Technology, Supplement 2, 184 (2002).
[30] G. Noguere et al., Physical Review C 74, 054602 (2006).
[31] N. Sugarman, Physical Review, 75, 1473 (1949).
[32] A. P. Baeg et al., Canadian Journal of Physics, 36, 863 (1958).
[33] T. Katoh et al., Journal of Nuclear Science and Technology, 34, 431 (1997).
[34] H. H. Jung et al., Proceedings of Nuclear Data for Reactors Conference, Helsinki, Vol. 1, p. 679 (1970).
[35] V. A. Anufriev et al., Atomnaya Energiya, 63, 346 (1987).; V. A. Anufriev et al., Soviet Atomic Energy, 63, 851 (1988).
[36] S. Jaag et al., Nuclear Physics A, 621, 247 (1997)

[37] N. Patronis et al., Physical Review C 69, 025803 (2004).
[38] H. Pomerance, Oak Ridge National Laboratory Reports, No. 1987, p. 50 (1955).
[39] S. Nakamura et al., Journal of Nuclear Science and Technology, 44, 21 (2007).
[40] R. L. Macklin et al., Nuclear Science and Engineering, 92, 525 (1986).
[41] R. L. Macklin, Astrophysics and Space Science, 115, 71 (1985).
[42] G. Tagliente et al., Physical Review C 87, 014622 (2013).
[43] S. Nakamura et al., Journal of Nuclear Science and Technology, 44, 103 (2007).
[44] U. N. Singh et al., Nuclear Science and Engineering, 67, 54 (1978).
[45] V. A. Anufriev et al., Proceedings of All Union Conference on Neutron Physics, Kiev, Vol. 2, p. 156 (1980).
[46] R. L. Macklin, Nuclear Science and Engineering, 89, 79 (1985).
[47] S. Zhang, et al., Radiochimica Acta, 94, 385 (2006).
[48] M. Igashira et al., Nuclear Instruments and Methods in Physics Research A, 600, 332 (2009).
[49] Y. Kiyanagi et al., Journal of the Korean Physical Society, 59, 1781 (2011).
[50] S. Nakamura et al., Journal of the Korean Physical Society, 59, 1773 (2011).
[51] S. Nakamura et al., Nuclear Data Sheets, 119, 143 (2014).
[52] K. Kino et al., Nuclear Data Sheets, 119, 140 (2014).

4. Cross-sections and Uncertainty Estimation through the R-matrix Analysis

S. Kunieda, K. Shibata and T. Fukahori
Japan Atomic Energy Agency, Tokai-mura, Naka-gun, Ibaraki 319-1195, Japan

T. Kawano, M. Paris and G. Hale
Los Alamos National Laboratory, Los Alamos, New Mexico 87545, USA

An R-matrix analysis is demonstrated for ^{17}O system to estimate ^{16}O neutron cross-sections with uncertainty in the resolved resonance range, where we try to effectively impose physical constraints to behaviors of the parameters and hence the cross-sections. Preliminary results suggest our present approach may reduce uncertainty caused by the differences among experimental and evaluated data.

1. Introduction

The R-matrix theory is straightforward to the quantum mechanics. Since the collision matrix derived from the R-matrix theory is the unitary, it brings physical constraints to behavior of the parameters and hence the cross-sections to be calculated. By imposing such a constraint effectively in the analysis, we may understand the causes of differences which still remain among the experimental and evaluated cross-sections. We are developing A MUlti-channel R-matrix code AMUR which is based on the Wigner-Eisenbud's formalism [1]. Although the photon channel is not included yet in the current version, it can be applied to the analysis for the light nuclei since the radiative capture cross-section is small as negligible. In this study, we have two purposes as follows.

One objective is to show the evidence of the physical constraint from the R-matrix theory. It is important to thoroughly understand the nature in the theory since we introduce some experimental parameters in the R-matrix fit to correct the measured values as described in the main text. It is also essential to present the accountability of uncertainty/covariance data to be obtained from the analysis. The second one is to present practical use of the physical constraint in the cross-section analysis. We demonstrate an R-matrix analysis for ^{17}O system to estimate the neutron cross-section of ^{16}O with uncertainty/covariance in the resolved resonance energy range. The reasons we focus on this isotope are as follows.

- The oxygen is one of the important materials in the nuclear applications, e.g., neutronics for the criticality safety, shielding design, and so on. The isotope is also a typical light nucleus to which our R-matrix code should be applied as the neutron capture cross-section is in the order of micro-barn.
- There are discrepancies among experimental data which make the present evaluations still uncertain. For typical example, those problems have been found for total cross-sections in lower energy range and $^{16}O(n,\alpha)^{13}C$ reaction cross-sections. Those are recognized in the world as listed in the CIELO (Collaborative International Evaluated Library Organization) pilot project [2].
- The uncertainty/covariance of the evaluated cross-section is required to estimate the margin of integral calculations. It is also important for the quality assurance of nuclear data themselves. However, so-called "low-fidelity" data are given in the present libraries for most of the light nuclei. For ^{16}O evaluations, they are inferred only from experimental information.

The paper briefly describes our preliminary results, and complements the other reports elsewhere [3,4].

2. Physical Constraint from the R-matrix theory

The collision matrix calculated from the R-matrix theory is the unitary. This ensures not only the flux conservation but also holds the explicit channel-channel correlation. Figure 1 illustrates the correlation matrices for ^{16}O neutron total cross-sections and $^{16}O(n,\alpha)^{13}C$ which we obtained in our preliminary analysis. We can see strong medium-range correlations among the different neutron energies. This is substantially because of the interference effect among the large resonances with the same spin-parity. That suggests the theory may complement a missing or an insufficient knowledge in experimental data. One also notices the traces of the unitarity limit where the correlation matrix elements sharply drop into nearly zero. The positions correspond with the peak energy of each resonance. That means the value of cross-section is constrained strongly at around peak positions. In other word, the cross-sections are nearly independent of the theoretical parameters very near the peak energies. As physical constraints certainly exist, we are making use of such intrinsic nature of the theory in our analysis to estimate more reasonable cross-sections with covariance.

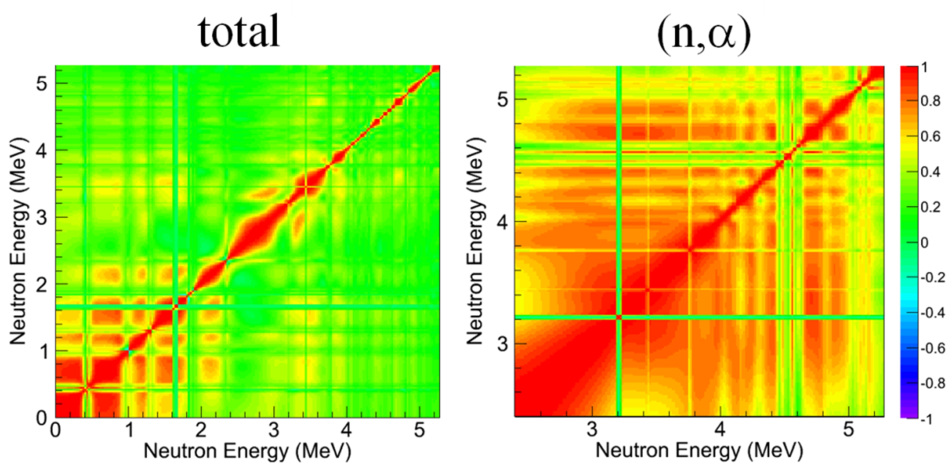

Fig. 1 : Correlation matrices for ^{16}O total and $^{16}O(n,\alpha)^{13}C$ cross-sections preliminary obtained in this study

3. Differences among Experimental Data

There are differences among measurements more or less. As long as we strongly rely on experimental data in the evaluation with less theoretical knowledge, such experimental differences make the evaluated cross-section uncertain.

In neutron total cross-section for ^{16}O, "3% difference" is observed below E_n~100 keV down to the thermal energy region where the measured values of Ohkubo [5] and Johnson et al. [6] are larger than the other experimental numbers [7-10]. Both ENDF/B-VII.1 [11] and JENDL-4.0 [12] follow the data of Ohkubo, however, Ohkubo himself has already pointed out that there would be plausible water contamination in the Al_2O_3 sample since it was in powder. Johnson et al. has also given similar comment in the literature. Therefore, the both evaluations are, most likely larger by ~3% than the true value, although there is not enough evidence at this stage.

Typical differences are also seen in measured $^{16}O(n,\alpha)^{13}C$ and/or the inverse reaction cross-sections where the recent experimental data are ~30% lower than the old measurements systematically. Indeed, ENDF/B-VI.x was evaluated based on the old data measured by Bair and Haas [13], but values were just normalized so as to follow the recent data of Harissopulos et al. [14] when switching to the ENDF/B-VII.0. The situation is essentially same in the JENDL evaluations. Such an approach just relies on measurements, but we believe both the experimental and theoretical knowledge should be reflected in the evaluation.

4. Analysis for ^{17}O Compound System

In this work, the maximum neutron energy is set to 5.2 MeV to study a simple case. The threshold energy of the $^{16}O(n,\alpha_0)^{13}C$ reaction is about 2.4 MeV, and the other reactions are still closed below 5.2 MeV. Therefore, we consider two partitions in this R-matrix analysis: n+$^{16}O_{g.s.}$ and α+$^{13}C_{g.s.}$. For the spin-parity assignments of the compound nucleus ^{17}O, we followed those given in the latest version of Nuclear Data Sheets except for a few minor levels. We considered levels of J^π = 1/2$^\pm$, 3/2$^\pm$, 5/2$^\pm$ and 7/2$^\pm$ which can be excited by the incoming partial waves of l=0 to 4. The R-matrix parameters to be searched for are the channel radii, reduced width amplitudes and the energy eigenvalues for compound nucleus ^{17}O. The contributions from the negative and distant levels are also treated as parameters, except for J^π = 5/2$^\pm$ and 7/2$^\pm$ in which the distant effect is found to be small as negligible.

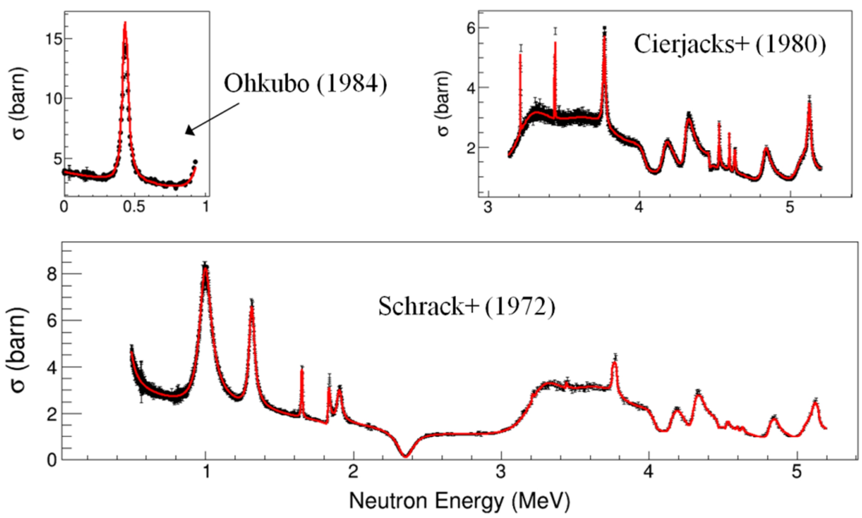

Fig. 2 :　Some of the fitted results for neutron ^{16}O total cross-sections

We analyze six sets of measured total cross-sections [5,6,15-18] and a recent measurements of $^{13}C(n,\alpha)^{16}O$ reaction cross-sections [14]. Since there are systematic differences among the measurements more or less, we introduced a renormalization factor to each measurement. The factor is one of the parameter to be searched for in the fitting procedure. Since the water contamination is likely remained in the data of Ohkubo and Johnson et al., the effective (scaled) hydrogen cross-sections are added to the theoretical calculations. The hydrogen cross-sections were taken from ENDF/B-VII.1, and the normalization value is treated as a parameter to be searched for in the fitting procedure. The fitting itself is quite successful as illustrated in Fig. 2 and 3 as examples. The R-matrix parameters are searched for together with experimental parameters with the least-square method based on the Bayes' theorem, where the calculations are broadened with experimental resolutions. The total χ^2/N value obtained is ~3.0, which means the spin-parity numbers given in ENDSF are consistent with experimental cross-sections we analyzed. In this paper, we present only the results of the experimental parameters in the next section because of the limitation of paper length.

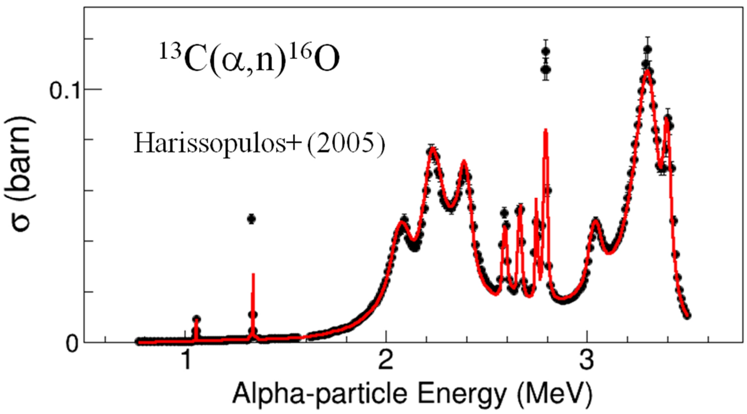

Fig. 3 : Fitted results for $^{13}C(\alpha,n)^{16}O$ cross-sections

5. Values of Experimental Parameters obtained

The renormalization parameter obtained for each total cross-section measurement is in-between 0.967 and 1.032 with uncertainty of less than 0.35%. Such near unity values suggest that the calculations and all the total cross-section measurements we used are consistent with the theory. It is noticeable that the uncertainties obtained are very small as less than 0.35%, which shows how strong the physical constraint from R-matrix theory is in the fitting procedure.

The situation is found to be different for $^{13}C(\alpha,n)^{16}O$ reaction where the renormalization value obtained is 1.52±1.1% for the recent measurements. That is, present renormalization values (hence the cross-sections) are consistent with old measurement of Bair and Haas, despite we analyzed only the recent measurements. Since the theory always holds the flux conservation, such large normalization values are guided so as to be consistent with the total cross-sections. That may suggest there is an inconsistency between a number of experimental total cross-sections and the recent measurements of $^{13}C(\alpha,n)^{16}O$ reaction cross-sections.

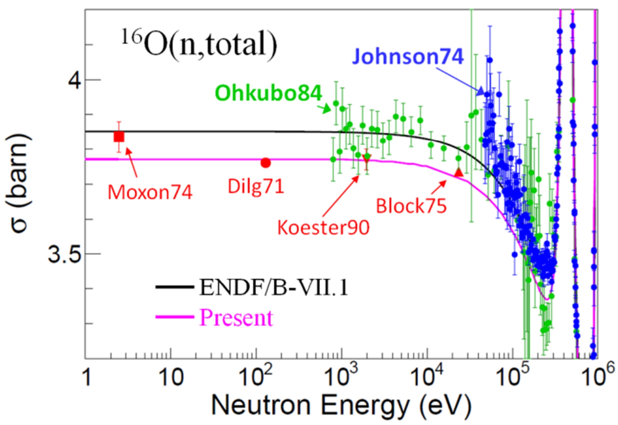

Fig. 4 : Estimated total cross-sections with experimental data in lower energy range

The normalization values to the hydrogen cross-section are found to be 0.0099±8.4% and 0.0167±6.0% for experimental data of Ohkubo and Johnson et al., respectively. The corresponding effective hydrogen cross-sections are 205±17 mb and 346±21 mb at thermal energy, respectively. Figure 4 shows calculated total cross-section together with experimental data in lower energy range. The present R-matrix calculation, without the contribution of hydrogen, is found to be consistent with most of the other experimental numbers. Those results suggest the present evaluation should be reduced by ~3% in the lower energy region.

6. Preliminary Results of Cross-sections with Uncertainty

The covariance of cross-sections is preliminary obtained by propagating those for the theoretical parameters only. Figure 5 illustrates the present results of total cross-sections with uncertainty. Again, we can still see traces of unitary limit at some peak positions where the uncertainty value is strongly reduced. The uncertainty values we obtained are about 0.5% on average. This is smaller than those given in the experimental data, which is a consequence of physical constraint from R-matrix. For $^{16}O(n,\alpha)^{13}C$ reaction cross-sections, we obtained uncertainty value of about 2.5% on average in spite of a large difference between the old and recent measurements.

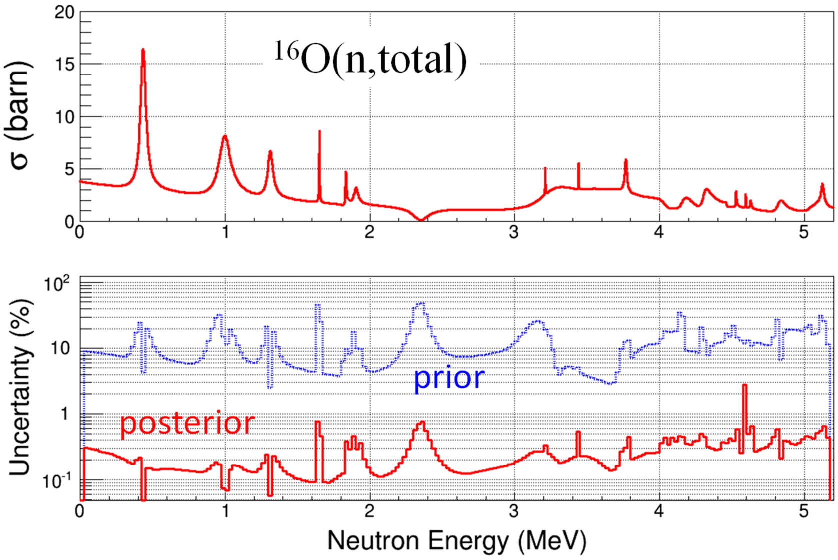

Fig. 5： Estimated total cross-sections with uncertainty

7. Summary and Outlooks

An R-matrix analysis was demonstrated for ^{17}O system to estimate the neutron cross-sections of ^{16}O with uncertainty in the resolved resonance range. Introducing the experimental parameters, we effectively impose the physical constraints to the analysis. Preliminary results suggested the present approach may solve/reduce uncertainty caused by the differences among experimental and evaluated data. The cross-sections and covariance/uncertainty we obtained mirror both the experimental and theoretical knowledge.

To obtain a complete set of cross-sections data, we are analyzing/calculating angle-differential cross-sections with covariance. Also, upper energy limit will be extended by considering in-elastic scattering channels. Once we complete a case study for ^{17}O system, the similar approach will be applied to the analysis for the other systems. For calculation of radiative capture cross-sections, we are planning to incorporate the Reich-Moore approximation [19] as a first step.

Acknowledgements

The authors would like to thank Drs. A. Plompen (IRMM) and C. Lubitz (KAPL) who provided us very useful experimental knowledge. One of the authors S.K. is also grateful to Dr. O. Iwamoto (JAEA) who gave us valuable comments on this work.

References

1. E. P. Wigner and L. Eisenbud, Phys. Rev. 72, 29 (1947).
2. M. B. Chadwick et al., Nuclear Data Sheets, 118, 1 (2014).
3. S. Kunieda, T. Kawano, M. Paris, G. Hale, K. Shibata, T. Fukahori, Nuclear Data Sheets, 118, 250 (2014).
4. S. Kunieda, T. Kawano, M. Paris, G. Hale, K. Shibata, T. Fukahori, NEA/NSC/DOC, 13 (2014).
5. M. Ohkubo, JAERI-M 86-193, (1987).
6. C. H. Johnson, L. A. Galloway, J. L. Fowler and N. W. Hill, ORNL-4937 (1973).
7. W. Dilg, L. Koester, W. Nistler, Phys. Lett., B36, 208 (1971).
8. M. C. Moxon, D. A. J. Endacott, J. E. Jolly, A.E.R.E. Harwell Reports, No.20, p.29 (1974), UK.
9. R. C. Block, Y. Fujita, K. Kobayashi, T. Oosaki, J. Nucl. Sci. Technol., 12, 1 (1975).
10. L. Koester, W. Waschkowski, J. Meier, Z. Phys. A, 337, 341 (1990).
11. M. B. Chadwick et al, Nucl. Data Sheets 112, 2887 (2011).
12. K. Shibata et al., J. Nucl. Sci. Technol. 48, 1 (2011).
13. J. K. Bair and F. X. Haas, Phys. Rev. C7, 1356 (1973).
14. S. Harissopulos, H. W. Becker, J. W. Hammer, A. Lagoyannis, C. Rolfs, F. Strieder, Phys. Rev. C72, 062801 (2005).
15. S. Cierjacks, P. Forti, D. Kopsch, L. Kropp, J. Nebe and H. Unseld, Kernforschungszentrum Karlsruhe Reports, No.1000 (1968).
16. R. A. Schrack, R. B. Schwartz and H. T. Heaton, Bulletin of the American Physical Society 17, 555 (1972).
17. F. G. Perey, T. A. Love, W. E. Kinney, Oak Ridge National Lab. Reports 4823 (1972).
18. S. Cierjacks, F. Hinterberger, G. Schmalz, D. Erbe, P. V. Rossen, and B. Leugers, Nucl. Instr. Meth., 169, 185-198 (1980).
19. C. W. Reich and M. S. Moore, Phys. Rev. 111, 929 (1958).

5. Cross-section Measurement in Pohang Neutron Experimental Facility

Ayano Makinaga[1], Guinyun Kim[3], Man-woo Lee[2], Kwang-Soo Kim[3], Muhammad Zaman[3], Muhammad Shahid[3], Sung-Gyun Shin[4], Mooh-Hyun Cho[4], Hidetoshi Akimune[5]
[1]Faculty of Science, Hokkaido University, Sapporo 060-0810, Japan
[2] Research Center, Dongnam Institute of Radiological and Medical Science, Busan 619-953, Korea
[4]Center for High Energy Physics, Kyungpook National University, Daegu 702-701, Korea
[5]Division of Advanced Nuclear Engineering, Pohang University of Science and Technology, Pohang 790-784, Korea
[2]Department of Physics, Konan University, Kobe 658-8501, Japan

*E-mail: makinaga@nucl.sci.hokudai.ac.jp

The Pohang Neutron Facility (PNF) was proposed in 1997 and constructed at the Pohang Accelerator Laboratory in 1998. A 100-MeV electron linac is located in the tunnel beside the 3 GeV Pohang Light Source (PLS) facility. The 100-MeV electron linac consists of RF-gun or by triode thermionic gun, an alpha magnet, four quadrupole magnets, two SLAC type accelerating sections, a quadrupole triplet, and a beam analyzing magnet. Neutron transmission, neutron capture and photon induced activation experiments can be performed by using the 100-MeV electron linear accelerator. In this report, recent measurement of the neutron total cross sections and photon induced activation experiments are introduced.

1. Introduction

Nuclear data are fundamental knowledge for the nuclear application such as nuclear transmutation technique, nuclear medicine, and nuclear astrophysics. Since 1997 [1-3], the Pohang Neutron Facility (PNF) begun to provide a pulsed neutron beam based on a 100-MeV electron linear accelerator. Its main purpose is to obtain the total neutron cross sections, neutron activation cross sections. PNF also provides bremsstrahlung photon beam for the photo activation experiments with the electron energy range from 45 to 100 MeV. Examples are shown below [4, 5].

- Neutron total cross sections: ^{93}Nb, ^{nat}Mo
- Neutron capture cross section: ^{165}Ho
- Neutron activation cross sections: ^{165}Ho, ^{197}Au, ^{115}In
- Photon activation experiments: ^{nat}Sb, ^{nat}Pb, ^{nat}Cd, ^{55}Mn, ^{197}Au, ^{93}Nb, ^{209}Bi, ^{232}Th, ^{238}U, ^{89}Y

In section 2 and 3, we introduce the recent results of the neutron transmission experiment on ^{nat}Sn and photon activation experiment on ^{197}Au.

2. Neutron Time of Flight Experiment at Pohang Accelerator Laboratory

The electron linac was operated with a repetition rate of 10 Hz, a pulse width of 1.0 μs and the electron energy of 60 MeV. The peak current in the beam current monitor located at the end of the second accelerator section was above 50 mA. Neutrons are produced via photo nuclear reaction of ^{181}Ta by using the bremsstrahlung photon with an electron beam. A water cooled Ta radiator system for the photo neutron source consists of ten Ta plates with a diameter of 4.9 cm and an effective thickness of 7.4 cm. There was a 0.15-cm water gap between Ta plates to cool the Ta plates effectively. Neutron yield per kW of beam power was estimated as 2.0×10^{12} n/sec on the Ta target [6-11].

A samples is located at the middle of the neutron guide tube which is placed perpendicularly to the electron beam. Neutrons were collimated by using shields made of H_3BO_3, Pb and Fe in the guide tube. A neutron detector was placed at the end of the guide tube. Set of notch filters, which consists of Co, In, and Cd plates with thickness of 0.5 mm, 0.2 mm, and 0.5 mm, was used for the back ground determination, and also for the energy calibration. Samples in the transmission experiment were automatically changed in every 5 minutes by using a sample changer. A ^{6}Li-ZnS(Ag) scintillation counter BC702 supplied by Bicron (Newbury, Ohio) with a diameter of 127 mm and a thickness of 15.9 mm mounted on an EMI-93090 photomultiplier was used as a detector for the neutron TOF spectrum measurement. The detection efficiency of the neutron detector was $\varepsilon_{eff}=1-\exp\{-N\sigma(0.0253/E_n)^{0.5}\}$ with σ=945 barn of the ^{6}Li(n, α)^{3}H reaction. Figure 1 shows recent our results of the n-TOF experiment for a natural Sn sample which have already been reported in [12].

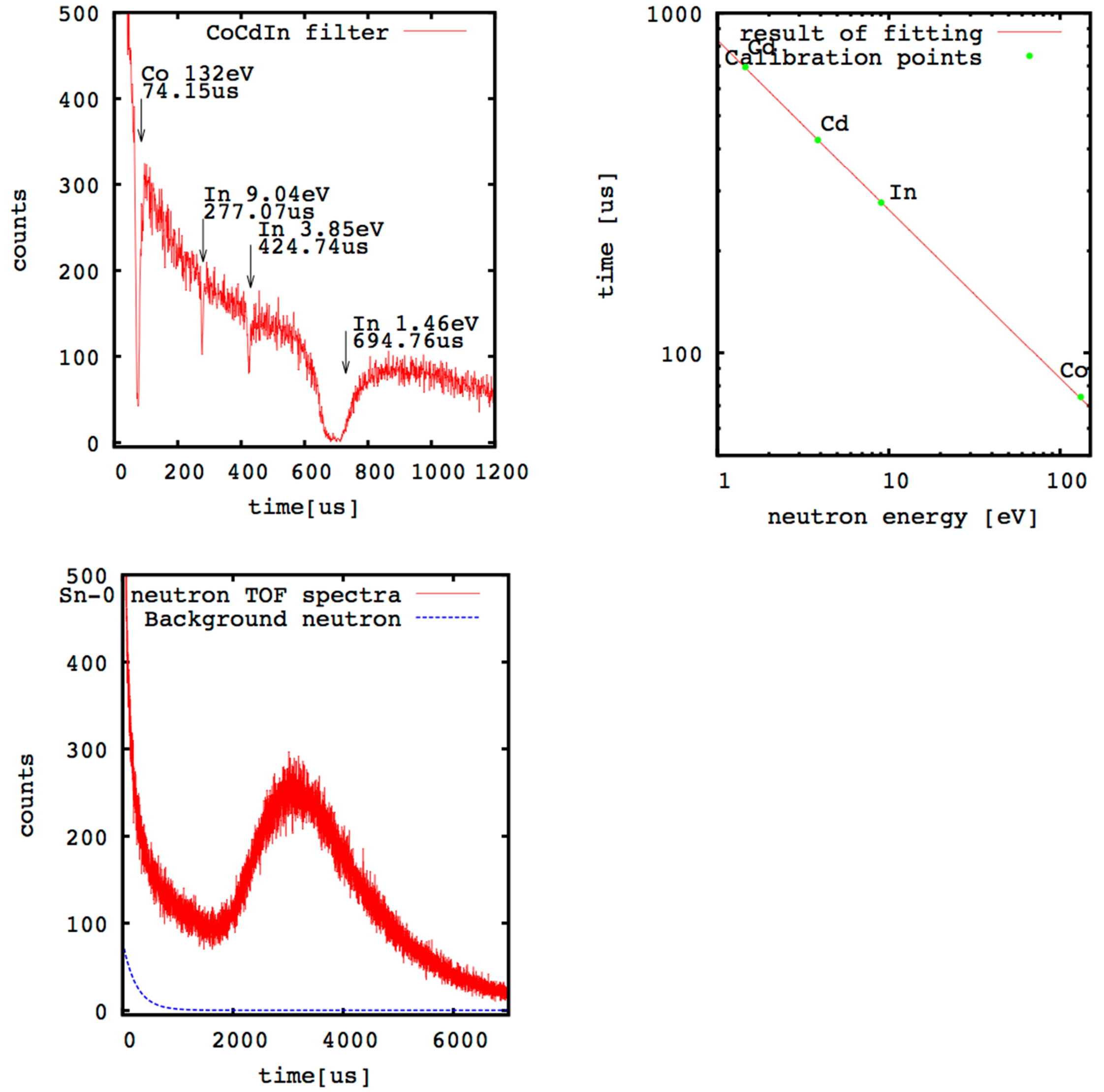

Figure 1. An example of n-TOF experiment for ^{nat}Sn. Left and Right: A CoInCd notch filter for energy calibration. Lower panel: n-TOF spectrum for ^{nat}Sn [12].

3. Photonuclear reaction experiment at Pohang Accelerator Laboratory

The electron linac was also used to produce bremsstrahlung x-ray in the energy range between 45-100MeV. While photonuclear reaction are well-studied around the energy of 25 MeV where the giant dipole resonance (GDR) is concerned, a small number of nuclear data for the inter-mediate energy regions are only available, and also have large uncertainties. In the Pohang, photon activation experiments have been actively performed to obtain the information of cross sections for (γ, n), (γ, 2n), (γ, 3n), (γ, 4n) and so on [4, 5]. Figure 2 shows an example of a photo activation experiment on ^{197}Au. Bremsstrahlung was produced by bombardment of 65 MeV electrons to W target in 0.1 mm in thickness. A Gold-197 samples was positioned at 18 cm downstream from the W target. As a flux monitor, ^{27}Al (γ, 2pn) ^{24}Na reaction was used. The electron current during the irradiation was ~35 mA and reputation rate was 15 Hz. After the 30 min irradiation, an activated ^{197}Au sample was measured by a HPGe detector. The energy and the efficiency calibration were performed by using ^{152}Eu γ–ray standard source. The activated ^{197}Au sample emits the γ-rays due to the ^{197}Au (γ, n) ^{196}Au, ^{197}Au (γ, 3n) ^{194}Au, ^{197}Au (γ, 4n) ^{193}Au and ^{197}Au (γ, 5n) ^{192}Au reactions, and that were clearly observed in its γ-ray spectrum.

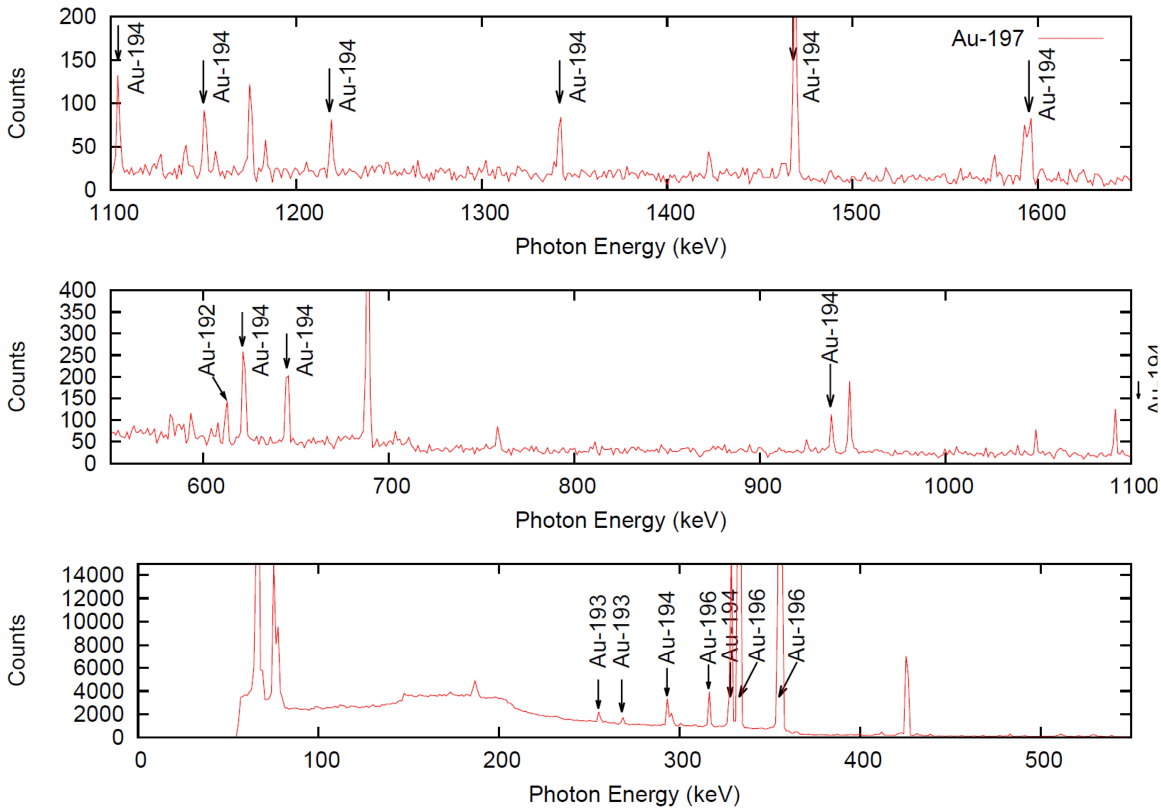

Figure 2. Typical γ-ray spectrum obtained from irradiated ^{197}Au samples together with ^{27}Al flux monitor. Bremsstrahlung energy was 65 MeV.

4. Summary

Neutron transmission experiments on natural Sn and Ni were performed at the Pohang Neutron Facility installed with a 100-MeV electron linac in Korea. The neutrons were produced via photo nuclear reaction of Ta and cooled in the water moderator, which lead to an energy range from 0.1 eV to 100 eV. Transmitted neutrons were detected with the ^{6}Li-ZnS (Ag) scintillator BC702 by using the time of flight method. We also introduced recent result of the photo activation experiment on ^{197}Au by using the bremsstrahlung photon beam. Detailed analysis is needed in the near future.

Acknowledgments

We thank the staff of the PAL accelerator for their cooperation during the experiments. The author also thanks Profs. K. Kato and M. Aikawa (Hokkaido Univ.), and Dr. N. Otsuka (IAEA) for their discussion on the nuclear data. This research as partly supported by the National Research Foundation of Korea (NRF) through a grant provided by the Korean Ministry of Education, Science & Technology (MEST) in 2011 (Project No.2011-0006306 and No. 2011-0025762), by the Institutional Activity Program of Korea Atomic Energy Research Institute, and by the World Class University (WCU) program (Grant No. R31-30005).

Reference

[1] Kim G *et al.* Measurement of the neutron total cross sections of Ta and Mo and proton induced reaction cross sections of ^{nat}Mo. Proc. ND2007 - International Conference on Nuclear Data for Science and Technology. 2007 April 22-27; Nice (France).
[2] Devan K *et al*. Photo-neutrons produced at the Pohang neutron facility based on an electron linac. Journal of the Korean Physical Society. 2006; 49(1):88.
[3] Kim G *et al.* Proc. the International Conference on Nuclear Data for Science and Technology. 1997:556.
[4] Kim G. Recent Activities of Nuclear Data Measurement in Korea. Proc. The 3rd Asian Nuclear Reaction Database Development Workshop.2012 August 27-29; Pohang (Korea).
[5] Zaman M *et al*. Measurement of photo-neutron cross-sections of 89Y with bremsstrahlung energies of 45 and 55 MeV. Journal of Radioanal Nuclear Chemistry. 2014; 299(3):1739.
[6] Kang S *et al*. Beam Acceleration Results of Test Linac. Proc. the First Asian Particle Accelerator Conference.1998 March 23-27; Tsukuba (Japan).
[7] Kim G *et al*. Measurement of photoneutron spectrum at Pohang Neutron Facility. Nuclear Instruments and Methods in Physics Research A. 2002; 485(3):458.
[8] Meaze A *et al*. Measurements of the neutron total cross-sections of tantalum by using pulsed neutrons based on an electron linac. Journal of Korean Physics Society.2006; 48(4):827.
[9] Lee Y *et al*. The status of neutron total cross-section measurement by using 100-MeV electron linear accelerator for nuclear data production in Korea. Radiation Measurements. 2002; 35:321.
[10] Baek W *et al*. Design of the photoneutron target for pulsed neutron sources at PAL. Proc. Workshop on Nuclear Data Production and Evaluation; 1998 August 7-8; Pohang (Korea).
[11] Kim G *et al*. Status of the pulsed neutron source with the 100-MeV electron linac at the Pohang accelerator laboratory. J. Accel. Plasma Res. 1999; 3(1):9.
[12] Makinaga A *et al*. Neutron Total Cross-section Measurements on Sn and Ni using Pohang Neutron Facility. Proc. The 2012 Symposium on Nuclear Data; 2012 November 15-16; Kumatori (Japan).

6. Nuclear Data Application in Monju

Taira HAZAMA

FBR Safety Technology Center
Japan Atomic Energy Agency
1 Shiraki, Tsuruga, Fukui pref., 919-1279, Japan
E-mail: hazama.taira@jaea.go.jp

Abstract

Various nuclear data have been applied to the reactor physics test analyses in Monju. Good accuracy is confirmed with JENDL-3.3 for the analysis of reactor physics tests performed in 1994-1995. On the other hand, a clear discrepancy is observed for the reactivity loss caused by the ^{241}Pu decay from 1994 to 2010. The discrepancy is resolved with JEDNL-4.0, where the revision of the ^{241}Pu fission cross section and ^{241}Am capture cross section contributes.

Use of covariance data is promising application in the future design calculation. Based on the reactor physics test analyses, the reliability of the covariance data is investigated and covariance data that needs improvement are extracted. It is suggested that data on the average cosine of the scattering angle of ^{23}Na need to be improved.

1. Introduction

Monju is the Japanese prototype fast breeder reactor with an electric power of 280MWe (Figure 1). The core fuel region is divided into two Pu-enrichment zones with the Pu fissile enrichment around 15wt% and 20wt% for the inner and outer cores, respectively. The core fuel region is surrounded by blanket and neutron shielding regions in the radial and axial directions.

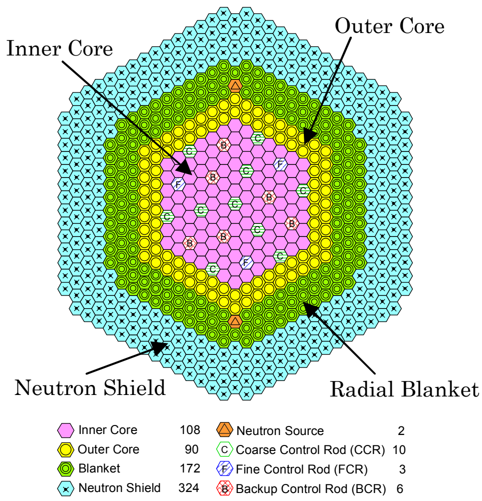

Reactor type	Sodium-cooled Fast Reactor, loop-type
Thermal output	714 MW
Electrical output	280 MW
Fuel type	Plutonium-uranium mixed oxide
Core Dimensions	
Equivalent diameter Approx.	1,800 mm
Height	930 mm
Volume	2,340 liters

Figure 1 Core specifications of Monju

The history of the nuclear data application in Monju started in the design (licensing) calculation applied in 1980, where nuclear data ENDF/B-II and III were employed. In 1994, reactor physics tests started and the initial criticality was achieved. The core parameters were predicted with JENDL-2 together with the E/C biasing based on the mockup critical experiments as those obtained in ZEBRA critical assembly. The discrepancy in the keff value for the initial full loading core was -0.1%Δk/k with the biasing and -0.7%Δk/k without the biasing. Since then various nuclear data have been applied to the analysis of reactor physics tests in Monju. In the present paper, the nuclear data application in the reactor physics test analysis is summarized and a request to nuclear data is discussed.

2. Application in the reactor physics test

2.1. Calculation method

The calculation is based on the detailed deterministic calculation scheme developed through the analysis of critical assemblies for fast reactors [1]. In general, the calculation accuracy is determined by that of the calculation methodology and that of the nuclear data libraries. The former accuracy has been confirmed to be sufficiently smaller than the latter through comparison with continuous energy Monte Carlo calculations [2]. At present, the calculation accuracy is mainly dominated by that of nuclear data.

2.2. Reactor physics tests in 1994-1995

The reactor physics test in Monju started in 1994 and a variety of core parameters had been measured until the sodium leakage accident occurred in December 1995. After the tests, the validity of the calculation system has been investigated for major physical parameters, such as criticality, control rod worth, isothermal temperature coefficient, fixed absorber reactivity worth, fuel sub-assembly reactivity worth, coolant reactivity worth, power coefficient, burnup coefficient, and reaction rate distribution. JENDL nuclear data is mainly employed in the investigation, starting from JENDL-3.2 (1996) to JENDL/AC-2008 (2008) according as the update of JENDL. The accuracy with JENDL-3.3 (2002) was confirmed within the experimental uncertainties (1σ) in most of the parameters [2,3]. In particular, the excellent result is obtained in the criticality (keff) with the accuracy less than 0.1%Δk/k.

Most of the reactor physics data employed was evaluated in the early days of the tests and some corrections applied to the measured value can be more accurately and precisely evaluated by introducing the calculation system available today. In addition, correlation information among data was not evaluated in the existing data. We will re-evaluate all the data in the high level recommended in the international data evaluation project as IRPhEP [4] for more reliable and detailed validation of nuclear data.

2.3. Reactor physics tests in 2010

In 2010, Monju restarted after 14-year's interruption. The prediction of the criticality was performed as in Figure 2 with JENDL-3.3 and the E/C biasing based on the tests carried out in 1994. In addition, various nuclear data (JENDL/AC-2008, ENDF/B-VII.0, and JEFF-3.1) were referred to assure the prediction accuracy for a large reactivity loss due to the ^{241}Pu decay and resulting ^{241}Am accumulation in which a large uncertainty was expected in JENDL-3.3. The covariance data in JENDL-3.3 was employed to evaluate uncertainty of the predicted value.

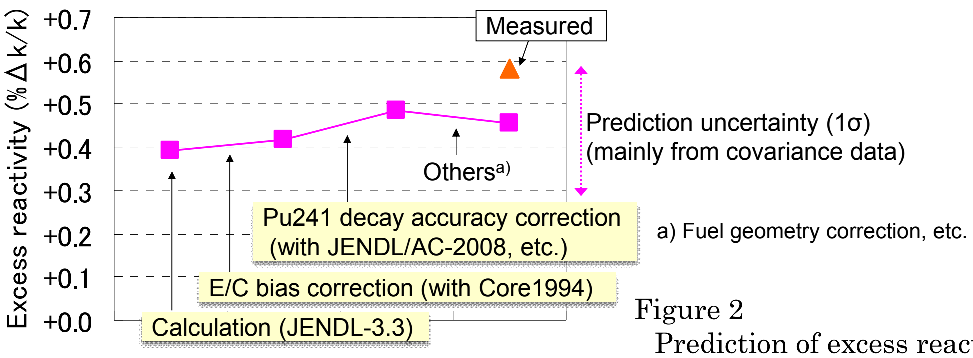

Figure 2
Prediction of excess reactivity in 2010 [5]

The excess reactivity was predicted as 0.45%Δk/k for the measured value of 0.58%Δk/k. The discrepancy is comparable to the experimental uncertainty of 0.13%Δk/k.

However, when we focus on the calculation accuracy of the cores measured in 1994 and 2010, an obvious discrepancy appears [6]. Figure 3 compares the change in the C-E values on the keff at critical state, that is, the C-E value for the core in 1994 minus that for the core in 2010. Four nuclear data files are applied in the calculation and the result by JENDL-3.3 shows the obvious discrepancy of 0.15%Δk.

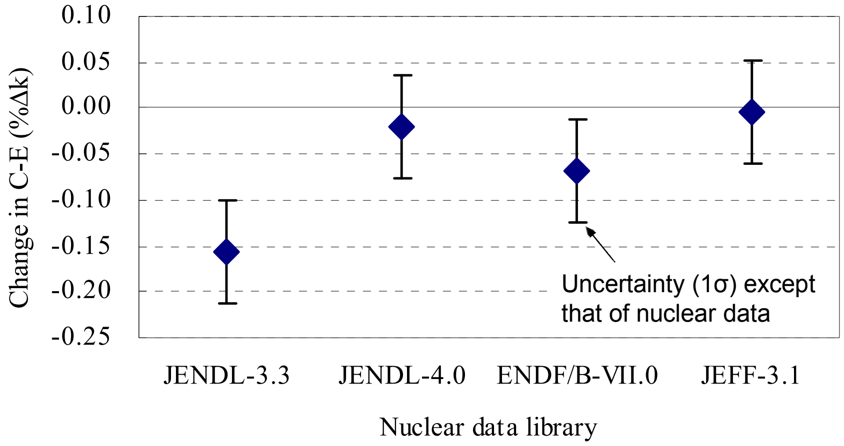

Figure 3 Change in calculation accuracy for criticality from Core1994 to Core2010 [6]

Figure 4 analyses the difference among the four nuclear data by sensitivity analysis. The change of the C-E value from that by JENDL-3.3 is illustrated by nuclide and reaction. The change mainly appears in ^{241}Pu and ^{241}Am, whose compositions were the major differences between the cores. It is interesting that the results of JENDL-4.0 and JEFF-3.1, both showing perfect agreement in Figure 3, come from different contributions. The contribution of ^{241}Am capture is almost common but the remaining major contribution is made by ^{241}Pu fission in JENDL-4.0 whereas by ^{241}Am ν (number of fission neutrons) in JEFF-3.1.

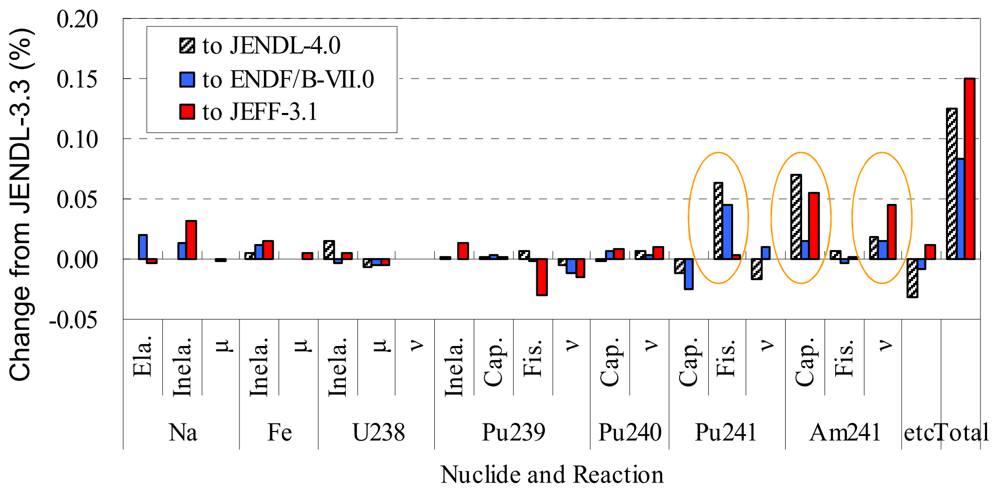

Figure 4 Comparison among nuclear data on the change in calculation accuracy [6]

The other reactor physics parameters, control rod worth and isothermal temperature reactivity do not show clear differences among nuclear data. We will continue the validation of nuclear data with the accumulation of Monju experimental data in the future.

3. Application of covariance data

3.1. Expected accuracy with JENDL-4.0 and Monju reactor physics tests

Based on the analysis results of Monju reactor physics tests, we can estimate the calculation accuracy achievable in the future licensing calculation. We can expect satisfactory accuracy especially for the criticality and control rod worth as follows.

(Criticality)
Analysis result: C/E 1.002, ΔE ±0.14%(1σ)
Expected accuracy inferred from the above: ±0.3% or smaller by E/C biasing
Current licensing calculation: ±0.6% (total 1%)
Target accuracy (1σ): 0.3% (suggested in OECD/NEA)
0.1% (at 200°C for reactor physics test)

(Control rod worth)
Analysis result: C/E 1.00, ΔE ±2%(1σ)
Expected accuracy inferred from the above: ±2%
Current licensing calculation: ±6% (total 10%)
Target accuracy (1σ): 3% (suggested in JAEA)
2% (for the prediction of criticality)

3.2. Uncertainty by covariance data

The target accuracies in the above parameters would be achievable thanks to the presence of accurate measurement data. On the contrary, there are parameters that are difficult to evaluate in the same way due to lack of good measured data in terms of measurement accuracy and representability of actual phenomena assumed in the design calculation. The sodium void reactivity is a typical one and a large design margin of 30% is considered in the existing design calculation, whereas the target accuracy (1σ): 7% is suggested in OECD/NEA.

In this case, use of covariance data (uncertainty data of nuclear data) is promising. We can estimate the uncertainty of the design calculation by combining that associated with nuclear data and that with calculation methods. Such attempt started in the late 1980s and more and more covariance data have been evaluated and added to the evaluated nuclear data file. Now JENDL-4.0 covers the data for most of nuclides and reactions of interest in the design calculation.

The quality assurance is the next issue to be tackled for the covariance data to be practically applied in the licensing calculation. Reliability of the covariance data is investigated for large fast reactors by K. Sugino [7]. The study compares design accuracies estimated by C/E dispersion and by covariance data. Equality is confirmed in general except too large uncertainty in the criticality (0.3% by C/E dispersion: 0.9% by covariance data).

Figure 5 shows the uncertainty evaluated with the covariance data of JENDL-4.0up1 for the criticality data of Monju. The result is similar to the preceding study as the total uncertainty 0.75% (1σ) larger than the expected accuracy of 0.3%. Relatively large contributions come from those of ^{238}U capture and inelastic, and ^{239}Pu fission. Their values originally come from the nuclear data uncertainty (diagonal component) of about 3%, 10%, and 1%, respectively. It seems that the current uncertainties would be in the small level practically achievable in the nuclear data measurement.

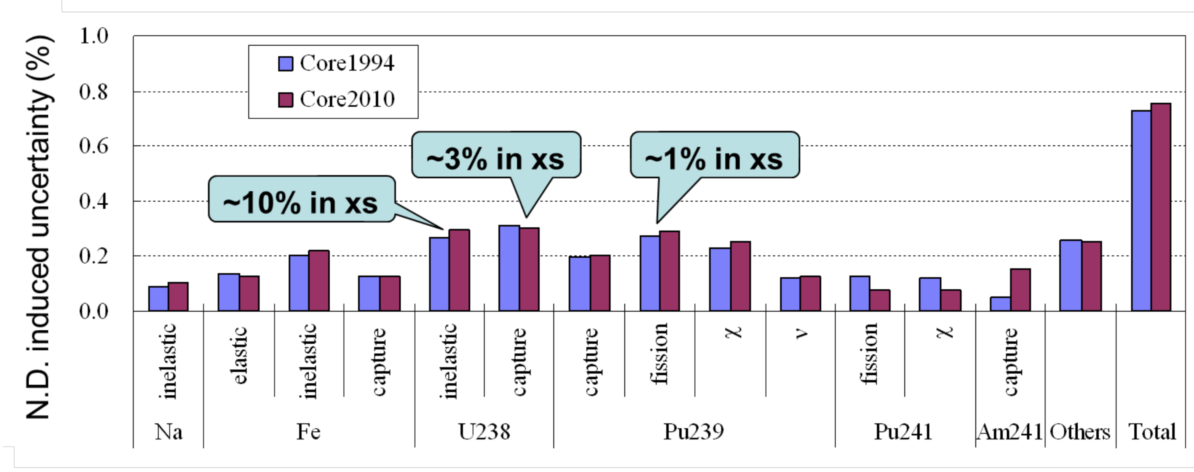

Figure 5 Nuclear data induced uncertainty for criticality measured in 1994 and in 2010

The reliability was investigated in another aspect by comparing the uncertainty with the dispersion among nuclear data. Figure 6 compares the results for the criticality data of Core2010. The dispersion is defined here by the change in the criticality brought by the change of nuclear data from JENDL-4.0 to ENDF/B-VII.0 or JEFF-3.1.
The uncertainties are smaller than the dispersion for ^{23}Na (inelastic and μ; average cosine of the scattering angle), ^{239}Pu fission, and ^{240}Pu (capture and fission). On the contrary, the uncertainties are larger for ^{238}U (capture and inelastic), ^{239}Pu (capture, χ; fission spectrum) and ^{241}Am capture.

In general, the dispersion and the uncertainty do not have to be consistent since the covariance data is also the result of nuclear data evaluation, which is independent of the other nuclear data. In addition, there is a possibility the three nuclear data may be biased in the same way. Nevertheless, the comparison gives a hint to extract covariance data that needs improvement. In particular, the smaller uncertainty needs to be checked very carefully since it may lead to erroneous modifications of cross sections when the cross section adjustment technique is applied. Among the data with the smaller uncertainty, μ data of ^{23}Na is the biggest concern since the analysis of BFS experiment indicates that the value of ENDF/B-VII.0 seems reasonable [8].

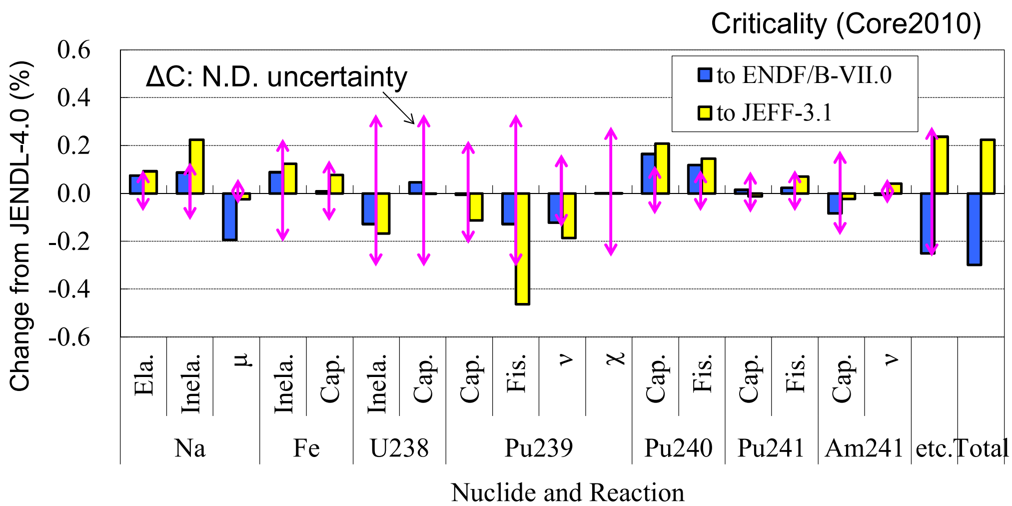

Figure 6 Nuclear data induced uncertainty vs. Dispersion among nuclear data

4. Conclusions

The nuclear data application in the Monju reactor physics tests was summarized. The calculation accuracy for the tests is in the satisfactory level in general. Valuable knowledge on ^{241}Am nuclear data is obtained. We will continue the validation of nuclear data through re-evaluation of the existing data and through the accumulation of reactor physics data in the future.

Use of covariance data is promising application to estimate the calculation accuracy of a wide variety of reactor physics parameters. Based on the reactor physics test analyses, the reliability of the covariance data was investigated and covariance data that needs improvement were extracted. It is suggested that μ data of ^{23}Na need to be improved.

Acknowledgments

The author wishes to express thanks to K. Sugino for providing information on the reliability study of covariance data.

References

[1] Ishikawa M. Consistency evaluation of JUPITER experiment and analysis for large FBR cores. Proc. Int. Conf. on Physics of Reactors; 1996 Sep 16–20; Mito (Japan). pp. E36–E45.
[2] Mouri T, Sato W, Uematsu M, Kishimoto Y, Hazama T, Suzuki T. Monju core physics test analysis with various nuclear data libraries. Proc. Int. Conf. Fast Reactors and Related Fuel Cycles (FR09); 2009 Dec 7–11; Kyoto (Japan). [CD-ROM].
[3] Takano K, Sugino K, Mouri T, Kishimoto Y, Usami S. Monju core physics test analysis with JAEA's calculation system. Proc. Int. Conf. on the Advances in Nuclear Analysis and Simulation (PHYSOR 2008); 2008 Sep 14–19; Interlaken (Switzerland). [CD-ROM].
[4] DEAN V. F., editor. ICSBEP guide to the expression of uncertainties. International Criticality Safety Benchmark Evaluation Project, OECD/NEA; 2007. [cited 2011. Feb 25] Available from: https://www.oecd-nea.org/science/wpncs/icsbep.
[5] FBR Plant Engineering Center (ed.), External evaluation on Monju core confirmation test in FY2010, JAEA-Evaluation 2011-002, 2011, pp. 69–75.
[6] Hazama T, Kitano A, Kishimoto Y. Criticality evaluation for the Monju restart core. Nucl. Technol. 2012 Aug; 179: 250–265.
[7] Sugino K., Application of the cross section covariance data to fast reactor core design, JAEA-Conf 2013-002, 2013, pp. 53-58.
[8] Hazama T., Sato, W., Evaluation of nuclear characteristics of minor actinide loaded core – Analyses of BFS-69 and BFS-66-2 critical experiments –, JAEA-Research 2010-028, 2010, 101p.

7. Development of a Neutronic Analysis Code using Data from Monju

W.F.G. van Rooijen*, N. Yamano, Y. Shimazu

Research Institute of Nuclear Engineering
University of Fukui
Kannawa-cho 1-2-4, Tsuruga-shi, Fukui-ken, T914-0055, Japan

October 31, 2014

Abstract

In recent years three major sets of modern evaluated nuclear data have become available: JENDL-4.0, JEFF-3.1.2 and ENDF/B-VII.1. The authors were involved with a research project to establish analysis method for a future commercial-scale LMFBR. This project focused on JENDL-4.0 and conventional Japanese codes. As a cross check, we decided to also apply the fast reactor code ERANOS. This necessitated to produce nuclear data (cross sections, etc) for the ERANOS code system, discussed in this paper. We developed a nuclear data processing system to produce cross sections, probability tables, delayed neutron data, and covariance data from the evaluated nuclear data files for ERANOS. A benchmark calculation on the MZA/MZB benchmark showed very satisfying results. Subsequently, we analyzed the prototype LMFBR Monju with ERANOS and our own sets of nuclear data. The results are very satisfactory. The results from ERANOS indicate that the target accuracies for nuclear data have not been met, although the three sets of evaluated nuclear data all performed very well in our analysis. In the future, the covariance on nuclear data should be reduced to meet the target accuracies on criticality and feedback coefficients.

Key Words: **Nuclear data processing, Monju, Reactor physics analysis, uncertainty analysis**

1 Introduction

In the so-called "Monju Tokushin" project, the University of Fukui was involved with the development of advanced analysis software for a commercial-size Fast Breeder Reactor [1]. In this project, JENDL-4.0 was selected as the reference nuclear data, and the analysis software is based on the "traditional" Japanese codes, such as SLAROM-UF. To provide a check, analysis with different software and data is desired.

It was chosen to use the well-established fast reactor code system ERANOS 2.0 [2]. However, the publicly available version of ERANOS 2.0 (NEA Data Bank) is delivered with a set of nuclear data based on JEF-2.2. For a proper comparison to the results obtained in Monju Tokushin, a set of cross sections based on JENDL-4.0[1] [3] is required. Since there exists no publicly available cross section processing tool for ERANOS, the necessary software was developed. Once the processing software is available, it is relatively easy to also prepare cross sections based on other sets of evaluated nuclear data. This paper will discuss the generation of cross section libraries for ERANOS 2.0, using JENDL-4.0, JEFF-3.1.2 [4], and ENDF/B-VII.1 [5]. The preparation and application of uncertainty data and delayed neutron production data are also discussed.

The accuracy of this system was tested with two relevant calculations: the MZA/MZB benchmarks of the MOZART program (measured in ZEBRA,

*Corresponding author, rooijen@u-fukui.ac.jp

[1] Throughout this paper, JENDL-4.0 is used with updates up to September 2013, also known as JENDL-4.0u

UK, in the 1970s, [6]), and the Monju start-up tests of 1994 and 2010 [7, 8]. For Monju, reactor physics parameters of 1994 and 2010 have been published in open literature: all-rods-out reactivity, and Isothermal Temperature Coefficient. The core composition in 2010 is not fully published but sufficient data can be obtained by combining information from several public reports. For the MOZART benchmarks and also for Monju, very good agreement was found with our combination of ERANOS and modern evaluated nuclear data.

2 Cross section processing software

Processing of nuclear data for ERANOS requires several processing tools, and there are several steps to take. A complete processing system was implemented in Python, focusing on consistency and uniformity, parallelization, as well as targeting a minimum of “outside input”, i.e. necessary data for the processing is taken as much as possible from the ENDF files directly. Several utility codes to extract information from ENDF files were written.

ECCO uses two or more energy group structures in one calculation. We applied the two conventional ECCO group structures (1968 groups and 33 groups). This feature of ECCO makes it necessary to produce two cross section libraries. In the following, isotopes which are included in the 1968-group library are referred to as *major isotopes*; isotopes which are present in the 33-group library only are referred to as *minor* isotopes. The production of an ECCO library takes several steps. A Python script was written to automate all of these steps. Where possible, parallel calculations are used, for example, the sequence NJOY - CALENDF - MERGE - GECCO concerns individual isotopes and can be done in parallel. A more detailed overview of the cross section processing for ERANOS is given in [7].

2.1 Covariance data

The covariance data is processed with the ERRORR module in NJOY for those isotopes for which covariance data is available. Only covariance data from MF31, MF32 and MF33 is processed. ERANOS cannot handle the ERRORR data directly, therefore a utility program was created to reformat the ERRORR library into the AMERE format. AMERE data is created for individual isotopes in 33 groups. Subsequently a unified AMERE file is created. The situation for the presence of covariance data is as follows:

- JENDL-4.0 with updates. This evaluation contains covariance data for 33 relevant isotopes.
- JEFF-3.1.2. This evaluation does not contain covariance data for the important isotopes. Therefore it was decided to use the BOLNA covariance data (15 energy groups, see [9]).
- ENDF-B-VII.1. This evaluation cotains covariance data for 94 relevant isotopes.

2.2 Delayed neutron data

Delayed neutron data is read from the evaluated nuclear data files when available. The delayed neutron data is then processed to fit the 33 energy groups used in ERANOS.

3 Results for MZA/MZB

Our objective is to use ERANOS in combination with JENDL-4.0 for the analysis of Monju. To check our newly made libraries, it was decided to perform a benchmark calculation: the MZA and MZB cores, which were built in the ZEBRA-facility in the UK in the 1970s as part of the MOZART program of experiments in support of the design of Monju. An extensive discussion of the benchmark calculations and the results can be found in elsewhere [7]. Here we want to present only the results for the reactivity of the MZA and MZB/3 cores. The results are given in Figure 1, which give the excess reactivity of the core (i.e. “all rods out” reactivity).

In the figures, there are 2 sets of results: one is labeled “RZ-model” and the other is labeled “XYZ-model”. The RZ-model is analyzed with 2D SN calculations; this model allows uncertainty analysis in ERANOS. The XYZ-model is analyzed in 3D with a nodal code. This model does not allow uncertainty analysis, however, the use of a nodal calculation implies there is no error due to spatial discretization.

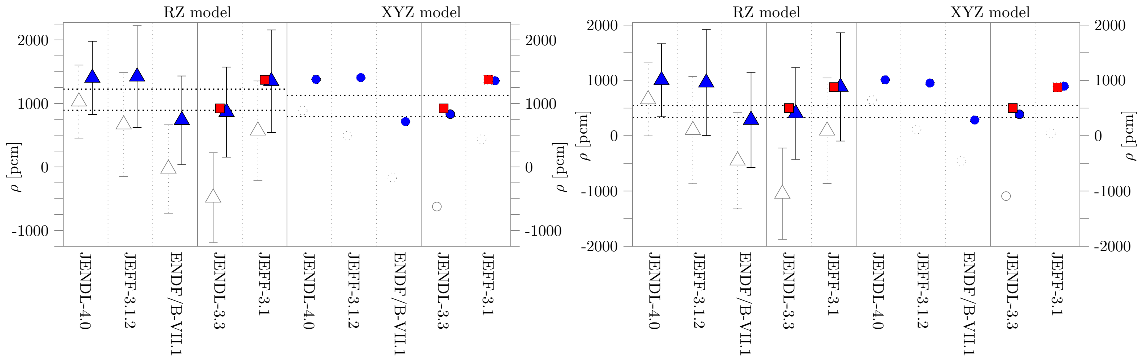

Figure 1: Left: Excess reactivity of the MZA core. Right: excess reactivity of the MZB core. Calculated with ERANOS and the ECCO libraries prepared in the present work. Symbols: △ = RZ CALENDF-preferred XS, ▲ = RZ NJOY-only XS, ○ = XYZ CALENDF-preferred XS, ● = XYZ NJOY-only XS, ■ = benchmark result.

In all cases, there are results for 5 sets of evaluated nuclear data; and for each set of evaluated nuclear data, there is a solid (colored) symbol and a white outline symbol. These symbols mean the following: as discussed before, ECCO requires both NJOY and CALENDF to prepare nuclear data. There are cases where NJOY and CALENDF do not agree about the cross section. In such a case, the user has to make a decision whether the NJOY cross section is taken as "correct", or the CALENDF cross section is "correct". The solid symbols represent calculations where the NJOY cross section is preferred. This allows an immediate comparison with the results described in the MZA/MZB benchmark materials. In the benchmark documents results are obtained with the MCNP code, using evaluated nuclear data from JEFF-3.1 and JENDL-3.3. MCNP relies entirely on NJOY for cross section processing. Results from the benchmark documentation are illustrated as solid circles. Clearly, our results are very near the benchmark results if we use "NJOY-only" cross sections. On the other hand, the outline symbols are results using "CALENDF-preferred" cross sections. It is clear that in general the NJOY-cross sections have a better performance. As a result, for the Monju analysis it was decided to prefer the NJOY-cross sections in all cases where it is required to make a decision.

4 Results for Monju

The prototype fast reactor was first started in 1994; in the period 1994 - 1995 the reactor was operated at 40% power for about 100 days. In this period, several reactor physical parameters were measured. In 2010 the reactor was restarted, and operated at zero power for approximately three months. Again, several reactor physical parameters were measured. The measurement results are described in publicly available documentation, see for example [10]. The 2010-core contains 5 different types of fuel. The loading pattern of the 2010-core is given in Figure 2.

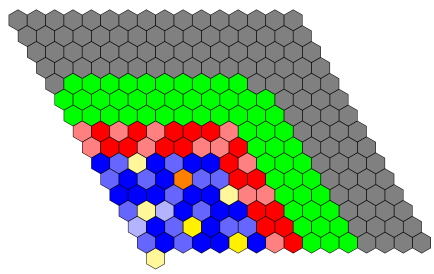

Figure 2: Monju core loading map in 2010. ⬢ = inner fuel 1, ⬢ = inner fuel 2, ⬢ = inner fuel 3, ⬢ = outer fuel 1, ⬢ = outer fuel 2, ⬢ = backup control rod, ⬢ = coarse control rod, ⬢ = fine control rod, ⬢ = blanket, ⬢ = reflector.

Results are given in Figure 3. One set of results is determined with 2D RZ-calculations, using an SN transport code, which allows uncertainty analysis;

the Hex-Z results are obtained with a nodal calculation without uncertainty analysis. In this case, solid symbols represent results for the 1994-core, whereas outline symbols are for the 2010-core. For the 1994-core the experimental uncertainty is not always known.

The excess reactivity is well predicted with ERANOS and the cross sections prepared in the present work. JENDL-4.0 gives the best performance as far the absolute reactivity is concerned with the smallest uncertainty interval (approximately 800 pcm).

In the measurement of the Isothermal Temperature Coefficient (ITC), the temperature of the entire core is increased slowly (isothermal situation), and the reactivity change due to the temperature change is recorded. This measurement contains the effect of Doppler broadening, as well as the effects of thermal expansion of the fuel and core components. In ERANOS, the ITC is calculated, as well as the Doppler coefficient. Our results indicate that the Doppler effect accounts for about 60% of the total temperature effect. Between 1994 and 2010 the ITC and Doppler coefficient decrease. The uncertainty on the Doppler coefficient was determined with Equivalent Generalized Perturbation Theory (EGPT). In 1994, the uncertainties are 2.6% for JENDL-4.0, 3.5% for JEFF-3.1.2, and 3.6% for ENDF/B-VII.1; in 2010, these numbers are 2.8%, 3.0% and 3.4% respectively.

The control rod worth is given in Figure 3. In [10] are given control rod worth curves for each control rod in Monju; however, our $2\pi/3$ symmetric model can only handle control rod insertion with 3 rods simultaneously. Therefore we have chosen to only analyse the control rod worth of the central control rod. As shown in Figure 4, the three data sets per-form quite well, with maximum errors of about 3%(note: without any correction factors). The calcu-lation was done with the nodal code, therefore no uncertainty calculation can be done. Two things need to be pointed out: first, the control rod curves in [10] are only available as figures, therefore the "measured data" line is read by the naked eye from the published figures, and second, the calculation for 400 mm has a large error. This is the deepest in-sertion point where the reactor remains critical. The error may be due to poor reading from the published graph. It should be noted that the control rods are completely neglected in all other calculations presented thusfar. The (energy-dependent) curvature of the flux, caused by the partially inserted control rod, may require more detailed settings in the nodal core calculation for optimal accuracy.

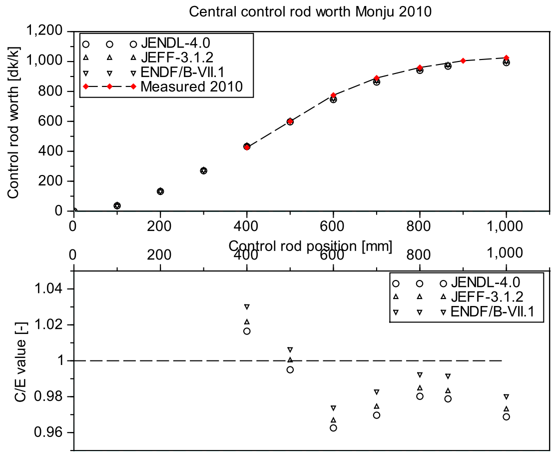

Figure 3: Control rod worth curve of the central control rod in Monju in 2010.

5 Comparison with uncertainty targets for fast reactor design

All results given in this paper are "raw" results from ERANOS, in other words, no correction factors have been applied anywhere. As such, the performance of ERANOS in combination with JENDL-4.0 is certainly satisfactory. It is interesting to compare the obtained uncertainties with the so-called target uncertainties for LMFBR design, for instance such as they are given in [12]. For convenience, we have reproduced some of the target accuracies in Table 1.

Looking at the table, it seems that even with the newest JENDL-4.0 the target accuracy of 300 pcm (0.3%) cannot be achieved; our calculations show a fairly constant 800 pcm (0.8%) uncertainty due to nuclear data in JENDL-4.0. That number does not include modeling uncertainty. As far as control rod worth is concerned, the central control rod has an error of about 2% in JENDL-4.0, which is within the target accuracy ("CR worth (element)"). However, the present work does not take into account the other control rods, so it is difficult to draw solid conclusions. As far as the Doppler-effect is concerned, target accuracies are achieved, but for the void effect

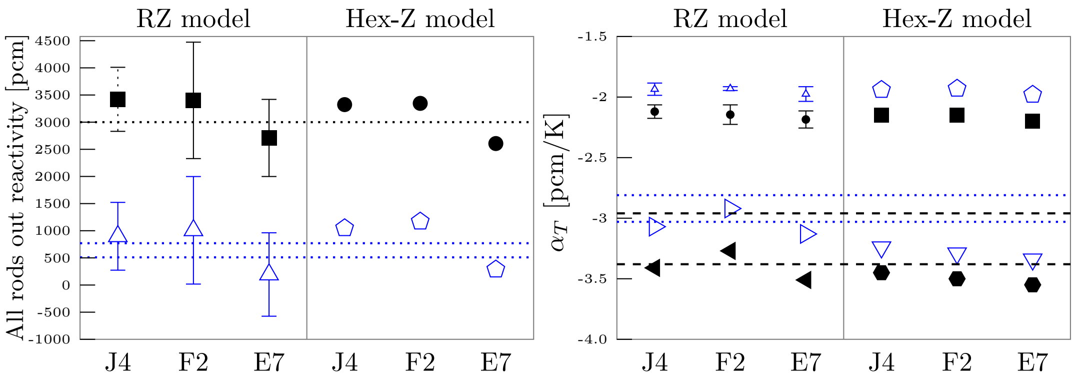

Figure 4: Left: All rods out reactivity; ■ 1994 RZ; △ 2010 RZ; ● 1994 Hex-Z; ⬠ 2010 Hex-Z. Reference values: 3000 pcm in 1994 [11] and 640±130 pcm in 2010 [10]. Right Temperature coefficients in Monju. Measured ITC values from [10]. The calculations compare well to measurements. ● Doppler 1994; △ Doppler 2010; ◀ ITC 1994; ▷ ITC 2010; ■ Doppler 1994; ⬠ Doppler 2010; ⬢ ITC 1994; ▽ ITC 2010; J4 = JENDL-4.0, F2 = JEFF-3.1.2, E7 = ENDF/B-VII.1. Dashed lines: confidence interval of measured value.

(not given in this paper because of a lack of measurement data) the result is not so promising, with initial calculations giving 15% to 20% uncertainty due to cross sections.

Table 1: Uncertainty targets (%) for FBRs, taken from [12]. All numbers presented in this table, including those labeled “current uncertainty”, are taken directly from the original publication. The original table mentions “reactivity coeff.” without further qualification.

Parameter	Current Uncer. [%]		Target
	Data	Model	Uncer. [%]
k_{eff}	1.5	0.5	0.3
CR worth	5	6	5
(element)	5	6	5
CR worth	5	4	2
(total)	5	4	2
$\Delta\rho$ burnup	0.7	0.5	0.3
Reactivity coeff. (total)	7	15	7
Reactivity coeff. (component)	20	20	10

6 Conclusion

This paper concerns the creation of a nuclear data processing system for the ERANOS fast reactor analysis code system. Specifically, our nuclear data processing system prepares data for the cell code ECCO (cross sections and probability tables), delayed neutron data, as well as covariance data for uncertainty analysis. The software is consists basically of a set of Python-routines and several utility codes written in FORTRAN that automate the processing steps, which involve NJOY, CALENDF, MERGE, GECCO, and ERANOS itself. To our knowledge, we are the only facility outside of CEA capable of producing nuclear data for ERANOS encompassing all aspects of cross sections, probability tables, delayed neutron data and covariance data.

In the present work, we presented results based on JENDL-4.0, JENDL-3.3, JEFF-3.1.2, JEFF-3.1 and ENDF/B-VII.1. To ascertain the adequacy of our cross section libraries, we analyzed the MZA/MZB benchmarks. A good performance for the MZA/MZB benchmark was found, provided that the correct calculation options are used when preparing the cross sections. Application of the combination of ERANOS and our cross sections to the prototype FBR Monju shows a very good result: reactor physical parameters are satisfactorily reproduced, both for the 1994 core and the 2010 core in Monju. Notably, our work does not rely on any correction factors.

A comparison to target accuracies for LMFBR design shows that improvement is still needed as far as the nuclear data is concerned. For criticality, the uncertainty due to cross sections is still on the order of 1%, whereas the target is 0.3%. For the Doppler-effect, results indicate a good agreement between measurement and calculations, and it seems that the accuracy is sufficient, but for the void effect and control rod worth improvements are still desired.

References

[1] University of Fukui. Tech. Rep. of FY2011 Core R&D program for commercialization of the fast breeder reactor by utilizing Monju, November 2012. (in Japanese).

[2] G. Rimpault, D. Plisson, J. Tommasi, R. Jacqmin, J.-M. Rieunier, D. Verrier, and D. Biron. The ERANOS code and data system for fast reactor neutronic analyses. In *Physor 2002*, Seoul, South Korea, October 7 – 10 2002. ANS.

[3] K. Shibata et.al., JENDL-4.0: A new Library for Nuclear Science and Engineering. *Journal of Nuclear Science and Technology*, 48(1):1 – 30, 2011.

[4] JEFF and EFF Working Groups. The JEFF Nuclear Data Library version 3.1.2, February 2012. URL http://www.oecd-nea.org/dbforms/data/eva/evatapes/jeff 31/JEFF312/.

[5] M.B. Chadwick et.al., ENDF/B-VII.1 Nuclear Data for Science and Technology: Cross Sections, Covariances, Fission Product Yields and Decay Data. *Nuclear Data Sheets*, 112:2887 – 2996, 2011. URL http://www.nndc.bnl.gov/exfor/endfb7.1.jsp.

[6] J. Rowlands, A. Zukeran, M. Nakagawa, P. Smith, and U.-K. Wehmann. The ZEBRA MOZART programme. part 1. MZA and MZB Zebra assemblies 11 and 12. Technical report, 81 South Court Avenue, Dorchester, DT1 2DA, United Kingdom, January 2008. URL http://zebra.webnik.org.

[7] W.F.G. van Rooijen. Analysis of the MZA/MZB benchmarks with modern nuclear data. *Annals of Nuclear Energy*, 62:504 - 525, 2013. doi: 10.1016/j.anucene.2013.07.013.

[8] W.F.G. van Rooijen and N. Yamano. Analysis of the neutronic properties of the prototype FBR Monju based on several evaluated nuclear data libraries. In *ND2013*, New York, NY, USA, March 14 - 18 2013. BNL.

[9] M. Salvatores and R. Jacqmin. Uncertainty and target accuracy assessment for innovative systems using recent covariance data evaluations. Technical Report NEA/WPEC-26, ISBN 978-92-64-99053-1, Argonne National Laboratory / CEA / OECD Nuclear Energy Agency, 2008. URL http://www.oecd-nea.org/science/wpec/volume26/volume26.pdf.

[10] The technical committee on Monju research utilization. External evaluation on Monju core confirmation t est i n F Y2010. Technical Report JAEA-Evaluation 2011-002, Japan Atomic Energy Agency, June 2011. URL http://jolissrch-inter.tokai-sc. jaea.go.jp/pdfdata/JAEA-Evaluation -2011-002.pdf/.

[11] K. Yabuki, A. Kitano, M. Fukushima, T. Miyagawa, and Y. Okawauchi. P-19: Prototype Fast Breeder Monju Core Confirmation Test (zero power reactor physics experiments) - (2) Criticality and control rod worth confirmation test. In *2010 Fall Meeting (15 - 17 September 2010, University of Hokkaido)*, page 896. Atomic Energy Society of Japan, September 2010.

[12] G. Palmiotti, M. Salvatores, G. Aliberti, H. Hiruta, R. McKnight, P. Oblozinsky, and W.S. Yang. A global approach to the physics validation of simulation codes for future nuclear systems. *Annals of nuclear energy*, 36:355 – 361, 2009.

8. Research Progress on Accelerator-driven System in Kyoto University Research Reactor Institute

Cheol Ho Pyeon

Nuclear Engineering Science Division, Research Reactor Institute, Kyoto University
Asashiro-nishi, Kumatori-cho, Sennan-gun, Osaka 590-0494, Japan
e-mail: pyeon@rri.kyoto-u.ac.jp

Abstract

The experimental studies on the accelerator-driven system (ADS) are being conducted for nuclear transmutation analyses with the combined use of the Kyoto University Critical Assembly (KUCA; A-core: solid-moderated and -reflected core) and the fixed-field alternating gradient (FFAG) accelerator, in the Kyoto University Research Reactor Institute. The ADS experiments with 100 MeV protons obtained from the FFAG accelerator had been carried out to investigate the neutronic characteristics of ADS, and the static and kinetic parameters were accurately analyzed through both the measurements and the numerical simulations (MCNPX; ENDF/B-VII.0; JENDL/HE-2007; JENDL-4.0; JENDL/D-99) and of reactor physics parameters, including the reaction rates, the neutron spectrum, the neutron multiplication (M), the subcritical multiplication factor (k_s), the neutron decay constants (α) and the subcriticality (ρ). In addition to the uranium-loaded core, the spallation neutrons generated by 100 MeV protons from the FFAG accelerator had been also injected into the thorium-loaded core to conduct the feasibility studies on the thorium-loaded ADS through the experimental analyses of the static conditions and kinetic behaviors.

An upcoming ADS at KUCA could be composed of highly-enriched uranium fueled and Pb-Bi zoned core, in consideration of an actual ADS designed by the Japan Atomic Energy Agency. The neutronic characteristics of Pb-Bi in ADS are considered importantly analyzed experimentally from the viewpoint of reactor physics: neutron yield and neutron spectrum by the solid Pb-Bi target; uncertainties of Pb-Bi cross sections in the core. At KUCA, as preliminary study on the solid Pb-Bi characteristics, the critical mass and the sample worth experiments relating Pb-Bi could be conducted to investigate the uncertainties of Pb-Bi cross sections with the use of solid Pb-Bi plates, in addition to solid Pb and Bi plates. Furthermore, irradiation experiments of the minor actinides (^{237}Np and ^{241}Am) could be conducted in hard spectrum core at KUCA to examine the feasibility of conversion analyses of nuclear transmutation.

1. Introduction

The experimental studies on the accelerator-driven system (ADS) are being conducted for nuclear transmutation analyses with the combined use of the Kyoto University Critical Assembly (KUCA; A-core: solid-moderated and -reflected core) and the fixed-field alternating gradient (FFAG) [1]-[2] accelerator, in the Kyoto University Research Reactor Institute. The ADS experiments [3]-[8] with 100 MeV protons obtained from the FFAG accelerator had been carried out to investigate the neutronic characteristics of ADS, and the static and kinetic parameters were accurately analyzed through both the measurements and the

Monte Carlo simulations of reactor physics parameters, including the reaction rates, the neutron spectrum, the neutron multiplication, the neutron decay constants and the subcriticality. In addition to the uranium-loaded core, the spallation neutrons generated by 100 MeV protons from the FFAG accelerator had been also injected into the thorium-loaded core [9]-[10] to conduct the feasibility studies on the thorium-loaded ADS through the experimental analyses of the static conditions and kinetic behaviors.

An upcoming ADS at KUCA could be composed of highly-enriched uranium (HEU) fueled and lead-bismuth (Pb-Bi) zoned core, in consideration of an actual ADS designed by the Japan Atomic Energy Agency. The neutronic characteristics of Pb-Bi are considered importantly analyzed experimentally from the viewpoint of reactor physics: neutron yield and neutron spectrum by the Pb-Bi target; uncertainties of Pb-Bi cross sections in the core. Furthermore, at KUCA, as preliminary study on the Pb-Bi characteristics, the critical mass and the sample worth experiments relating Pb-Bi could be conducted to investigate the uncertainties of Pb-Bi cross sections with the use of solid Pb-Bi plates, in addition to solid Pb and Bi plates. Furthermore, irradiation experiments of the minor actinides (^{237}Np and ^{241}Am) could be conducted in hard spectrum core at KUCA to examine the feasibility of conversion analyses (^{237}Np capture and ^{241}Am fission) of nuclear transmutation. The objective of this study was to review a series of previous ADS experiments with 100 MeV protons carried out at KUCA, and perspectives on upcoming ADS experiments with the use of HEU and Pb-Bi zoned core. The experimental and numerical settings are shown in Sec. 2. The results of experiment and numerical simulations by Monte Carlo calculation code coupling with nuclear data libraries are presented in Sec. 3 and the conclusions are summarized in Sec. 4.

2. Experimental Settings and Numerical Simulations

2.1. Experimental Settings

At KUCA, A and B are polyethylene-moderated and -reflected cores, and C is a light water-moderated and -reflected one. The three cores are operated at a low mW power in the normal operating state, whereas the maximum power is 100 W. The ADS experiments were carried out in the A-core with the combined use of HEU fuel and polyethylene reflector rods. In the A-core, the fuel assembly is composed of 36 unit cells and upper and lower polyethylene blocks about 540 and 590 mm long, respectively, in an aluminum (Al) sheath 54×54×1520 mm. The target is located outside the core and is not easily moved to the center of the core, because control and safety rods are fixed in the core as the control driving system at KUCA.

In the ADS experiments at the A core, the neutron flux information was acquired from ^{115}In(n, γ)^{116m}In reactions using the indium (In) wire (1 mm diameter and 800 mm length), under the assumption that, in thermal region, the cross sections of ^{235}U(n, f) are proportional to those of ^{115}In(n, γ)^{116m}In. The In wire was set along the vertical direction at the axial center position. Another In foil (10×10×1 mm) was attached at the location of the target to obtain the spallation neutron information through ^{115}In(n, n')^{115m}In reactions (threshold energy of 0.3 MeV neutrons). The ^{115}In(n, γ)^{116m}In reaction rates normalized by ^{115}In(n, n')^{115m}In ones were estimated in the experiments, and interpreted as the actual values of reaction rates in consideration of the effect of external neutron source. The main characteristics of proton beams were shown as follows: 100 MeV energy, 10 pA intensity, 30 Hz repetition rate, 60 ns pulsed width and 1.0×10^{6} 1/s neutron yield. The irradiation time of the In wire was about three hours. The subcriticality level 0.77 %$\Delta k/k$ (770 pcm) of the core was obtained by the full insertion of three control rods and the full withdraw of three safety rods.

For optimizing the effect of moving the target from its original location outside the core, additional experiments were carried out in the same core. The effect of moving the target was investigated through analyses of neutron multiplication, as in the previous study at KUCA. In the experiments, the ^{115}In(n, γ)^{116m}In reaction rates were measured in the core region, and neutron multiplication was deduced by the reaction rate distribution, when the tungsten (W) target was moved from the original location to another one close to the core center. The subcriticality level was 0.75 %$\Delta k/k$ (750 pcm), and the protons were injected into a subcritical system under the following parameters: 100 MeV energy; 30 pA beam intensity; 30 Hz repetition rate; 200 ns pulsed width; 1.0×10^7 1/s neutron yield.

Another experiment was carried out separately at the original target location and the core target one. And the combination of materials W and beryllium (Be) was selected as plural targets for the aim for accomplishment of the neutron spectrum in high-energy region and the neutron yield of high-energy neutrons in the core. The combined use of the heavy- (W, Pb and Bi) and the light-nuclide (Be and lithium) was considered useful for accomplishment of the research objectives relating the neutron spectrum and the neutron yield. Here the plural targets with the combined use of heavy- and light-nuclide were called “two-layer target” in this study.

In the thorium-loaded ADS with 100 MeV protons, the fuel rod was composed of a thorium (Th) metal plate and a polyethylene (PE), graphite (Gr) or Be moderator arranged. Other components were selected from HEU and natural uranium (NU; 2”×2”×1/8”) plates. The cores comprised Th-PE, Th-Gr, Th-Be, Th-HEU-PE and NU-PE. The thorium-loaded ADS experiments were conducted especially to investigate the relative influence of different thermal neutron profiles on capture reactions of ^{232}Th and ^{238}U: the reaction of ^{238}U was taken as reference data for evaluating the validity of ^{232}Th capture cross sections. The proton beam parameters were 100 MeV energy, 0.3 nA intensity, 20 Hz pulsed frequency, 100 ns pulsed width and 40 mm diameter spot size at the W target (50 mm diameter and 9 mm thick). The level of the neutron yield generated at the target was over 1.0×10^7 1/s by the injection of 100 MeV protons onto the W target. The reaction rates for thermal neutrons were acquired from the ^{115}In wire (1.5 mm diameter, and 600 mm length). The ^{115}In wire was placed vertically at the axial center position. The ^{115}In foil (10×10×1 mm) was set at the location of the W target with 100 MeV protons. The irradiation time of the ^{115}In wire was about four hours.

2.2. Numerical Simulations

The numerical calculations were performed by the Monte Carlo transport code, MCNPX [11] together with ENDF/B-VI.8 [12] or ENDF/B-VII.0 [13] for transport, and JENDL/D-99 [14] for reaction rates and JENDL/HE-2007 [15]-[16] for high-energy protons. Here, in MCNPX, the calculated reaction rate was obtained from evaluation of volume tallies of activation foils. Since the effects of their reactivity are not negligible, they were included in the simulated geometry and transport calculations. The precision of numerical subcriticality in the eigenvalue calculations was attained within the relative difference of 3% between the experiment and the calculation. The fixed-source calculations were performed by a total of 1.0×10^8 histories, which led to a statistical error of less than 5% in the reaction rates.

3. ADS Experiments with 100 MeV Protons

3.1. Results and Discussion

To obtain the information on the detector position dependence of the prompt neutron decay measurement, the neutron detectors were set at three positions: near the tungsten target; around the core. The prompt and delayed neutron behaviors (Fig. 2 in Ref. [3]) were experimentally confirmed by observing the time evolution of neutron density in ADS: an exponential decay behavior and a slowly decreasing one, respectively. These behaviors clearly indicated the fact that the neutron multiplication was caused by an external-source: the sustainable nuclear chain reactions were induced in the subcritical core by the spallation neutrons through the interaction of the W target and the protons from the FFAG accelerator. In these kinetic experiments, the subcriticality was deduced from the prompt neutron decay constant by the extrapolated area ratio method. The difference of measured results of 0.74 %$\Delta k/k$ and 0.61 %$\Delta k/k$, respectively, from the experimental evaluation of 0.77 %$\Delta k/k$, which was deduced from the combination of both the control rod worth by the rod drop method and its calibration curve by the positive period method, was within about 20%.

The difference in the experimental results, by changing the location of the W target to another one: in front of the original target; between the target and the core; in front of the fuel region. From the experimental results (Fig. 6 in Ref. [5]), the reaction rate distribution was observed to be high in the SV and fuel regions, when the tungsten target was set at medium location between the original and core locations. Neutron multiplication M and subcritical multiplication factor k_s were experimentally and numerically analyzed (Table 4 in Ref. [5]). The neutron multiplication was considered to involve a large discrepancy caused by the evaluation of the C/E values of fission and source terms; inversely, the subcritical multiplication factor was considered fairly good in the evaluation of C/E values. The constant values of the measured and the calculated k_s demonstrated that the source term was not contributed largely to that of k_s, since the external source was located outside the core. While the accuracy of the neutron multiplication was attributable to the experimental variation of the In reaction rates, the actual effect of setting the W target at the medium location was found to be more significant than setting the target in the original location.

From the numerical results (Fig. 11 in Ref. [7]), the neutron spectrum was observed high in high-energy region with the combined use of W and Be. In the design of two-layer target, the proton beams could be actually penetrated into Be target, and inversely stopped inside W target, and the dimensions of two-layer target were determined to be in W (50 mm diameter and 9 mm thick) and Be (50 mm diameter and 6 mm thick).

In the thorium-loaded ADS experiments, the ^{115}In(n, γ)^{116m}In reaction rates in the NU-PE core were higher than in other cores, demonstrating that the reaction rates of ^{238}U in the NU-PE core were larger than those of ^{232}Th in the thorium cores with the use of 100 MeV protons. This tendency was caused by the fact that, in the thermal neutron regions, the neutron spectrum of the NU-PE core was softer than that of the Th-PE core, although, in the thermal neutron regions, the capture cross sections of ^{238}U were smaller than those of ^{232}Th. Additionally, the effect of the neutron spectrum on the reaction rates was observed with 100 MeV protons by comparing the measured results of reaction rates.

Subcriticality in dollar units was deduced by the extrapolated area ratio method with the use of prompt and delayed neutron components, and experimentally evaluated according to the kind of external neutron source. These results revealed subcriticality dependence on the kind of external neutron source, although the value of subcriticality was theoretically unchanged, regardless of the external neutron source. Nonetheless, special attention was paid to the conversion coefficient (β_{eff}: effective delayed neutron fraction) of subcriticality in dollar units into one in pcm units, and β_{eff} was estimated with the use of the diffusion base in 3-dimentional and 107-energy-group. Consequently, the experimental results showed that the subcriticality in pcm units for 14 MeV neutrons was different from that for 100 MeV protons; remarkably, the discrepancy was also observed between the experiments and calculations.

3.2 Upcoming and Perspectives of ADS Experiments

An upcoming ADS at KUCA could be composed of the HEU fueled and Pb-Bi zoned core, in consideration of the actual ADS. The neutronic characteristics of Pb-Bi are considered importantly analyzed experimentally from in the viewpoint of reactor physics: neutron yield and neutron spectrum by the solid Pb-Bi target; uncertainties of Pb-Bi cross sections in the core. At KUCA, as preliminary study on the solid Pb-Bi characteristics, the critical mass and the sample worth experiments relating Pb-Bi could be conducted to investigate the uncertainties of Pb-Bi cross sections with the use of Pb-Bi solid plates, in addition to the solid Pb and Bi plates. Furthermore, irradiation experiments of the minor actinides (^{237}Np and ^{241}Am) could be conducted in hard spectrum core at KUCA to examine the feasibility of conversion analyses of nuclear transmutation.

4. Conclusion

At KUCA, the ADS experiments with 100 MeV protons were carried out with the combined use of the KUCA A-core and the FFAG accelerator. To resolve the drawback of the location of the target outside the core, the concept of moving the target and two-layer target composed of W and Be were introduced in the ADS experiments. The effects of moving the target location and introducing the two-layer target were found apparently well on the neutron multiplication deduced by the ^{115}In(n, γ)^{116m}In reaction rates.

Thorium-loaded ADS study was conducted as observed by the prompt neutron behavior and the reaction rates through the kinetic and static experiments, respectively. Further, mockup experiments of thorium-loaded ADS were successfully carried out in the subcritical states with the use of external neutron source (14 MeV neutrons and 100 MeV protons), respectively.

In the future, the upcoming ADS experiments with 100 MeV protons could be carried out at the HEU fueled and Pb-Bi zoned core of KUCA to investigate the neutronic characteristics of solid Pb-Bi material used in the core and at the target. Furthermore, irradiation experiments of ^{237}Np and ^{241}Am could be conducted in hard spectrum core at KUCA to examine the feasibility of conversion analyses of nuclear transmutation.

Acknowledgements

This work was supported by KUR Research Program for Scientific Basis of Nuclear Safety from the Ministry of Education, Culture, Sports, Science and Technology (MEXT) of Japan. The authors are grateful to all the technical staff of KUCA for their assistance during the experiments.

References

[1] Lagrange JB, Planche T, Yamakawa E, et al. Straight scaling FFAG beam line. Nucl. Instrum. Methods A. 2013; 691: 55-63.
[2] Yamakawa E, Uesugi T, Lagrange JB et al. Serpentine acceleration in zero-chromatic FFAG accelerators. Nucl. Instrum. Methods A. 2013; 716: 46-53.
[3] Pyeon CH, Misawa T, Lim JY, et al. First injection of spallation neutrons generated by high-energy protons into the Kyoto University Critical Assembly. J. Nucl. Sci. Technol. 2009; 46: 1091-1093.
[4] Pyeon CH, Shiga H, Abe K, et al. Reaction rate analysis of nuclear spallation reactions generated by 150, 190 and 235 MeV protons. J. Nucl. Sci. Technol. 2010; 47: 1090-1095.
[5] Lim JY, Pyeon CH, Yagi T et al. Subcritical multiplication parameters of the accelerator-driven system with 100 MeV protons at the Kyoto University Critical Assembly. Sci. Technol. Nucl. Install. 2012;

395878, 9.

[6] Pyeon CH, Azuma T, Takemoto Y et al. Experimental analyses of external neutron source generated by 100 MeV protons at the Kyoto University Critical Assembly. Nucl. Eng. Technol. 2013; 45: 81-88.

[7] Takahashi Y, Azuma T, Nishio T et al.. Conceptual design of multi-target for the accelerator-driven system experiments with 100 MeV protons. Ann. Nucl. Energy. 2013; 54: 162-166.

[8] Yagi T, Pyeon CH, Misawa T. Application of wavelength shifting fiber to subcriticality measurements. Appl. Radiat. Isot. 2013; 72: 11-15.

[9] Pyeon CH, Lim JY, Takemoto Y et al. Preliminary study on the thorium-loaded accelerator-driven system with 100 MeV protons at the Kyoto University Critical Assembly. Ann. Nucl. Energy. 2011; 38: 2298-2302.

[10] Pyeon CH, Yagi T, Sukawa K et al. Mockup experiments on the thorium-loaded accelerator-driven system in the Kyoto University Critical Assembly. Nucl. Sci. Eng. 2014;117:156-168.

[11] Hendricks JS, McKinney GW, Waters LS, et al. MCNPX user’s manual, version 2.5.0. LA-UR-05-2675. 2005. Los Alamos National Laboratory.

[12] Mclane V, ed. ENDF-102: Data formats and procedures for the evaluated nuclear data file ENDF-6. BNL-NCS-44945-01/04-Rev. 2001.

[13] Chadwick MB, Oblozinsky P, Herman M et al. ENDF/B-VII.0: Next generation evaluated nuclear data library for nuclear science and technology. Nucl. Data Sheets. 2006; 107: 2931-3060.

[14] Kobayashi K, Iguchi T, Iwasaki S et al. JENDL dosimetry file 99 (JENDL/D-99). JAERI Report 1344. 2002.

[15] Fukahori T. JENDL High-Energy File. J. Nucl. Sci. Technol., suppl. 2002; 2: 25-30.

[16] Takada H, Kosako K, Fukahori T. Validation of JENDL high-energy file through analyses of spallation experiments at incident proton energies from 0.5 to 2.83 GeV. J. Nucl. Sci. Technol. 2009; 46: 589-598.

9. Study of Deuteron-induced Reactions for Engineering Design of Accelerator-driven Neutron Sources

Yukinobu WATANABE, Shinsuke NAKAYAMA, Shouhei ARAKI, and Tadahiro KIN
Department of Advanced Energy Engineering Science, Kyushu University,
Kasuga, Fukuoka 816-8580, Japan
e-mail: watanabe@aees.kyushu-u.ac.jp

A comprehensive research project is outlined on deuteron nuclear data consisting of measurement, theoretical model analysis, cross section evaluation, and application to radioisotope production for medical use. The goal is to develop a state-of-the-art deuteron nuclear data library up to 200 MeV which will be necessary for engineering design of future (d,xn) neutron sources. The current status and future plan are described.

1. Introduction

In recent years, research and development of intensive accelerator-driven neutron sources has led to renewed interest in the study of deuteron-induced reactions. In Fig.1, experimental thick target neutron yields at 0 degree are compared between (p,xn) and (d,xn) reactions on ^{9}Be [1-3]. The comparison shows some superior features of (d,xn) neutron sources: more intensive neutron yields than (p,xn) neutron sources and broad peak structure around half the incident energy which becomes prominent with increase in incident energy. In addition, the (d,xn) reaction has strongly forward-peaked angular distribution that is one of favorable characteristics from the point of view of shielding.

By taking advantage of these characteristics, the accelerator neutron sources using deuteron-induced reactions on ^{7}Li, ^{9}Be, ^{12}C, etc., are proposed for various neutron beam applications such as production of radioisotopes (RIs) for medical use [4], boron neutron capture therapy (BNCT) [5], irradiation testing of fusion reactor materials [6], and production of high intensity RI beams of neutron-rich nuclei [7]. The engineering design of such (d,xn) neutron sources requires nuclear-physics based knowledge about not only the interaction of deuterons with target materials but also various nuclear reactions due to deuteron beam loss in beam collimators and dumps in the transport system. Thus, comprehensive nuclear data of deuteron-induced reactions over the wide ranges of incident energy and target mass number are indispensable for accurate estimation of neutron yields and induced radioactivity.

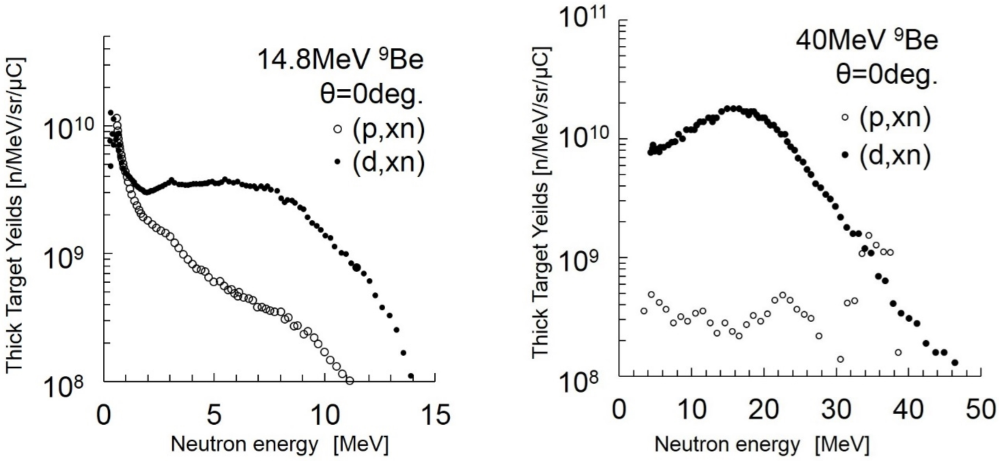

Fig.1 Thick target neutron yields from (p,xn) and (d,xn) reactions on ^{9}Be at 14.8 MeV and 40 MeV. The experimental data are taken from Refs. [1-3].

An evaluated nuclear data library called TENDL-2013[8] is now available for deuteron-induced reactions up to 200 MeV. Recently, the data have been stored in FENDL-3[9] for fusion technology. However, TENDL-2013 was created by the theoretical model code TALYS [10], and has not yet been well-validated for available experimental data.

According to the current status of (d,xn) measurements [11], there are no available experimental data of double differential (d,xn) cross sections above 20 MeV except for the Li(d,xn) data at 25 and 40 MeV. Thick target neutron yield (TTNY) data do exist for deuteron energies up to 53.8 MeV. On the other hand, a variety of measured (d,xp) spectra are currently available over the wide range of target mass number for incident energies below 100 MeV.

Taking into consideration these circumstances, we have launched a comprehensive and systematic research project on deuteron nuclear data consisting of measurement, theoretical model analysis, evaluation, and application. Our goal is to develop a state-of-the-art deuteron nuclear data library up to 200 MeV necessary for the engineering design of (d,xn) neutron sources. The current status and future plan are presented in the following sections.

2. Theoretical model analyses and code development

We have been studying a model calculation method that is capable of describing inclusive nucleon emission quantitatively [12-16]. Figure 2 illustrates a schematic view of (d,xn) reaction mechanisms and the corresponding theoretical models used in our calculation approach. The model calculation uses the continuum discretized coupled channels (CDCC) method for elastic breakup process, the Glauber model for nucleon stripping process to continuum, a zero-range DWBA approach for nucleon stripping process to bound states in the residual nuclei, and the exciton plus Hauser-Feshbach model for pre-equilibrium and evaporation processes. Our proposed method has been applied to the ^{7}Li(d,xn) reaction at 40 MeV [12] for the first time, and then to the inclusive (d,xp) reactions which were measured systematically for ^{9}Be, ^{12}C, ^{27}Al, ^{58}Ni, ^{93}Nb, ^{181}Ta, ^{208}Pb, and ^{238}U at 100 MeV [14]. It should be noted that a phenomenological moving source model for the pre-equilibrium and evaporation processes was used and the stripping process to bound states in the residual nuclei was neglected in Refs. [12-14]. These earlier studies have encouraged us to develop an integrated code system for nuclear data evaluation of deuteron-induced reactions. As a result, the integrated code system [15,16] has been developed by combining additional codes: CCONE [17] for pre-equilibrium and evaporation processes and DWUCK4 [18] for the stripping process to bound states.

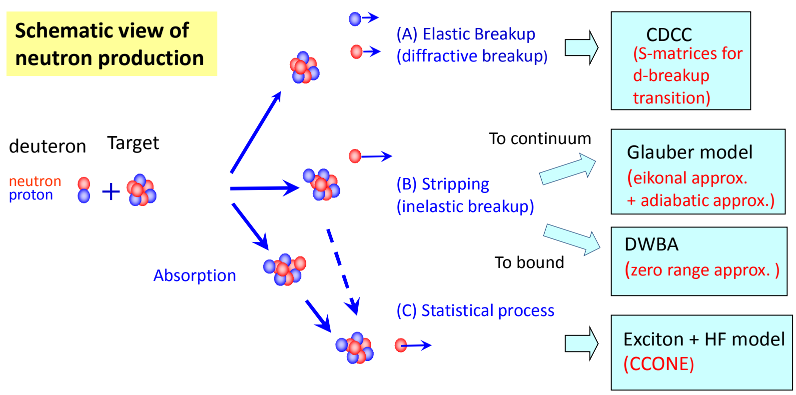

Fig.2 Schematic illustration of (d,xn) reaction mechanisms and the corresponding theoretical models

Typical results of the (d,xp) reactions at 56 and 100 MeV on ^{27}Al are shown in Fig.3. The calculation reproduces fairly well both the shape and magnitude of the experimental (d,xp) spectra including the peak structure observed in the high emission energy range, which is formed by the stripping process to bound states. The stripping process to continuum described by the Gauber model is a predominant (d,xp) mechanism leading to the broad peak observed at half the incident energy.

For the engineering design of deuteron accelerator neutron sources, it is also important to estimate production of radioactive nuclei. Production cross sections of ^{28}Al ($T_{1/2}$ = 2.24 min) via ^{27}Al(d,p)^{28}Al are calculated and compared with experimental data in Fig.4 [16]. All of the neutron stripping reactions to 35 final excited states up to 5.135MeV are taken into account for production of ^{28}Al. The sum of the statistical decay component and the contribution from stripping to bound states reproduce the experimental data fairly well in the low incident energy range. This result indicates that it is important to consider the stripping reaction to bound states appropriately in accurate estimation of induced radioactivity.

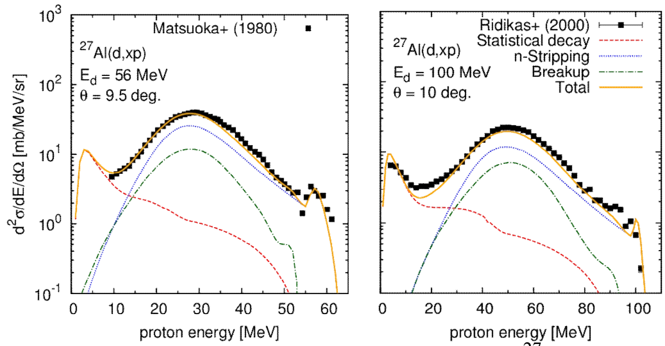

Fig.3 Calculated and experimental DDXs for ^{27}Al (d,xp) reactions at 56 and 100 MeV. The experimental data are taken from Refs. [19,20].

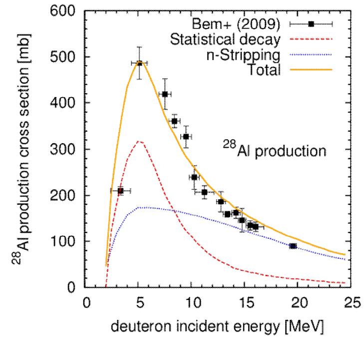

Fig.4 Production cross sections of ^{28}Al. The experimental data are taken from Ref.[21].

3. Nuclear data measurement at Kyushu University Tandem accelerator Laboratory

So far, we have performed systematic measurements of double-differential thick target neutron yields (DDTTNYs) from thick targets irradiated by deuterons at the Kyushu University Tandem accelerator Laboratory (KUTL) [22-25]: carbon, aluminum, titanium, cupper and niobium for bombardment energies of 5 and 9 MeV. Details of the experimental set up and procedure have been reported in Refs. [22,23].

A deuteron beam accelerated to 5 or 9 MeV was delivered to a compact vacuum target chamber in the target room. The chamber was insulated from other experimental apparatus to acquire the whole beam charge induced on a target. The target thickness was chosen so that incident deuterons are stopped completely in the target. The target chamber 260 mm in diameter equipped a target frame which enabled to mount up to four target foils at the center of the chamber. An NE213 liquid organic scintillator 50.4 mm thick and 50.4 mm in diameter coupled optically with a Hamamatsu H6410 photomultiplier was used as a neutron detector. The detector was placed in the distances from 1.6 to 2.4 m from the center of the target. Neutron yields from the target were measured at nine angles of 0°, 15°, 30°, 45°, 75°, 90°, 120° and 140° by changing the detector position. In order to estimate the contribution of background neutrons scattered from the floor and walls in the experimental room, a background measurement with an iron shadow bar 150 mm x 150 mm x 300 mm thick placed between the target and the neutron detector was performed for each direction.

The neutron energy spectra were obtained by means of an unfolding method using FORIST code [26] with the response function of the NE213 scintillator calculated by SCINFUL-QMD code [27]. The experimental result was compared with the calculation based on intra-nuclear cascade of Liège (INCL) model in PHITS code [28].

The experimental DDTTNY data for aluminum at 9 MeV are shown with the INCL calculation in Fig.5 as an example of all the measured results. The INCL calculation reproduces the experimental data well at emission energies below 7 MeV over the whole angular range, while there are some discrepancies between them at higher emission energies, especially, for hump structure observed around the high-energy end. Figure 6 presents angular distributions of neutron yields integrated over emission energy above 2 MeV. Forward-peaked angular distribution is observed for each target, and the trend becomes prominent as the target atomic number decreases. The INCL calculation fails to reproduce the experimental angular distribution; there is a tendency having overestimation at forward angles and underestimation at backward angles, except for carbon where the INCL calculation underestimates the measured result over the whole angular range even at the smallest angle. Since the intra-cascade model generally works well at high incident energies, the application of the INCL model to 9 MeV incidence might be beyond the scope of the model. Further study to examine the application will be needed for higher incident energies than the present measurements.

In the future, we plan to carry out further measurements for targets with larger atomic and mass number than niobium in order to study the systematics of neutron yields for deuteron bombardment at energies below 10 MeV. Moreover, these measured data will be useful for benchmark testing of the prototype deuteron nuclear data that will be developed using the above-mentioned theoretical model code system.

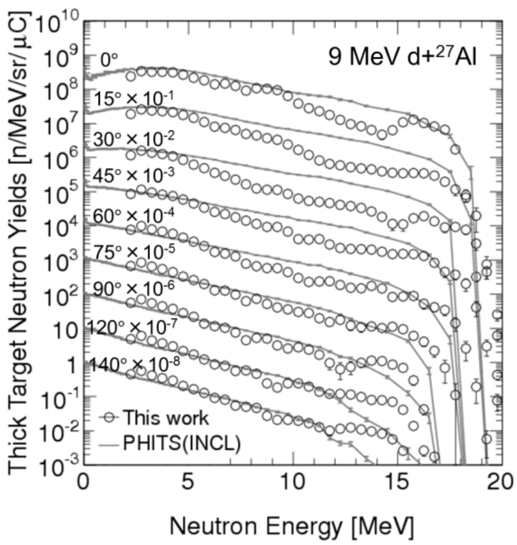

Fig.5 Comparison of experimental neutron spectra from a thick aluminum target bombarded by 9 MeV deuterons at nine laboratory angles with INCL calculation.

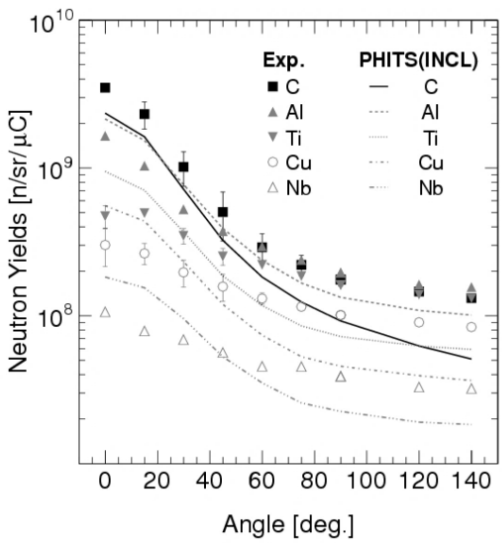

Fig.6 Comparison of angular distributions of neutron yields integrated over emission energy above 2MeV for C, Al, Ti, Cu, and Nb at 9 MeV with INCL calculation.

4. Application to radioisotope production for medical use

Recently, a new system has been proposed for the generation of radioisotopes with accelerator neutrons by deuterons (GRAND) [4], aiming mainly at production of ^{99}Mo used for nuclear medicine diagnosis. In the GRAND project, the C(d,xn) reaction is a candidate reaction as a neutron source. We pay attention to the generation of ^{64}Cu ($T_{1/2}$= 12.7 h) with accelerator neutrons by deuterons from the needs for a longer half-life PET radionuclide to diagnose the dynamics of a medicine in living body (cf. ^{18}F: $T_{1/2}$ = 1.8 h) [29]. The radioisotope ^{64}Cu is a promising radionuclide suitable for labeling many radiopharmaceuticals for PET imaging because it decays by positron emission with a maximum energy of 0.653MeV.

To generate ^{64}Cu, the ^{64}Zn(n,p)^{64}Cu reaction with neutrons below 10 MeV will be effective as shown in Fig.7, because it is expected that by-products via the other reactions is suppressed. As mentioned in the preceding section, the neutron yield from thick carbon bombarded by 9-MeV deuterons has been measured. Its energy spectrum at 0 degree is presented in Fig.8. The generation of intense neutrons below 10 MeV is possible, and the ^{64}Zn(n,p)^{64}Cu reaction has a large cross section in the energy range as can be seen in Fig.7.

More recently, we have performed a test experiment to produce ^{64}Cu from a natural Zn target using mono-energetic neutron source based on the D(d,n) reaction for validation of the evaluated production cross sections at KUTL. The data analysis is now in progress. In addition, we will organize a new experiment to generate ^{64}Cu from a natural Zn target using a prototype neutron source with the C(d,xn) reaction at KUTL, in order to optimize the incident deuteron energy and the design of Zn target.

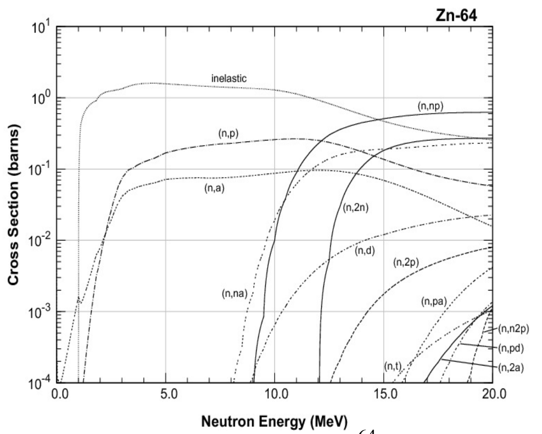

Fig.7 Neutron cross sections for ^{64}Zn taken from JENDL-4 [30].

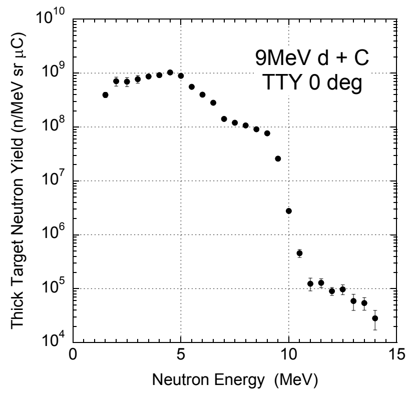

Fig.8 Neutron spectrum at 0 degree for thick target neutron yields for carbon bombarded by 9-MeV deuterons taken from Ref. [24].

5. Summary and future outlook

The outlines are sketched of our new research project on comprehensive and systematic study of deuteron nuclear data for engineering design of accelerator-driven neutron sources. It consists of nuclear data measurements including thick target neutron yields, theoretical model analyses and code development, cross section evaluation and benchmark test, and application to production of radioisotopes for medical use. Toward our goal to develop a state-of-the-art nuclear data library up to 200 MeV, the following actions will be taken in the future:

- Continued measurements of neutron production and activation cross sections
- Validation of the above-mentioned code system using a variety of differential data.
- Cross section evaluation and creation of a prototype nuclear data library for specific nuclei such Li, Be, C and so on.
- Benchmark testing of Monte Carlo transport codes (e.g., PHITS) with newly-evaluated nuclear data library using experimental thick target neutron yields.
- Application of our proposed deuteron transport calculation method to the design of radioisotope production for medical use.

With regard to the measurements, a new systematic measurement of neutron production from deuteron-induced reactions is planned for incident energies of 100-200 MeV using the neutron TOF facility at RCNP. In the first campaign planned in 2014, double differential cross sections and thick target yields at 100 MeV will be measured at forward angles for some targets such as beryllium, carbon, and aluminum.

Acknowledgements

The authors wish to thank all the co-workers for their kind cooperation and fruitful discussion: N. Shigo, K. Hirabayashi, Y. Tajiri, K. Sagara, S. Maebara, H. Takahashi, and H. Sakaki for TTY measurements at KUTL; O. Iwamoto, K. Ogata, and T. Ye for theoretical model and code development. This work was supported in part by Grant-in-Aid for Scientific Research of the Japan Society for the Promotion of Science (Grant No. 19560844 and No. 22560820).

References

[1] Lone MA, C.B. Bigham CB, Fraser JS, Schneider HR, Alexander TK, Ferguson AJ, McDonald AB. Thick target neutron yields and spectral distributions from the ^{7}Li(d, n) and ^{9}Be(d, n) reactions. Nucl. Instr. Meth. 1977; 143: 331-344.
[2] Saltmarsh MJ, Ludemann CA, Fulmer CB, Styles RC. Characteristics of an intense neutron source based on the d+Be reaction. Nucl. Instr. Meth. 1977; 145: 81-90.
[3] Uwamino Y, Ohkubo T. Semi-monoenergetic neutron field for activation experiments up to 40 MeV. Nucl. Instr. Meth. Phys. Res., Sect. A. 1988; 271: 546-552.
[4] Nagai Y, Hashimoto K, Hatsukawa Y, Saeki H, Motoishi S, Sato N, Kawabata M, Harada H, Kin T, Tsukada K, Sato TK, Minato F, Iwamoto O, Iwamoto N, Seki Y, Yokoyama K, Shiina T, Ohta A, Takeuchi N, Kawauchi Y, Sato N, Yamabayashi H, Adachi Y, Kikuchi Y, Mitsumoto T, Igarashi T. Generation of Radioisotopes with Accelerator Neutrons by Deuterons. J. of Phys. Soc. of Japan. 2013; 82(6), 064201.
[5] Agosteo S, Curzio G, d'Erricoc F, Nath R, Tintie R. Characterisation of an accelerator-based neutron source for BNCT versus beam energy. Nucl. Instr. Meth. Phys. Res., Sect. A. 2002; 476: 106-112.
[6] Garin P, Sugimoto M. IFMIF's new design: Status after 2 years of the EVEDA project. J. Nucl. Mater. 2011; 417: 1262-1266, and references therein.
[7] Fadil M, Rannou B, and the SPIRAL2 project team. About the production rates and the activation of the uranium carbide target for SPIRAL 2. Nucl. Instr. Meth. Phys. Res., Sect. B. 2008; 266: 4318-4321.
[8] TENDL-2013 [internet]. Available from: http://www.talys.eu/tendl-2013/
[9] Forrest R, Capote R, Otsuka N, Kawano T, Koning AJ, Kunieda S, Sublet J-Ch, Watanabe Y. FENDL-3 Library Summary documentation. Vienna: International Atomic Energy Agency, Nuclear Data Section; 2012. (INDC(NDS)-0628).
[10] Koning AJ, Hilaire S, Duijvestijn MC, TALYS-1.0. In: Bersillon O, Gunsing F, Bauge E, Jacqmin R, Leray S, editors. Proceedings of International Conference on Nuclear Data for Science and Technology; 2007 April 22-27; Nice (France): EDP sciences; c2008. pp.211-214.
[11] EXFOR [internet]. Available from: https://www-nds.iaea.org/exfor/exfor.htm
[12] Tao Y, Watanabe Y, Ogata K, Analysis of deuteron breakup reactions on ^{7}Li for energies up to 100 MeV. Phys. Rev. C. 2009; 80: 014604.
[13] Watanabe Y, Ye T, Ogata K, In: Bonneau L, Dubray N, Gunsing F, Jurado B, editors. Proceedings of Second International Workshop on Compound Nuclear Reactions and Related Topics (CNR*09); 2009 Oct. 5-8; Bordeaux (France): EPJ Web Conferences. 2010; 2: 11003.
[14] Tao Y, Hashimoto S, Watanabe Y, Ogata K, Yahiro M. Analysis of inclusive (d,xp) reactions on nuclei from ^{9}Be to ^{238}U at 100 MeV. Phys. Rev. C. 2011; 84: 054606.
[15] Nakayama S, Araki S, Watanabe Y, Iwamoto O, Ye T, Ogata K. Cross Section Calculations of Deuteron-induced Reactions Using Extended CCONE. Paper presented at International Conference on Nuclear Data for Science and Technology; 2013 March 22-27; New York (USA): Nucl. Data Sheets 2014; 118: 305-307.
[16] Nakayama S, Araki S, Watanabe Y, Iwamoto O, Ye T, Ogata K. Development of a calculation code system for evaluation of deuteron nuclear data. Paper presented at the Fourth International Symposium on Innovative Nuclear Energy Systems (INES-4), 2013 Nov. 6-8; Tokyo (Japan).
[17] Iwamoto O. Development of a Comprehensive Code for Nuclear Data Evaluation, CCONE, and Validation Using Neutron-Induced Cross Sections for Uranium Isotopes. J. Nucl. Sci. Technol. 2007; 44(5), 687-697.
[18] Kunz PD. DWUCK4. 1974. http://spot.colorado.edu/~kunz/DWBA.html

[19] Matsuoka N, Kondo M, Shimizu A, Saito T, Nagamachi S. Deuteron break-up in the fields of nuclei at 56 MeV. Nucl. Phys. A. 1980; 345: 1-12.
[20] Ridikas D, Mittig W, Savajols H, Roussel-Chomaz P, Förtsch SV, Lawrie JJ, Steyn GF. Inclusive proton production cross sections in (d,xp) reactions induced by 100 MeV deuterons. Phys. Rev. C. 2000; 63: 014610.
[21] Bem P, Simeckova E, Honusek M, Fischer U, Simakov SP, Forrest RA, Avrigeanu M, Obreja AC, Roman FL, Avrigeanu V. Low and medium energy deuteron-induced reactions on ^{27}Al. Phys. Rev. C. 2009; 79: 044610.
[22] Shigyo N, Hidaka K, Hirabayashi K, Nakamura Y, Moriguchi D, Kumabe M, Hirano H, Hirayama S, Naitou Y, Motooka C, Lan C, Watanabe T, Watanabe Y, Sagara K, Maebara S, Sakaki H, Takahashi H. Measurement of Deuteron Induced Thick Target Neutron Yields at 9 MeV. J. Kor. Phys. Soc. 2011; 59(2): 1725-1728.
[23] Hirabayashi K, Nishizawa T, Uehara H, Hirano H, Kajimoto T, Shigyo N, Maeda M, Yasumune T, Maehata K, Tajiri Y, Umishio H, Abe S, Watanabe Y, Sagara K, Maebara S, Takahashi H, Sakaki H. Measurement of Neutron Yields from Thick Al and SUS304 Targets Bombarded by 5-MeV and 9-MeV Deuterons. Prog. in Nucl. Sci. and Technol. 2012; 3: 60-64.
[24] Tajiri Y, Watanabe Y, Shigyo N, Hirabayashi K, Nishizawa T, Sagara K. Measurement of double differential neutron yields from thick carbon target irradiated by 5-MeV and 9-MeV deuterons. Prog. in Nucl. Sci. and Technol, 2014; 4: 582-586.
[25] Araki S, Watanabe Y, Kin T, Shigyo N, Sagara K. Measurement of double differential neutron yields from thick aluminum target irradiated by 9 MeV deuteron. Paper presented at the Fourth International Symposium on Innovative Nuclear Energy Systems (INES-4), 2013 Nov. 6-8; Tokyo (Japan).
[26] Johnson RH, Ingersoll DT, Wehring BW, Dorning JJ. NE-213 neutron spectrometry system for measurements from 1.0 to 20 MeV. Nucl. Instr. Meth. 1977; 145: 337-346.
[27] Satoh D, Sato T, Shigyo N, Ishibashi K. SCINFUL-QMD: Monte Carlo Based Computer Code to Calculate Response Function and Detection Efficiency of a Liquid Organic Scintillator for Neutron Energies up to 3 GeV. Japan Atomic Energy Research Institute; 2006. (JAEA-Data/Code 2006-023).
[28] Sato T, Niita K, Hashimoto S, Iwamoto Y, Noda S, Ogawa T, Iwase H, Nakashima H, Fukahori T, Okumura K, Kai T, Chiba S, Furuta T, Sihver L. Particle and Heavy Ion Transport Code System PHITS, Version 2.52. J. Nucl. Sci. Technol. 2013; 50(9): 913-923.
[29] Kin T, Nagai Y, Iwamoto N, Minato F, Iwamoto O, Hatsukawa Y, Segawa M, Harada H, Konno C, Ochiai K, Takakura K. New Production Routes for Medical Isotopes ^{64}Cu and ^{67}Cu Using Accelerator Neutrons. J. of Phys. Soc. of Jpn. 2013; 82(3): 034201.
[30] Shibata K, Iwamoto O, Nakagawa T, Iwamoto N, Ichihara A, Kunieda S, Chiba S, Furutaka K, Otuka N, Ohsawa T, Murata T, Matsunobu H, Zukeran A, Kamada S, Katakura J. JENDL-4.0: A New Library for Nuclear Science and Engineering. J. Nucl. Sci. Technol. 2011; 48(1): 1-30.

10. Application of CDCC Theory to Nuclear Data Evaluation for Nucleon-induced Reactions on ^{6,7}Li

Hairui Guo[a], Kohei Nagaoka[a], Yukinobu Watanabe[a], Takuma Matsumoto[b],
Kazuyuki Ogata[c], and Masanobu Yahiro[b]
[a]Department of Advanced Energy Engineering Science, Kyushu University, Kasuga,
Fukuoka 816-8580, Japan
[b]Department of Physics, Kyushu University, Fukuoka 812-8581, Japan
[c]Research Center for Nuclear Physics, Osaka University, Ibaraki, Osaka 567-0047, Japan
Email: ghr@aees.kyushu-u.ac.jp

Nucleon-induced reactions on ^{6,7}Li are analyzed systematically over a wide range of incident energies up to 150 MeV by using three-body continuum discretized coupled channels method (CDCC) capable of treating the breakup of ^{6,7}Li. The diagonal and coupling potentials in the CDCC equation are obtained by folding the complex JLM effective nucleon-nucleon interaction with transition densities. The normalization factors of the complex effective interaction are determined so as to reproduce experimental data on neutron total and proton reaction cross sections. Triton emission from ^{7}Li breakup channel and p(n)+^{7}Li→t+^{5}Li*(^{5}He*) channel is also analyzed by the sequential decay (SD) model and final state interaction model, respectively. The triton emission spectra from ^{7}Li breakup channel obtained from CDCC and SD model are basically consistent. In most cases, the calculated results are in good agreement with experimental data except for the double differential nucleon and triton production cross sections at relatively low emission energies.

1. Introduction

In fusion technology, lithium is an important element relevant to not only a tritium breeding material in D-T fusion reactors but also a candidate for target material in the intense neutron source of International Fusion Materials Irradiation Facility [1]. The accurate nuclear data of nucleon induced reactions on ^{6,7}Li are therefore currently required for incident energies up to 150 MeV [2]. Since ^{6}Li and ^{7}Li can easily break up, namely, ^{6}Li→ d + α and ^{7}Li → t + α, breakup reactions influence all the other reaction channels. Therefore, systematic understanding of the breakup reaction mechanism is of great significance for the nuclear data evaluation of nucleon-induced reactions on ^{6,7}Li.

2. Theoretical model

Neutron total cross sections, proton reaction cross sections, nucleon scattering spectra and triton emission spectra from the breakup process of ^{7}Li are analyzed with three-body CDCC [3-4]. In CDCC, ^{6}Li and ^{7}Li are considered as a d+α and a t+α cluster, respectively. The breakup continuum states of ^{6,7}Li are truncated and discretized to finite number of discrete states by the pseudostate method [5] with the internal interactions as Gaussian forms, sequentially the breakup effect is analyzed by coupled channel method considering the discretized states. The diagonal and coupling potentials between nucleon and ^{6,7}Li are obtained by folding complex JLM effective nucleon-nucleon interaction [6] with the transition densities between the corresponding bound and discretized states. The normalization factors of JLM interaction are determined so as to reproduce the experimental data of neutron total and proton reaction cross sections. The detailed description of the formulation of CDCC and normalization factors of JLM nucleon-nucleon interaction used is given in Ref. [7]. The triton production double differential cross section (DDX) from the breakup process of ^{7}Li is obtained using the S matrix from CDCC. The formula [3] is expressed as

$$\frac{d^2\sigma}{dE_t d\Omega_t} = \int \frac{2\pi}{\hbar} \frac{\mu_{Li-N}}{P_0} \left| T_{fi} \right|^2 \rho(E_t) d\Omega_\alpha, \tag{1}$$

where ρ is the phase space factor, μ_{Li-N} is the reduced mass of nucleon and ^{7}Li, $\hbar P_0$ is the incident momentum, T is the transition matrix obtained from the S matrix calculated by CDCC,

$$T_{fi} = i \frac{(2\pi\hbar)^3}{\sqrt{2\mu_{t-\alpha}\mu_{Li-N}}} \frac{1}{k\sqrt{PP_0}} \sum_{ljLJM} \sqrt{2J+1} [Y_l(\hat{k}) \otimes Y_L(\hat{P})]_{JM} e^{i(\delta_{ljk}+\sigma_{ljk})} S^J_{ljL}(k). \tag{2}$$

Here δ and σ are the nuclear and Coulomb scattering phase shifts between t and α, $\hbar \boldsymbol{P}$ is the momentum of the center of mass of t+α cluster with respect to the nucleon, $\hbar \boldsymbol{k}$ is the relative momentum between t and α.

The SD model [8] is also used to calculate the triton production DDX from the breakup process of ^{7}Li. The formula is expressed as

$$\left(\frac{d^2\sigma}{dE_t d\Omega_t} \right)^{J^\pi}_{\text{seq}} = \sum_i \frac{\sigma_i^{J^\pi}}{2\pi} \int L_1(E_N \to E_{\text{Li}}) L_2(E_{\text{Li}} \to E_t) \Lambda(\eta_{Nt}) dE_{\text{Li}}, \tag{3}$$

where $\sigma_i^{J^\pi}$ is the breakup cross section from the i-th discretized state of ^{7}Li which is obtained with CDCC. L_1 denotes the probability that an incident nucleon with energy E_N produces a particle ^{7}Li with energy E_{Li}. L_2 denotes the probability that an intermediate ^{7}Li with energy E_{Li} produces a triton with energy E_t. The triton emission is assumed to be isotropic, then L_1 and L_2 can be obtained using the conservation of momentum and energy [8]. $\Lambda(\eta_{Nt})$ stands for the probability of the cosine of the angle between the direction of incident nucleon and emitted triton being η_{Nt}.

The incident energies of the existing experimental data of triton production DDX are below 20 MeV where there are other reaction processes, n(p)+^{7}Li→t+^{5}He*(^{5}Li*), contributing to triton emission. In order to compare the calculated results with experimental data, the triton emission from these reaction processes is also calculated by the final state interaction (FSI) model [9]. Here, ^{5}He* and ^{5}Li* are considered as α-n and α-p systems, respectively. The formula is expressed as

$$\left(\frac{d^2\sigma}{dE_t d\Omega_t} \right)_{\text{FSI}} = N_F \cdot \sin^2 \beta_l \cdot \frac{F_l^2(k_{N\alpha}a) + G_l^2(k_{N\alpha}a)}{(k_{N\alpha}a)^2} \cdot \rho_t(E_t^{lab}), \tag{4}$$

where N_F is an adjustable parameter which is determined by fitting to experimental data, F_l and G_l are the first-order spherical Bessel functions for the α-n system and the Coulomb wave functions for the α-p system, k denotes the wave number of p(n) in α-p(n) system, ρ is the phase space factor, and β_l denotes the α-p(n) phase shift .

3. Results and discussion

Neutron total cross sections, proton reaction cross sections and nucleon elastic and inelastic scattering differential cross sections are calculated with CDCC and reported in Ref. [7]. In most cases, they are in good agreement with experimental data. Figs. 1 and 2 show comparisons of calculated results and experimental data [10–13] of the reaction cross section and elastic scattering differential cross section for p+^{7}Li reaction, respectively. Since the measured proton reaction cross sections for ^{7}Li [10] are not sufficient, we scale the experimental data [11] from p+^{9}Be reaction as supplement, which are shown by the solid circles in Fig. 1. The scaling method is described in Ref. [7]. Generally good agreement with the experimental data is obtained for both of the calculated results.

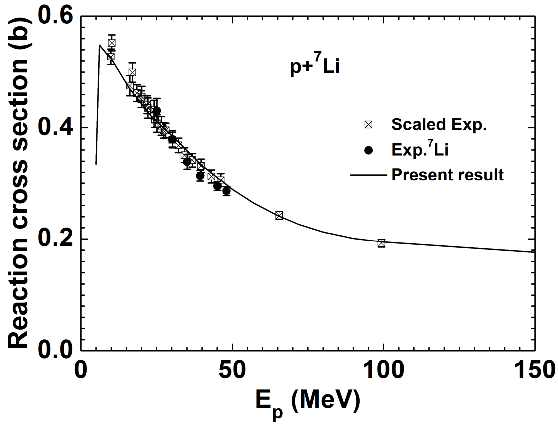

Fig. 1 Comparison of the calculated result (solid line) of reaction cross section for p+^{7}Li reaction with experimental data [10,11]. The circles and squares denote the experimental data for p+^{7}Li reaction and the scaled experimental data transformed from p+^{9}Be reaction, respectively.

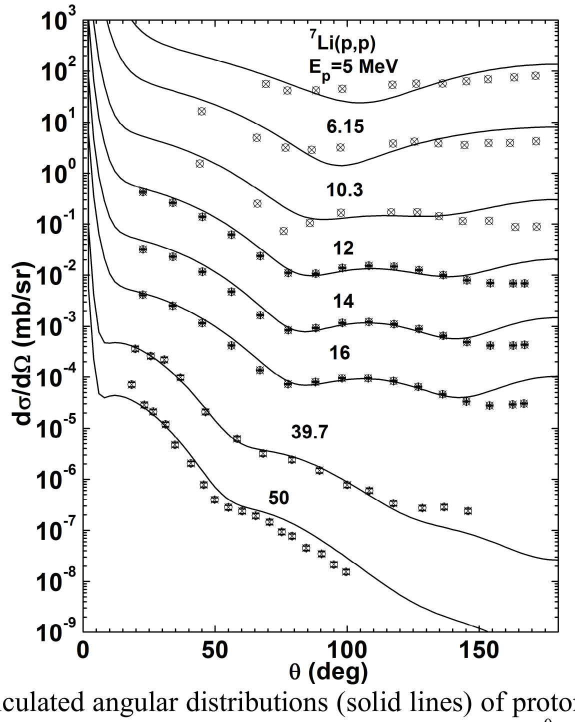

Fig. 2 Comparison of the calculated angular distributions (solid lines) of proton elastic scattering from ^{7}Li with experimental data [12]. The data are shifted downward by factors of 10^0, 10^{-1}, 10^{-2}, and so on.

The proton (neutron) production DDXs for p(n)+^{6}Li reactions are also calculated with CDCC. The calculated results reproduce experimental data well except for relatively low emission energy. Fig. 3 shows the calculated result of neutron production DDX for n+^{6}Li reaction at an incident energy of 14.1 MeV compared with experimental data [13]. The contributions corresponding to unbound ^{1}S, ^{1}D, ^{2}D and ^{3}D states of ^{6}Li are denoted by dash-dot-dotted, dashed, short dashed and dash-dotted lines, respectively. Three peaks of the calculated results represent the elastic, inelastic to the 3^+ resonance and 2^+ resonance components, respectively, from high emission energy end. The calculated result is in good agreement with the experimental data at relatively high emission energies, while it underestimates the experimental data in the low emission energy region. The reason for the discrepancy is that some other reaction channels, e.g., four-body breakup channel ^{6}Li(n,nnp)α [4], contribute to this energy region, which cannot be calculated with the present three-body CDCC.

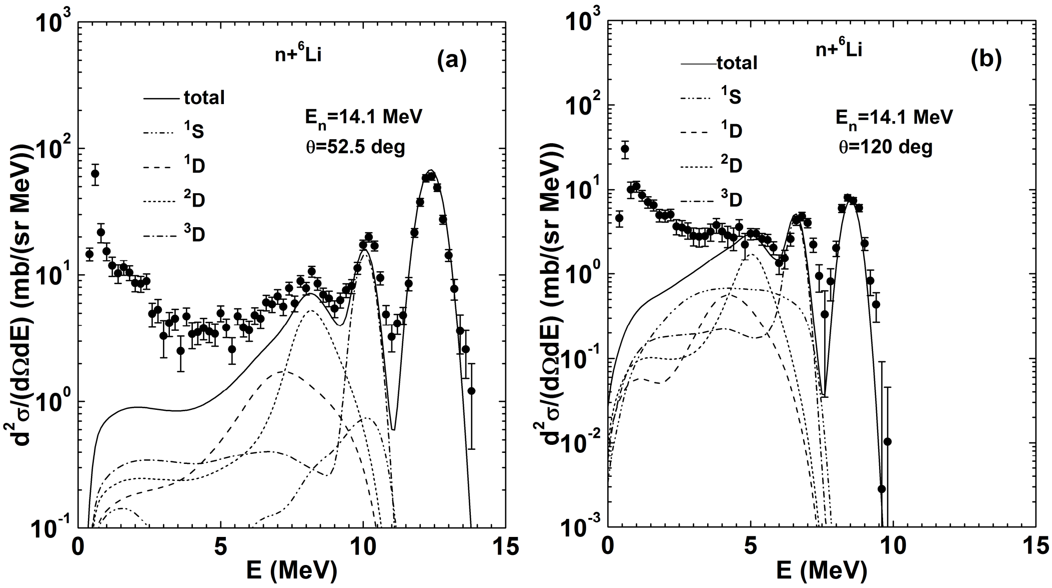

Fig. 3 The neutron production DDX (solid lines) calculated by CDCC compared with experimental data [13] for n+^{6}Li reaction in the laboratory system. The dash-dot-dotted, dashed, short dashed and dash-dotted lines denote the contributions corresponding to unbound ^{1}S, ^{1}D, ^{2}D and ^{3}D states of ^{6}Li, respectively.

The preliminary results of proton (neutron) production DDXs for p(n)+^{7}Li reactions are obtained with CDCC, FSI and SD models. The calculated results reproduce experimental data well for relatively high emission energy. Fig. 4 shows the comparison of the calculated result and experimental data [12] of proton production DDX for p+^{7}Li reaction at an incident energy of 14 MeV. It should be noted that several elastic and inelastic peaks due to contamination elements in target, such as ^{1}H, ^{12}C, ^{16}O, are observed in the experimental data. The contributions corresponding to unbound $^{3/2}$P, $^{1/2}$P, $^{7/2}$F and $^{5/2}$F states of ^{7}Li in CDCC result are denoted by dash-dot-dotted, dashed, short dashed and dash-dotted lines, respectively. The total CDCC result is denoted by thin solid lines. The CDCC calculation gives good agreement with the experimental data in the relatively high emission energy region, while it underestimates the experimental data at low energies. The proton emission from ^{7}Li(p,t)^{5}Li*→p+α channel is calculated with FSI and SD models and shown by dotted lines. The summation of this component and CDCC result denoted by thick solid lines improves the CDCC result considerably in the low emission energy region, but it still underestimates the experimental data at small angles, because there may be other reaction processes contributing to this energy region, such as (p,2p) reaction, which cannot be calculated with these theoretical models. It is also shown that the calculated result overestimates the experimental data for medium emission energy. One of the reasons is that the contribution corresponding to unbound P state of ^{7}Li is overestimated.

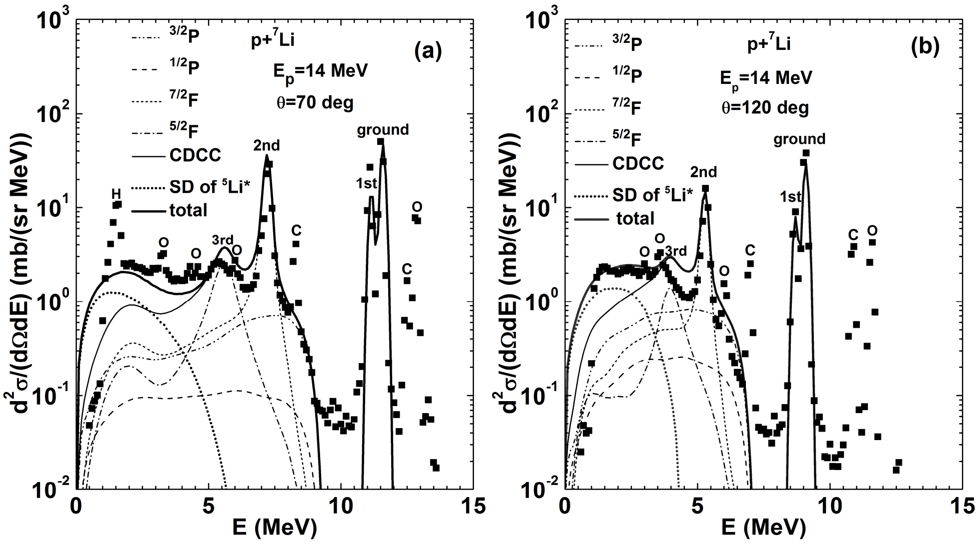

Fig. 4 The proton production DDX (thick solid lines) calculated by CDCC, SD and FSI models compared with experimental data [12] for p+^{7}Li reaction in laboratory system. The dash-dot-dotted, dashed, short dashed and dash-dotted lines denote the contributions corresponding to unbound $^{3/2}$P, $^{1/2}$P, $^{7/2}$F and $^{5/2}$F states of ^{7}Li in CDCC results, respectively. The total CDCC result is denoted by the thin solid lines. The dotted lines represent the proton emission from ^{7}Li(p,t)^{5}Li*→p+α channel calculated by FSI and SD models.

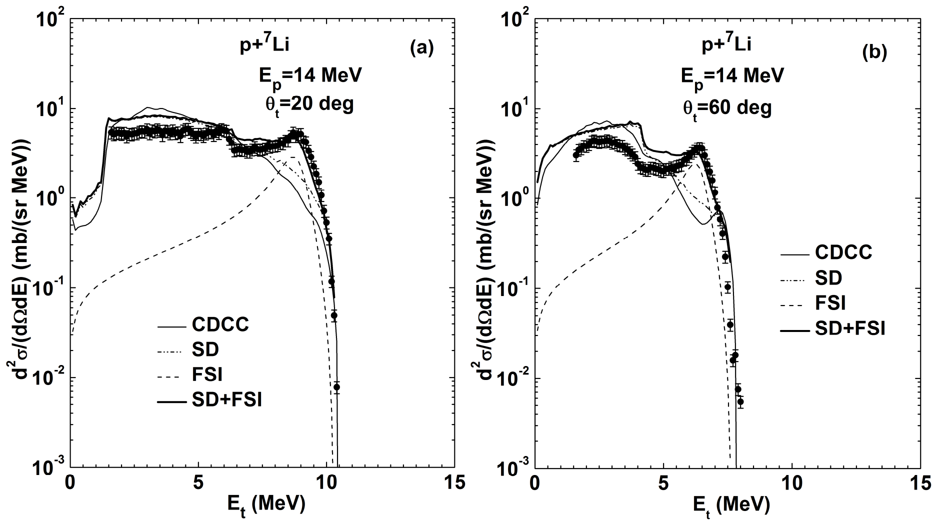

Fig. 5 The calculated triton production DDX (thick solid lines) compared with experimental data [12] for p+^{7}Li reaction in the laboratory system. The thin solid and dash-dot-dotted lines denote the component from breakup process of ^{7}Li calculated with CDCC and SD model, respectively, while the dash lines denote the contribution from p+^{7}Li→t+^{5}Li* reaction calculated with FSI model.

The preliminary results of triton production DDXs from breakup of ^{7}Li* are obtained by using CDCC and SD model, respectively. The result of the triton production DDX from the breakup channel for p+^{7}Li reaction at 14 MeV calculated by CDCC and SD model are shown by the thin solid and dash-dot-dotted lines respectively in Fig. 5. The two results are similar to each other, however, the one calculated by CDCC is time-consuming, which is less acceptable for nuclear data evaluation. Therefore the SD model can be used in nuclear data evaluation instead of CDCC. The calculated results overestimate the experimental data [12] at low emission energies, while they underestimate distinctly the experimental data at relatively high emission energies. It is expected that the large discrepancy at high emission energies is due to another reaction channel, $p+^7Li \rightarrow t+^5Li^*$. The contribution of this reaction is predicted by the FSI model, and shown by dotted lines in Fig. 5. It can be seen that the triton emission from this reaction channel contributes mainly to high emission energy region. The total triton production DDX obtained by summing the SD and FSI results shown by the thick solid lines can reproduce the experimental data fairly well at high energies, but overestimate the experimental data for low emission energy region. The reason for the overestimation is that the contribution from the unbound P state of ^7Li is overestimated.

4. Summary and conclusion

Neutron total cross sections, proton reaction cross sections, nucleon elastic and inelastic scattering differential cross sections, proton (neutron) production DDXs for $p(n)+^{6,7}Li$ reactions and triton production DDXs for $p(n)+^7Li$ reactions are calculated with CDCC, SD and FSI models. The theoretical results are compared with the existing data. For the cross sections and differential cross sections, the calculated results are in good agreement with the experimental data. For the nucleon production DDXs, the calculated results can reproduce the experimental data well at relatively high emission energies, while they underestimate the experimental data at low emission energies. The reason for the discrepancy is that some other reaction channels contribute to this energy region. The calculated triton production DDXs can also reproduce the experimental data well at high emission energies, while they overestimate the experimental data for relatively low emission energy region. One of the reasons for this discrepancy is because the contribution from the unbound P state of ^7Li is overestimated.

References

[1] Garin P, Sugimoto M. IFMIF's new design: Status after 2 years of the EVEDA project. J. Nucl. Mater. 2011; 417: 1262-1266, and references therein.

[2] Forrest R, Capote R, Otsuka N, Kawano T, Koning AJ, Kunieda S, Sublet J-Ch, Watanabe Y. FENDL-3 Library Summary documentation. Vienna: International Atomic Energy Agency, Nuclear Data Section; 2012. (INDC(NDS)-0628).

[3] Yahiro M, Ogata K, Matsumoto T, Minomo K. The continuum discretized coupled-channels method and its applications. Prog. Theor. Exp. Phys. 2012; 01A206: 1-44, and references therein.

[4] Matsumoto T, Ichinkhorloo D, Hrabayashi Y, Katō K, Chiba S. Systematic description of the $^6Li(n,n') \rightarrow d+\alpha$ Reactions with microscopic coupled-channels method. Phys. Rev. C. 2011; 83: 064611.

[5] Matsumoto T, Kamizato T, Ogata K, Iseri Y, Hiyama E, Kamimura M, Yahiro M. New treatment of breakup continuum in the method of continuum discretized coupled channels. Phys. Rev. C. 2003; 68: 064607.

[6] Jeukenne JP, Lejeune A, Mahaux C. Optical model potential in finite nuclei from Reids hard core interaction. Phys. Rev. C. 1977 ; 16 : 80-96.

[7] Guo H, Watanabe Y, Matsumoto T, Ogata K, Yahiro M. Phys. Rev. C. 2013; 87: 024610.

[8] Beynon TD, Sim BS, Modelling of the $^9Be(n,2n)$ double differential cross section. Ann. Nucl. Energy. 1988; 15: 27-43.

[9] Rausch T, Zell H, Wallenwein D, Witsch W-Von. Final-state interactions and quasi-free scattering in the $^2H(\alpha,p\alpha)n$ reaction. Nucl. Phys. A. 1974; 222: 429-444.

[10] Carlson RF, Cox AJ, Nasr TN, De Jong MS, Ginther DL, Hasell DK, Sourkes AM, Van Oers WTH, Margaziotis DJ. Messuremnts of proton total reaction cross sections for ^6Li,^7Li ^{14}N,^{20}Ne and ^{40}Ar between 23 and 49 MeV. Nucl. Phys. A. 1985; 445: 57-69.

[11] Mcgill WF, Carlson RF, Short TH, Cameron JM, Reginald Richardson J, Slaus I, Van Oers WTH, Verba JW, Margaziotis DJ, Doherty P. Phys. Rev. C. 1974; 10: 2237-2246.

[12] Koori N, Kumabe I, Hyakutake M, Watanabe Y, Orito K, Akagi K, Iida A, Eriguchi M, Wakuta Y, Sagara K, Nakamura H, Maeda K, Nakashima T. Polarized proton induced reactions on lithium isotopes around 14 MeV, JAERI-M 91-009, 1990, 56p.

[13] Baba M, Matsuyama S, Fujisawa M, Iwasaki T, Iwasaki S, Sakamoto R. Application of Post Acceleration Beam Chopper For Neutron Emission Cross Section Measurements, JAERI-M 90-025, 1990, pp. 383-392.

11. Cross Section Measurement for Photo Nuclear Reaction using Laser Compton-scattering γ-ray

Fumito KITATANI[1], Hideo HARADA[1], Shinji GOKO[1],
Hiroaki UTSUNOMIYA[2], Hidetoshi AKIMUNE[2],
Hiroyuki TOYOKAWA[3], Kawakatsu YAMADA[3]
[1] Japan Atomic Energy Agency, 2-4 Shirane, Shirakata, Tokai-mura, Naka-gun, Ibaraki 319-1195, Japan
[2]Konan University, 8-9-1 Okamoto, Higashinada, Kobe 658-8501, Japan
[3] National Institute of Advanced Industrial Science and Technology, 1-1-1 Umezono, Tsukuba-shi, Ibaraki 305-8568, Japan
e-mail: kitatani.fumito@jaea.go.jp

Accurate measurement method of photonuclear cross sections has been developed by utilizing Laser Compton-Scattering γ-ray (LCS γ-ray) source supplied at the National Institute of Advanced Industrial Science and Technology (AIST). In this paper, developed methodology is described and some obtained results are shown on the photonuclear cross section of Se isotopes.

I. Introduction

Many studies of photonuclear reactions have been made from 1960s to 1980s. The giant dipole resonance (GDR) in the energy region of 10 to 30 MeV[1)] has been of central interest in these studies. In recent years, photonuclear reactions have gotten attention to obtain neutron capture cross sections for radioactive nucleus using the inverse reaction method; (n, γ) cross sections are deduced from (n, γ) cross sections with help of statistical model calculations[2)-4)]. For this method, accurate photonuclear cross sections near the neutron separation energy are essentially important.

In order to measure photonuclear cross sections with high precision, we have developed a methodology measuring photonuclear cross sections using a Laser Compton-Scattering γ-ray (LCS γ-ray) and a high-resolution and high-energy photon spectrometer (HHS)[5)]. In past, a positron pair annihilation γ source had been used for photonuclear cross section measurements. Since the γ source has a huge background due to Bremsstrahlung, there are typically large systematic uncertainties of about ± 5 % at 15 MeV[1)]. The LCS γ-ray is a quasi-monochromatic and energy tunable γ source, and free from background due to

Bremsstrahlung. Therefore, a precise measurement is expected to be achieved by utilizing the LCS γ-rays. Actually, the photonuclear cross sections have been measured for some nuclei, such as Pd, Se, Sn, Mo by a collaboration between Konan University, the National Institute of Advanced Industrial Science and Technology (AIST)[6], and Japan Atomic Energy Agency (JAEA). In this paper, the developed methodology is described focusing on recently developed data reduction method and some obtained results are shown on the photonuclear cross section of Se isotopes.

II. Experiment

1. Experiment equipment

The experiment was performed in the Tsukuba Electron Ring for Acceleration and Storage (TERAS) at the AIST [6]. LCS γ-rays were produced in TERAS through head-on collisions of laser photons with relativistic electrons. The energy distribution of the LCS γ-rays was measured using a HHS[7)8)]. Neutrons from (γ,n) reactions were detected using a 4π-type neutron detector, consisting of 20 ^{3}He proportional counters (Eurisys Measures 94NH45) arranged in three rings (the 1st , 2nd and 3rd rings), inside a polyethylene moderator. The irradiated flux of the LCS γ-rays was monitored by a large volume NaI(Tl) detector set after the neutron detector (20 cm in diameter and 30 cm in thickness). The experimental setup is shown in **Figure 1**.

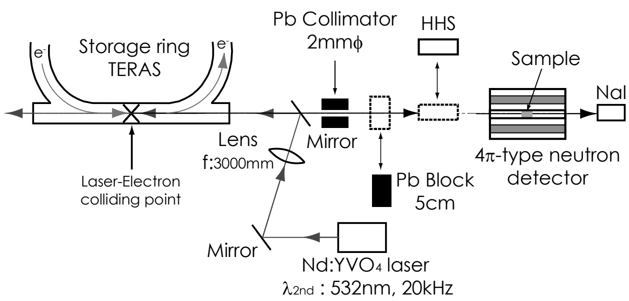

Fig.1 The experimental setup

2. Sample

Se samples were produced from metal Se powder, isotopically enriched to 99.67 % for ^{76}Se, 99.39 % for ^{78}Se and 99.90 % for ^{80}Se. The powder was formed into pellets using a hot-press with a diameter of 8 mm.

3. Measurement

Details of the measurement and analysis are described in Ref.7), and are therefore only briefly described here. Items measured to decide the cross sections were the energy distribution of LCS γ-rays, the flux of LCS γ-rays irradiating the sample and the number of neutrons due to (γ,n) reactions. The energy distribution of LCS γ-rays was measured using the HHS. The energy distribution was deduced by unfolding the pulse-height spectrum using the response functions of the HHS, as calculated by Monte Carlo simulation code EGS4. The details on the simulations were described in Ref.9) and 8). **Figure 2** shows the LCS γ-ray spectrum measured by the HHS and the energy distribution deduced by the unfolding procedure.

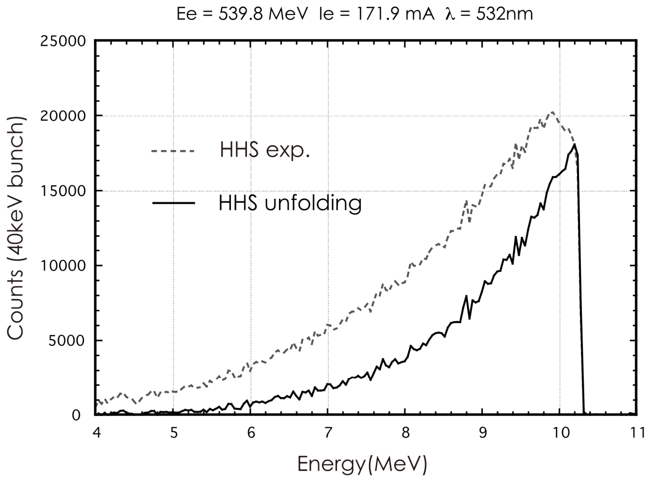

Fig.2 LCS γ-ray spectrum (solid line) measured with the HHS and the corresponding energy distribution of LCS γ-rays deduced by unfolding procedure (dashed line)

The flux of LCS γ-rays irradiating a sample was measured using the large volume NaI(Tl) detector set after the neutron detector. The pile-up spectrum was obtained by irradiating a sample while measuring neutrons. To deduce the number of incident photons from the pile-up spectrum, a pulse-height spectrum representing single LCS γ-ray events was required. The pulse-height spectrum of single LCS γ-ray events was obtained by reducing the LCS γ-ray intensity for each neutron measurement. **Figure 3** shows the spectrum of single LCS γ-ray events and the pile-up spectra measured by the large volume NaI(Tl). The flux of the LCS γ-rays was calculated using the reported method[7)10)] from these spectra.

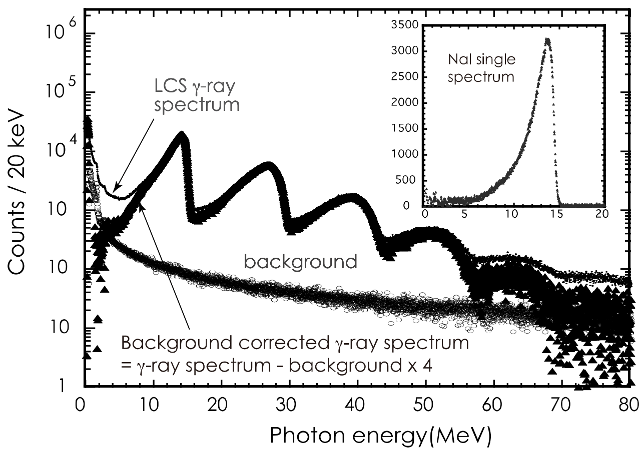

Fig.3 Multi-photon pulse-height spectrum of the LCS γ-rays measured with the NaI(Tl) detector (dots), the background spectrum (open circles), and the background corrected γ-ray pulse-height spectrum (open triangles) and single LCS γ-ray pulse-height spectrum measured by the NaI(Tl) detector

The number of neutrons due to the (γ,n) reactions was measured using a scalar counter. Neutron counts below the discrimination level were corrected, the averaged correction factors for each ring being 1.09 for the 1^{st} ring and 1.11 for the 2^{nd} and 3^{rd} rings.

Measurements were carried out as follows. The energy distribution of LCS γ-rays was measured using the HHS (the first HHS measurement). The pulse-height spectrum of a single LCS γ-ray with reduced intensity was measured using the NaI(Tl). Neutrons from ^{76,78,80}Se(γ,n) reactions were measured using the neutron detector and the pulse-height spectrum of the pile-up LCS γ-ray using the NaI(Tl). Then, the energy distribution of LCS γ-rays was measured using the HHS (the second HHS measurement).

III. Results

The cross sections were first calculated using the monochromatic approximation $\sigma_s(E_0)$. The representative energy E_0 of LCS γ-rays with a quasi-monochromatic energy distribution was defined by

$$E_0 = \int_{S_n}^{E_{Max}} E_\gamma N_\gamma(E_\gamma) dE_\gamma \Big/ \int_{S_n}^{E_{Max}} N_\gamma(E_\gamma) dE_\gamma , \tag{1}$$

where E_γ is the energy of the LCS γ-rays, $N_\gamma(E_\gamma)$ is the energy distribution of the LCS γ-rays, E_{Max} is the maximum energy of the LCS γ-rays, and S_n is the (γ,n) reaction threshold energy.

In the case of the monochromatic approximation, the cross section $\sigma_s(E_0)$ was deduced by

$$\sigma_s(E_0) = \frac{(N'_n/\varepsilon)}{N_t \cdot N'_\gamma \cdot f_a \cdot f_b} , \tag{2}$$

where N'_n is the number of detected neutrons, ε is the neutron total detection efficiency, N'_γ is the number of incident LCS γ-rays, $f_a \equiv e^{\mu t} \cdot (1 - e^{-\mu t})/\mu t$ is the correction factor for γ-ray attenuation by a thick sample (where μ is the photon attenuation coefficient of the sample material and t is the sample thickness), and f_b is the fraction of the γ flux above the neutron separation energy. Next, the cross section $\sigma_s(E_0)$ was corrected by applying an accurate energy distribution of LCS γ-rays to the calculation ref.7).

The correction of the monochromatic approximation cross section was carried out as follows. A trial function was assumed, and this was used to fit the cross section. The yield of neutrons emitted from a sample, N_n^c, was calculated from the trial function and the energy distribution of LCS γ-rays, accurately measured using the HHS. N_n^c and $N_n^E = N'_n/\varepsilon$ (N_n^E : the number of neutrons counted experimentally) were then compared. The cross section was renormalized to satisfy the condition $N_n^E/N_n^c = 1$. The steps were repeated until the point of convergence.

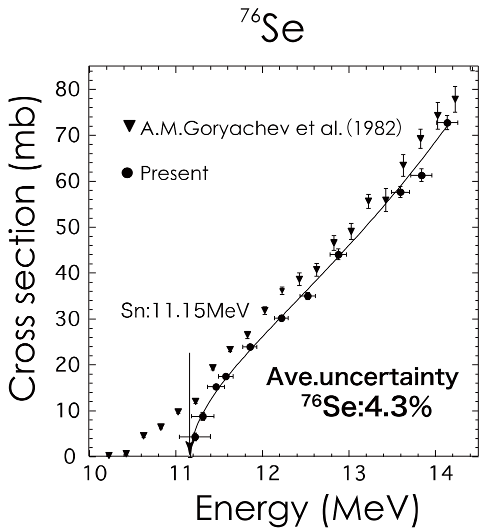

Fig.4 ^{76}Se cross section data corrected using energy distribution of LCS γ –ray with previous experimental data

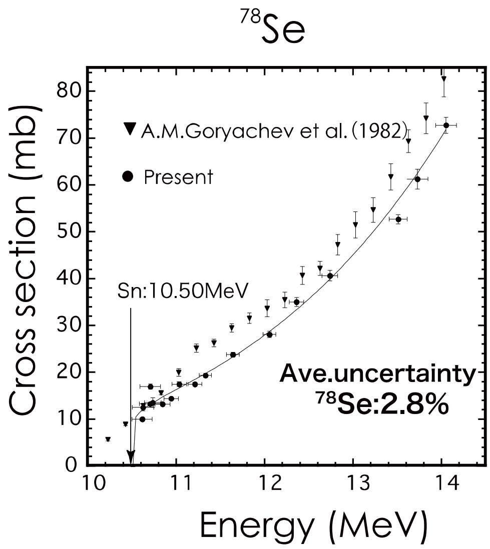

Fig.5 ^{78}Se cross section data corrected using energy distribution of LCS γ –ray with previous experimental data

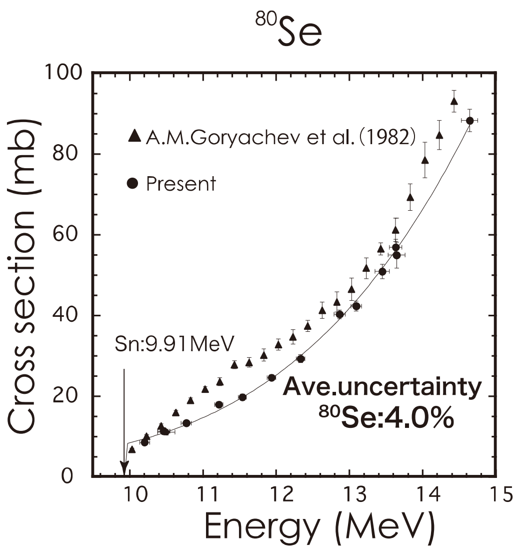

Fig.6 ^{80}Se cross section data corrected using energy distribution of LCS γ –ray with previous experimental data

Figures 4, 5 and 6 show the cross sections of ^{76}Se, ^{78}Se and ^{80}Se. Closed triangles show the cross sections measured by Goryachev and Zalesny [11]. The previous data of ^{76}Se and ^{78}Se in ref.11) had a problem that the cross section values under neutron separation energies are apparently positive. In order to examine this problem, the upper energy limit and energy distribution of the input LCS γ-rays was carefully determined. In our measurements, the non-zero cross sections below under neutron separation energy was not observed.

V. Conclusion

The ^{76,78,80}Se(γ,n) cross sections were measured using LCS γ-rays for the energy range from each near neutron separation energy to the threshold energy of the (γ, 2n) reactions. The deduced uncertainties of the ^{76}Se cross sections ranged from 5.9 % to 19.2 %, those of the ^{78}Se cross sections from 5.8 % to 9.4 %, and those of the ^{80}Se cross sections from 6.6 % to 13.0 %. The experimental techniques for precise measurements were developed in this work. The obtained systematic data will be used to improve the accuracy of the calculation of the ^{79}Se (n, γ) cross section, which is difficult to be measured by direct method because of difficulty of the sample preparation. The inverse reaction method using LCS γ-rays will be a useful took to deduce neutron capture cross sections for nuclei for which a direct measurement method is difficult to be applied.

References

[1] B.L. Berman, S.C. Fultz. Measurement of the giant dipole resonance with monoenergetic photons. Rev. Mod. Phys. 1975 Jul: 47; 731-761.

[2] H. Utsunomiya, S. Goriely, H. Akimune, H. Harada, F. Kitatani, S. Goko, H. Toyokawa, K. Yamada, Y.-W. Lui. The γ SF method – determination of radiative neutron-capture cross sections for unstable nuclei. J. Korean Phys. Soc. 2011 Aug; 59: 1713-1716.

[3] H. Utsunomiya, S. Goriely, H. Akimune, H. Harada, F. Kitatani, S. Goko, H. Toyokawa, K. Yamada, T. Kondo, O. Itoh, M. Kamata, T. Yamagata, Y.-W. Lui, S. Hilaire, and A. J. Koning. Photoneutron cross section for ^{96}Zr: A systematic experimental study of photoneutron and radiative neutron capture cross sections for zirconium isotopes. Phys. Rev. 2010 Mar; C81: 035801.

[4] H. Utsunomiya, S. Goriely, M. Kamata, T. Kondo, O. Itoh, H. Akimune, T. Yamagata, H. Toyokawa, Y. -W. Lui, S. Hilaire, and A. J. Koning. Photoneutron cross sections for $^{118\text{-}124}$Sn and the γ-ray strength function method. Phys. Rev. 2011 Nov; C84: 055805.

[5] H. Harada, K. Furutaka, S. Nakamura, K. Osaka, H. Akimune, H. Utsunomiya, T. Ohsaki, M. Igashira. Response of a high-resolution high-energy photon spectrometer (HHS) to monochromatic high-energy gamma-rays. Nucl. Instr. Meth. 2005 Dec; A554 : 306-313.

[6] http://unit.aist.go.jp/riif/qrg/Linac/teras-en.htm

[7] F. Kitatani, H. Harada, S. Goko, H. Utsunomiya, H. Akimune T. Kaihori, H. Toyokawa, K. Yamada. Measurement of the ^{80}Se(γ,n) cross section using laser-compton scattering γ-rays. J. Nucl. Sci. Technol. 2010 Jan; 47: 367-375.

[8] F. Kitatani, H. Harada, S. Goko . Utsunomiya, H. Akimune T. Kaihori, H. Toyokawa, K. Yamada. Measurement of ^{76}Se and ^{78}Se(γ,n) cross sections. J. Nucl. Sci. Technol. 2011 Jan; 48:1017-1024.

[9] F. Kitatani, H. Harada, K.Y. Hara, M. Ohsima, H. Utsumomiya, H. Toyokawa, K. Yamada. Determination of energy distribution of LCS γ–ray with HHS and Ge detectors by unfolding method. In: Proceedings of 2006 Fall Meeting of the Atomic Energy Society of Japan; 2006 Sep 28, Sapporo.(JP); 2006

[10] H. Utsunomiya, S. Goko, H. Toyokawa, H. Ohgaki, K. Soutome, H. Yonehara, S. Goriely, P. Mohr, Zs. Fulop. Photonuclear reaction data and γ-ray sources for astrophysics. Eur. Phys. J. 2006 Feb; A**27** s01: 153-153.

[11] A.M. Goryachev, G.N. Zalesnyy, The studying of the photoneutron reactions cross sections in the region of the giant dipole resonance in zinc, germanium, selenium, and strontium isotopes. Voprosy Teoreticheskoy i Yadernoy Fiziki. 1982; 8: 121-135.

12. Recent Progress in Experimental and Theoretical Studies of Proton-induced Fragment Production Cross Section at Intermediate Energies

M.Hagiwara[1), T.Sanami[1), D.Mancusi[2), A. Boudard[2), J. Cugnon[3), S. Leray[2) and M.Baba[4)

[1) High Energy Accelerator Research Organization, KEK, Oho 1-1, Tsukuba-shi, Ibaraki-ken 305-0801

[2) CEA, Centre de Saclay, IRFU/Service de Physique Nucléaire

[3) Fundamental Interactions in Physics and Astrophysics, University of Liège

[4) Cyclotron Radioisotope Center, Tohoku University

e-mail: hagi@post.kek.jp

Energy and angular double-differential cross sections (DDXs) for nucleon-induced reactions at incident energies from tens of MeV to GeV resulting to the emission of light mass fragments (LMFs) heavier than α-particles are of particular importance in the microscopic analysis of radiation effects such as soft errors of micro-electronic devices, material damage and human dose. The radiation effects and damage should be carefully considered in the design of high-energy accelerator applications such as accelerator-based neutron sources, proton radiotherapy and so on. In this paper, recent progress in the experimental and theoretical studies corresponding the DDXs for the LMF production are briefly summarized, especially focusing on the Liège intra-nuclear cascade model (INCL4.6) which gave most encouraging results for prediction of the DDXs for composite particle emissions when coupled with an appropriate evaporation model such as the generalized evaporation model (GEM) which describes heavier nuclei emissions up to Mg in the evaporation process. To improve further the prediction accuracy for the production of LMFs, we revised the INCL4.6 based on the recent experimental data systematically obtained in a wide range of targets and reactions. Besides, we incorporated the statistical multi-fragmentation model (SMM) into GEM to reproduce high multiplicity reactions. The typical calculation results are presented with comparison with the relevant experimental data.

1. Introduction

In the last few decades, there have been a strong development of applications involving nuclear reactions at incident energies from tens of MeV to GeV, such as accelerator-based neutron sources for scientific research and industrial development [1], accelerator-driven system (ADS) for transmutation of nuclear waste [2], particle radiotherapy [3], microscopic analysis of irradiation effect resulting to soft errors and damage of micro-electronic devices [4], DNA breakage and embrittlement of materials, design of high-energy accelerators and set-ups of nuclear physics experiments [5], shielding and protection against radiation near accelerators and in space missions and so on. These activity require reliable and experimentally-validated nuclear reaction data on the energy and angular distribution of secondary products not only for neutrons, protons and α-particles but also fragments heavier than α-particles as one of key parameters in the detailed analyses of these studies. On the other hand, the existing evaluated data libraries are limited at the incident energies typically below 150 MeV and at reaction channels corresponding to the emissions of particles lighter than α-particles [6]. Actually, the number of reactions channels becomes too large to allow the generation of data sets for all the reactions opened at intermediate energies from tens of MeV to GeV. Besides, the dynamical correlations between secondary products, which are important in the microscopic analysis of irradiation effects, are not contained in the existing evaluated nuclear data libraries. It is therefore more convenient to compute the cross-sections and characteristics of the secondary products for high-energy nuclear reactions producing high-multiplicity events by a Monte-Carlo event generator such as an intra-nuclear cascade model coupled with an evaporation model. The nuclear reaction models equipped with an event generator can be directly implemented into general-purpose high-energy particle transport codes, such as PHITS [7], to use in the simulation analyses with the practical geometry.

A significant effort has been recently undertaken in several places to collect systematic experimental data of proton-induced reactions including DDXs for the emission of light mass fragments (LMFs). It has been therefore possible to make an extensive comparison between the experimental data and calculations by the relevant physics models for assessment of their prediction capability. In this paper, typical studies on experiments and physics models associated with DDXs for the LMF production induced by protons are briefly summarized. To improve the data quality of the DDXs for the LMF production, we revised the latest version of the Liège intra-nuclear cascade (INCL4.6) [8], which gave most encouraging results in the previous IAEA benchmark test of spallation models, using the recent experimental DDX data on proton-induced reactions for various targets at intermediate incident energies for wide range of the emitted particles including neutrons, light charged particles (LCPs) lighter than α-particles and LMFs. Moreover we incorporated the statistical multi-fragmentation model (SMM) [9] into the generalized evaporation model (GEM) [10] to improve the prediction accuracy of the DDXs for LMFs produced by high-energy reactions above 1 GeV/u.

2. Present status of DDXs on proton-induced reactions producing fragments

Experimental data on DDXs for the emission of LMFs in proton- and neutron-induced reactions have been scarce so far, due to the high stopping power of fragments and the low production yields. Recently, systematic experiments has been undertaken in several places to measure DDXs of the several targets for the LMF production induced by protons at incident energies from tens of MeV to GeV, although there have been a considerable number of experimental data obtained by activation method which provides no information on energy and angular distributions. Our group has been conducted series of experiments for the DDX measurement focusing on the fragment production. Under this program, we developed a Bragg curve counter (BCC) with improving acceptable energy range to measure various LMFs with the detection threshold less than 0.5 MeV/u [11-13]. The DDXs of C, N, O, Al, Si, Ti, and Cu targets for LMF production were obtained using protons of 40 to 300 MeV incident energies at 30 to 120 degree emission angles [14, 15]. The PISA collaboration measured the DDXs of Al, Ni, Au targets for LMF production using protons of incident energies of 175 MeV, 1.2, 1.9, 2.5 GeV at 15 to 100 degree emission angles by the similar BCC technique. [16-19] Green et al. measured the DDXs of a Ag target for various LMF production using protons of 190, 210, 300 and 480 MeV incident energies by a counter-telescope and time-of-flight technique [20]. Machner et al. measured the DDXs of Al, Ni, Co, Au targets for LMF production using 200 MeV protons by a counter-telescope technique [21]. Most of these data are available in the EXFOR database [22] and useful as benchmark data not only for assessment of existing physics models and phenomenological systematics but also for their improvements.

A significant progress in the physics models on LMF production was made by Boudard et al. by introducing a kind of many-body effects into a framework of the intra-nuclear cascade model which is generally based on the two-body interaction between nucleons in the nuclear potential to account for the emission of composite particles in the cascade process, which is accomplished by means of a semi-empirical phase-space dynamical coalescence model implemented in the Liège intra-nuclear cascade model (INCL) [23]. When a leading nucleon reaches the surface of the nucleus, it is assumed to bind with nucleons close by in phase space and form a candidate cluster. More precisely, the phase-space proximity criterion is

$$r_{i,[i-1]} p_{i,[i-1]} \le h_0(i) \qquad \mathrm{i} = 2, 3, \ldots\ldots, \mathrm{A}, \qquad (1)$$

where $r_{i,[i-1]}$ and $p_{i,[i-1]}$ are the Jacobian coordinates of the *i-th* nucleon with respect to the subgroup constituted of the first *i-1* nucleons, $h_0(i)$ is a parameter and *A* is the maximum cluster mass considered. The model has been shown to accurately predict DDXs for the production of LCPs from a variety of targets at energies ranging from few tens of MeV to a few GeV [23].

Another important progress was achieved by Furihata et al. by improving the Dostrovsky's evaporation model, which originally described the emission of LCPs lighter than α-particles [24], to account the emission of fragments heavier than α-particle in evaporation process. The generalized evaporation model (GEM), which can treat the emission of composite particles up to Mg, considerably improve the prediction accuracy of cross section for LMF production induced by protons at intermediate incident energies in the previous studies [10, 15]. On the other hand, the original GEM model did not account for a multi-fragmentation process which is a dominant process on LMF production in the high-energy reaction above 1 GeV/u [9]. To reproduce high multiplicity events in the high-energy reaction above 1 GeV/u, the statistical multi-fragmentation model (SMM) [9] have been proposed and successfully improved prediction accuracy of the cross sections in multi-fragmentation reactions induced by the relativistic heavy ions [25].

3. Improvements of INCL

The Liège intra-nuclear cascade model (INCL), which have been continuously developed by CEA-Saclay (France) and the University of Liège (Belgium), gave most encouraging results in the previous

IAEA benchmark test of spallation models [26] and it is widely recognized as one of the most predictive existing intra-nuclear cascade models. The last version of INCL (INCL4.6) was implemented in major high-energy particles transport codes such as PHITS [7], MCNPX [27], GEANT4 [28]. One of the most distinct feature in INCL4.6 is extension of the applicable range of the composite particle emission by a semi-empirical phase-space dynamical coalescence model up to carbon (originally up to α-particle). However the models have not experimentally validated well for LMF production due to the scarcity of the experimental data at that time when the model was developed. So we assessed prediction capability of the INCL4.6 coupled with GEM plus multi-fragment process of SMM (GEM/SMM) using the recent experimental DDX data on proton-induced reactions for various targets at intermediate incident energies from 50 MeV to 2.5 GeV for wide range of the emitted particles including neutrons, LCPs and LMFs up to Mg. As the results, it was observed that the calculated spectra of composite particles at intermediate energies (hundreds of MeV) are systematically too hard. Therefore the coalescence model implemented in INCL4.6 was partially revised in the phase-space proximity criterion to ameliorate the DDXs for composite particle emission by introducing the following constraint for the acceptable momentum of nucleons in the center-of-mass frame of the running cluster in addition to Eq. (1).

$$p_{i,[i-1]} \le h_1 \text{, with } h_1 = 240 \text{ MeV/c} \tag{2}$$

In other words, we exclude nucleons with a large momentum in the center-of-mass frame of the running cluster. This effect is illustrated in Fig.1 by the DDXs for the production of ^{6}Li produced in the 200-MeV p+Au reaction. The slope of the spectra above 100 MeV is improved. The examples shown here are typical of the effect of this momentum cut in the proton-induced reactions at incident energies of hundreds of MeV. At incident energies of tens of MeV, the momentum cut are essentially unaffected. Figure 2 illustrate the DDX for the production of carbon produced in the 1.9 GeV p+Au reaction as the typical effect of multi-fragmentation process of SMM added into GEM. The modification successfully improved prediction accuracy of the cross sections in which multi-fragmentation process is dominant.

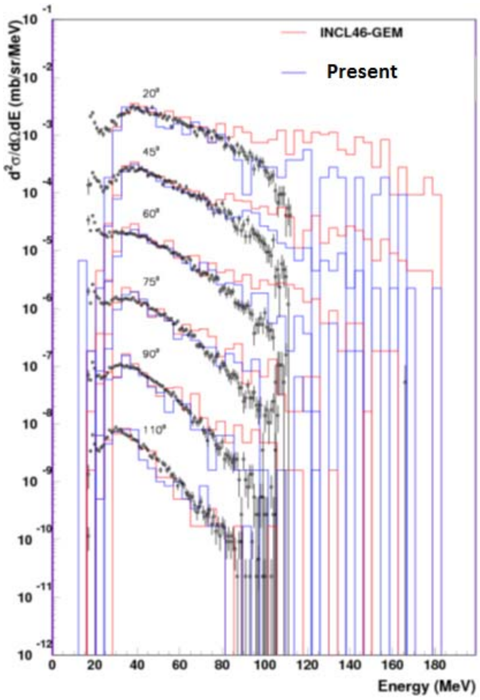

Fig.1 DDXs for the production of ^{6}Li produced in 200-MeV p+Au reaction in comparison between experimental data [21] (symbols), original INCL4.6+GEM (red lines) and improved INCL4.6 + GEM/SMM (blue lines) [See the color image on the electric version of the proceedings].

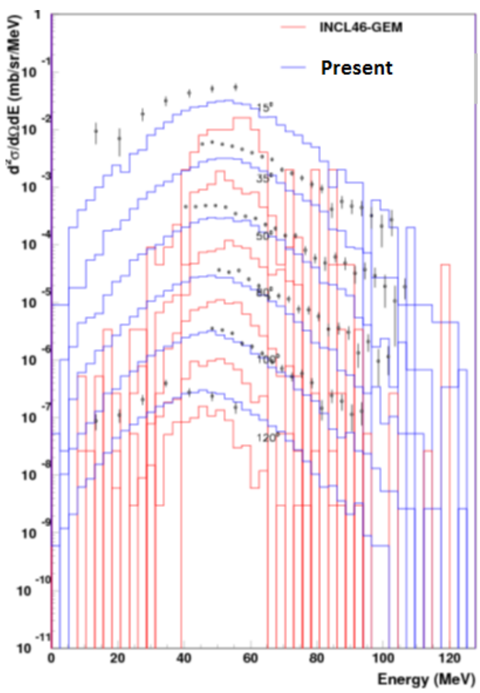

Fig.2 DDXs for the production of C produced in 1.9 GeV p+Au reaction in comparison between experimental data [17] (symbols), original INCL4.6+GEM (red lines) and improved INCL4.6 + GEM/SMM (blue lines) [See the color image on the electric version of the proceedings].

4. Summary

We have reviewed the recent progress in the experimental and theoretical studies corresponding the DDXs for the LMF production. The coalescence model implemented in INCL4.6 was partially revised in the phase-space proximity criterion by introducing the constraint for the acceptable momentum of nucleons in the center-of-mass frame of the running cluster less than 240 MeV/c to ameliorate the DDXs of various targets for composite particle emission in proton-induced reactions at intermediate incident energies. Besides, we incorporated the statistical multi-fragmentation model (SMM) into the generalized evaporation model (GEM) to reproduce high multiplicity reactions. The typical calculation results are illustrated with comparison with the relevant experimental data.

Acknowledgements

The authors wish to thank the members of SPhN (Nuclear Physics Department) in CEA-Saclay for their help to perform this study. This study was partly supported by the KEK fellowship for research abroad at FY2013 and JSPS "KAKENHI (25871111).

REFERENCES

[1] Filges D, Goldenbaum F. Handbook of Spallation Research: Theory, Experiments and Applications: Berlin: Wiley VCH; 2010.
[2] Gudowski W. Accelerator-driven transmutation projects. The importance of nuclear physics research for waste transmutation. Nucl. Phys. A. 1999 Sep;654:c436-c457.
[3] Kraft G. The radiobiological and physical basis for radiotherapy with protons and heavier ions. Strahlenther. Onkol. 1990 Jan;166(1):10-13.
[4] Tang HHK. Nuclear physics of cosmic ray interaction with semiconductor materials: Particle-induced soft errors from a physicist's perspective. IBM J. Res. Dev. 1996 Jan;40:91-108.
[5] Agostinelli S, et al., Geant4—a simulation toolkit. Nucl. Instr. Meth. Phys. Res. A. 2003 Jul;506:250-303
[6] Chadwick MB, et al., Cross-section evaluations to 150 MeV for accelerator-driven systems and implementation in MCNPX. Nucl Sci Eng. 1999 Mar;131:293-328.
[7] Sato T, et al., Particle and heavy ion transport code system, PHITS, version 2.52. J. Nucl. Sci. Technol. 2013 Sep;50:913-923.
[8] Boudard A, Cugnon J, David JC, Leray S, Mancusi D. New potentialities of the Liège intranuclear cascade model for reactions induced by nucleons and light charged particles. Phys. Rev. C. 2013 Jan; 87:014606.
[9] Bondorf JP, et al., Statistical multifragmentation of nuclei. Phys. Rep. 1995 Jun;257:133-221.
[10] Furihata S. Statistical Analysis of light fragment production from medium energy proton-induced reactions. Nucl. Instrum. Meth. B. 2000 Nov;171:251-258.
[11] Sanami T, et al., A Bragg curve counter with an active cathode to improve the energy threshold in fragment measurements. Nucl. Instrum. Meth. A. 2008 May;589:193-201.
[12] Hagiwara M, et al., Extension of energy acceptance of Bragg curve counter at the high-energy end. Nucl. Instrum. Meth. A. 2008 Jul;592:73-79.
[13] Sanami T, et al., A Bragg curve counter with an internal production target for the measurement of the double-differential cross-section of fragment production induced by neutrons at energies of tens of MeV. Nucl. Instrum. Meth. A. 2009 Nov;610:660-668.
[14] Sanami T, et al., Fragment DDX Measurement of Proton Induced Reactions on Light-medium Nuclei for Energy Range from Reaction Threshold to a Few Hundred MeV. J Korean Phys Soc. 2011 Aug;59:1805-1808.
[15] Hagiwara M, et al., Differential cross sections on fragment ($2 \leq Z \leq 9$) production for carbon, aluminum and silicon induced by tens-of-MeV protons. J. Nucl. Sci. Technol. 2012 Jun;49:571-587.
[16] Bubak A, et. al., Non-equilibrium emission of complex fragments from p+Au collisions at 2.5 GeV proton beam energy. Phys. Rev. C. 2007 Jul;76:014618.
[17] Budzanowski A, et al., Competition of coalescence and "fireball" processes in nonequilibrium emission of light charged particles from p+Au collisions. Phys. Rev. C. 2008 Aug;78:024603.
[18] Budzanowski A, et al., Variation of nonequilibrium processes in the p+Ni system with beam energy. Phys. Rev. C. 2009 Nov;80:054604.
[19] Budzanowski A, et al., Comparison of nonequilibrium processes in p+Ni and p+Au collisions at GeV energies. Phys. Rev. C. 2010 Sep;82:034605.
[20] Green REL, Korteling RG. Fragment production from p+Ag interactions at intermediate energies. Phys. Rev. C. 1980 Oct;22:1594-1611.
[21] Machner H, et al., Isotopic production cross sections in proton-nucleus collisions at 200 MeV. Phys. Rev. C. 2006 Apr;73:044606.
[22] Experimental Nuclear Reaction Data (EXFOR) [internet]. International Atomic Energy Agency; [cited 2013 Dec 31] Available from https://www-nds.iaea.org/exfor/exfor.htm.
[23] Boudard A, et al., A new model for production of fast light clusters in spallation reactions. Nucl Phys A. 2004 Aug;740:195-210.
[24] Dostrovsky I, Fraenkel Z, Friedlander G. Monte Carlo calculations of nuclear evaporation processes. III. Applications to low-energy reactions. Phys Rev. 1959 Nov;116:683-702.
[25] Ogawa T, et al., Analysis of multi-fragmentation reactions induced by relativistic heavy ions using the statistical multi-fragmentation model. Nucl. Instrum. Meth. A. 2013 Sep;723:36-46.
[26] Leray S, et al., Results from the IAEA benchmark of spallation models. J. Korean Phys. Soc. 2011 Aug;59:791-796.
[27] Pelowitz DB, eiditor LA-CP-07-1473: MCNPX^{TM} USER'S MANUAL Version 2.6.0. Los Alamos National Laboratory; 2008.
[28] Mancusi D,et al., New capabilities of the Liège intranuclear-cascade model for particle-transport codes. In: Proceedings of SNA + MC 2013; Paris.

13. Overview of Particle and Heavy Ion Transport Code System PHITS

Yosuke IWAMOTO[1*], Tatsuhiko SATO[1], Koji NIITA[2], Norihiro MATSUDA[1], Shintaro HASHIMOTO[1], Takuya FURUTA[1], Shusaku NODA[1], Tatsuhiko OGAWA[1], Hiroshi IWASE[3], Hiroshi NAKASHIMA[1], Tokio FUKAHORI[1], Keisuke OKUMURA[1], Tetsuya KAI[1], and Lembit SIHVER[4]

[1]*Japan Atomic Energy Agency, Shirakata-Shirane 2-4, Tokai, Ibaraki, 319-1195, Japan;*
[2]*Research Organization for Information Science and Technology, Shirakata-Shirane 2-4, Tokai, Ibaraki, 319-1106, Japan;*
[3]*High Energy Accelerator Research Organization, Oho 1-1, Tsukuba, Ibaraki, 305-0801, Japan;*
[4]*Chalmers University of Technology, Göteborg SE-412 96, Sweden*
[*]E-mail: iwamoto.yosuke@jaea.go.jp

A general purpose Monte Carlo Particle and Heavy Ion Transport code System, PHITS, is being developed through the collaboration of several institutes in Japan and Europe. PHITS can deal with the transport of nearly all particles, including neutrons, protons, heavy ions, photons, and electrons, over wide energy ranges using various nuclear reaction models and data libraries. It is written in Fortran language and can be executed on almost all computers. More than 1,000 researchers have been registered as PHITS users, and they apply the code to various research and development fields such as nuclear technology, accelerator design, medical physics, and cosmic-ray research. This paper briefly summarizes the physics models implemented in PHITS, and introduces the event generator mode useful for specific applications and requests to the nuclear data community.

1. Introduction

Particle and Heavy Ion Transport code System, PHITS [1], is one of the most successful Monte Carlo particle transport simulation codes that are widely used in all over the world. It can deal with the transport of nearly all particles, including neutrons, protons, heavy ions, photons, and electrons, over wide energy ranges using various nuclear reaction models and data libraries.

PHITS is written in Fortran language, and is originally derived from the NMTC/JAM code. [2] The source files of PHITS can be compiled using Intel Fortran 11.1 (or later versions) or GFortran 4.71 (or later versions). The platforms on which PHITS can be executed are Windows, Mac, Linux, and Unix. Distributed and shared memory parallelization techniques are available using MPI protocols and OpenMP directives, respectively. Hybrid parallelization using both MPI and OpenMP is also feasible [3]. The geometrical configuration of the PHITS simulation must be set with either general geometry (GG) or combinatorial geometry (CG). Various quantities, such as heat deposition, track length, and production yields, can be deduced from the PHITS simulation using implemented “tally” estimator functions. Estimation of the time evolution of radioactivity has become feasible after the realization of version 2.52 owing to the incorporation of an activation calculation program DCHAIN-SP [4] into the PHITS package.

This paper briefly summarizes the physics models implemented in PHITS, and introduces some important functions useful for specific applications.

2. Brief Summary of Physics Models

Figure 1 summarizes the physics models recommended for use in PHITS for simulating nuclear and atomic collisions. The intra-nuclear cascade models JAM [5] and INCL4.6 [6] and the quantum molecular dynamics model JQMD [7] are generally employed for simulating the dynamic stage of nuclear reactions induced by hadrons and nucleus, respectively. On the other hand, the evaporation and fission model GEM [8] are adopted for simulating their static stage. The statistical multi-fragmentation model SMM [9,10] can be optionally activated before the simulation of GEM. The energy losses of charged particles, except for electrons, are calculated using the SPAR [11] or ATIMA [12] codes with the continuous slowing down approximation. The generation of knocked-out electrons, so-called δ-rays, around the trajectory of a charged particle can be explicitly considered. Nuclear and atomic data libraries are generally used for simulating low-energy neutron-induced nuclear reactions and photo- and electro-atomic interactions, respectively. Photo-nuclear reactions can be treated only below 150 MeV, since photo-pion production cannot be considered in the current version of JQMD.

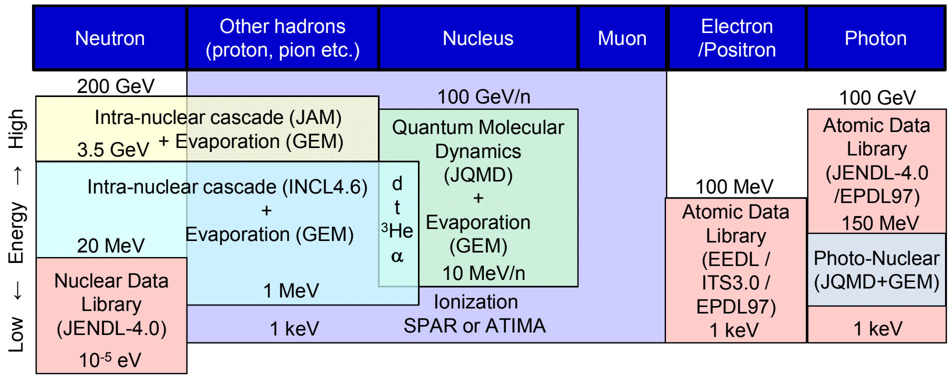

Figure 1: Physics models recommended for use in PHITS for simulating nuclear and atomic collisions

The highest energies of particles recommended to be simulated using PHITS are 200 GeV for hadrons, 100 GeV/n for nucleus, 100 MeV for electrons and positrons, and 100 GeV for photons. Note that PHITS can deal with the transport of particles above these energies, but the accuracy of simulations for such high-energy particles has not been verified. On the other hand, the lowest particle energy that can be simulated using PHITS is 1 keV, except for neutrons, because the continuous slowing down approximation cannot be applied to the transport simulation of charged particles below this energy. Thus, the minimum spatial resolution reliably achieved by PHITS simulations is approximately 10^{-4} g/cm^2, e.g. 1 μm in liquid water. For neutrons, PHITS can handle transport down to 10^{-5} eV using the neutron data library. More detailed information on the physics models implemented in PHITS is given in our previous reports [1].

3. Event Generator Mode

The important functions of PHITS are (i) an event generator mode for low-energy neutron interaction, [13] (ii) a function for calculating the displacement per atom (DPA), [14,15] (iii) beam transport functions, [16-18] and (vi) a microdosimetric tally function [19]. The detail of an event generator mode is described in this section.

There are two types of Monte Carlo methods for simulating nuclear reactions, viz. "event generators" and "non-event generators." The former conserves the energy and momentum before and after a reaction called the "event", whereas the latter does not. Most nuclear reaction models, such as the intra-nuclear cascade model, are "event generators", but Monte Carlo simulations using nuclear data libraries are generally "non-event generators", because only inclusive cross-section data are contained in the libraries. For example, the sum of the energies of two neutrons emitted from an (n,2n') reaction is occasionally greater than the incident energy, because the energies of outgoing particles are independently sampled using the inclusive cross section. Thus, only the mean values can be deduced from "non-event generator" simulations. However, it is occasionally necessary to estimate the distribution around the mean value, such as for the response function of detectors and the soft-error rates of semiconductor devices.

Based on these considerations, we implemented a unique "event generator mode" in PHITS for simulating low-energy neutron-induced reactions using nuclear data libraries. A special evaporation model [13] was developed for this purpose to maintain conservation of energy and momentum in an event. Any observables, such as the energy and momentum of residual nuclides, can be deduced using this mode. Owing to this mode, PHITS has been used for the estimation of soft-error rates of semi-conductor devices, [20,21] and for the calculation of the dose equivalents in human bodies irradiated by various particles in order to determine radiological protection needs [22-24] and medical physics issues [25].

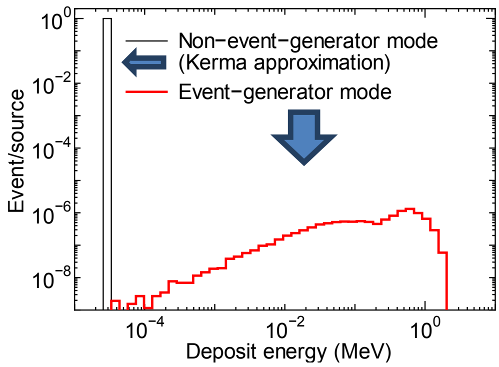

Figure 2: Calculated frequency distributions of deposition energies in a cylindrical silicon chip with a height and diameter of 3 μm, irradiated by 19 MeV neutrons. The simulations were performed using PHITS both with and without the use of the event generator mode.

Figure 2 shows the calculated frequency distributions of deposition energies in a cylindrical silicon chip having a height and diameter of 3 μm irradiated by 19 MeV neutrons. The simulations were performed by PHITS both with and without the use of the event generator mode. A shape peak is clearly observed in the distribution obtained from the non-event generation simulation, which employs the Kerma approximation in the calculation of deposition energy. This result indicates that every neutron passing through this small silicon chip deposits a certain amount of its energy in the same manner as charged particles. This fact is obviously in contradiction to reality, because the Kerma approximation can be used only for calculating the mean deposition energy. On the other hand, the distribution obtained using the event generator mode is widespread, and neutrons occasionally deposit energies of more than 1 MeV in such a small silicon chip. The soft error of semi-conductor devices occurs only when such high energies are deposited in their sensitive region, and thus, the event generator mode is indispensable in the estimation of their soft error rates. It should be mentioned that the transport of residual nuclei is also necessary to be considered in the estimation, since they can move out from the sensitive region of the devices.

4. Requests to the nuclear data community

To extend a maximum energy of the event generator mode up to 150 MeV, we are developing a new event generator mode. For development of the new model, we need channel-specific evaluated double differential cross sections for various incident particles such as neutron, proton, deuteron and alpha. To reduce size of ACE-format JENDL-HE files, nuclear data in the energy range above 150 MeV are not needed because the intra nuclear cascade models in PHITS can simulate many body phenomena.

We also request evaluated nuclear data in ACE format for lighter systems such as p-Li and p-Be for the design of neutron sources at accelerator facilities because the nuclear reaction models in PHITS cannot simulate these reactions, correctly.

5. Summary

The important features of PHITS are that (1) it can analyze the motion of nearly all particles over wide energy ranges, (2) it can be executed on almost all computers, (3) it implements sophisticated nuclear reaction models and nuclear data libraries, and (4) it has some special functions useful for specific applications. Owing to these features, PHITS has been used by more than 1,000 users in various research fields, such as nuclear technology, accelerator design, medical physics, and cosmic-ray research.

However, several tasks necessary for the further development of PHITS remain to be undertaken. The incorporation of the EGS5 code [26] and photo-pion production mechanisms are currently in progress for improving the accuracy of electron-, positron-, and photon-transport simulations, particularly for higher energies. Improvements in the nuclear reaction models for lighter systems such as p-Li reactions are also necessary. For this purpose, the development of a new nuclear reaction model has been initiated by combining an intra-nuclear cascade model and a distorted-wave Born approximation calculation [27]. This model will be incorporated in a future version of PHITS.

Acknowledgment

The development and distribution of PHITS have been greatly supported by the Center for Computational

Science & e-Systems of JAEA. We thank our colleagues at Kyushu University, RIKEN, CEA/Saclay, and JAXA for their supports in improving PHITS under the collaboration contracts between JAEA and each institute.

References

[1]Sato T, Niita K, Matsuda N, Hashimoto S, Iwamoto Y, Noda S, Ogawa T, Iwase H, Nakashima H, Fukahori T, Okumura K, Kai T, Chiba S, Furuta T, Sihver L. Particle and heavy ion transport code system PHITS, version 2.52. J Nucl Sci Technol. 2013;50:913-923.

[2] Niita K, Takada H, Meigo S, Ikeda Y, High-energy particle transport code NMTC/JAM. Nucl Instruments Methods B. 2001; 184: 406-420.

[3] Furuta T, Ishikawa K.L, Fukunishi N, Noda S, Takagi S, Maeyama T, Fukasaku K, Himeno R. Implementation of OpenMP and MPI hybrid parallelization to Monte Carlo dose simulation for particle therapy. IFMBE Proceedings, 2012;39: 2099-2102.

[4] Kai T, Maekawa F, Kosako K, Kasugai Y, Takada H, Ikeda Y. DCHAIN-SP 2001: High energy particle induced radioactivity calculation code. JAERI-Data/Code 2001-016, 2001. [in Japanese]

[5] Nara Y, Otuka H, Ohnishi A, Niita K, Chiba S. Relativistic nuclear collisions at 10A GeV energies from p+Be to Au+Au with the hadronic cascade model. Phys Rev C. 2000; 61: 024901.

[6] Boudard A, Cugnon J, David J.C, Leray S, Mancusi D. New potentialities of the Liege intranuclear cascade model for reactions induced by nucleons and light charged particles. Phys Rev C. 2013;87: 014606.

[7] Niita K, Chiba S, Maruyama T, Maruyama T, Takada H, Fukahori T, Nakahara Y, Iwamoto A. Analysis of the (N,Xn') reactions by quantum molecular-dynamics plus statistical decay model. Phys Rev C. 1995;52: 2620-2635.

[8] Furihata S. Statistical analysis of light fragment production from medium energy proton-induced reactions. Nucl Instruments Methods B. 2000;171: 251-258.

[9] Bondorf J.P, Botvina A.S, Iljinov A.S, Mishustin I.N, Sneppen K. Statistical multifragmentation of nuclei. Phys. Rep. 1995;257: 133-221.

[10]Ogawa T, Sato T, Hashimoto S, Niita K. Analysis of multi-fragmentation reactions induced by relativistic heavy ions using the statistical multi-fragmentation model. Nucl Instruments Methods A. 2013;**723:**36-46.

[11] Armstrong T.W, Chandler K.C. SPAR, a FORTRAN program for computing stopping powers and ranges for muons, charged pions, protons and heavy ions. 1973; ORNL-4869.

[12]Geissel H, Scheidenberger C, Malzacher P, Kunzendorf J, Weick H. ATIMA. GSI. Aveiravle from: http://web-docs.gsi.de/~weick/atima/

[13] Niita K, Iwamoto Y, Sato T, Matsuda N, Sakamoto Y, Nakashima H, Iwase H, Shiver L. Event generator models in the particle and heavy ion transport code system; PHITS. J. Korean. Phys. Soc. 2011; 59: 827-832.

[14] Iwamoto Y, Niita K, Sawai T, Ronningen R.M, Baumann T. Improvement of radiation damage calculation in PHITS and tests for copper and tungsten irradiated with protons and heavy-ions over a wide energy range. Nucl. Instrum. Meth. B. 2012;274: 57-64.

[15]Iwamoto Y, Iwamoto H, Harada M, Niita K. Calculation of displacement cross-sections for structural materials in accelerators using PHITS event generator and its applications to radiation damage. J. Nucl. Sci. Technol. 2014; 51:98-107.

[16] Furusaka M, Niita K, Suzuki S, Fujita K, Suzuki J, Oku T, Shimizu H.M, Otomo T, Misawa M. Monte-Carlo simulation codes development and their applications to neutron optical devices and neutron scattering instruments. Nucl. Instrum. Meth. A. 2004; 529: 223-230.

[17]Nose H, Niita K, Hara M, Uematsu K, Azuma O, Miyauchi Y, Komori M, Kanai T. Improvement of three-dimensional Monte Carlo code PHITS for heavy ion therapy. J. Nucl. Sci. Technol. 2005; 42: 250-255.

[18]Sakaki H, Nishiuchi M, Hori T, Bolton P.R, Yogo A, Katagiri M, Ogura K, Sagisaka A, Pirozhkov A.S, Orimo S, Kondo K, Iwase H, Niita K, Souda H, Noda A, Iseki Y, Yoshiyuki T. Prompt in-line diagnosis of single bunch transverse profiles and energy spectra for laser-accelerated ions. Appl. Phys. Express, 2010; 3:126401 (3 pages).

[19]Sato T, Kase Y, Watanabe R, Niita K, Sihver L. Biological dose estimation for charged-particle therapy using an improved PHITS code coupled with a microdosimetric kinetic model. Radiat. Res.2009; 171: 107-117.

[20] Kobayashi H, Kawamoto N, Kase J, Shiraish K. Alpha particle and neutron-induced soft error rates and scaling trends in SRAM. Proceedings of IEEE International Reliability Physics Symposium (IRPS); 2009; Montreal, Canada. pp. 206-211.

[21]Abe S, Watanabe Y, Shibano N, Sano N, Furuta H, Tsutsui M, Uemura T, Arakawa T. Multi-scale Monte Carlo simulation of soft errors using PHITS-HyENEXSS code system. IEEE Trans. Nucl. Sci.2012; 59: 965-970.

[22] Sato T, Endo A, Zankl M, Petoussi-Henss N, Niita K. Fluence-to-dose conversion coefficients for neutrons and protons calculated using the PHITS code and ICRP/ICRU adult reference computational phantoms. Phys. Med. Biol. 2009; 54: 1997-2014.

[23] Sato T, Endo A, Niita K. Fluence-to-dose conversion coefficients for heavy ions calculated using the PHITS code and the ICRP/ICRU adult reference computational phantoms. Phys. Med. Biol. 2010; 55: 2235-2246.

[24] Endo A, Sato T. Analysis of linear energy transfers and quality factors of charged particles produced by spontaneous fission neutrons from ^{252}Cf and ^{244}Pu in the human body. Radiat. Prot. Dosim. 2013; 154: 142-147.

[25] Yonai S, Matsufuji N, Namba M. Calculation of out-of-field dose distribution in carbon-ion radiotherapy by Monte Carlo simulation. Med. Phys. 2012; 39: 5028-5039.

[26] Hirayama H, Namito Y, Bielajew A.F, Wilderman S.J, Nelson W.R. The EGS5 code system. 2005; SLAC-R-730 and KEK Report 2005-8.

[27] Hashimoto S, Iwamoto Y, Sato T, Niita K, Boudard A, Cugnon J, David J.C, Leray S, Mancusi D. New approach for describing nuclear reactions based on intra-nuclear cascade coupled with DWBA. Prog. Nucl. Sci. Technol. 2014; 4: 418-241.

14. Recent Developments in Intranuclear Cascade Model at Kyushu University

Yusuke UOZUMI, Takahiro YAMADA, Akifumi SONODA
Department of Applied Quantum Physics and Nuclear Engineering, Kyushu University
Motooka 744, Nishi-ku, Fukuoka, 819-0395
e-mail: uozumi@nucl.kyushu-u.ac.jp

Masahiro NAKANO
Department of Nursing, Junshin Gakuen University
Chikushigaoka 1-1-1, Minami-ku, Fukuoka, 815-0036

The Intranuclear Cascade with Emission of Light Fragment (INC-ELF) code has been developed at Kyushu University and implemented in the Particle and Heavy Ion Transport code System, PHITS. In this report, we describe recent developments in INC model. The applicable range of incident energies is lowered for (p, p'x) reactions down to about 30 MeV with inclusion of trajectory deflection, collective excitation and transmission coefficient. The exclusive (p, d) reaction is considered by introducing a strength function. For pion-induced reactions, a microscopic treatment of the pion absorption by deuteron inside nucleus is described in a consistent way with that of deuteron knockout in (p, dx) reactions. The calculation results of the proposed model show good agreements with experimental data of (p, p'x), (p, dx), (π^+, px), (π^-, px) and (π^+, dx) reactions.

1. Introduction

The intranuclear cascade (INC) model is a powerful method for predicting the double-differential cross section (DDX) of nucleon-nucleus spallation reactions. The intranuclear cascade with Emission of Light Fragment (INC-ELF) code [1] has been developed at Kyushu University and implemented in the Particle and Heavy Ion Transport code System (PHITS). The INC-ELF code explicitly includes nucleon correlations within the framework of the INC model to describe light fragment emissions from nuclear spallation reactions. Further efforts were devoted for the INC model to improve its accuracy and to widen its applicable range of reactions.

One of the developments is to lower the applicable range of incident energies. The applicable energy range of INC was believed to be above a few hundred MeV of bombarding energies. To expand the applicable energy range of INC to the lower energy regime is essential for particle transport codes. In our previous study [2], the INC model was successfully extended to the lower incident energies by introducing trajectory deflections and the energy loss process via collective excitations. The improved INC model accounted well experimental DDXs of ^{56}Fe(p, p'x) reactions at 40-60 MeV. In the recent study [3], further developments were carried out to explain the barrier effect. The quantum transmission coefficient is essential to describe the proton emission in the barrier energy range. A phenomenological transmission coefficient was investigated to give the best fit of experimental data. The second improvement is the direct pickup (p, d) reaction. For the better accounts of (p, dx) reactions of around 50 MeV, the direct pickup process of exclusive (p, d) reaction has been included by using a strength function. The third improvement is to include pion-induced reactions. A microscopic treatment of the pion-deuteron absorption inside the target nucleus was investigated in a consistent way with deuteron knockout in inclusive (p, dx) reactions. In the present work, the model is validated by comparison with experimental observables stored in EXFOR.

2. (p, p'x) reaction in 50-MeV-range

Since the details are available in Ref.[2,3], a brief explanation is described. In the INC model, DDX is given in a simplified form:

$$\frac{d^2\sigma}{d\varepsilon\, d\Omega_f} = \pi R^2 \frac{1}{2\pi \Delta E \Delta \cos\theta} P(\theta, \varepsilon)\,, \tag{1}$$

where P is the probability to find an emitted proton of energy ε and emission angle θ. Its form is assumed to be

$$P(\theta,\varepsilon) = P_{def}^{in}(\theta_{ei}, t_1)\big(1 + P_{co}(\varepsilon_{co}, t_2)\big)\, G_{cas}(\theta_{cas}, \varepsilon_{cas})\, T_c P_{def}^{ex}(\theta_{ee}, t_m) \tag{2}$$

with

$$G_{cas}(\theta,\varepsilon) = \Gamma + \Gamma\, P_{nc}(\theta_{m1}, \varepsilon_{m1}, t_{m1})\, \Gamma + \Gamma\, P_{nc}(\theta_{m2}, \varepsilon_{m2}, t_{m2})\, \Gamma\, P_{nc}(\theta_{m3}, \varepsilon_{m3}, t_{m3})\, \Gamma + \cdots,$$

where P_{def}, P_{co}, P_{nc}, are probability of deflection, collective excitation and non-collective excitation, respectively. The transmission coefficient T_c is introduced [3] for only the exit channel. Its functional form was chosen to be that of the Gamow factor, which is better than other candidates such as the Hill-Wheeler formula, the step function and the energy reciprocal function. Since the Gamow factor was deduced for α-decay, we consider that the classical turning point outside of the potential and the Coulomb potential at the point are ambiguous. We take these two free parameters and determine them to fit experimental data best. The cascade process is given by G_{cas}, which includes propagation operator Γ. The collective excitation is assumed to occur at the nuclear surface in the entrance channel. We obtained P_{def} and P_{co} to fit experimental elastic scattering angular distributions and DWBA calculations, respectively.

Typical calculation results are shown in Figs. 1 and 2 for ^{197}Au(p, p'x) reactions at 61 MeV and 29 MeV, respectively. The present results shown by solid lines are in good agreements with experiments. The peaks at the highest energy are attributed to the inclusion of the deflection, and may correspond to the nuclear elastic scattering. The results of standard INC model, which includes neither deflection nor collective excitation, are displayed by long-dashed lines. Dotted lines indicate evaporation components, results of GEM calculations, which were executed after the cascade phase. At 61 MeV incidence case, the evaporation contribution is too strong and INC component is negligible. In contrast at 29 MeV incidence case, the main contribution is from INC, but evaporation is very weak.

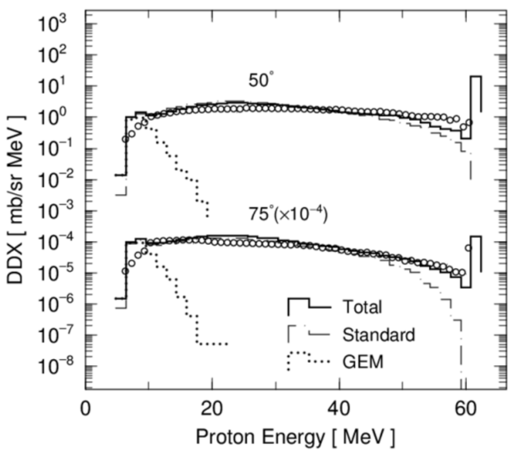

Fig.1 ^{197}Au(p, p'x) reaction at 61 MeV

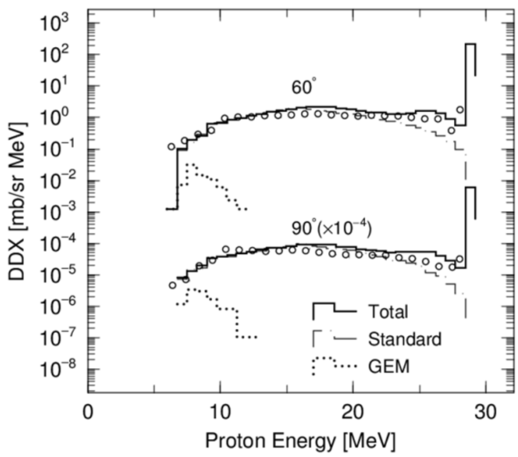

Fig.2 ^{197}Au(p, p'x) reaction at 29 MeV

3. Direct (p, d) reaction

In our previous study [1,4,5], knockout and indirect-pickup processes were introduced into the INC model to describe light cluster emission. The indirect-pickup is the process in which an outgoing particle picks up a bound particle at the surface, and may be called the coalescence process elsewhere. The calculation results give good accounts of entire energy range of DDX spectra of inclusive (p, dx) reactions at 300-400 MeV. It should be stressed that the quasi-free peaks in deuteron spectra are accounted by the knockout process. The underestimation observed at the higher energy range of spectra than the quasi-free peak at small angles is attributed to the lack of the direct pickup process, which was disregarded previously. Since the direct pickup populates a shell model state, its contribution is expected to be significant at incident energies of around 50 MeV. The inclusion of the direct pickup process was achieved by the similar way to that of the collective excitation process in (p, p'x) reactions. The strength function of a (p, d) reaction is given by the Breit-Wigner function. We assumed a single-orbit strength function, which gives the highest probability for the ground state and zero for the 40-MeV excitation. The integrated strength was determined to fit the experimental DDX spectra. In the present work, the proton deflection angle is used for that of deuterons. Since this may be a poor assumption for (p, d) reactions, it is necessary to conduct further study for the deuteron deflection angle. More efforts should be needed to study strength functions.

Examples of the results are shown in Figs. 3 and 4 for the 42-MeV ^{27}Al, ^{40}Zr(p, dx) reactions, respectively. Laboratory angles are 30˚ and 60˚. Present results are in reasonable agreements with experimental spectra covering excitations up to about 15 MeV, where the direct pickup process governs.

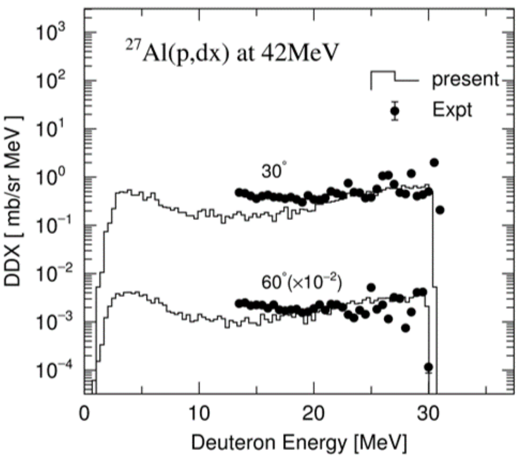

Fig. 3 Spectra of ^{27}Al (p,dx) at 42 MeV

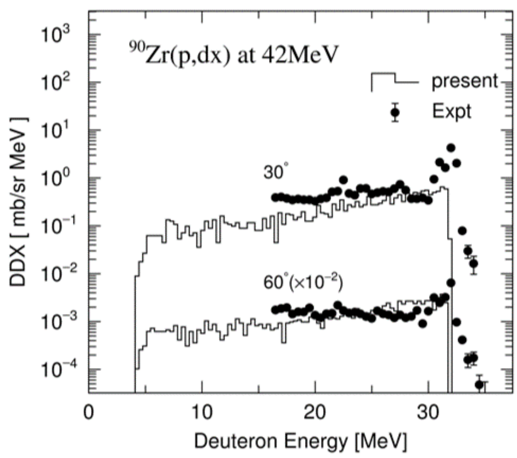

Fig. 4 Spectra of ^{40}Zr (p,dx) at 42 MeV

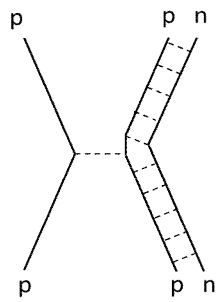

Fig. 5 The pd knockout scheme

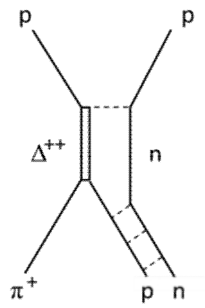

Fig. 6 The π^+d absorption scheme

4. Pion induced reaction

It is widely known [6] that spectra of (π^+, px) reactions at 150-300 MeV consist of two peaks: the higher energy peak is attributed to pion absorption by a deuteron or an NN pair, and the lower energy peak is due to the pion-nucleon elastic scattering. Since we have introduced the nucleon correlation to explain deuteron knockout by an incident proton in inclusive (p, dx) reactions, this correlation can be used to describe the pion absorption process. An example of the deuteron knockout scheme is shown in Fig.5, that is treated in our INC model [4,5] for inclusive (p, dx) reactions. An example of the π^+ absorption process, $\pi^+d \rightarrow pp$, which is mediated by Δ^{++}, is shown in Fig.6. The pion absorption is possible by not only a deuteron (or a pn-pair) but also other pp and nn pairs. We consider also the pp and nn pairs with the charge conservation. The π^- induced reactions are treated in the same way. Parameters for cross sections of π^+N and π^-N reactions are summarized in [7].

Typical results are shown in Figs. 7 and 8 for ^{58}Ni(π^+, px) and (π^-, px) reactions at 160 and 220 MeV, respectively in comparison with experiments and other reaction model codes implemented in PHITS: INCL, Bertini. The present results given by solid lines are in good agreements with experiments for both reactions. A similar comparison is shown in Fig. 9 for the (π^+, dx) reaction on ^{180}Ta at 280 MeV with an experimental deuteron spectrum taken from [8]. The present result agrees well with the experiment below 100 MeV. It is noted that Bertini include no cluster emission models. Results of Bertini are due to the deuteron evaporation of GEM.

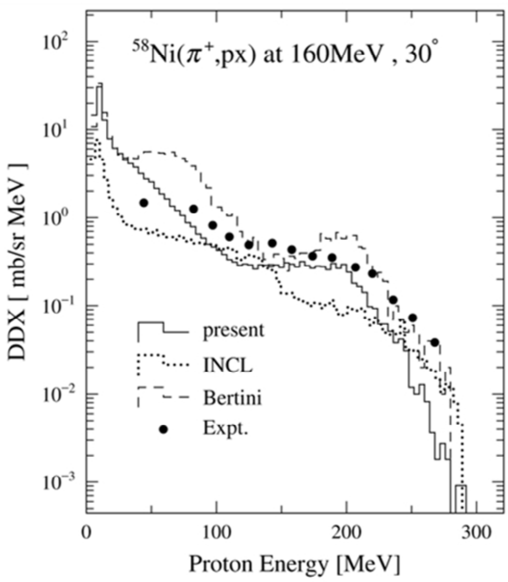

Fig. 7 ^{58}Ni(π^+, px) reaction at 160 MeV

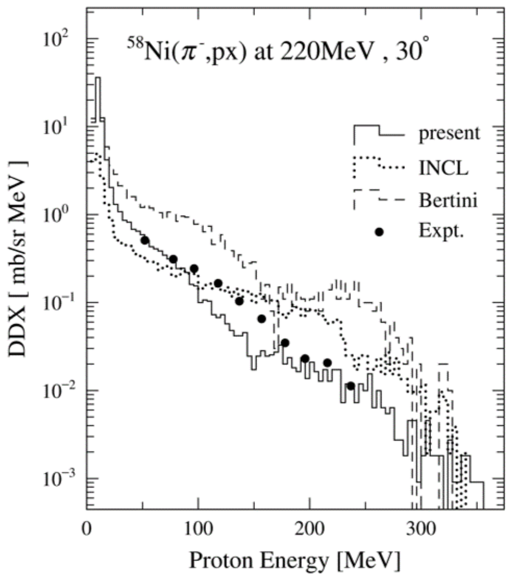

Fig. 8 ^{58}Ni(π^-, px) reaction at 220 MeV

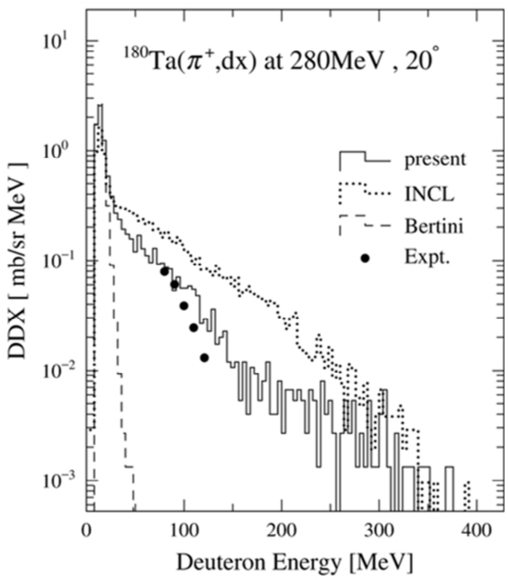

Fig. 9 ^{180}Ta(π^+, dx) reaction at 280 MeV

5. Conclusion

Recent developments in the INC model were described in this report. The DDX spectra of (p, p'x) reactions of about 30-60 MeV are well accounted by inclusion of trajectory deflection, collective excitation and transmission coefficient. Good accounts of the inclusive (p, dx) spectra are given by inclusion of exclusive (p, d) reactions at around 40 MeV by introducing a strength function. For pion-induced reactions, a microscopic treatment of the pion absorption by deuteron inside nucleus is described in a consistent way with that of deuteron knock out in (p, dx) reactions. However, further efforts are needed for general use in transport codes.

References

[1] Sawada Y, Uozumi Y, Nogamine S, Yamada T, Iwamoto Y, Sato T, Niita K. Intranuclear Cascade with Emission of Light Fragment Code Implemented in the Transport Code System PHITS. Nucl. Instr. Meth. B. 2012; 291: 38-44.

[2] Uozumi Y, Yamada T, Nogamine S, Nakano M. Intranuclear cascade model including collective excitations and trajectory deflections for (p,p'x) reactions around 50 MeV. Physical Review C. 2012;86:034610.

[3] Uozumi Y, Yamada T, Nakano M. Intranuclear cascade model for 50-MeV-region (p, p'x) reactions over a wide target mass range. J. Nucl. Sci. Technol. 2014. (in printing)

[4] Uozumi Y, Sawada Y, Mzhavia A, Nogamine S, Iwamoto H, Kin T, Hohara S, Wakabayashi G, Nakano M. Deuteron-production Double-differential Cross Sections for 300- and 392-MeV Proton-induced Reactions Deduced from Experiment and Model Calculation. Physical Review C. 2011; 84:064617.

[5] Uozumi Y, Sawada Y. Intranuclear cascade model for cluster production reaction. JAEA-Conf 2011-002. 2011;65-70.

[6] McKeown RD, Sanders SJ, Schiffer JP, Jackson HE, Paul M, Specht JR, Stephenson EJ, Redwine RP, Segel RE. Inclusive reactions of pions on nuclei. Physical Review C. 1981;24:211-220.

[7] Aoust Th, Cugnon J. Pion physics in the Liège intranuclear cascade model, Physical Review C. 2006; 74: 064607.

[8] Mzhavia A. Study of Double Differential Cross Sections of Nuclear Reactions Induced by Protons, Pions and Oxygen-ions [dissertation]. Fukuoka (Japan): Kyushu University; 2012.

15. Measurement of Neutron Production Cross Sections from Heavy Ion Induced Reaction

Nobuhiro SHIGYO[1], Yusuke UOZUMI[1], Youichi IMAHAYASHI[1], Yutaro ITASHIKI[1], Daiki SATOH[2], Tsuyoshi KAJIMOTO[3], Toshiya SANAMI[4], Yusuke KOBA[5], Masashi TAKADA[5], Naruhiro MATSUFUJI [5], Tae-Yung SONG[6], Cheol Woo LEE[6], Jong Woon KIM[6] and Sung-Chul YANG[6]

[1] *Kyushu University, Fukuoka, 819-0395, Japan*
[2] *Japan Atomic Energy Agency, Ibaraki-ken, 319-1195, Japan*
[3] *Hiroshima University, Higashi Hiroshima, 739-8527, Japan*
[4] *High Energy Accelerator Research Organization, Tsukuba, 305-0801, Japan*
[5] *National Institute of Radiological Sciences, Chiba, 263-8555, Japan*
[6] *Koera Atomic Energy Research Institute, Daejeon, 305-353, Korea*
e-mail: shigyo@kune2a.nucl.kyushu-u.ac.jp

Heavy ion induced double differential neutron production cross sections and thick target yields from 0.6 MeV to several hundred MeV were measured at HIMAC facility to validate mainly calculation accuracy of Monte Carlo simulation codes for neutron production in a patient body in heavy ion cancer therapy. Incident ions were 290 and 100 MeV/u carbon, oxygen and nitrogen. 290 MeV/u argon beam was also used for radiation shielding data. Carbon, aluminum nitride, aluminum oxide, aluminum were adopted as targets. Two sizes of NE213 organic scintillators were applied to detect neutrons in a wide energy range. Measurement angles were from 15°to 90°. Neutron energy was determined by the time-of-flight between a detector in front of a target and a neutron detector. Experimental results were compared with calculated data by Monte Carlo simulation codes.

1 Introduction

Cancer therapy using heavy ion beam has been applied as highly advanced medical treatment by reason of its clinical advantages. It has become more important to estimate the risk of secondary cancer from recent survey[1, 2]. During treatment, secondary particles such as neutrons and γ-rays are produced in a patient body as well as beam delivery apparatuses. For the risk assessment of secondary cancer, it is essential to know contribution of secondary neutrons by extra dose to organs in the vicinity of the irradiated tumor because the secondary neutron has a long mean free path and gives undesired dose to normal tissues in a wide volume. The experimental data of neutron energy spectra are required for dose estimations with high accuracy. Especially, precise data around neutron energy of 1 MeV are required because neutron of the such energy region has a large radiation weighting factor. The secondary neutron yield data is important for estimation of radiation safety on both of workers and public in treatment facilities.

Neutron production double differential cross sections and thick target neutron yields for heavy ion incidence on many element targets have been measured in Heavy Ion Medical Accelerator in Chiba (HIMAC)[3, 4, 5, 6, 7]. Experimental data of neutron energy spectra above several MeV were provided in the measurements. However, neutron data around 1 MeV which are important for radiation safety were not given.

Thick target neutron energy spectra from a water phantom bombarded by 200 MeV/u carbon beam showed discrepancies between experimental data measured by GSI and simulation results by the Monte Carlo particle transport code [8]. The experimental condition is essential to get knowledge of radiation effect in a human body.

A new heavy ion accelerator facility project RAON which means “joyful” and “happy” in Korean to produce various kinds of rare isotope beams is in progress in Korea[9]. One of candidates of combination of accelerated ions and target materials are 300 MeV/u argon and a carbon, respectively. Neutron energy spectrum from heavy ion induced reaction plays an important role as a radiation source term in shielding design of the facility.

In the basis of lack of neutron experimental energy spectrum in low energy region, the discrepancy between measured and calculated data in a water phantom and the request of knowledge about shielding design in a heavy ion accelerator, we have aimed measurements of neutron energy spectra from several hundred keV to several hundred MeV from heavy ion induced reactions in order to obtain data for evaluation of dose by secondary neutrons in cancer therapy and radiation safety in an accelerator facility. In this paper, brief explanation of a series of experiments and some of measured data and comparisons with Monte Carlo simulation particle transport codes are described.

2 Experiments

All measurements of neutron energy spectra were carried out at the PH2 course of HIMAC, National Institute for Radiological Sciences. Detailed information of these experiments are mentioned in references[10, 11, 12]. Brief summaries are pointed here.

We measured neutron energy spectra for incident heavy ions and target combinations in **Table 1**. Detailed information of targets and flight path length are mentioned in the references.

Table 1. Combinations of incident heavy ions and targets.

Incident ion	Energy [MeV/u]	Target	Reference
C	290	C, AlN, Al_2O_3, Al, Water	[10, 11, 13, 14]
O	290	C	[10]
C	100	C, AlN, Al_2O_3, Al	[12, 14]
N	100	C	[14]
O	100	C	[14]
Ar	290	C	N/A

The experimental setup is illustrated in **Figure 1**. The beam passed through a beam pick-up detector at the front of a target. the detector provided the signal for the time-of-flight (TOF) measurement and the number of incident particles.

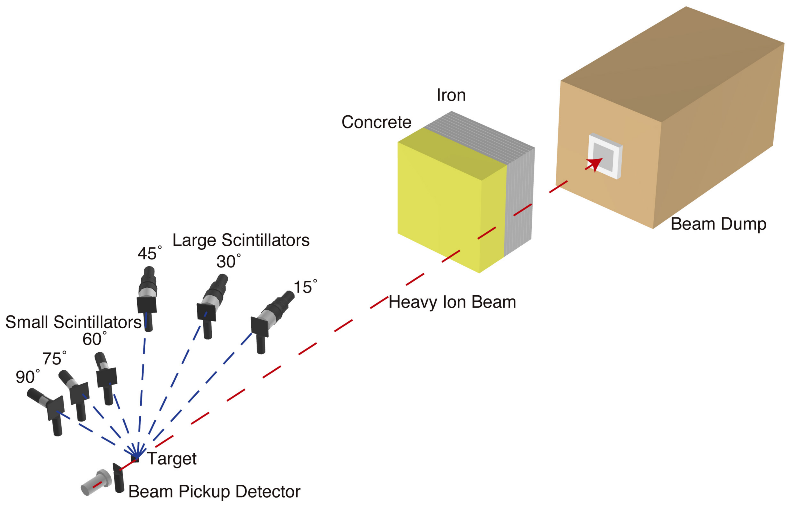

Figure 1. Experimental setup at the PH2 course of HIMAC. Large and small detectors are located at 15° to 45° and 60° to 90°, respectively.

Emitted neutrons were detected with two sizes of NE213 liquid organic scintillators to cover wide neutron energy range. Large and small detector sizes were 127 mm in diameter and 127 mm long and 50.8 mm in diameter and 50.8 mm long, respectively. The scintillators were placed at 6 directions from 15° to 90°. Three large detectors are located at 15°, 30° and 45° and three small ones at 60°, 75° and 90°, respectively in Fig. 1. Measurements with opposite detector arrangement were also performed. Distance between the target and NE213 scintillators were varied from 1.8 m to 4.0 m for large scintillators and from 1.0 m to 2.1 m for small ones, respectively. The kinetic energy of neutron was obtained by TOF technique using the time difference between the beam pickup scintillator and the neutron detector. A veto detector was put in front of each NE213 scintillator to separate charged particle events.

In order to reduce neutrons from the beam dump, iron plates and a concrete block were placed between the neutron detectors and beam dump as shown in Fig. 1. For estimation of neutrons from floor or other items in the experimental room, the measurements with iron shadow bars placed between a target and a neutron detector were also done.

3 Results

First, 290 MeV/u carbon incident neutron double differential cross sections on the carbon were measured. The Monte Carlo particle transport code PHITS[15] reproduces the experimental data well[10]. Next, 290 MeV/u oxygen beam was used. Neutron energy spectra were obtained down to 0.6 MeV in the measurement[10].

Figure 2 stands for neutron double differential cross sections for 290 MeV/u carbon incidence on an aluminum target. One can see that neutron energy spectra are obtained down to 0.6 MeV and PHITS with NASA nucleus-nucleus cross sections[16, 19] reproduces experimental data well except for the energy range from 3 to 10 MeV.

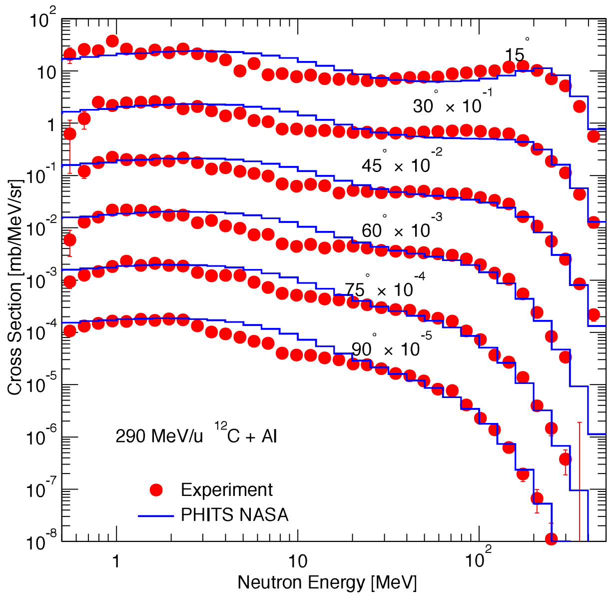

Figure 2. Neutron double differential cross sections for 290 MeV/u carbon incidence on an aluminum. Circles, solid lines stand for experimental data and calculation results by PHITS, respectively.

Thick target neutron yields for 290 MeV/u carbon incidence on a water phantom are shown in **Figure 3**. Experimental data will be published in reference [13]. Both of PHITS with NASA nucleus-nucleus cross sections and FLUKA[17] overestimate experimental data below several tens MeV from 15° to 45°. PHITS reproduces measured data at 90° but FLUKA also overestimates at the direction.

Neutron production double differential cross sections for 290 MeV/u argon incidence on a carbon are

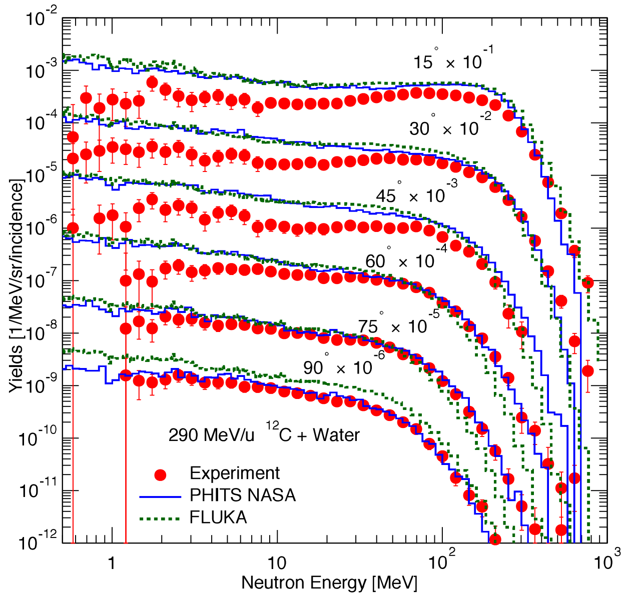

Figure 3. Thick target neutron yields for 290 MeV/u carbon incidence on a water phantom. Circles, solid and dashed lines stand for experimental data, calculation results by PHITS and FLUKA, respectively.

indicated in **Figure 4**. Experimental data below 5 MeV for all directions are higher than expected ones because it was difficult to eliminate background neutrons in the measurement. Shorter flight path lengths were adapted for small detectors which covered low neutron energies in the later experiments in order to reduce effect of scattered neutrons in low energy region[12].

Nucleus-nucleus cross sections by Kurotama[18] and NASA gives almost same neutron cross sections as seen the figure. Geant4[20] with Binary Cascade model[21] produces less neutrons than PHITS and Geant4 with INCL++ model[22]. Geant4 with INCL++ model estimates more neutrons below 5 MeV than that by other calculations.

4 Summary

In order to get knowledge of neutron production in a wide energy range for radiation safety, neutron production double differential cross sections and thick target neutron yields were obtained for heavy ion induced reactions. Neutron energy spectra were also obtained in the wide energy range from 0.6 MeV to several hundred MeV using two sizes of scintillators.

Monte Carlo codes reproduce experimental data of neutron double differential cross sections and thick target neutron yields to some extent. PHITS shows better agreement with measured data than FLUKA and Geant4.

Acknowledgement

This work is supported by grand-aid of ministry of education (KAKENHI 22360406) in Japan and was performed as a Research Project with Heavy Ions at NIRS-HIMAC.

References

[1] Clasie B, Wroe A, Kooy A, Depauw N, Flanz J, Paganetti H. Assessment of out-of-field absorbed dose and equivalent dose in proton fields. Med Phys. 2010 Jan;37:311-321.

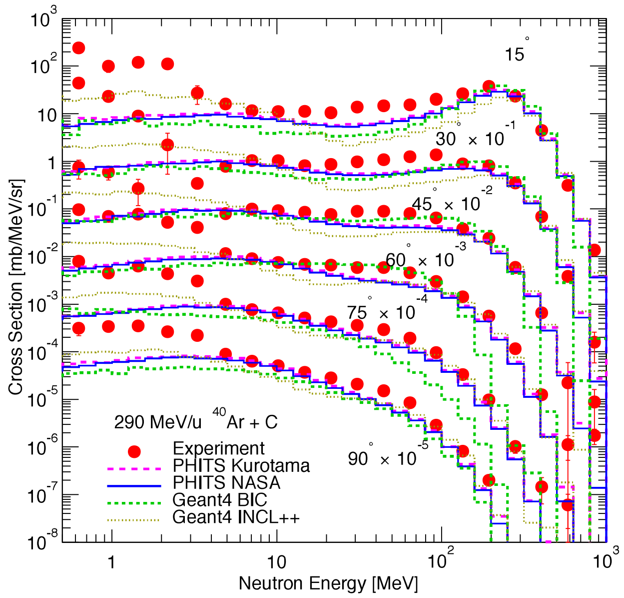

Figure 4. Neutron double differential cross sections for 290 MeV/u argon incidence on a carbon target. Circles, solid and long, middle and short dashed lines stand for experimental data, calculation results by PHITS with Kurotama, PHITS with NASA cross sections and Geant4 with binary cascade and Geant4 with INCL++ model, respectively.

[2] Hall EJ. Intensity-modulated radiation therapy, protons, and the risk of second cancers. Int J Radiat Oncol Biol Phys. 2006 Jan;65:1-7.

[3] Iwata Y, Murakami T, Sato H, Iwase H, Kurosawa T, Heilbronn L, Ronningen RM, Ikei K, Tozawa Y, Niita K. Double-differential cross sections for the neutron production from heavy-ion reactions at energies E/A=290-600 MeV. Phys Rev C. 2001 Oct;64:054609.

[4] Kurosawa T, Nakao N, Nakamura T, Iwase H, Sato H, Uwamino Y, Fukumura A. Neutron yields from thick C, Al, Cu, and Pb targets bombarded by 400 MeV/nucleon Ar, Fe, Xe and 800 MeV/nucleon Si ions. Phys Rev C. 2000 Sep;62:044615.

[5] Kurosawa T, Nakao N., Nakamura T, Uwamino Y, Shibata T, Fukumura A, Murakami K. Measurements of Secondary Neutrons Produced from Thick Targets Bombarded by High Energy Neon Ions. J Nucl Sci Technol. 1999 Jan;36:41-53.

[6] Kurosawa T, Nakamura T, Nakao N, Shibata T, Uwamino Y, Fukumura A. Spectral measurements of neutrons, protons, deuterons and tritons produced by 100 MeV/nucleon He bombardment. Nucl Instrum Meth A. 1999 Jul;430:400-422.

[7] Kurosawa T, Nakao N, T. Nakamura, Uwamino Y, Shibata T, Nakanishi N, Fukumura A, Murakami K. Measurements of Secondary Neutrons Produced from Thick Targets Bombarded by High-Energy Helium and Carbon Ions. Nucl Sci Eng. 1999 May;132:30-57.

[8] GunzertMarx K. Nachweis leichter Fragmente aus Schwerionenreaktionen mit einem BaF2TeleskopDetektor [dissertation]. Darmstadt Germany: Technische Universitt Darmstadt; 2004. [in German].

[9] Ryu MS, Kang BH, Kim YK, Jeong SC, Yun CC, Characteristics of rare isotope beams in the KoRIA facility. J Korean Phys Soc. 2012 Jan;60:19-25.

[10] Satoh D, Moriguchi D, Kajimoto T, Uehara H, Shigyo N, Ueyama M, Yoshioka M, Uozumi Y, Sanami T, Koba Y, Takada M, Matsufuji N. Measurement of neutron-production double-differential cross-sections on carbon bombarded with 290-MeV/nucleon carbon and oxygen ions. Nucl Instrum Meth A. 2011 May;644:59-67.

[11] Moriguchi D, Nakamura Y, Kajimoto T, Koba Y, Ueyama M, Yoshioka M, Shigyo N, Uozumi Y, Satoh D, Sanami T, Takada M, Matsufuji N. Measurement of Neutron-Production Cross Sections for 290 MeV/u Carbon Ion Incidence. J Korean Phys Soc. 2011 Aug;59:1789-92.

[12] Imahayashi Y, Shigyo N, Uozumi Y, Itashiki Y, Satoh D, Kajimoto T, Sanami T, Koba Y, Takada M, Matsufuji N. Measurement of cross section and thick target yield of neutron produced by 100 MeV/u C(C,xn) reaction. Poster session presented at: 2013 Symposium on Nuclear Data; 2013 Nov 14; Tsuruga, Fukui, Japan.

[13] Shigyo N. Uozumi Y, Uehara H, Nishizawa T, Hirabayashi K, Satoh D, Sanami T, Koba Y, Takada M, Matsufuji N. Measurement of neutron yields from a water phantom bombarded by 290 MeV/u carbon ions. Prog Nucl Sci Technol. Vol. 4 709 (2014).

[14] Shigyo N, Uozumi Y, Uehara H, Nishizawa T, Mizuno T, Takamiya M, Hashiguchi T, Satoh D, Sanami T, Kob Y, Takada M, Matsufuji N. Measurement of 100- and 290-MeV/u Carbon Incident Neutron Production Cross Sections for Carbon, Nitrogen and Oxygen. Oral session presented at: International Conference on Nuclear Data for Science and Technology, 2013 Mar 7: New York, NY.

[15] Sato T, Niita K, Matsuda N, Hashimoto S, Iwamoto Y, Noda S, Ogawa T, Iwase H, Nakashima H, Fukahori T, Okumura K, Kai T, Chiba S, Furuta T, Sihver L. Particle and Heavy Ion Transport Code System PHITS, Version 2.52. J Nucl Sci Technol. 2013 Sep;50:913-923.

[16] Tripathi RK, Wilson JW, Cucinotta FA. Accurate universal parameterization of absorption cross sections II — neutron absorption cross sections. Nucl Instrum Meth B. 1997 Jun;129:11-15.

[17] Battistoni G, Muraro S, Sala PR, Cerutti F, Ferrari A, Roesler S, Fassò A, Ranft J. The FLUKA code: Description and benchmarking. In: Albrow A, Rja R , etditors. the Hadronic Shower Simulation Workshop 2006. Proceedings; 2006 Sep 6-8; Batavia (IL): AIP Conference Proceeding. 2007;896:31-49. Ferrari A, Sala PR, Fassò A, Ranft J. FLUKA: a multi-particle transport code. Geneva (Switzerland): CERN (Switerland); 2005. (CERN-2005-10, INFN/TC_05/11, SLAC-R-773).

[18] Iida K,Kohama K, K Oyamatsu K. Formula for proton- nucleus reaction cross section at intermediate energies and its application. J Phys Soc Jpn. 2007 Apr;76:044201.

[19] Tripathi RK, Cucinotta FA, Wilson JW. Accurate universal parameterization of absorption cross sections. Nucl Instrum Meth B. 1996 Oct;117:347-349.

[20] Allison, J. Manchester Univ. Amako K, Apostolakis J, Araujo H, Dubois PA, Asai M, Barrand G, Capra R, Chauvie S, Chytracek R, Cirrone GAP, Cooperman G, Cosmo G, Cuttone G, Daquino GG, Donszelmann M, Dressel M, Folger G, Foppiano F, Generowicz J, Grichine V, Guatelli S, Gumplinger P, Heikkinen A, Hrivnacova I, Howard A, Incerti S, Ivanchenko V, Johnson T, Jones F, Koi T, Kokoulin R, Kossov M, Kurashige H, Lara V, Larsson S, Lei F, Link O, Longo F, Maire M, Mantero A, Mascialino B, McLaren I, Lorenzo PM, Minamimoto K, Murakami K, Nieminen P, Pandola L, Parlati S, Peralta L, Perl J, Pfeiffer A, Pia MG, Ribon A, Rodrigues P, Russo G, Sadilov S, Santin G, Sasaki T, Smith D, Starkov N, Tanaka S, Tcherniaev E, Tome B, Trindade A, Truscott P, Urban L, Verderi M, Walkden A, Wellisch JP, Williams DC, Wright D, Yoshida H. Geant4 Developments and Applications. IEEE Tras Nucl Sci. 2006 Feb;53:270-278. Agostinelli S, Allison J, Amako K, Apostolakis J, Araujo A, Arce P, Asagi M, Axen D, Banerjee S, Barrand G, Behner F, Bellagamba L, Boudreau J, Broglia L, Brunengo A, Burkhardt H, Chauvie S, Chuma J, Chytracek R, Cooperman G, Cosmo G, Degtyarenko P, Dell'Acqua A, Depaola G, Dietrich D, Enami R, Feliciello A, Ferguson C, Fesefeldt H, Folger G, Foppiano F, Forti A, Garelli S, Giani S, Giannitrapani R, Gibin D, Gòmez Cadenas JJ, González I, Gracia Abril G, Greeniaus G, Greiner W, Grichine V, Grossheim A, Gutalli S, Gumplinger P, Hamatsu R, Hashimoto K, Hasui H, Heikkinen A, Howard A. Geant4—a simulation toolkit. Nucl Instrum Meth A. 2003 Jul;506:250-303.

[21] Folger G, Ivanchenko VN, Wellisch JP. The Binary Cascade, Nucleon nuclear reactions. Eur Phys J A. 2004 Sep;21:407-417.

[22] Boudard A, Cugnon J, David JC, Leary S, Mancusi M. New potentialities of the Liège intranuclear cascade model for reactions induced by nucleons and light charged particles. Phys Rev C. 2013 Jan;87:014606.

16. Response Function for the Measurement of (n,γ) Reactions with the ANNRI-Cluster Ge Detectors at J-PARC

K.Y. Hara[1)], S. Goko[1,a)], H. Harada[1)], K. Hirose[1,b)], A. Kimura[1)], T. Kin[1,c)], F. Kitatani[1)], M. Koizumi[1)], S. Nakamura[1)], Y. Toh[1)], M. Igashira[2)], T. Katabuchi[2)], K. Kino[3)], Y. Kiyanagi[3)], and J. Hori[4)]

1) Nuclear Science and Engineering Directorate, Japan Atomic Energy Agency (JAEA)

2) Research Laboratory for Nuclear Reactors, Tokyo Institute of Technology

3) Graduate School of Engineering, Hokkaido University

4) Research Reactor Institute, Kyoto University

Present address: a) Japan Nuclear Energy Safety Organization, b) Advanced Science Research Center, JAEA, c) Department of Engineering Science, Kyushu University

For a new experimental setup, response functions of cluster-Ge detectors were measured with standard γ-ray sources, γ-rays of the ^{24}Na β-decay, and prompt γ-rays of the ^{35}Cl(n,γ)^{36}Cl reaction in ANNRI at J-PARC/MLF. The experimental data and calculation with the EGS5 code are compared.

1. Introduction

Response functions of a γ-ray detector are necessary for data analysis of neutron capture reaction using the pulse height weighting technique [1]. We had measured the response functions of the cluster-Ge detectors [2] at the Accurate Neutron-Nucleus Reaction measurement Instrument (ANNRI) [3, 4] in the Japan Proton Accelerator Research Complex (J-PARC). However, the γ-ray (or neutron) shields of the Ge detectors were repaired in March 2012 because these were damaged by the big earthquake in March 2011. In addition, the neutron shields made of boron rubber sheets were replaced by enriched ^{6}LiF tiles in October 2012 because the rubber sheets caused γ-ray backgrounds due to the ^{10}B(n,$\alpha\gamma$) reaction. For the new experimental setup, in order to determine the response functions, the efficiencies and pulse height spectra of the cluster-Ge detectors were measured and simulated.

2. Experimental setup

The schematic view of the new experimental setup is shown in Fig. 1. The detector system which comprises 2 cluster-Ge detectors with BGO anti-coincidence detectors is placed at a neutron flight length of 21.5 m. Each cluster-Ge detector consists of 7 pure germanium crystals, where the upper and lower cluster-Ge detectors are called as “cluster1” and “cluster2”, respectively. The distance is 124 mm from a sample position to the front surface of the cluster-Ge detector. As shown in Fig. 1, the neutron and γ-ray shields (^{6}LiH plates, ^{6}LiF tiles and Pb collimators) are arranged between the sample and the detectors.

Using the cluster-Ge detector system, γ-rays of ^{137}Cs and ^{152}Eu standard sources were measured for the low-energy region (E_γ<2MeV). Prompt γ-rays emitted from the ^{35}Cl(n,γ) reaction were measured for the high-energy region (E_γ>2MeV). A 0.5-g NaCl crystal (natural abundance) was used as the sample. In addition, γ-rays emitted in the β-decay of ^{24}Na nuclei, which were made by irradiating the NaCl sample with the neutron beam, were measured.

For a dead time correction of a data acquisition system, random timing pulses from a pulse generator were input to pre-amplifiers for every Ge crystal. As well as the pulse height of the random pulses, the number of the random timing pulses was counted with a counter module. The pulse rate was approximately 100 cps.

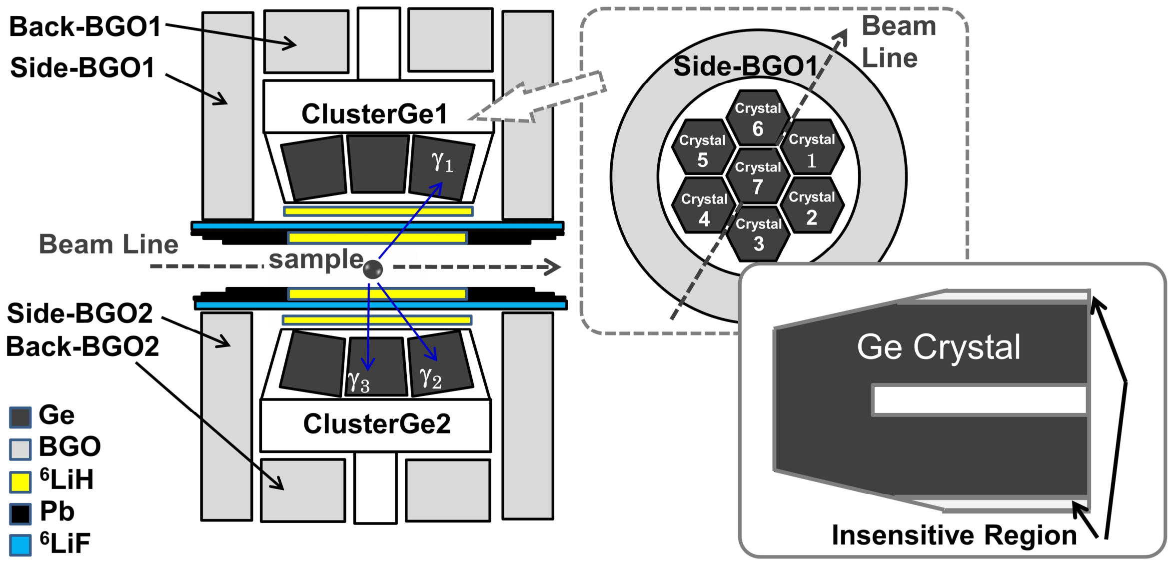

Figure 1: Schematic illustration of the new experimental setup of the Ge spectrometer

3. Full-energy peak efficiencies

The full-energy peak efficiencies measured with the cluster1 and cluster2 detectors are shown in Fig. 2(a) and (b), respectively, where the efficiency is a sum of those of the seven crystals in each cluster. The data of the ^{137}Cs and ^{152}Eu standard sources are shown as the diamond and circle, respectively. The data of the ^{35}Cl(n,γ) reaction (inverted triangle) are normalized to the data of the standard sources in the overlap energy region. The γ-ray pulse-height spectrum for the ^{35}Cl(n,γ) reaction gated in the neutron energy region of 0.002-10 eV were used to obtain the efficiencies.

The dashed lines show the calculated efficiencies using the Monte Carlo simulation code, EGS5 [5] in the γ-ray energy region of 0.2-10 MeV, where a γ-ray source was defined as a point source at the sample position. The simulation parameters were adjusted so as to reproduce the dataset of the measured efficiencies. In the simulation, each Ge crystal was defined as a hexagonal shape with a distance between sides of hexagon of 58 mm, an external diameter of 70 mm, and a depth of 78 mm. Although the shape outside of the electrode well described the effective volume of the product specification sheet, the calculated efficiencies were overestimated as compared with the experimental data. We additionally defined the insensitive region in each Ge crystal as shown in the inset of Fig.1. And the ^{6}LiH density parameter was increased to the theoretical density (0.82 g/cm^3). The energy dependence of the simulated efficiencies reasonably reproduces the measurement results in Fig. 2.

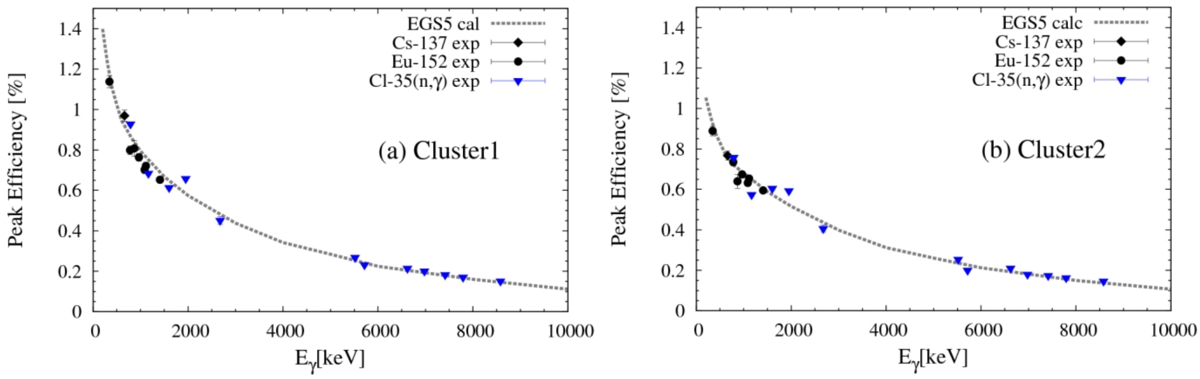

Figure 2: Full-energy peak efficiencies for the γ-rays from the standard sources (^{137}Cs and ^{152}Eu) and the prompt γ-rays from the ^{35}Cl(n,γ) reaction. The data points were measured with the cluster1 (a) and cluster2 detectors (b), respectively. The dashed lines were calculated using the EGS5 code.

4. γ-ray pulse-height spectra

The measured γ-ray pulse-height spectra are plotted by the black circles in Fig. 3 and Fig. 4. After the dead time correction and the background subtraction, 7 spectra of Ge crystals in the cluster1 (or cluster2) are summed into the “single” spectrum. The pulse-height spectra which were calculated with the present simulation parameters are shown by the gray lines.

Figure 3 shows the spectrum for the 662-keV γ ray of the ^{137}Cs source. The vertical axis is the efficiency per keV in Fig. 3. The measured (or calculated) peak-to-total ratios of the cluster1 and cluster2 detector are 0.24 (0.27) and 0.22 (0.25), respectively, where the total area was integrated in the region from 200 to 700 keV.

Figure 4 shows the spectrum for the γ-rays emitted in the ^{24}Na β-decay. In Fig. 4, the vertical axis is the counts per keV because of the relative measurement. The full-energy peak area of the calculated spectrum was normalized by one of the measured spectrum at the 2754-keV γ-ray peak. While several γ-rays are emitted in the ^{24}Na β-decay, the dominant decay pattern is a cascade that emits two γ-rays (1369 and 2754 keV). The 1369-keV and 2754-keV peak areas were used for the peak-to-total ratio. The measured (or calculated) peak-to-total ratios of the cluster1 and cluster2 detectors are 0.15 (0.18) and 0.14 (0.17), respectively, where the total area was integrated in the region from 200 to 4200 keV.

The differences between the measured and calculated peak-to-total ratios are within 20%. The additional adjustments of the simulation parameters are needed to reproduce the γ-ray pulse-height spectra and peak-to-total ratio.

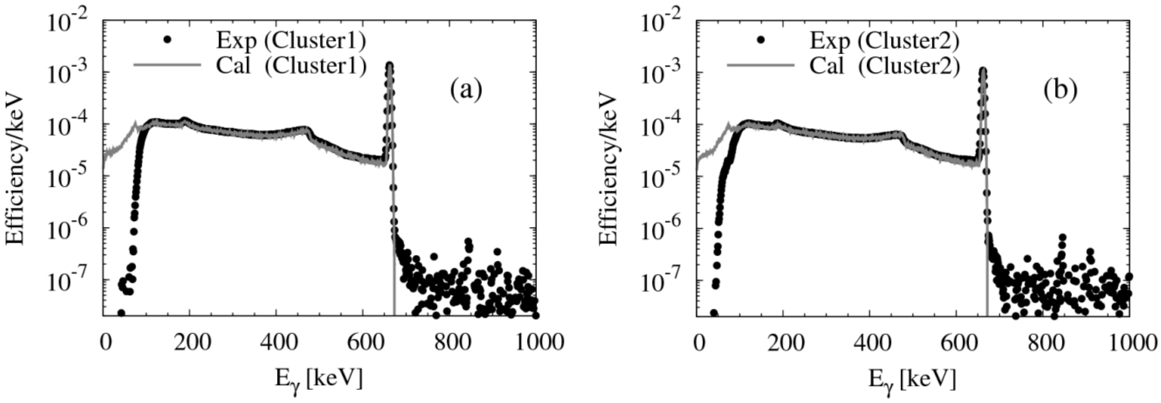

Figure 3: γ-ray pulse height spectra for the ^{137}Cs source were measured with the BGO anti-coincidence by the cluster1 (a) and cluster2 detectors (b), respectively (black circles). The simulated spectra are shown by the gray lines.

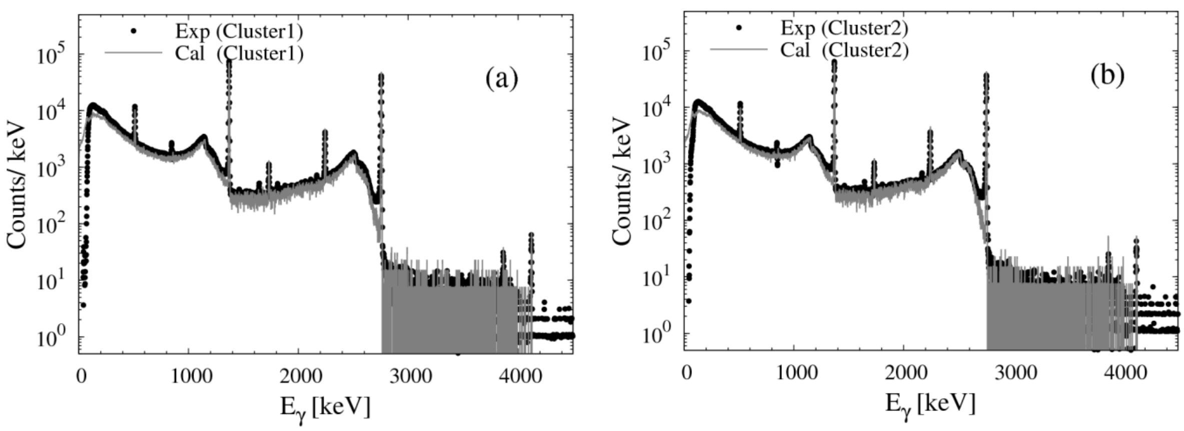

Figure 4: γ-ray pulse height spectra for the ^{24}Na β-decay were measured with the BGO anti-coincidence by the cluster1 (a) and cluster2 detectors (b), respectively (black circles). The simulated spectra are shown by the gray lines.

5. Conclusion

To obtain the response functions, the γ-rays of the standard sources (^{137}Cs and ^{152}Eu), γ-rays of the ^{24}Na β-decay, and prompt γ-rays of the ^{35}Cl(n,γ)^{36}Cl reaction were measured with the cluster-Ge detector system at ANNRI in J-PARC/MLF. The peak efficiencies, γ-ray pulse-height spectra, and peak-to-total ratio were compared with the simulations using the EGS5 code. The calculated efficiencies were reasonably in agreement with the measured one, although the additional adjustments of the simulation parameters are needed for the γ-ray pulse-height spectra and the peak-to-total ratio. Based on this information, a pulse height weighting function will be deduced.

Acknowledgements

The authors would like to thank the staffs of J-PARC and MLF for their operations of the accelerators and the neutron production target. This work was supported by JSPS KAKENHI Grant Number 22226016.

References

[1] Abbondanno U (n_TOF Collaboration). New experimental validation of the pulse height weighting technique for capture cross-section measurements. Nucl. Instr. Methods. 2004;A521: pp.454-467.

[2] Hara KY, Goko S, Harada H, Hirose K, Kimura A, Kin T, Kitatani F, Koizumi M, Nakamura S, Toh Y. Measurements and simulations of the responses of the cluster Ge detectors to gamma rays. Proceedings of the 2012 Annual Symposium on Nuclear Data: JAEA-Conf 2013-002: pp.161-166.

[3] Goko S, Kimura A, Harada H, Oshima M, Ohta M, Furutaka K, Kin T, Kitatani F, Koizumi M, Nakamura S, Toh Y, Igashira M, Katabuchi T, Mizumoto M, Kiyanagi Y, Kino K, Furusaka M, Hiraga F, Kamiyama T, Hori J, Fijii T, Fukutani S, Takamiya K. Measurement of neutron capture cross section ratios of ^{244}Cm resonances using NNRI. J. Nucl. Sci. Technol. 2010;47: pp.1097-1100.

[4] Kimura A, Fujii T, Fukutani S, Furutaka K, Goko S, Hara KY, Harada H, Hirose K, Hori J, Igashira M, Kamiyama T, Katabuchi T, Kin T, Kino K, Kitatani F, Kiyanagi Y, Koizumi M, Mizumoto M, Nakamura S, Ohta M, Oshima M, Takamiya K, Toh Y. Neutron-capture cross-sections of ^{244}Cm and ^{246}Cm measured with an array of large germanium detectors in the ANNRI at J-PARC/MLF. J. Nucl. Sci. Technol. 2012;49: pp.708-724.

[5] Hirayama H, Namito Y, Bielajew AF, Wilderman SJ, Nelson WR. 2005. The EGS5 Code Systems. KEK Report 2005-8, SLAC-R-730. High Energy Accelerator Research Organization (KEK), Stanford Linear Accelerator Center (SLAC).

17. Study of the γ-ray Strength Function in a ^{80}Se (γ ,γ') Experiment at ELBE

A. Makinaga[1], R. Schwengner[2], R.Massarczyk[2], M. Anders[2], M. Roeder[2], T. Al-Abdullah[2], R. John[2], S. Meuller[2], H. Otsu[3], K. Schmidt[2], R. Hannske[2], A. Wagner[2], S. Ebata[4]

[1]Faculty of Science, Hokkaido University, 060-0810, Sapporo, Japan
[2]Institute of Radiation Physics, Helmholtz-Zentrum Dresden-Rossendorf,, 01328 Dresden, Germany
[3]RIKEN Nishina Center, RIKEN, Hirosawa, Wako, Saitama 351-0918, Japan
[4]Meme Media Laboratory, Hokkaido University, 060-0810, Sapporo, Japan
*E-mail: makinaga@nucl.sci.hokudai.ac.jp

Abstract

The photon strength of ^{80}Se is a key parameter to estimate the ^{79}Se neutron capture cross section. Selenium-79 is important from the point of view of nuclear transmutation of the long-lived fission product ^{79}Se into the stable nucleus ^{80}Se. Currently, a lack of a proper target sample makes a direct measurement of (n, γ) cross sections for ^{79}Se unfeasible. In previous work, photo neutron cross sections were measured for ^{80}Se directly above the neutron separation energy with LCS photon beams to experimentally constrain the E1 γ-ray strength function for ^{80}Se. The uncertainty of the predicted neutron capture cross sections for ^{79}Se (~a factor of 4) was still very large in terms of the transmutation of the nuclear waste ^{79}Se [1-3]. To test the model calculation, a photon scattering experiment on ^{80}Se up to the neutron separation energy was performed by using the bremsstrahlung facility of the superconducting electron accelerator ELBE at Helmholtz-Zentrum Dresden-Rossendorf. We report on the current status of the experimental data analysis.

1 Introduction

Photon strength on ^{80}Se is a key parameter to estimate the ^{79}Se neutron capture cross section. ^{79}Se is important from the view point of nuclear transmutation of the long-lived fission product, ^{79}Se (half-life is 2.95 x 10^5 years [4]), into a stable nucleus ^{80}Se. On the other hand, in s-process conditions in stellar interior, the property of the competition between the neutron capture rate and beta-decay rate of ^{79}Se exhibits a strong temperature dependence due to thermal population of the isomeric state at 95.7 keV [5]. This property makes ^{79}Se s-process thermometer [6-8]. Currently, the lack of a proper target sample makes a direct measurement of (n, γ) cross sections for ^{79}Se unfeasible. In the previous work, photo neutron cross sections were measured for ^{80}Se immediately above the neutron-separation energy with laser Compton scattering (LCS) photon beams at Advanced Industrial Science and Technology (AIST) to experimentally constrain the E1 γ-ray strength function for ^{80}Se [9,10]. The uncertainty of the predicted neutron capture cross sections for ^{79}Se (~a factor of 4) was still very large from the view point of the transmutation of the nuclear waste ^{79}Se as well as s-process thermometer ^{79}Se. A unified statistical-model analysis of (γ, n) cross sections and (n, γ) cross sections on Se isotopes is expected to significantly reduce the uncertainty in model-predicting (n, γ) cross sections for ^{79}Se. Indirect efforts include a study of the gamma-ray strength function of ^{80}Se below neutron threshold.

In this work, to test the model calculation, photon scattering cross sections were measured for ^{80}Se up to the neutron separation energy with bremsstrahlung facility ELBE at Helmholtz Zentrum Dresden-Rossendorf. Experimental details are given in Sec. 2. In Sec. 3, systematic evaluation of the photo absorption cross sections for ^{76}Se, ^{78}Se, ^{80}Se, ^{82}Se by using statistical model code TALYS [11] and Cb-TDHFB (Canonical-basis Time-Dependent Hartree-Fock-Bogoliubov Theory) [12] are shown.

2 Photon-scattering experiment at ELBE

Photon scattering cross section $\sigma_{\gamma f}(E_R)$ can be measured via γ ray transition from given excitation level E_R to a level E_f in the target. In case of non-overlapping resonances, photon scattering is described to process via a compound nucleus reaction with uncorrelated channels f characterized by the partial width Γ_f, so photon-scattering cross section $\sigma_{\gamma f}(E_R)$ can be described as:

$$\sigma_{\gamma f}(E_R)=\sigma_\gamma(E_R)\frac{\Gamma_f}{\Gamma} \qquad (1)$$

Where, all partial widths contribute to the total level width $\Gamma=\Sigma\Gamma_f$.

$$I_S=\int_0^\infty \sigma_{\gamma\gamma}(E)dE=\frac{2J_R+1}{2J_0+1}\left(\frac{\pi\hbar c}{E_R}\right)^2\Gamma_0\frac{\Gamma_f}{\Gamma} \qquad (2)$$

Where, I_S is the integral of scattering cross section for the level R and Γ_f is the partial width for a transition from R to a level f. Measured intensity of γ-rays emitted to the ground state at $E_\gamma=E_R$ with an angle θ can be expressed as:.

$$I_\gamma(E_\gamma,\theta)=I_s(E_R)\Phi(E_R)\varepsilon(E_\gamma)N_{at}W(\theta)\frac{\Delta\Omega}{4\pi} \qquad (3)$$

Where, N_{at} is number of the target nuclei per unit area, $\varepsilon(E_\gamma)$ is the absolute full-energy peak efficiency at E_γ , $\Phi(E_R)$ is the absolute photon flux at E_R ,$W(\theta)$ is the angular correlation of this transition, and $\Delta\Omega$ is solid angle for the detector.

If electron energy is high enough above a particular level, the experiments with bremsstrahlung lead to the possibility of the population of a level by a feeding transition from a level in higher energy region. Such feeding increases the intensity of the transition to the ground state from the considered resonance R. The intensity of the transition to the ground state becomes a superposition of the rate of elastic scattering and the intensity of the transitions feeding level R. The cross-section integral I_{s+f} can be expressed as:

$$I_{s+f}=\int_0^\infty \sigma_{\gamma\gamma}(E)dE+\sum_{i>R}\sigma_{\gamma i}\frac{\Gamma_0}{\Gamma}dE$$

$$=\frac{2J_R+1}{2J_0+1}\left(\frac{\pi\hbar c}{E_R}\right)^2\frac{\Gamma_0^2}{\Gamma}+\sum_{i>R}\frac{\Phi(E_i)}{\Phi(E_R)}\frac{2J_i+1}{2J_0+1}\left(\frac{\pi\hbar c}{E_i}\right)^2\Gamma_0^i\frac{\Gamma_R^i}{\Gamma^i}\frac{\Gamma_0}{\Gamma} \qquad (4)$$

Where, summation over i>R is that the energy E_i of a level which feeds the considered resonance R is higher than the energy E_R of this resonance. Γ_i, Γ_{i0}, and Γ^i_R are the total width of the level E_i, the partial width of the transition to the ground state and the partial width of the transition to the level R, respectively. Details of the experimental method are given in [13-19].

Photon-scattering cross section measurement on ^{80}Se was performed at the superconducting electron accelerator ELBE of the Research Center Dresden-Rossendorf. Bremsstrahlung was produced by bombarding 7 μ m niobium radiator with electron beams of 11.8 MeV electron kinetic energy and average currents of 500 μ A. Produced Bremsstrahlung was collimated by an Al collimator with a length of 2.6 m and an opening angle of 5 mrad. A 10 cm length of cylindrical Al absorber was placed between the radiator and the collimator to reduce the low-energy part of the bremsstrahlung spectrum. The scattered photon was measured with four 100% HPGe detectors surrounded by BGO escape-suppression shields. Two Ge detectors were placed vertically at 90 degrees relative to the photon-beam direction. The other two Ge detector placed at 127 degrees were used to reduce angular distributions of the γ-ray. To deduce the low-energy part of background photons, absorbers of 8 mm Pb plus 3 mm Cu were placed in front of the detectors at 127 degrees and 13 mm Pb plus 3 mm Cu were used for the detectors at 90 degrees. A ^{80}Se target enriched to 99 %, with a mass of 1.95 g was irradiated with bremsstrahlung. The target was combined with a disk of ^{11}B (enrichement 99.5 %) that was used to determine the photon flux. In photon-scattering experiment, the spectrum includes the contributions of elastic, inelastic and cascade transition from an excited states to a given states. To obtain the intensities of the ground-state transitions and their branching ratio, a Monte Carlo code for the simulation of γ-ray cascades is used. The simulation code is based on the nuclear statistical model. In the simulation, the BSFG (back-shifted Fermi gas) model is used for level density. The level density parameter and the back-shift energy for ^{80}Se are taken from ref. [21]. The Wigner distribution is used for the nearest-neighbor spacing. The parameters for E1 γ-strength function was taken from RIPL-2 [22]. The Porter-Thomas distribution is used for the fluctuations of the partial decay widths. Inelastic scattering correction scheme is described more detail in the literature [23].

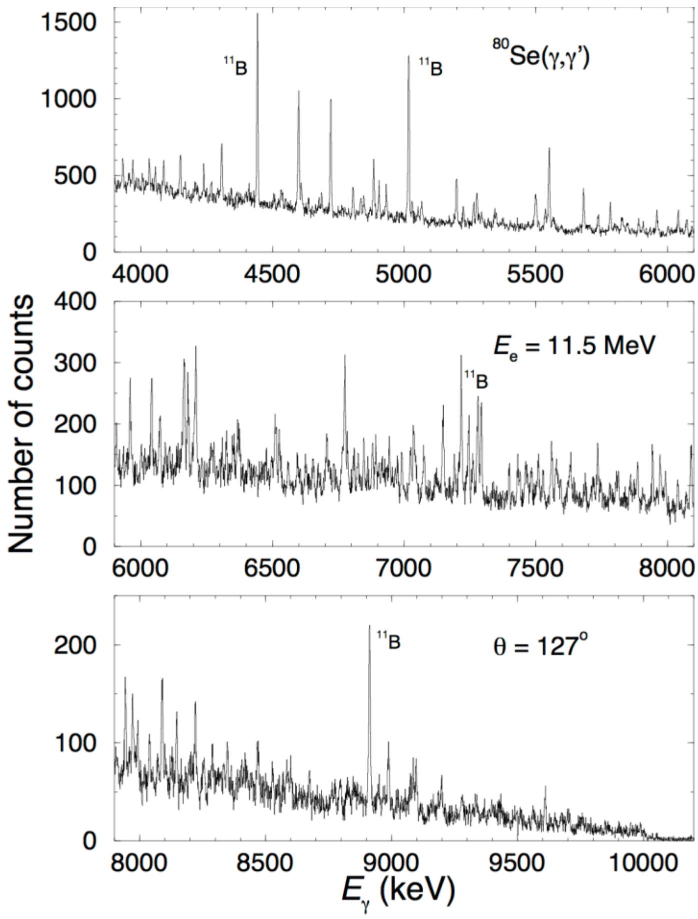

Figure 1 Gamma-ray spectrum from ^{80}Se (γ, γ') reaction

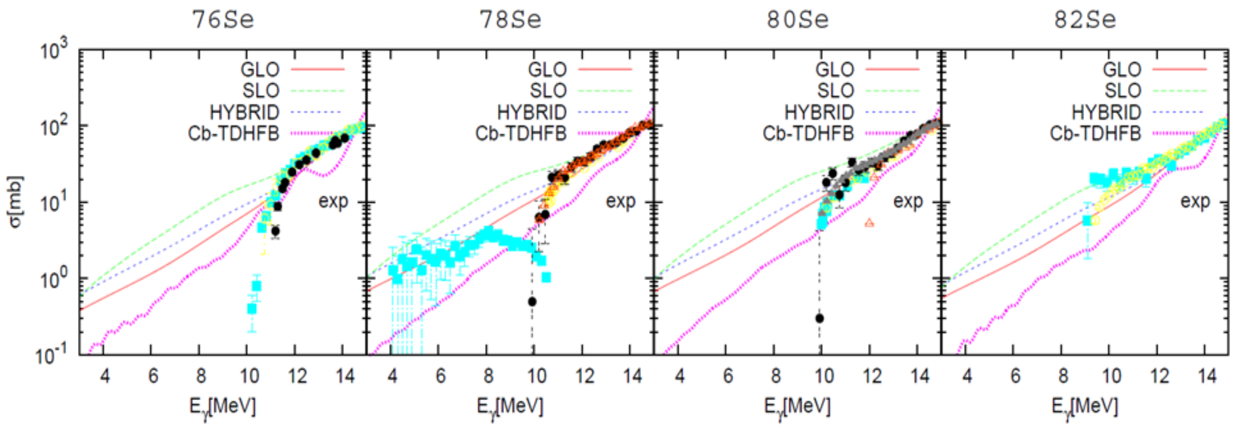

Figure 2 Systematic analysis of the photo absorption cross sections for ^{76}Se, ^{78}Se, ^{80}Se, ^{82}Se. TALYS code and Cb-TDHFB calculations are compared with the experimental data.

3 Systematic evaluation of the photo absorption for Se isotopes

The experimental data were systematically analyzed on the basis of a Hauser-Feshbach statistical model by using TALYS code. We considered various photon strength function to compare with the experimental data sets for ^{76}Se, ^{78}Se, ^{80}Se and ^{82}Se. The standard strength functions implemented in TALYS are the single Lorentz curve (SLO) [24, 25] and the generalized Lorentz curve (GLO) [26, 27]. HYBRID means the Goriery's hybrid model [28].

We also applied the Canonical-basis time-dependent Hartree-Fock-Bogoliubov (Cb-TDHFB) to explain the gamma strength function. The Cb-TDHFB is a simplified theory of the full TDHFB [29, 30] theory, treating pairing energy functional with a BCS-like approximation which is assumed to be diagonal in the canonical basis. By using a real-space and real-time method, nuclear excitations and dynamics are taken account fully self-consistently. Applying Cb-TDHFB to a linear response calculations, strength functions of isovector dipole and isoscalar quadrupole excitations for some spherical and deformed nuclei can be estimated microscopically. Fig.2 shows the preliminary result of calculations.

4 Summary

Photon-scattering cross sections for ^{80}Se were measured at bremsstrahlung facility ELBE of the Research Center Dresden-Rossendorf at an electron kinetic energy of 11.8 MeV. On the other hand, we estimated photo absorption cross sections for ^{76}Se, ^{78}Se, ^{80}Se, ^{82}Se by using TALYS code and Cb-TDHFB calculation. The experimental data for ^{80}Se (γ, γ') are currently analyzed. Further discussions will be performed in the near future.

Acknowledgments

We thank the staff of the ELBE accelerator for their cooperation during the experiments. We also thank to H. Utsunomiya for his teaching in the early stage of this research for photo neutron experiment at AIST. A. M also thanks Prof. M. Aikawa, Prof. Kato (Hokkaido Univ.) and Prof. H. Sakurai (Tokyo Univ. and RIKEN) for their useful discussion of nuclear data. This work was supported by Hokkaido University and Helmholtz-Zentrum Dresden-Rossendorf.

Reference

[1] H. Utsunomiya *et al.*, Nucl. Phys. **A738**, 136 (2004).
[2] http://pceet075.cern.ch/ (The n_TOF Collaboration).
[3] http://j-parc.jp/MatLife/en/index.html (J-PARC Material and Life Science Facility).
[4] B. Singh, Nucl. Data Sheets **70**, 437 (1993).
[5] N. Klay and F. Kaeppeler, Phys. Rev. C **38**, 295 (1998).
[6] G. Walter *et al.*, Astron. Astrophys. **155**, 247 (1986).
[7] G. Walter *et al.*, Astron. Astrophys. **167**, 186 (1986).
[8] F. Kaeppeler *et al.*, Rep. Prog. Phys. **52**, 945 (1989).
[9] A. Makinaga *et al.*, Phys. Rev. **C79**, 025801 (2009).
[10] F. Kitatani *et al.*, J. Nucl. Sci. Technol. (Tokyo) **47**, 367 (2010).
[11] A. J. Koning *et al.*, AIP Conf. Proc. **769**, 1154 (2005).
[12] S. Ebata *et al.*, Pyhs. Rev. **C82**, 034306 (2010).
[13] G. Rusev *et al.*, Phys. Rev. **C 77**, 064321 (2008).
[14] R. Schwengner *et al.*, Phys. Rev. **C 81**, 054315 (2010).
[15] A. Makinaga *et al.*, Phys. Rev. **C 82**, 024314 (2010).
[16] R. Schwengner *et al.*, Phys. Rev. **C 76**, 034321 (2007).
[17] R. Schwengner *et al.*, Phys. Rev. **C 87**, 024306 (2013).
[18] R. Massarczyk *et al.*, Phys. Rev. **C 86**, 014319 (2012).
[19] G. Schramm *et al.*, Phys. Rev. **C 85**, 014311 (2012).
[20] R. Schwengner *et al.*, Nucl.Instr.Meth. **A555**, 211 (2005).
[21] T. von Egidy and D. Bucurescu, Phys. Rev. C **72**, 044311 (2005).
[22] http://www-nds.iaea/RIPL2/.
[23] G. Rusev, PhD dissertation, Technische Universität Dresden, 2007 (Wissenschaftlich-Technische Berichte, FZD-478, 2007); https://www.fzd.de/publications/010008.pdf.
[24] P. Axel, Phys. Rev. **126**, 671 (1962).
[25] R. Bergere *et al.*, Nucl. Phys. **A 121**, 463 (1968).
[26] S. G. Kadmenskii *et al.*, Sov. J. Nucl. Phys. **37**, 165 (1983).
[27] J. Kopecky *et al.*, Phys. Rev. **C 41**, 1941 (1990).
[28] S. Goriely, Phys. Lett. **B 436**, 10 (1998).
[29] A. Bulgac *et al.*, Phys. Rev. C84, 051309 (2011).
[30] Y. Hashimoto, Eur. Phys. J. **A 48**, 55 (2012).

18. Analysis of Tritium Production from Nucleon-induced Reactions on ^{7}Li and its Application to Nuclear Data Evaluation

Kohei Nagaoka, Hairui Guo, Yukinobu Watanabe
Department of Advanced Energy Engineering Science, Kyushu University
Kasuga, Fukuoka 816-8580, Japan
e-mail: nagaoka@aees.kyushu-u.ac.jp

Double-differential cross sections (DDXs) of ^{7}Li(p,t) and ^{7}Li(n,t) reactions are calculated with a sequential decay model and a final state interaction (FSI) model in the incident energy range below 20 MeV. The calculated DDXs of the ^{7}Li(n,t) reaction are integrated to JENDL-4.0 which includes no triton production DDXs. The integrated nuclear data are applied to simulation of triton transport in Li_2TiO_3 that is one of candidate materials for fusion reactor blanket using PHITS code. The effect of triton production DDXs on transport calculations is investigated.

1. Introduction

Double-differential cross section (DDX) data of the ^{7}Li(n,t) reaction are important to engineering design of DT fusion reactors and International Fusion Material Irradiation Facility (IFMIF). However, only an experimental result (DDX at 0° and 14.4 MeV [1]) is available for the reaction, and the DDX data are not included in any evaluated nuclear data libraries, e.g. JENDL-4.0 [2] and FENDL-3 [3]. Under the situation, triton transport in blanket materials has not so far been taken into account properly in engineering design for DT fusion reactors. Therefore, it is worthwhile to investigate the effect of rigorous triton transport on estimation of final tritium production by using evaluated nuclear data of ^{7}Li including triton production DDXs. In the present work, we make an evaluation of triton DDXs for ^{7}Li on the base of theoretical model calculation and apply them to transport calculations of tritons in fusion reactor blanket using PHITS code [4].

2. DDX calculation

The final state of nucleon-induced reactions on ^{7}Li is expected to be a three-body system, when ^{7}Li is assumed as $t + \alpha$ cluster. Therefore, the following two reaction channels should be considered in nucleon-induced triton production:

(a) $n(p) + {}^7\mathrm{Li} \rightarrow t + {}^5\mathrm{He}({}^5\mathrm{Li}) \rightarrow n(p) + t + \alpha$,

(b) $n(p) + {}^7\mathrm{Li} \rightarrow n(p) + {}^7\mathrm{Li}^* \rightarrow n(p) + t + \alpha$.

Here n and p denote neutron and proton, respectively. The triton energy spectra have a characteristic peak formed by the reaction (a) in the high emission energy end. Although any available calculation codes, such as CCONE [5] and TALYS [6], cannot reproduce the peak satisfactorily, the final state interaction (FSI) model [7] can reproduce the peak structure. Thus, the FSI model is used for the reaction (a). The FSI formula is expressed as

$$\left(\frac{d^2\sigma}{dE_t d\Omega_t}\right)_{\text{FSI}} = N_F \cdot \sin^2\beta_l \cdot \frac{F_l^2(k_{N\alpha}a) + G_l^2(k_{N\alpha}a)}{(k_{N\alpha}a)^2} \cdot \rho_t\left(E_t^{\text{lab}}\right), \tag{1}$$

where N_F is a normalization factor which is determined by fitting to experimental data, β_l is the phase shift between α and $n(p)$, l is the orbital angular momentum, F_l and G_l are the Coulomb wave functions, $k_{N\alpha}$ is the relative momentum between $n(p)$ and α, a is the channel radius, ρ_t is the phase space distribution, and E_t^{lab} is the triton energy in laboratory system. As mentioned above, only one experimental (n,t) data exists. Therefore, the angular distribution of reaction (a) for neutron incidence is assumed to be that deduced from the measured data for proton incidence at 14 MeV, regardless of incident energy. The normalization of the cross section for reaction (a) is made so that total triton production cross section is equal to that of JENDL-4.0. As a result, the relationship of tritium production cross sections and angular distributions of the reaction (a) for neutron incidence are given by

$$\sigma_{nt}^{\text{FSI}}(E_t^{\text{lab}}) = \sigma_{nt}^{\text{J40}}(E_t^{\text{lab}}) - \sigma_{nt}^{\text{seq}}(E_t^{\text{lab}}), \tag{2a}$$

$$\frac{d\sigma_{nt}^{\text{FSI}}(E_t^{\text{lab}})}{d\Omega_t} = \frac{\sigma_{nt}^{\text{FSI}}(E_t^{\text{lab}})}{\sigma_{pt}^{\text{FSI}}(14\text{ MeV})} \cdot \frac{d\sigma_{pt}^{\text{FSI}}(14\text{ MeV})}{d\Omega_t}, \tag{2b}$$

where $\sigma_{nt}^{\text{FSI}}(E_t^{\text{lab}})$ is the cross section of reaction (a) for neutron incidence, $\sigma_{nt}^{\text{J40}}(E_t^{\text{lab}})$ is the triton production cross section of JENDL-4.0, $\sigma_{nt}^{\text{seq}}(E_t^{\text{lab}})$ is the cross section of reaction (b) for neutron incidence and $\sigma_{pt}^{\text{FSI}}(14\text{ MeV})$ is the cross section of reaction (a) for proton incidence at 14 MeV. N_F in Eq. (1) is determined so that energy integration of Eq. (1) is equal to Eq. (2b).

On the other hand, the sequential decay model [8] based on kinematics is applied for the reaction (b). In the sequential decay calculation, the nucleon production DDXs calculated by CDCC method [9,10] are used. The DDX formula of the sequential decay model is expressed as

$$\left(\frac{d^2\sigma}{dE_t d\Omega_t}\right)_{\text{seq}}^{J^\pi} = \sum_i \frac{\sigma_i^{J^\pi}}{2\pi} \int L_1(E_N \to E_{\text{Li}}) L_2(E_{\text{Li}} \to E_t) \Lambda(\mu_{Nt}) dE_{\text{Li}}, \tag{3}$$

where J^π corresponds to unbound states of ^{7}Li ($J^\pi = 1/2^-, 3/2^-, 5/2^-, 7/2^-$), $\sigma_i^{J^\pi}$ is the nucleon production DDX from the i th discretized state of ^{7}Li which is calculated by the CDCC method as shown in **Fig. 1**, L_1 is the probability that a nucleon with energy E_N will produce a ^{7}Li nucleus with energy between E_{Li} and $E_{\text{Li}} + dE_{\text{Li}}$, L_2 is the probability that a ^{7}Li nucleus with energy E_{Li} will produce a triton with energy between E_t and $E_t + dE_t$, and $\Lambda(\mu_{Nt})$ is the probability of the cosine of the angle between the direction of incident nucleon and emitted triton being μ_{Nt}.

Finally, total triton production DDXs have been calculated as the sum of reaction (a) and reaction (b) for all of the unbound states of ^{7}Li:

$$\left(\frac{d^2\sigma}{dE_t d\Omega_t}\right) = \left(\frac{d^2\sigma}{dE_t d\Omega_t}\right)_{\text{FSI}} + \sum_{J^\pi} \left(\frac{d^2\sigma}{dE_t d\Omega_t}\right)_{\text{seq}}^{J^\pi}. \tag{4}$$

The calculation results are shown in **Fig. 2**. The calculated triton DDXs reproduce

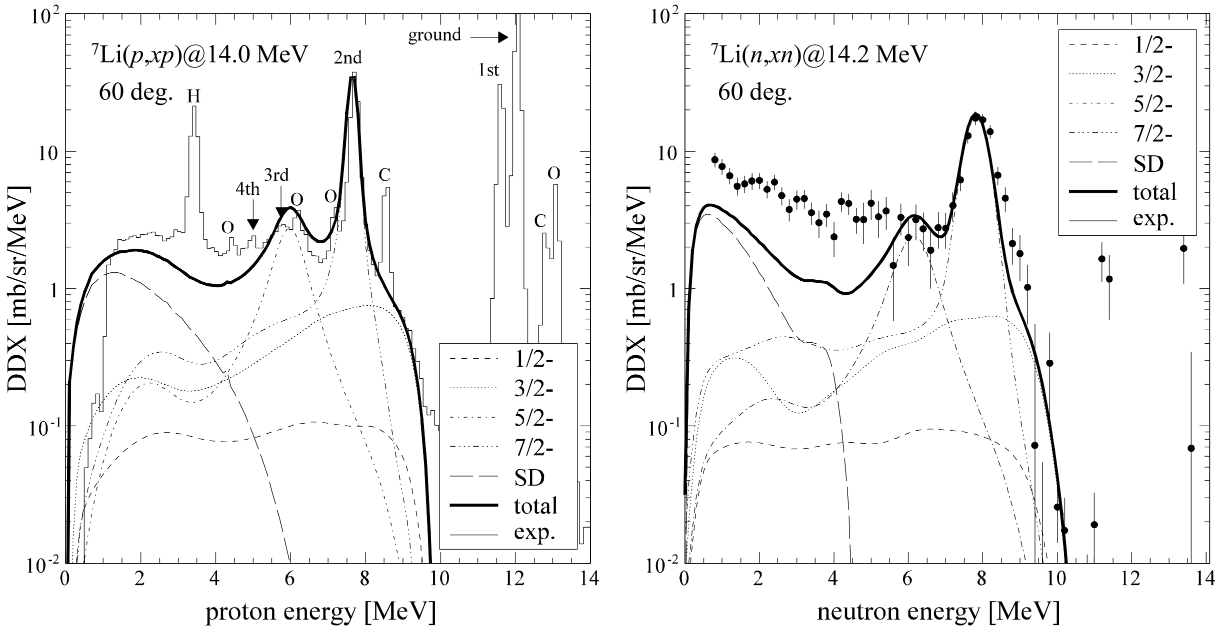

Fig. 1 The nucleon production DDX calculated by CDCC method compared with experimental data [11,12] in the laboratory system. The elastic scattering and 1st inelastic scattering components are not included in these results because these components have no relation to triton production channels. The left figure presents the result of proton DDX at 14.0 MeV and 60 degrees. The right figure presents the result of neutron DDX at 14.2 MeV and 60 degrees. The dashed lines denote the contributions corresponding to unbound states of ^{7}Li and sequential decay from ^{5}Li or ^{5}He. The bold solid line denotes the sum of dashed lines. Underestimation in low energy regions is probably due to other reaction channels such as (*n*,2*n*) or (*n*,*np*).

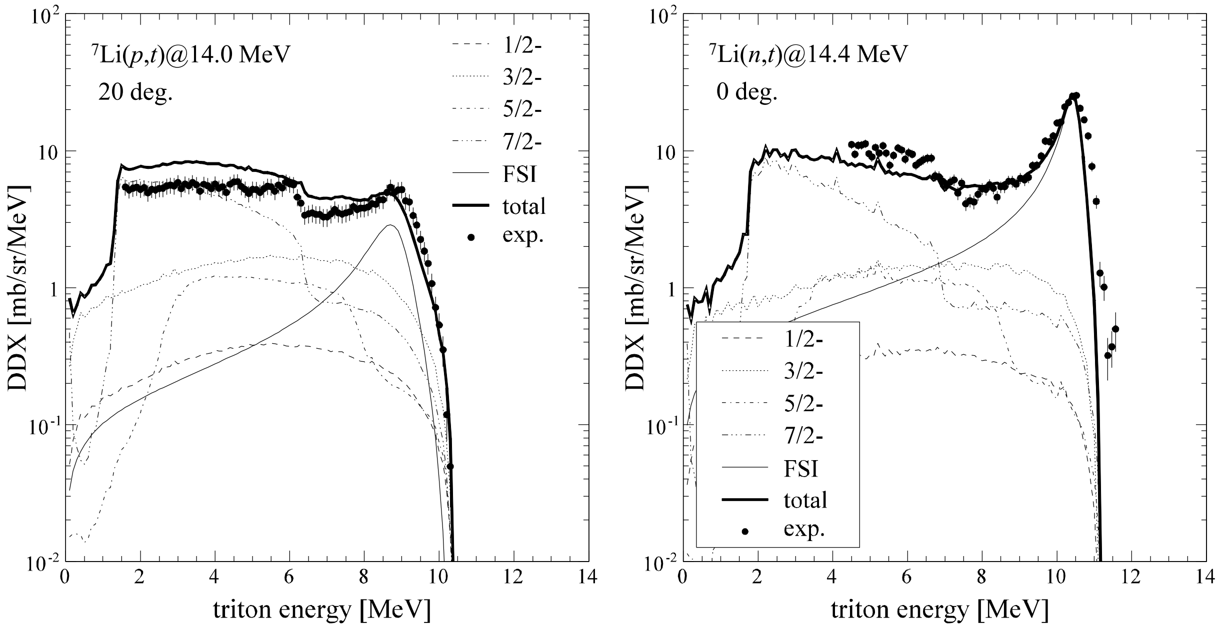

Fig. 2 The triton production DDX calculated by sequential decay and FSI model compared with experimental data [13,1] in the laboratory system. The left figure presents the result of proton-induced reaction at 14.0 MeV and 20 degrees. Uncertainties of this reaction include combined statistical and systematic errors. The right figure presents the result of neutron-induced reaction at 14.4 MeV and 0 degree. The dashed lines denote the contributions corresponding to unbound states of ^{7}Li calculated by the sequential decay model and thread solid line denotes the contribution calculated by FSI model. The bold solid line denotes the sum of sequential decay and FSI results.

reasonably well both experimental results for proton induced reaction at 14 MeV [13] and for neutron induced reaction at 14.4 MeV [1], especially the broad peaks around the high-energy end.

3. Nuclear data preparation and transport calculation

The obtained DDXs for the ^{7}Li(n,t) reaction below 20 MeV are integrated into the ENDF file of JENDL-4.0, and the ACE file is generated from the ENDF file by using NJOY99.364 [14] with patch for JENDL/HE [15]. Then, the present nuclear data are applied to transport calculations of triton generated in blanket material for fusion reactors using PHITS code. The result is compared with that calculated by event generator mode (e-mode) with the original JENDL-4.0. In the simulation geometry, a Li_2TiO_3 sphere 0.5mm in diameter is irradiated by a uniform mono-energetic neutron source from the left side as shown in **Fig. 3**. It is assumed that the abundance ratio of ^{7}Li is 100 % and the theoretical density (3.43 g/cm^3) is used in the present simulation. The energy distribution of leaked tritons and the leakage fraction are predicted for four neutron energies of 5.0, 10.0, 14.1 and 20.0 MeV.

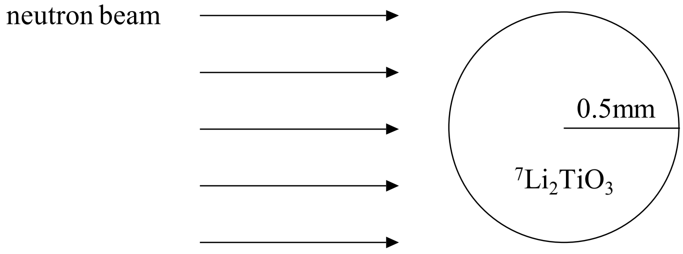

Fig. 3 Schematic view of simulation geometry for triton transport in a Li_2TiO_3 sphere in blanket module.

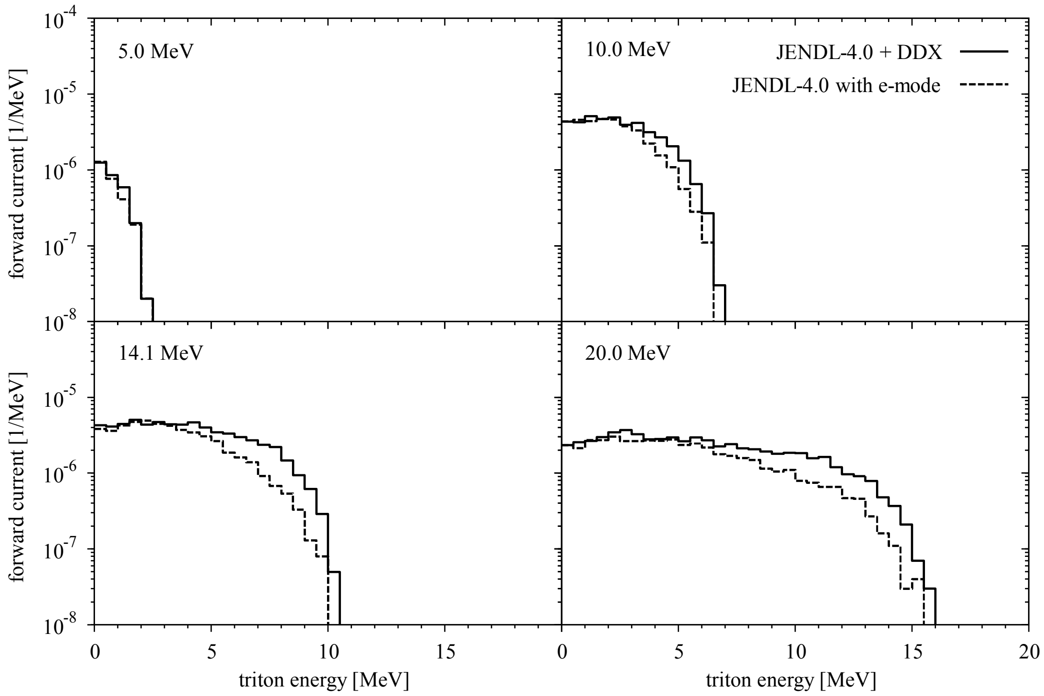

Fig. 4 Comparison of the forward currents of leaked tritons calculated by PHITS code in the laboratory system. The solid lines denote the results with the present nuclear data and the dashed lines denote the results calculated by event generator mode with JENDL-4.0.

The results are shown in **Figs. 4** and **5**. The results calculated with the present nuclear data are larger than those calculated by e-mode with JENDL-4.0, and the difference becomes larger as the neutron energy becomes higher. This is because that the DDX calculated by e-mode have no broad peak around 10 MeV which corresponds to triton emission via the reaction process (a) and does not reproduce the peak well, as shown in **Fig. 6**. It is found that the improvement of nuclear data affects obviously the simulation results of triton transport in matter.

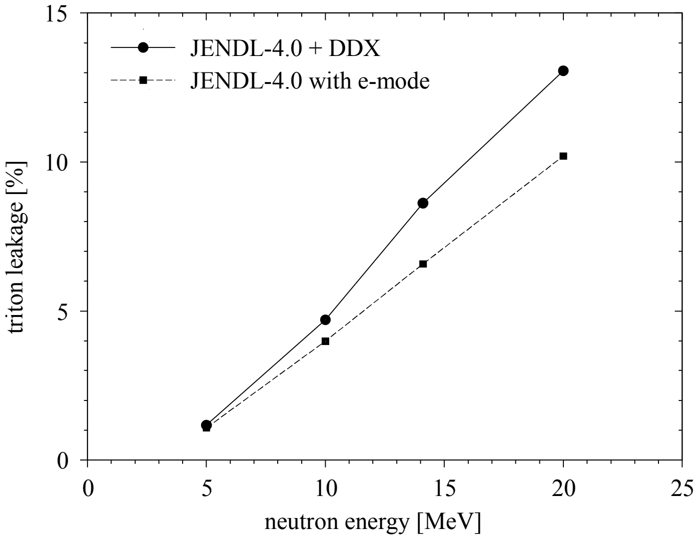

Fig. 5 Comparison of the triton leakage, namely the ratio of the number of leaked tritons and produced tritons, which is calculated by PHITS code. The solid line denotes the result using the present nuclear data with triton DDXs and the dashed line denotes the result using e-mode with the original JENDL-4.0.

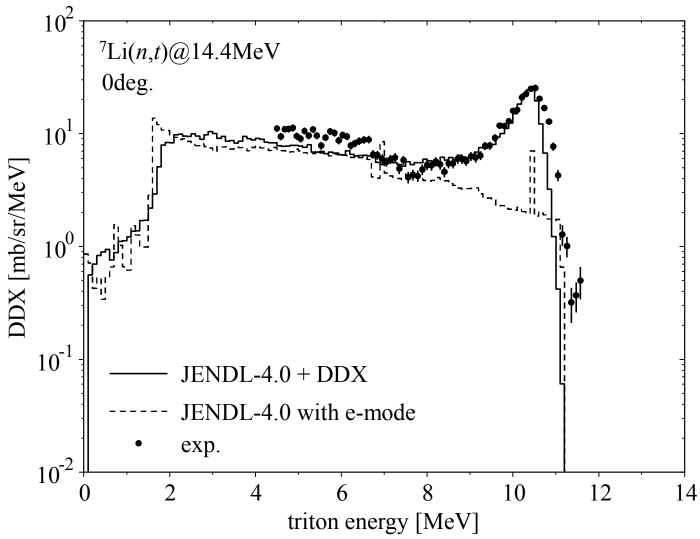

Fig. 6 The triton production DDX calculated by PHITS code compared with experimental data for n + ^{7}Li reaction at 14.4 MeV and 0 degree in the laboratory system. The solid line denotes the result of present nuclear data and the dashed line denotes the result of event generator mode with JENDL-4.0.

4. Conclusion

The calculation method of DDXs is proposed for triton production in nucleon-induced reactions on ^{7}Li by combination of the sequential decay model and the FSI model. The obtained DDXs of the ^{7}Li(n,t) reaction are integrated into the ENDF file of JENDL-4.0, and the ACE file is generated by NJOY. Furthermore, the transport calculations by PHITS code with the present nuclear data reveals that the improvement of nuclear data affects the simulation results of triton transport in matter. Upon request of IFMIF design, the incident energy range of nuclear data should be expanded up to 50 MeV and the impact of triton DDXs on tritium transport in liquid Li target will be studied in the future.

Acknowledgment

The authors would like to thank K. Kosako for useful information about NJOY.

References

[1] Valkovic V. Triton spectrum from the n+^{7}Li reaction. Nucl. Phys. 1964; 60: 581-587.
[2] Shibata K, Iwamoto O, Nakagawa T, Iwamoto N, Ichihara A, Kunieda S, Chiba S, Furutaka K, Otuka N, Ohsawa T, Murata T, Matsunobu H, Zukeran A, Kamada S, Katakura J. JENDL-4.0: A New Library for Nuclear Science and Engineering. J. Nucl. Sci. Technol. 2011; 48(1): 1-30.
[3] Forrest R, Capote R, Otsuka N, Kawano T, Koning AJ, Kunieda S, Sublet J-Ch, Watanabe Y. FENDL-3 Library Summary documentation. Vienna: International Atomic Energy Agency, Nuclear Data Section; 2012. (INDC(NDS)-0628).
[4] Sato T, Niita K, Hashimoto S, Iwamoto Y, Noda S, Ogawa T, Iwase H, Nakashima H, Fukahori T, Okumura K, Kai T, Chiba S, Furuta T, Sihver L. Particle and Heavy Ion Transport Code System PHITS, Version 2.52. J. Nucl. Sci. Technol. 2013; 50(9): 913-923.
[5] Iwamoto O. Development of a Comprehensive Code for Nuclear Data Evaluation, CCONE, and Validation Using Neutron-Induced Cross Sections for Uranium Isotopes. J. Nucl. Sci. Technol. 2007; 44(5), 687-697.
[6] Koning AJ, Hilaire S, Duijvestijn MC, TALYS-1.0. In: Bersillon O, Gunsing F, Bauge E, Jacqmin R, Leray S, editors. Proceedings of International Conference on Nuclear Data for Science and Technology; 2007 April 22-27; Nice (France): EDP sciences; c2008. pp. 211-214.
[7] Rausch T, Zell H, Wallenwein D. Final-state interactions and quasi-free scattering in the ^{2}H(α, pα)n reaction. Nucl. Phys. A. 1974; 222: 429-444.
[8] Beynon TD, Oastler AJ. Kinetics modelling for three-body sequential reactions with applications to ^{7}Li(n,n')αT. Ann. Nucl. Energy. 1979; 6: 537-547.
[9] Yahiro M, Ogata K, Matsumoto T, Minomo K. The continuum discretized coupled-channels method and its applications. Prog. Theor. Exp. Phys. 2012; 01A206: 1-44, and references therein.
[10] Matsumoto T, Ichinkhorloo D, Hrabayashi Y, Katō K, Chiba S. Systematic description of the ^{6}Li(n,n')→d+α reactions with microscopic coupled-channels method. Phys. Rev. C. 2011; 83: 064611.
[11] Koori N, Kumabe I, Hyakutake M, Orito K, Akagi K, Iida A, Watanabe Y, Sagara K, Nakamura H, Maeda K, Nakashima T, Kamimura M, Sakuragi Y. Polarized proton scattering on lithium isotopes at 14 MeV. Japan Atomic Energy Research Institute; 1989 Nov. (JAERI-M 89-167).
[12] Chiba S, Baba M, Nakashima H, Ono M, Yabuta N, Yukinori S, Hirakawa N. Double-Differential Neutron Emission Cross Sections of ^{6}Li and ^{7}Li at Incident Neutron Energies of 4.2, 5.4, 6.0 and 14.2 MeV. J. Nucl. Sci. Technol. 1985; 22(10): 771-787.
[13] Koori N, Kumabe I, Hyakutake M, Watanabe Y, Orito K, Akagi K, Iida A, Eriguchi M, Wakuta Y, Sagara K, Nakamura H, Maeda K, Nakashima T. Polarized proton induced reactions on lithium isotopes around 14 MeV. Japan Atomic Energy Research Institute; 1991 Feb. (JAERI-M 91-009).
[14] MacFarlane RE, Muir DW. The NJOY nuclear data processing system. Version 91, Los Alamos National Laboratory; 1994. (LA-12740-M).
[15] Watanabe Y, Kosako K, Kunieda S, Chiba S, Fujimoto R, Harada H, Kawai M, Maekawa F, Murata T, Nakashima H, Niita K, Shigyo N, Shimakawa S, Yamano N, Fukahori T. Status of JENDL High Energy File. J. Kor. Phys. Soc. 2011; 59(2): 1040-1045.

19. Theoretical Study of Beta Decay for Delayed Neutron and Decay Heat

Hiroyuki Koura[1)], Satoshi Chiba[2)]

[1)]Advanced Science Research Center, Japan Atomic Energy Agency, Tokai, Ibaraki 319-1195, Japan

[2)]Research Laboratory for Nuclear Reactors, Tokyo Institute of Technology, 2-12-1, Ookayama, Meguro-ku, Tokyo 152-8550, Japan

e-mail: koura.hiroyuki@jaea.go.jp

Abstract:

Theoretical calculation of beta decay for delayed neutron and decay heat is studied. The number of averaged delayed neutron emission is estimated from the idea of the summation method, in which the number of emitted neutron is expressed as the sum of each beta-delayed neutron emission probability multiplied by the cumulative fission yield. Under the consideration of the gross theory of the beta decay, current status for reproduction of the beta decay rate, delayed neutron probability, and decay heat is studied.

1. Introduction

Delayed neutron plays an important role on nuclear reactor to be manipulated safely due to duration of the delay from neutron-induced fission. The number of averaged delayed neutron emission, $\overline{\nu_d}$, comes from the sum of delayed neutron probabilities of nuclei on fission products multiplied by the cumulative fission yield from fissioning nuclei. Therefore estimation of delayed neutron probabilities of all corresponding nuclei is required to understand the mechanism of the delayed neutron as an accumulation of nuclear decays. In experiment, however, those of some nuclei have not been measured and many of nuclei have large ambiguities. Furthermore, if we apply the nuclear energy from fission events to more innovative nuclear reactors as high burn-up reactors, in which minor actinides can contribute to accumulating decay processes, we need more data which are unmeasured or less known. In the other hand, nuclear decay heat occurs during beta decay of fission fragments, and estimation of these absolute values and property of time-dependency is inevitable to control the reactors. Both of delayed neutron and decay heat are accompanied phenomena of the beta decay. Theoretical study in view of the beta decay is therefore required in order to understand and estimate them. In this report, we will discuss the delayed neutron as an accompanied process of the beta decay in the nuclear theory.

In section 2, we will show the idea of summation method of delayed neutron and present the current status of this method. The theory of the beta decay will be shown in section 3. Some results and discussion will be devoted in section 4.

2. Theory of the beta decay

The decay rate of the beta decay is obtained as the sum of partial decay rates. Under the usual approximation, each decay rate can be written with the nuclear matrix elements, $|M_\Omega(E)|$, which can be calculated in the framework of the nuclear physics, and the integrated Fermi function, f, which represents a distortion of wave functions due to the Coulomb force. In the case if the Gamow-Teller type transition, which is generally dominant in the medium-heavy and neutron-rich nuclear mass region, the beta-decay rate is expressed as [1]

$$\lambda_{\mathrm{GT}} = \frac{m_e{}^5 c^4}{2\pi^3 \hbar^7} |g_{\mathrm{A}}|^2 3 \int_{-Q_\beta}^{0} |M_{\mathrm{GT}}(E)|^2 f(-E) dE. \quad (1)$$

Here, the coefficient is composed of the coupling constant of the weak interaction and the physical constants. The integral is performed from $-Q_\beta$ to 0 and Q_β is the total (maximum) decay energy from the ground state of parent to daughter nuclei, namely beta-decay Q-value.

The delayed neutron is also an accompanied phenomenon of the beta decay. Figure 1 shows a schematic view of the beta decay and delayed neutron. In the beta decay, a nucleus decays from the parent state to the daughter states as shown in the figure. If the neutron separation energies of the daughter nucleus, S_n, is smaller than the β-decay Q-value, Q_β, the nucleus can emit a neutron with energy from 0 to $Q_\beta - S_n$ measured from the ground state of the parent nucleus. The delayed neutron emission probability is calculated by integrating from threshold energy to the ground-state energy of the parent nucleus as

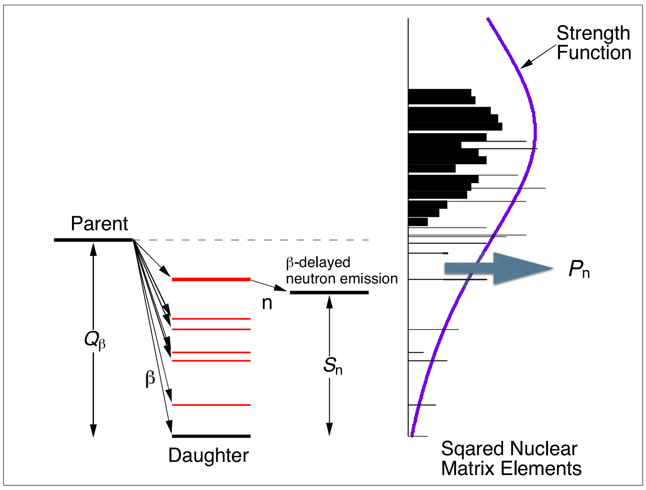

Figure 1: Schematic view of beta decay and delayed neutron

$$P_{\mathrm{n}} = \frac{C}{\lambda}\int_{-Q_\beta - S_{\mathrm{n}}}^{0} |M(E)|^2 f(-E) \frac{\Gamma_{\mathrm{n}}}{\Gamma_{\mathrm{n}}+\Gamma_\gamma} dE, \tag{2}$$

where C is a constant related to the coefficient in Eq. (1). The decay width Γ is introduced to express a decay competition between neutron emission and gamma decay from excited states. Regarding decay heat, the average energies of beta decay and gamma decay are (only expressed for the Gamow-Teller type transition) [2]

$$\overline{E_{\beta}} = \frac{1}{2\pi^3\lambda}|g_{\mathrm{A}}|^2 3 \int_{-Q_\beta}^{0} \left|M_{\mathrm{GT}}(E_g)\right|^2 \int_1^{-E_{\mathrm{g}}+1} mc^2(E-1)pE(-E_{\mathrm{g}}+1-E)^2 F(E) dE\, dE_{\mathrm{g}} \tag{3}$$

$$\overline{E_{\gamma}} = \frac{1}{2\pi^3\lambda}|g_{\mathrm{A}}|^2 3 \int_{-Q_\beta}^{0} \left|M_{\mathrm{GT}}(E_g)\right|^2 mc^2(Q_\beta + E_{\mathrm{g}}) \int_1^{-E_{\mathrm{g}}+1} pE(-E_{\mathrm{g}}+1-E)^2 F(E) dE\, dE_{\mathrm{g}} \tag{4}$$

where F is the Fermi function. As shown in Eqs. (1)-(4), the nuclear matrix elements and the Fermi function are required for theoretical calculation of the β-decay rate, the delayed neutron emission probability, and the decay heat energy. Regarding the integrated Fermi function, the numerical values can be rather easily and precisely obtained [3]. The calculation of the nuclear matrix elements is, however, difficult because of a complexity of the nuclear many body problem with the complicated nuclear force. In order to obtain the nuclear matrix elements overall of nuclei, an approach from the bulk feature of the beta decay has been developed, we refer to it as the gross theory. The gross theory is constructed under a consideration that the sum of strengths of the transition from the initial state to the sum of the final states in the quantum mechanics. The beta decay also obeys such a sum (and an energy-weighted sum) rule.

The gross theory is succeeded in describing the beta decay for entire region of nuclear mass [4,5]. Until recently only the gross theory was enable to apply to the overall calculation including the forbidden transition. Regarding delayed neutron probability in the gross theory, however, parameters and functional form in the theory were optimized to the total decay rate, and have not been fully optimized to the delayed neutron probabilities. Simultaneous optimization might be difficult in general, therefore we give a short discussion on that in the next section. In the following analysis and calculation report, we adopt the gross theory first version [1] with improved pairing correction [6].

3. Analysis of nuclear matrix elements

Calculating of total decay rate and delayed neutron are similar in expression as in Eq. (4) and Eq. (5). In the actual calculation, however, these two have different features due to the different ranges of integrals. To remove the effect of total decay constant from delayed neutron, we define the following quantity:

$P_n/\lambda_\beta = P_{n0} \sim \int_{-Q+S_n}^{0} |M(E)|^2 f(-E) dE$ (5)

Furthermore, the decomposition of the decay constants, dλ, can be defined as

$\lambda_\beta = \int_{-Q_\beta}^{0} d\lambda$ (9)

Figure 2 shows an example of the decomposition in the case of ^{145}Cs. The top panel shows squared nuclear matrix elements in the logarithmic scale. In the matrix element, first forbidden transition gives larger amount compared with the allowed transition. The middle panel shows component of decay constant in logarithmic scale. Regarding the total decay constant in the case of ^{145}Cs, Gamow-Teller transition is dominant comparing with the other types of transitions. As seen in Figure, the total decay rate proves to be quite sensitive to the ground-state (left side) feature of the nuclear matrix element and is almost governed by the ground state and its neighboring nuclear matrix elements because of these extremely larger values. The pulsed matrix elements represents discrete components due to the eigenstate (and some corrections) of the quantum many body solution. On the other hand, delayed neutron probability is governed by rather higher excited states (ranging from $-S_n$ to 0 in the Figure), and properties of the matrix elements in the energy region seems to have no drastic change comparing to those in neighboring the ground states.

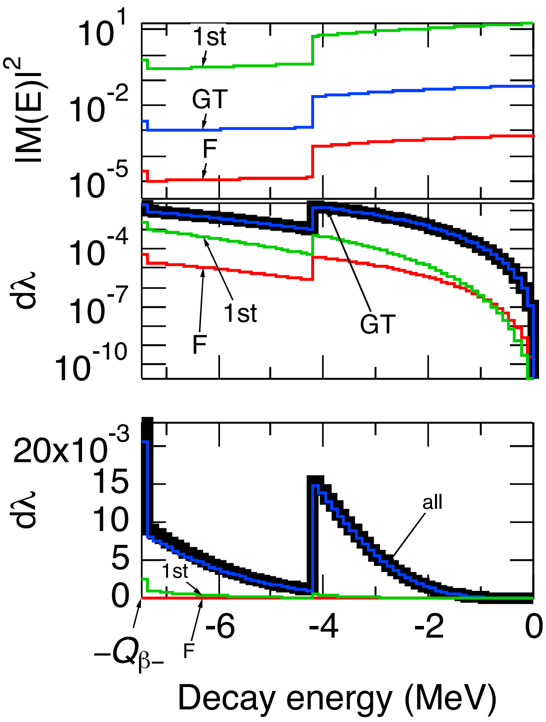

Figure2: Nuclear matrix elements and decomposition of decay rate for ^{145}Cs.

Under these considerations, we survey systematical properties of both of total decay constant and delayed neutron in the nuclear mass region. In the next section we give some results. By considering these systematical properties, we will improve theoretical calculation in the following way. Firstly we survey and improve the one-particle strength function for delayed neutron. Then we modified quantities related to the nuclear shell structure as the nuclear matrix element and the level density in the energy region of the ground state and its neighboring states.

The competition factor between neutron emission and gamma decays appeared in Eq. (5) is treated as unity in the following results. In the method we perform overall calculation in the neutron-rich nuclei for the β-decay rate, λ_β, and delayed neutron probability, P_n.

4. Results and Discussion

Figure 3 (Top) shows the ratio of calculated half-lives to the experimental ones. The root-mean-square (RMS) deviation is 0.70 in log10, which corresponds to 5 times or 1/5 as shown in two dotted lines along the horizontal axis. The ratio diverges in the small Q-values (left side), while it coverges in the large Q-values (right side). The ratio of calculated beta-delayed neutron probabilities to the experimental ones is shown in Figure 3 (Bottom). The RMS deviation is 0.54 in log10, which corresponds to 3.5 times or 1/3.5. Trend of convergence along increase of Q-values is similar to each other, while in the small-Q region there is no large discrepancy for the case of the delayed neutron. The Q-values dependency is rather clear in this plot, however other notable features including the even-odd effect classified in both figures are unclear [7].

Figure 4 (Top) shows the same ratio of T_β in the N-Z plane. There are three underestimated regions located around the $Z = 20$ and $N = 28$, in the $50 < N < 60$ and $28 < Z < 40$, and around the $Z = 82$ and $N = 126$, as emphasized in circles. These regions are related to the nuclear shell closures as 20, 28, 50, 82, of number of neutron and protons. This indicates that a kind of improvement based on the shell structure is rather more important than that of one-particle strength functions because the one-particle strength

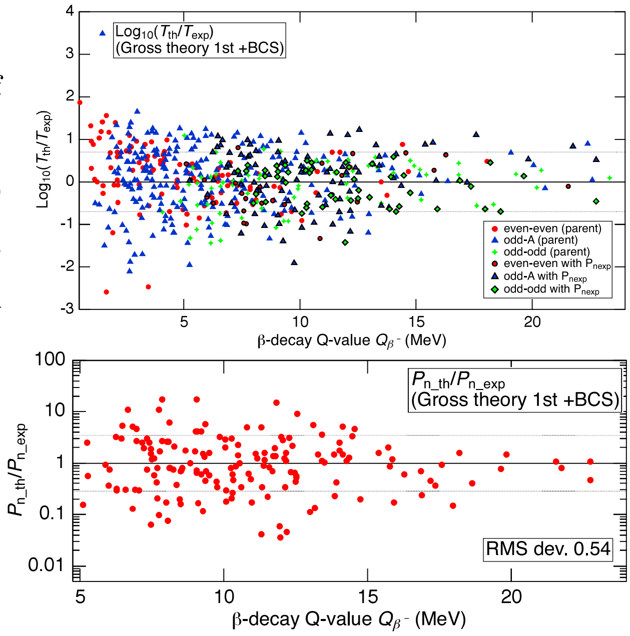

Figure 3: Ratio between experiment and calculation. (Top): Half-lives. (Bottom): Delayed-neutron probabilities.

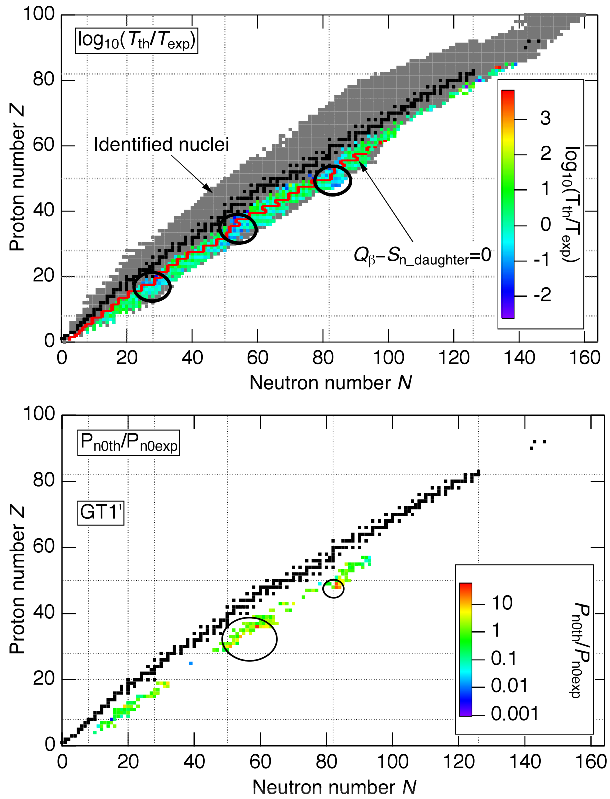

Figure 4: Ratio between experiment and calculation in the N-Z plane. (Top): half-lives. (Bottom): delayed neutron probabilities.

function in the current framework of the gross theory only gives gradual changes against excited energies and proton and neutron numbers of nuclei.

The ratio of P_{n0} defined in Eq. (8) in the N-Z plane is shown in Fig. 4 (Bottom). There are two overestimated regions located in the $30 < Z < 40$ and $50 < N < 70$, and in the $Z < 50$ and $82 < N$, as emphasized in circles. The former region is different from the three regions in the case of T_{β}, and this discrepancy seems to be caused by nuclear collective properties as nuclear deformations, which has not been introduced to the original gross theory without Q-value effects [7]. This information will help for reconstruction of the strength function in the highly excited energy region. The latter region is just after the 'south-east' from the doubly-magic nuclei, ^{132}Sn. This discrepancy cannot be divided easily in the current analysis, and more precise treatment is required.

Acknowledgement

Present study is the results of “Comprehensive study of delayed-neutron yields for accurate evaluation of kinetics of high-burn up reactors” entrusted to Tokyo Institute of Technology by the Ministry of Education, Culture, Sports, Science and Technology of Japan (MEXT).

References

[1] K. Takahashi, M. Yamada and T. Kondoh, Atom. Dat. Nucl. Dat. Tabl. **12**, 101-142 (1973).

[2] T. Yoshida and R. Nakajima, J. Nucl. Sci. Technol. **18**, 393-407 (1981).

[3] N.B. Gove and M.J. Martin, Atom. Dat. Nucl. Dat. Tabl. **10**, 205-219 (1971).

[4] T. Tachibana, M. Yamada and Y. Yoshida, Prog. Theor, Phys. **84**, 641 (1990).

[5] T. Tachibana and M. Yamada, *Proc. Int. Conf. on Exotic Nuclei and Atomic Masses, ENEM95*, (Editions Frontueres, Gif-sur-Yvette, 1995), p.763.

[6] K. Kondoh, T. Tachibana, M. Yamada, Prog. Theor. Phys. **74**, 108 (1985).

[7] H. Koura and S. Chiba, Energy Procedia, in press.

20. Evaluation of Neutron Induced Reaction Cross Sections on Rh Isotopes

Nobuyuki IWAMOTO
Nuclear Data Center, Nuclear Science and Engineering Directorate,
Japan Atomic Energy Agency, Tokai, Ibaraki 319-1195, Japan
e-mail: iwamoto.nobuyuki@jaea.go.jp

Evaluations of neutron nuclear data on ^{101,102,103,105}Rh in the incident energies up to 20 MeV were performed, using theoretical nuclear reaction model code CCONE. The calculated cross sections of stable ^{103}Rh are in good agreement with measured inelastic scattering, capture, $(n,2n)$, (n,p), (n,α) and $(n,n\alpha)$ reaction cross sections. The production cross section for the meta-state of ^{99}Tc with half-life of 6.0 h was evaluated for the estimation of nuclear medicine use and resulted in 2.4 mb at a maximum.

1 Introduction

Natural rhodium (Rh, the atomic number $Z = 45$) consists of one stable isotope ^{103}Rh. This isotope is known to be one of the important fission products: for example, cumulative fission yields are 3% in ^{235}U fission at thermal energy and 6.8% in ^{239}Pu fission at fast energy [1]. Therefore, accurate nuclear data on ^{103}Rh have been requested to assess the nuclear reactor safety and to perform the fuel burnup evaluation for the design of a high-burnup core. In the nuclear medicine point of view, the ^{103}Rh$(n,n\alpha)$ reaction generates ^{99}Tc. The meta-state of this unstable isotope is often used for nuclear diagnosis. The reliable production cross section is needed to evaluate the amount produced by this reaction with fast neutrons which are generated by accelerators.

Neutron nuclear data on Rh isotopes (^{103,105}Rh) are included in JENDL-4.0 (released in 2010) [2]. However, the main revision was made by updating resolved resonance parameters in the development of JENDL-4.0. The original evaluations of data above the resolved resonance region were done at JENDL-3.2 (released in 1994) [3] for inelastic scattering and capture cross sections and at JENDL-3 (released in 1989) for the other reaction cross sections. Two unstable isotopes ^{101}Rh and ^{102}Rh have relatively long half-lives for ground and meta-states. Each of half-lives is 3.3 y and 4.34 d for ^{101}Rh and 207 d and 3.74 y for ^{102}Rh. The nuclear reactions of those unstable isotopes with fast neutrons create Tc isotopes with half-lives much longer than 10^5 y, and thus the activation cross sections of ^{101,102}Rh were also considered to be important. Therefore, new evaluations for ^{103,105}Rh as well as for ^{101,102}Rh were necessary to revise the general purpose and activation files.

The neutron nuclear data on the Rh isotopes were evaluated by theoretical nuclear reaction model code CCONE [4] in the incident energy region between 1 eV and 20 MeV. In this paper the new evaluated results of ^{103}Rh are presented in comparison with available experimental data and major evaluated ones (JENDL-4.0, ENDF/B-VII.1 [5] and JEFF-3.1.2 [6]).

2 Evaluation Methods

The spherical optical model was employed to calculate neutron transmission coefficients of the target isotopes. The parameters of optical model potential (OMP) were taken from Table 1(B) in the ^{103}Rh file of JENDL-4.0. The calculated total cross section is shown in **Fig. 1**, in which total cross sections of JENDL-4.0, ENDF/B-VII.1 and JEFF-3.1.2 are also

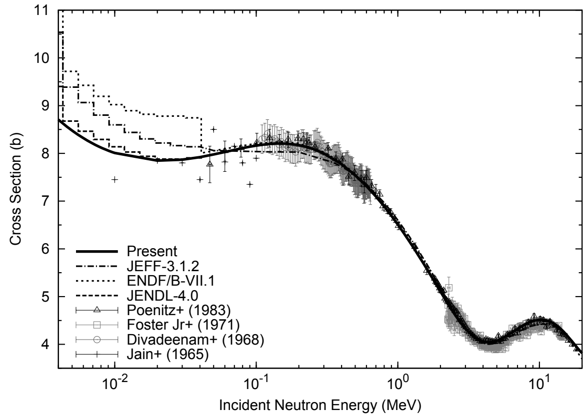

Figure 1: Total cross section with averaged cross sections in the resolved resonance region

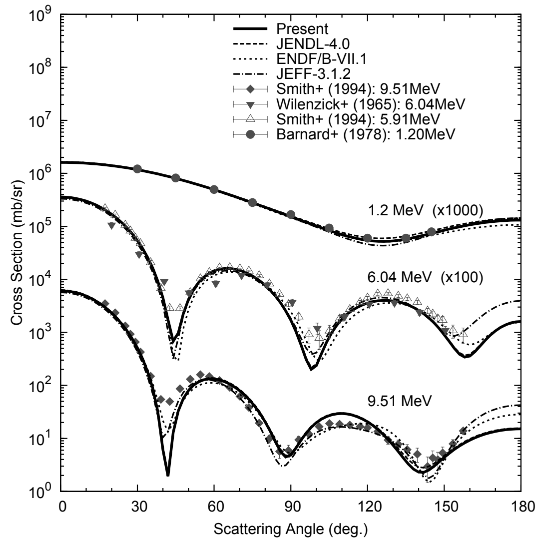

Figure 2: Angular distributions of elastically scattered neutrons

illustrated with averaged cross sections in the resolved resonance region. **Figure 2** represents elastic scattering angular distributions for incident energies of 1.2, 6 and 9.5 MeV. The proton OMP for Rh isotopes was adopted from the global parameters of Koning and Delaroche [7], in which the constant term of diffuseness in real and imaginary volume components was changed into 0.56. The neutron and proton OMPs for the other nuclides were employed from the global ones of Koning and Delaroche. The OMPs for the other particle emissions were taken from Lohr and Haeberli [8] for deuterons, Becchetti and Greenlees [9] for tritons and ^{3}He, and McFadden and Satchler [10] for α-particles.

Reaction cross sections were derived by the nuclear reaction model code CCONE, which is composed of Hauser-Feshbach statistical model, preequilibrium two-component exciton model and distorted wave Born approximation (DWBA) model in addition to the optical model. Information of discrete levels was taken from RIPL-3 database [11]. The number of discrete levels adopted for ^{103}Rh was 40 (the upper limit of excitation energy E_x was 1605 keV) in the present evaluation, although it was only 12 (the upper limit was 920 keV) in JENDL-4.0. It is noted that the 920 keV-level corresponds to the 15th level in the present data. Level density above the discrete levels was adopted from the formulation of Mengoni and Nakajima [12]. The level density parameter a was re-fixed so as to reproduce experimental average level spacings of s-wave resonances [11]. Gamma-ray strength function for E1 transition was represented by standard Lorentzian form with global parameters [13]. The gamma-ray emission channels by M1 and E2 radiations were also included by adopting the systematics of Kopecky and Uhl [14].

3 Evaluated Results

Direct inelastic scattering cross sections were taken into account by DWBA calculations for 6 excited levels, $E_x = 39.8$, 295.0, 357.4, 536.8, 650.1 and 847.6 keV, from the ground-state. The normalization parameters (β_L) together with angular momentum transfer L were selected as $\beta_{L=3} = 0.181$, $\beta_{L=2} = 0.14$, $\beta_{L=2} = 0.155$, $\beta_{L=2} = 0.08$, $\beta_{L=2} = 0.08$ and $\beta_{L=3} = 0.08$, respectively. These parameters were determined so as to reproduce the cross sections of inelastic scattering to each level. The comparisons between measured data and the present results are made in **Figs. 3**, **4** and **5**, in which the cross section of meta-state ($E_x = 39.8$ keV) production and those of inelastic scattering to 295.0 and 357.4 keV-levels, respectively, are illustrated. The

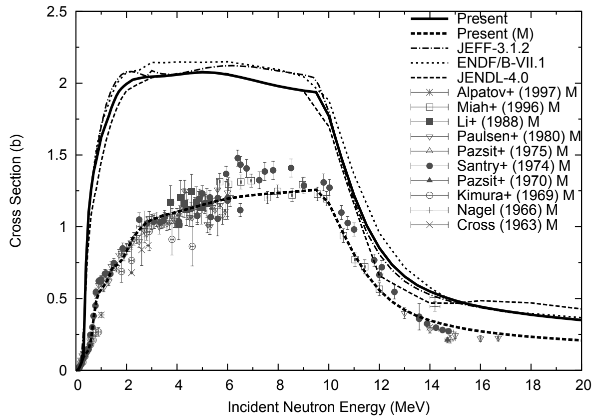

Figure 3: Inelastic scattering cross section. The symbol "M" in the legend indicates the production cross sections for meta-state ($E_x = 39.8$ keV) of ^{103}Rh.

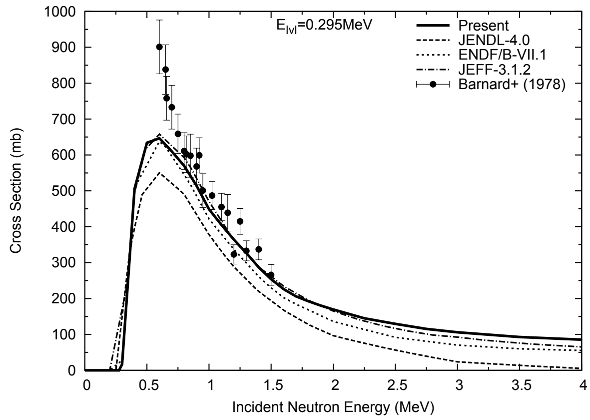

Figure 4: Cross section of inelastic scattering to 295 keV-level

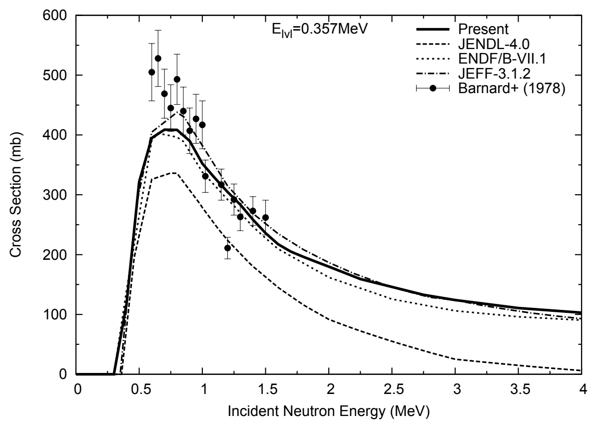

Figure 5: Cross section of inelastic scattering to 357 keV-level

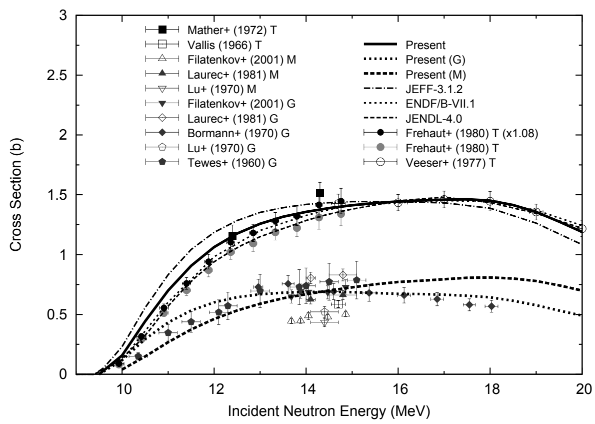

Figure 6: $(n, 2n)$ reaction cross section. The symbols "T", "G" and "M" in the legend indicate the total $(n, 2n)$ reaction cross section and the production cross sections for ground- and meta-states of ^{102}Rh, respectively.

evaluated data are consistent with available experimental data. It is found that JENDL-4.0 gives remarkably smaller cross sections in Figs. 4 and 5.

Figure 6 represents the calculated $(n, 2n)$ reaction cross sections, together with measured and evaluated data. In the evaluation of this reaction we considered the production cross sections of ^{102g}Rh and ^{102m}Rh and their summed (total) cross section. Many cross section measurements have been performed for the ^{103}Rh$(n, 2n)^{102g}$Rh reaction. The present evaluation gives almost consistent result with available data. Especially, the present result agrees with the data of Filatenkov and Chuvaev [15] and Bormann *et al.* [16] at around 14 MeV. On the other hand, for the ^{102m}Rh production reaction measurements are limited due to the relatively long half-life of ^{102m}Rh. If the most up-to-date data of Filatenkov and Chuvaev were chosen to fix the production cross section of ^{102m}Rh, the total $(n, 2n)$ reaction cross sections becomes 1.1-1.2 b at around 14 MeV. These total cross sections are considerably small, compared with the

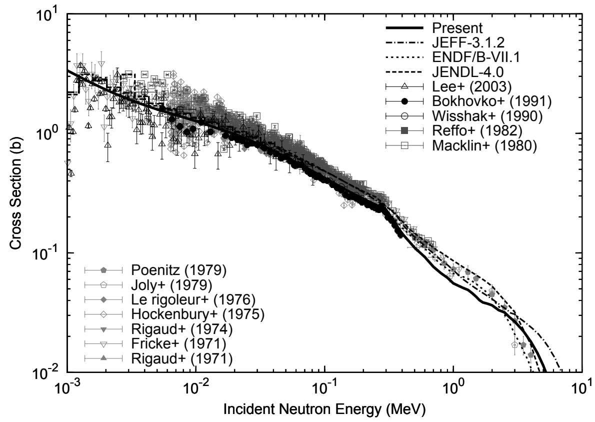

Figure 7: Capture cross section

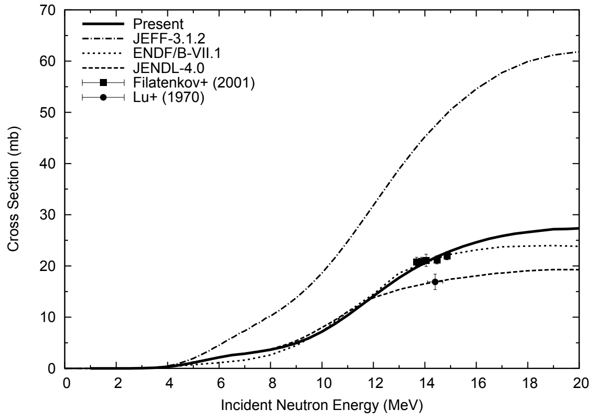

Figure 8: (n, p) reaction cross section

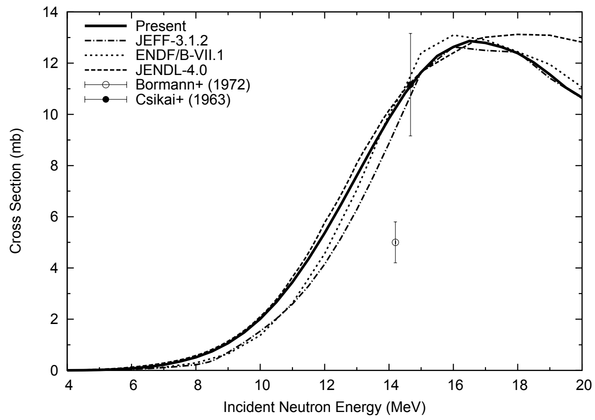

Figure 9: (n, α) reaction cross section

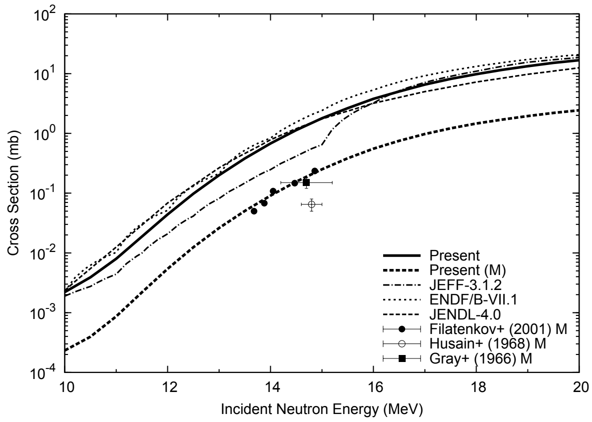

Figure 10: $(n, n\alpha)$ reaction cross section. The symbol "M" in the legend indicates the production cross sections for meta-state (E_x = 142.7 keV) of ^{99}Tc.

data reported by Frehaut *et al.* [17] and Veeser *et al.* [18]. Therefore, the measured data of Filatenkov and Chuvaev could not be used for the evaluation of ^{103}Rh$(n, 2n)^{102m}$Rh reaction cross section. The resulting cross section of ^{102m}Rh production is almost comparable to that of ^{102g}Rh production at around 14 MeV. It should be noted that the data of Frehaut *et al.* were multiplied by 1.08, following the suggestion by Vonach *et al.* [19]. The present evaluation obtains the total $(n, 2n)$ reaction cross section almost consistent with the measured data from the threshold energy to 20 MeV.

The capture cross sections are illustrated in **Fig. 7**. The measured data of Macklin and Halperin [20] are larger than the recent ones of Lee *et al.* [21], Bokhovko *et al.* [22] and Wisshak *et al.* [23]. The present evaluation was carried out to reproduce the latter data, and thus the calculated result has smaller cross sections than those of JENDL-4.0 and JEFF-3.1.2. The calculated excitation function is in good agreement with the data of Bokhovko *et al.* in the energy region where the channel of inelastic scattering to the third excited level ($E_x = 295$ keV) opens. **Figure 8** compares the (n, p) reaction cross sections. The present calculation was fitted to the updated data of Filatenkov and Chuvaev with the modified OMP for proton emission as mentioned above. JENDL-4.0 has a smaller cross section above 12 MeV, since the data of Lu *et al.* [24] were the only ones at the original evaluation in JENDL-3. It is found that JEFF-3.1.2

provides factors of 2 larger cross section without considering the recent measurement. The (n,α) reaction cross sections are represented in **Fig. 9**. The present result as well as all the evaluated data is consistent with the data of Csikai *et al.* [25] and has similar excitation functions each other. **Figure 10** shows the obtained $(n,n\alpha)$ reaction cross sections in comparison with JENDL-4.0, ENDF/B-VII.1 and JEFF-3.1.2. This reaction produces long-lived fission product ^{99}Tc. The measurements only provided the production cross sections for meta-state ($E_x = 142.7$ keV) of ^{99}Tc with half-life of 6.0 h. The present result fitted by enhancing pick-up and knock-out contributions is in good agreement with the up-to-date data of Filatenkov and Chuvaev. The evaluated production cross section of ^{99m}Tc results in 0.09 mb at 14 MeV and 2.4 mb at 20 MeV. The obtained total $(n,n\alpha)$ reaction cross section does not show large differences from the evaluated data, except for the cross section below 16 MeV in JEFF-3.1.2.

4 Conclusion

Evaluations of neutron nuclear data on Rh isotopes (^{101,102,103,105}Rh) in the incident energies from 1 eV to 20 MeV were performed, using the nuclear reaction model code CCONE. The calculated results for ^{103}Rh, the only stable isotope of Rh, well reproduce the available experimental data of inelastic scattering, capture, $(n,2n)$, (n,p), (n,α) and $(n,n\alpha)$ reactions. Especially, the cross sections of inelastic scattering to low-lying excited levels are improved by applying the DWBA model, while those are underestimated in JENDL-4.0. The production cross section of ^{99m}Tc, which is important for nuclear medicine use, is carefully evaluated to estimate the produced amount of ^{99m}Tc by accelerator neutrons. The present data for Rh isotopes will be opened as a part of new general purpose and activation cross section files.

Acknowledgments

This work was supported by JSPS KAKENHI Grant Number 23602015.

References

[1] Katakura J. JENDL FP Decay Data File 2011 and Fission Yields Data File 2011. Japan: Japan Atomic Energy Agency; 2012, JAEA-Data/Code 2011-025.

[2] Shibata K, Iwamoto O, Nakagawa T, Iwamoto N, Ichihara A, Kunieda S, Chiba S, Furutaka K, Otuka N, Ohsawa T, Murata T, Matsunobu H, Zukeran A, Kamada S, Katakura J. JENDL-4.0: A New Library for Nuclear Science and Engineering. J. Nucl. Sci. Technol. 2010; 48:1-30.

[3] Nakagawa T, Shibata K, Chiba S, Fukahori T, Nakajima Y, Kikuchi Y, Kawano T, Kanda Y, Ohsawa T, Matsunobu H, Kawai M, Zukeran A, Watanabe T, Igarasi S, Kosako K, Asami T. Japanese evaluated nuclear data library, version 3 revision-2; JENDL-3.2. J. Nucl. Sci. Technol. 1995;32:1259-1271.

[4] Iwamoto O. Development of a Comprehensive Code for Nuclear Data Evaluation, CCONE, and Validation Using Neutron-Induced Cross Sections for Uranium Isotopes. J. Nucl. Sci., Technol. 2007;44:687-697.

[5] Chadwick MB, Herman M, Obložinský P, Dunn ME, Danon Y, Kahler AC, Smith DL, Pritychenko B, Arbanas G, Arcilla R, Brewer R, Brown DA, Capote R, Carlson AD, Cho YS, Derrien H, Guber K, Hale GM, Hoblit S, Holloway S, Johnson TD, Kawano T, Kiedrowski BC, Kim H, Kunieda S, Larson NM, Leal L, Lestone JP, Little RC, McCutchan EA, MacFarlane RE, MacInnes M, Mattoon CM, McKnight RD, Mughabghab SF, Nobre GPA, Palmiotti G, Palumbo A, Pigni MT, Pronyaev VG, Sayer RO, Sonzogni AA, Summers

NC, Talou P, Thompson IJ, Trkov A, Vogt RL, van der Marck SC, Wallner A, White MC, Wiarda D, Young PG. ENDF/B-VII.1 Nuclear Data for Science and Technology: Cross Sections, Covariances, Fission Product Yields and Decay Data. Nucl. Data Sheets. 2011;112:2887-2996.

[6] JEFF project. 2012. Available from: http://www.oecd-nea.org/dbdata/jeff/.

[7] Koning A, Delaroche JP. Local and global nucleon optical models from 1 keV to 200 MeV. Nucl. Phys. 2003;A713:231-310.

[8] Lohr JM, Haeberli W. Elastic scattering of 9-13 MeV vector polarized deuterons. Nucl. Phys. 1974:A232;381-397.

[9] Becchetti Jr. FD, Greenlees GW. Polarization Phenomena in Nuclear Reactions. Univ. of Wisconsin Press; 1971. p. 682.

[10] McFadden L, Satchler GR. Optical-model analysis of the scattering of 24.7 MeV alpha particles. Nucl. Phys. 1966;84:177-200.

[11] Capote R, Herman M, Oblozinsky P, Young PG, Goriely S, Belgya T, Ignatyuk AV, Koning AJ, Hilaire S, Plujko VA, Avrigeanu M, Bersillon O, Chadwick MB, Fukahori T, Ge Z, Han Y, Kailas S, Kopecky J, Maslov VM, Reffo G, Sin M, Soukhovitskii ESh, Talou P. RIPL - Reference Input Parameter Library for Calculation of Nuclear Reactions and Nuclear Data Evaluations. Nucl. Data Sheets. 2009;110:3107-3214.

[12] Mengoni A, Nakajima Y. Fermi-Gas Model Parametrization of Nuclear Level Density. J. Nucl. Sci. Technol. 1994;31:151-162.

[13] Chadwick MB, Fukahori T, Ignatyuk AV, Kailas S, Molnar G, Oblozinsky P, Reffo G, Su Z, Uhl M, Young PG. Handbook for Calculations of Nuclear Reaction Data - Reference Input Parameter Library. International Atomic Energy Agency; 1998, IAEA-TECDOC-1034.

[14] Kopecky J, Uhl M. Test of gamma-ray strength functions in nuclear reaction model calculations. Phys. Rev. 1990;C41:1941-1955.

[15] Filatenkov AA, Chuvaev SV. Measurement of a set of badly known neutron induced cross sections. 2001, RI-258.

[16] Bormann M, Bissem HH, Magiera E, Warnemunde R. Total cross sections and isomeric cross section ratios for $(n, 2n)$ reactions in the energy region 12-18 MeV. Nucl. Phys. 1970;A157:481-496.

[17] Frehaut J, Bertin A, Bois R, Jary J, Mosinski G. Status of $(n, 2n)$ cross section measurements at Bruyeres-le-Chatel. 1980, INDC(USA)-84:399.

[18] Veeser LR, Arthur ED, Young PG. Cross sections for $(n, 2n)$ and $(n, 3n)$ reaction above 14 MeV. Phys. Rev. 1977;C16:1792-1802.

[19] Vonach H, Pavlik A, Strohmaier B. Accurate determination of $(n, 2n)$ cross sections for heavy nuclei from neutron production spectra. Nucl. Sci. Eng. 1990;106:409-414.

[20] Macklin RL, Halperin J. ^{100,101,102,104}Ru(n, γ) and ^{103}Rh(n, γ) cross sections above 2.6-keV. Nucl. Sci. Eng. 1980;73:174-185.

[21] Lee S, Yamamoto S, Kobayashi K, Kim G, Chang J. Neutron capture cross section measurement of rhodium in the energy range from 0.003 eV to 80 KeV by LINAC Time-of-Flight method. Nucl. Sci. Eng. 2003;144:94-107.

[22] Bokhovko MV, Kononov VN, Rabotnov NS, Voevodskiy AA, Manturov GN, Timokhov VM. Neutron radiation cross-section, neutron transmission and average resonance parameters for some fission product nuclei. 1991, FEI-2168.

[23] Wisshak K, Voss F, Kaeppeler F, Reffo G. Measurements of keV neutron capture cross sections with a 4π barium fluoride detector: Examples of ^{93}Nb, ^{103}Rh, and ^{181}Ta. Phys. Rev. 1990;C42:1731-1750.

[24] Lu WD, Ranakumar N, Fink RW. Activation cross sections for (n, p), $((n, np) + (n, pn) + (n, d))$, and (n, α) reactions in the region of $Z = 40$ to 58 at 14.4 MeV. Phys. Rev. 1970;1:358-361.

[25] Csikai J, Bacso J, Daroczy A. Investigation of the cross-section of neutron reactions in the nucleus Rh^{103}. Nucl. Phys. 1963;41:316-322.

21. Measurement of Neutron Capture Cross Section of ^{241}Am Using NaI(Tl) Spectrometer at J-PARC

T. Arai[1)], T. Katabuchi[1)], M. Mizumoto[1)], K. Terada[1)], M.Igashira[1)], K. Hirose[2)], A. Kimura[2)], S. Nakamura[2)], Y. Toh[2)], K. Y. Hara[2)], F. Kitatani[2)], K. Furutaka[2)], M. Koizumi[2)], M. Oshima[2)], H. Harada[2)], J. Hori[3)], K. Kino[4)], T. Kamiyama[4)], Y. Kiyanagi[4)]

1) Research Laboratory for Nuclear Reactors, Tokyo Institute of Technology

2) Japan Atomic Energy Agency

3) Research Reactor Institute, Kyoto University

4) Graduate School of Engineering, Hokkaido University

email : arai.t.ap@m.titech.ac.jp

Measurement of the neutron capture cross section of ^{241}Am using an NaI(Tl) spectrometer was carried out at J-PARC. The experiments were made by the time-of-flight method with a pulsed neutron beam from a spallation neutron source. The neutron capture cross section was derived by the pulse-height weighting technique. Preliminary results are presented.

1. Introduction

Nuclear transmutation systems have been suggested as an option for reducing the radiological hazard of minor actinides (MA) and long-lived fission products (LLFP) in nuclear waste. Accordingly, reliable nuclear data of MAs and LLFPs are necessary for the design of nuclear transmutation systems. To develop a nuclear transmutation system, ^{241}Am is particularly important among MAs and LLFPs because a large amount of ^{241}Am is produced mainly by the decay of ^{241}Pu and hence exists in spent nuclear fuel. In addition, the radioactivity of high level nuclear waste is dominated by ^{241}Am after several hundred years that the early dominant nuclides ^{90}Sr and ^{137}Cs decay, and their activity weaken. However there are inconsistencies between existing experimental data of the capture cross section of ^{241}Am [2]. New measurements to reduce the inconsistencies have been desired. In the present work, we measured the neutron capture cross section of ^{241}Am.

2. Experiments

Experiments were carried out using a neutron beam from a spallation neutron source in the Materials and Life Science Facility (MLF) of the Japan Proton Accelerator Research Complex (J-PARC). The pulsed neutron beam was produced by the spallation reaction with a 3 GeV proton beam impinging on a mercury target. The proton beam power was about 300 kW and the repetition rate was 25 Hz. Gamma-rays from the neutron capture reaction were detected with the NaI(Tl) spectrometer placed in the Accurate Neutron-Nucleus Reaction Measurement Instrument (ANNRI) [3]. The experimental setup is shown in **Fig. 1**. The sample was placed at a flight path length of 27.9 m and irradiated with the neutron beam. The detection angle of the NaI(Tl) spectrometer was 90° with respect to the neutron beam axis.

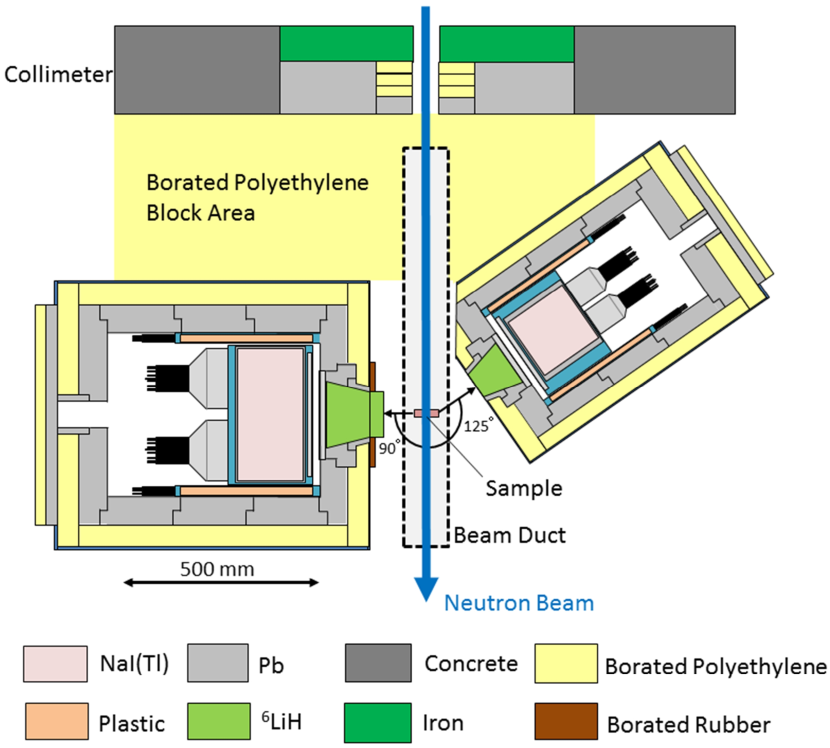

Fig.1：Experimental Area in ANNRI

The ^{241}Am sample encapsulated in an aluminum container was used for the measurement. The chemical form was americium oxide (AmO_2). The net weight of ^{241}Am was 7.5 mg. The isotopic enrichment of the sample was 99.9%. Aluminum powder was mixed with AmO_2 in order to solidify the sample. Samples of boron, gold, carbon and lead were used for derivation of neutron spectrum and background subtraction. Neutron energy was determined by the time-of-flight (TOF) method. A relative neutron energy distribution was determined by detecting 478 keV γ-rays from the $^{10}B(n,\alpha\gamma)^{7}Li$ reaction. Background of scattered neutrons from the sample was estimated from runs of carbon and lead. A dummy container having the identical dimensions to the ^{241}Am sample was also used for background subtraction of the aluminum container. The pulse-height weighting technique was employed to derive the neutron capture cross section [4]. The absolute neutron intensity was determined by the saturated resonance method using the 4.9 eV resonance of ^{197}Au.

Data acquisition was based on pulse-width measurement with a fast multiple event time digitizer (FAST ComTec MCS6). The negative anode signal of the NaI(Tl) spectrometer was fed into a time discriminator that converts the input signal into a square-shaped pulse having a pulse width equal to the time duration for which the input anode signal stays under a preset threshold level. The pulse width of the output signal of the time discriminator was measured with the time digitizer MCS6. A calibration curve to convert the pulse width to the detector-deposited energy was determined from discrete γ-rays of standard γ-ray sources and neutron-induced reactions. The obtained conversion curve is shown in **Fig. 2**.

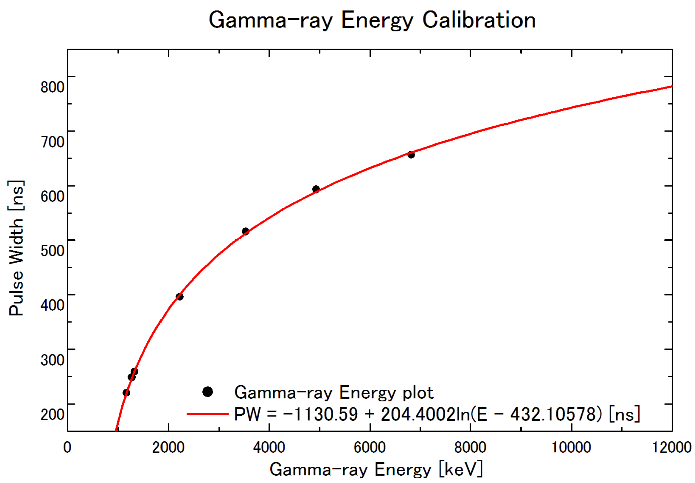

Fig. 2 : Calibration curve to convert the pulse width to the detector-deposited energy

3. Results

Data analysis to derive the neutron capture cross section of ^{241}Am is ongoing. Only preliminary results are given here. The obtained neutron energy distribution is shown in **Fig. 3**. The relative neutron capture cross section of ^{241}Am is shown in **Fig. 4.** Normalization using the saturated resonance of ^{197}Au has not been completed. The cross section shown in **Fig. 4** is given in arbitrary scale.

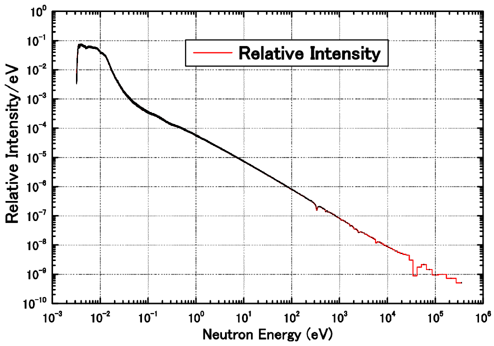

Fig. 3: Incident neutron energy distribution

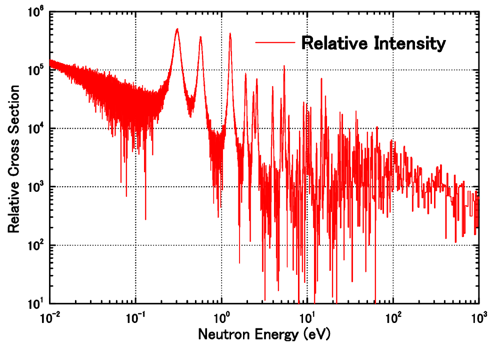

Fig. 4: Relative neutron capture cross section of ^{241}Am

4. Conclusion

We carried out the measurement of neutron capture cross section of ^{241}Am using an NaI(Tl) spectrometer at J-PARC. A pulsed neutron beam from a spallation neutron source in J-PARC was used. The TOF method was employed to determine the cross section. Data analysis is ongoing. Preliminary results of the cross section data were presented.

Reference

[1] M. I. Ojovan and W. E. Lee, An Introduction to Nuclear Waste Immobilisation, Elsevier Science, 2005.

[2] D. Bernard and O. Bouland, "Americium-241 phase I: reevaluation for JEFF-3.1.1 and a step forward", Journal of Nuclear Science and Technology, 49, 132, (2012).

[3] M. Igashira et al., "Nuclear Data Study at J-PARC BL04", Nuclear Instruments and Methods in Physics Research A, 600, 332, (2009).

[4] R. L. Macklin and J. H. Gibbons, "Capture-Cross-Section Studies for 30-220-keV Neutrons Using New Technique", Physical Review, 159, 1007, (1967).

22. Neutron Capture Cross Section Measurements on ^{232}Th with a Total Absorption BGO Spectrometer at KURRI-LINAC

Jun-ichi HORI, Tadafumi SANO, Yoshiyuki TAKAHASHI,
Hironobu UNESAKI, Ken NAKAJIMA

Research Reactor Institute, Kyoto University
2-1010, Asashiro-nishi, Kumatori-cho, Sennan-gun, Osaka 590-0494
e-mail: hori@rri.kyoto-u.ac.jp

We have measured the neutron capture cross section of ^{232}Th by the neutron time-of-flight (TOF) method in the energy range from 1 eV to 800 eV using a 46-MeV electron linear accelerator (linac) at the Research Reactor Institute, Kyoto University (KURRI). An assembly of 12 pieces of $Bi_4Ge_3O_{12}$ (BGO) scintillators, which was placed at a distance of 12.7 m from the neutron source, was employed as a total energy absorption detector for neutron capture gamma-ray measurement. The incident neutron flux was determined with the ^{10}B(n,$\alpha\gamma$) standard reaction and the relative capture cross sections of ^{232}Th were normalized to the evaluated values of JENDL-4.0 at the 21.8-eV resonance. This paper presents preliminary results.

1. Introduction

The use of thorium in the nuclear cycle for either critical or subcritical systems is now a topic of great interest since it has an advantage in view of less radio toxic wastes production compared with the conventional uranium/plutonium cycle. However, the nuclear database for Th-U system is scantly and less reliable compared with the well-established U-Pu system. In the thorium-uranium fuel cycle, the fissile ^{233}U is generated by two successive β-decays after a neutron capture reaction of the fertile nucleus ^{232}Th. Therefore, accurate neutron capture cross section data of ^{232}Th are strongly requested for the safe and economical design of nuclear reactors with thorium fuels [1].

The evaluated cross sections for ^{232}Th(n,γ) reaction of JENDL-4.0 [2] were drastically revised from the values of JENDL-3.3 [3] in the neutron energy region of 0.1 – 100 eV. In order to check the validity of the present revise, several integral experiments have been already reported [4, 5]. In this study, we started an experimental study on the differential neutron capture cross section of ^{232}Th in the neutron energy region from thermal to keV. A part of preliminary results will be shown in this paper.

2. Experimental Procedure

The neutron capture cross section measurements were carried out by the TOF method with the 46-MeV linac at the KURRI. A water-cooled target assembly, 5 cm in diameter and 6 cm long, which was composed of 12 sheets of tantalum (Ta) plates with total thickness of 29 mm was used as a photo-neutron source [6]. This target was set at the center of an octagonal water tank, 30 cm in diameter and 10 cm thick, to moderate the neutron energies. The linac was operated with a repetition rate of 300Hz, a pulse width of 100 ns, a peak current of 5 A, and an electron energy of about 30 MeV. The experimental arrangement is shown in Fig. 1. The flight path used in the experiment is in the direction of 135-degree to the linac electron beam. In order to reduce the gamma-flash generated by the electron burst from the target, a lead block, 7 cm in diameter and 10 cm long, was placed in front of the entrance of flight tube. The neutron collimation system was mainly composed of B_4C, Li_2CO_3 and Pb materials, and tapered from about 12 cm in diameter at the entrance of the flight tube to about 2 cm in beam diameter at the capture sample, which was placed at a distance of 12.7±0.02 m from the Ta target. A Cd sheet of 0.5 mm in thickness was also inserted into the TOF neutron beam to avoid overlap of neutrons from the previous pulsed due to the high frequency of the linac operation. A BF_3 proportional counter was set at the exit of the flight tube as shown in Fig. 1 and used as a neutron intensity monitor between the experimental runs.

An assembly of 12 pieces of $Bi_4Ge_3O_{12}$ (BGO) scintillators [7, 8] was employed as a total energy absorption detector for neutron capture gamma-ray measurement. A sample was inserted at the center of the BGO through-hole. The inside of the through-hole was covered with ^{6}LiF tiles of 3 mm in thickness to absorb neutrons scattered by the sample. Signals from the BGO detectors were summed up and fed into the Yokogawa's WE7562 multi-channel analyzer. In the module, the pulse-height value obtained with a digital sampling method and the timing of detection were stored as two dimensional data. Signals from the injector of linac were used as a trigger signal.

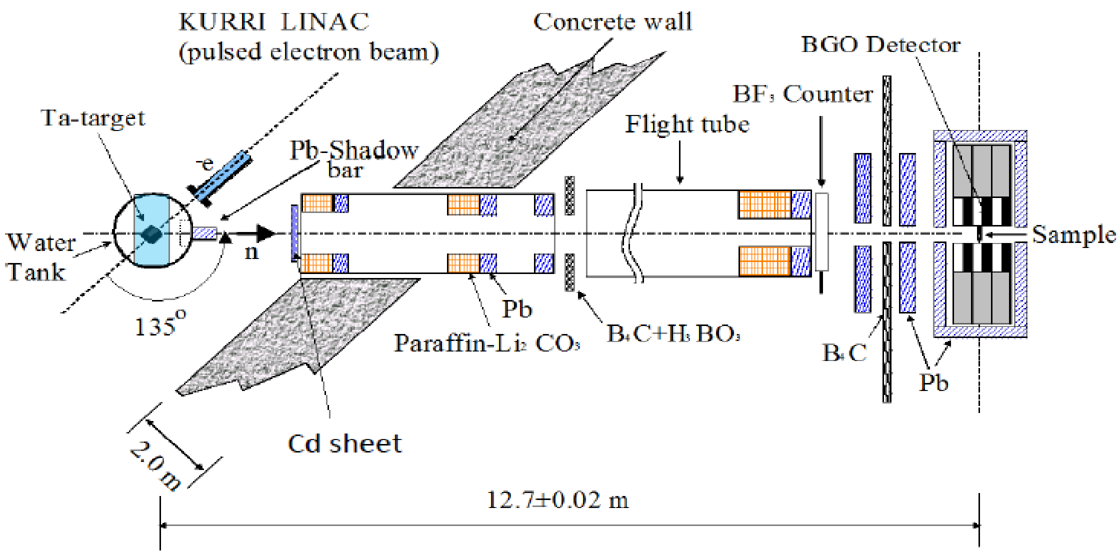

Fig.1 Experimental arrangement of the TOF measurement at the 12.7-m flight path

A thorium metal, whose purity was 99.97 %, of 12.7 mm in diameter and 0.05 mm in thick was used as a capture sample. A ^{10}B sample, whose purity was 96.98 %, was used for the measurement of the incident neutron spectrum on the sample. The ^{10}B sample was encapsulated in a thin aluminum case, 18 mm×18 mm and 8 mm in thickness (0.872 g/cm^2). A graphite sample, 18 mm×18 mm and 5 or 10 mm in thickness, was also applied to the measurement of background level due to neutrons scattered by the capture sample. The measurement time was about 30 hours for the ^{232}Th sample.

3. Data Processing and Analysis

The neutron spectrum incident on the sample position was deduced from the net TOF spectrum corresponding to the 478-keV γ ray emitted via the ^{10}B(n,αγ)^{7}Li reaction as shown in Fig. 2. In order to estimate the neutron capture yield in the ^{10}B sample, the cross sections of the ^{10}B(n,αγ)^{7}Li reaction were taken from JENDL-4.0 [2].

A part of the TOF spectrum for ^{232}Th(n,γ) is shown in Fig. 3. Two resonances were clearly observed at 21.8 and 23.5 eV. Two gates were set in the 23.5-eV resonance and off-resonance regions of the TOF spectrum, respectively. Figure 4 shows the gamma-ray pulse-height spectra corresponding to the resonance and off-resonance regions. The thorium background is originated from the gamma-ray cascades following the beta decay of ^{208}Tl. In order to obtain the TOF spectrum with better signal to noise ratio, the gate was set in the region from 50 to 180 ch on the P. H. spectrum.

A sample-independent background was removed by subtracting the normalized TOF spectrum of blank run without sample. In the case of BGO scintillator, the time-dependent background due to neutrons scattered by the sample is mainly originated from the neutron capture by ^{73}Ge included in the detector material. The neutron binding energy of ^{73}Ge, 10.196 MeV, is larger than that of ^{232}Th, 4.786 MeV. Therefore, gamma rays with energies between 4.786 and 10.196 MeV can be considered as the background due to neutron scattered by the sample. The normalized gamma-ray P. H. spectra corresponding to the neutron energy range from 10 to 800 eV for the graphite samples with a thickness of 5 or 10 mm are shown in Fig. 5. The components due to scattered neutrons were observed below 350 ch. On the other hands, there are no differences among three runs with a ^{232}Th sample of 50 or 250 μm in thickness and without sample in the region from 180 to 350 ch as shown in Fig. 6. It means that the background due to scattered neutrons is negligible small in the neutron energy region below 800 eV. The time-independent background level due to ^{232}Th decay and natural gamma rays was determined around long flight time, where no time-correlated events were expected. The normalized TOF spectra of ^{232}Th and background are shown in Fig. 7.

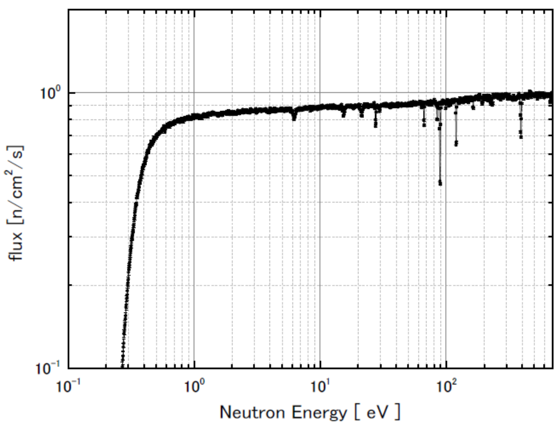

Fig. 2 Neutron spectrum incident on the sample obtained using the ^{10}B(n,αγ)^{7}Li reaction.

Correction for the neutron scattering and self-shielding in the sample was made by the Monte Carlo code MCNP-4C [9] using JENDL-4.0 cross section data [2]. The estimated correction function for ^{232}Th sample is shown in Fig. 8.

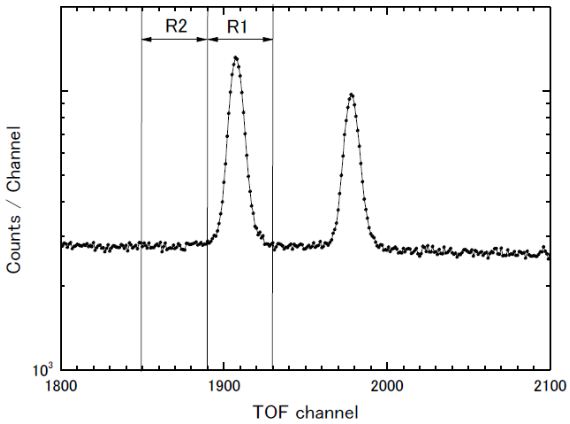

Fig. 3 TOF spectrum for ^{232}Th(n,γ) in the energy range from 19 to 26 eV

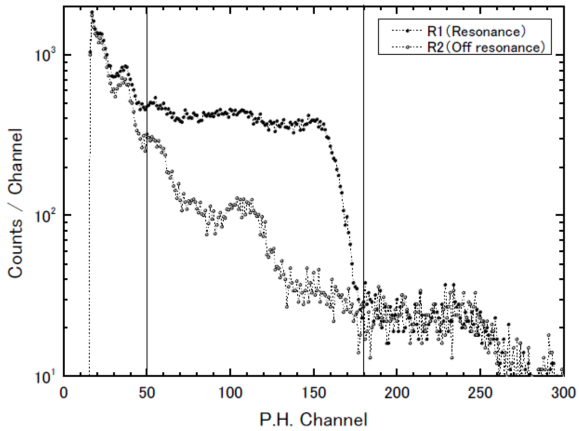

Fig. 4 γ-ray pulse-height spectra of the resonance and off resonance regions

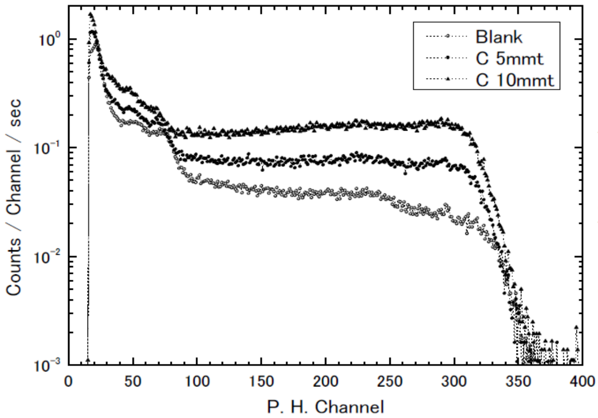

Fig. 5 γ-ray pulse-height spectra of blank, graphite samples with a thickness of 5 or 10 mm

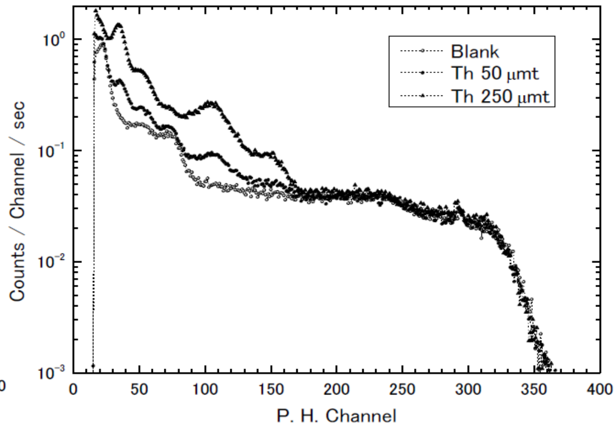

Fig. 6 γ-ray pulse-height spectra of blank, ^{232}Th samples with a thickness of 50 or 250 μm

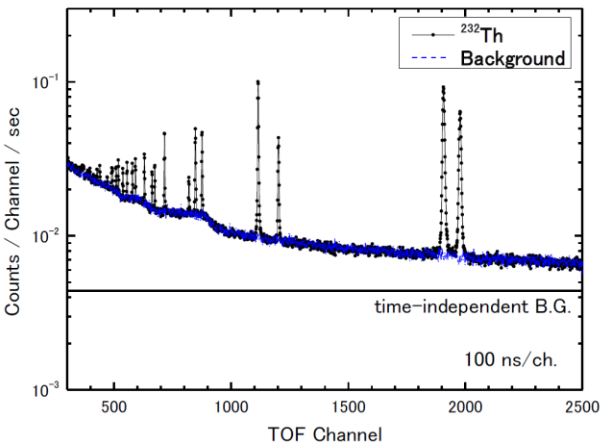

Fig. 7 TOF spectra of ^{232}Th sample and background

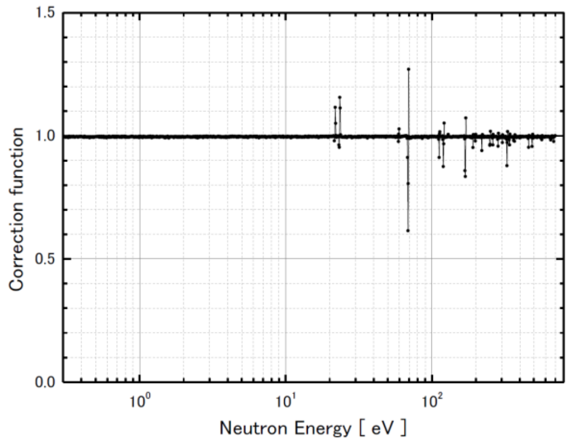

Fig. 8 Correction function for the neutron self-shielding and multiple scattering in the ^{232}Th sample

4. Results and Discussion

The relative neutron capture cross sections of ^{232}Th have been obtained from 1 to 800 eV as a function of neutron energy. The relative cross sections were normalized to the evaluated values of JENDL-4.0 [2] at the 21.8-eV resonance. In order to compare with the evaluated data library and the previous results, the cross sections integrated over the resonance peak were derived in the energy range from 21.5 to 121 eV as shown in Table 1.

Recently, Baek *et al.* measured the neutron capture cross sections of ^{232}Th at the 122 m flight path of the IBR-30 pulsed neutron source of JINR in Dubna [10]. The energy and the average power of the electron beam were 40 MeV and 10 kW, respectively. The pulse width was 4 μs. A multi-section liquid scintillator was used as a capture gamma-ray detector and the coincidence multiplicity method was applied. A 5.0 g thorium plate of 4.5 cm × 4.5 cm and 0.023 cm in thickness was used. The weight and thickness were about seventy and five times larger than those of the sample used in the present experiment, respectively.

The evaluated values of JENDL-4.0 are in general agreement with the measurement, although the integrated values of JENDL-4.0 show lower about 10 % for the 113- and 121-eV resonances. Slight discrepancies between the data by Baek *et al.* and the present results are found for the 60-, 69- and 121-eV resonances within 10 %. Further detailed analyses are needed.

Table 1 Comparison of the averaged neutron capture cross sections of ^{232}Th for the resolved resonances in the energy range from 21.5 to 120 eV

E_res [eV]	Present [b・eV]			JENDL-4.0 C/E			Baek *et al.* [b・eV]			Baek *et al.* ratio		
21.79	356.6	±	6.9	1.00(normalized)			371.6	±	12.5	1.04	±	0.04
23.46	554.1	±	11.5	1.04	±	0.02	572.7	±	19.2	1.03	±	0.04
59.51	225.6	±	4.9	1.02	±	0.02	252.6	±	10.1	1.12	±	0.05
69.19	808.9	±	18.5	0.97	±	0.02	877.8	±	30.3	1.09	±	0.04
113.03	342.3	±	23.3	0.89	±	0.06	346.9	±	16.0	1.01	±	0.08
120.85	454.5	±	33.2	0.85	±	0.06	407.9	±	16.5	0.90	±	0.07

5. Summary

The neutron capture cross section measurement on ^{232}Th was carried out by the neutron time-of-flight (TOF) method in the energy range from 1 eV to 800 eV at the KURRI-LINAC relative to the $^{10}B(n,\alpha\gamma)$ reaction. The relative capture cross sections of ^{232}Th were normalized to the evaluated values of JENDL-4.0 at the 21.8-eV resonance. We obtained the cross section integrated over the resonance peak in the energy range from 21.5 to 121 eV and compared with those of JENDL-4.0 and the previous experiment. Slightly discrepancies were found for several resonances. In future, we will perform the detail analyses and additional measurement in the lower energy region to determine the negative resonance parameter of ^{232}Th.

Acknowledgments

The authors would like to express their thanks to the linac staff of the KURRI for making it possible to operate the accelerator steadily. A part of this study was supported by CHUBU Electric Power Co., Inc.

References

[1] S. Pelloni *et al.*, "Impact of Different Nuclear Data on the Performance of Fast Spectrum Systems Based on the Thorium-Uranium Fuel Cycle," *Proc. Int. Conf. on Nuclear Data for Science and Technology*, Trieste, Italy, May 19-24, 1997, p. 1172.

[2] K. Shibata *et al.*, "JENDL-4.0: A New Library for Nuclear Science and Engineering," *J. Nucl. Sci. Technol.*, **48**, 1 (2011).

[3] K. Shibata *et al.*, "Japanese Evaluated Nuclear Data Library Version 3 Revision-3: JENDL-3.3," J. Nucl. Sci. Technol., 39, 1125 (2002).

[4] T. Fujii *et al.*, "Critical Experiment with Thorium at KUCA," JAEA-Conf 2012-001, 171 (2012).

[5] T. Mishiro *et al.*, "The evaluation of Thorium cross-section by the experimental analysis of Thorium replacement worth," Proc. of AESJ Fall Meeting, 2013, Hachinohe, J56 (2013) [in Japanese].

[6] K. Kobayashi *et al.*, "KURRI-Linac as a Neutron Source for Irradiation," *Annu. Rep. Res. Reactor Inst., Kyoto Univ.*, **22**, 142 (1987).

[7] S. Yamamoto *et al.*, "Application of BGO Scintillators to Absolute Measurement of Neutron Capture Cross Sections between 0.01 eV and 10 eV," *J. Nucl. Sci. Technol.*, **33**, 815 (1996).

[8] S. Lee *et al.*, "Neutron Capture Cross-Section Measurement of Rhodium in the Energy Region from 0.003 eV to 80 keV by Linac Time-of-Flight Method," *Nucl. Sci. Engin.*, **144**, 1 (2003).

[9] J. F. Briesmeister, Ed. "MCNP-A general Monte Carlo N-Particle Transport code, version 4c," LA-137090M (2000).

[10] W. Y. Baek *et al.*, "Investigation of γ-multiplicity spectra and neutron capture cross-sections of ^{232}Th in the energy region 21.5-215 eV," *Nucl. Instrum. Methods*, B **168**, 453 (2000).

23. Measurement of Proton, Deuteron, and Triton Production Double Differential Cross Sections on Carbon by 290 MeV/nucleon Ar ions

T. Kajimoto[1], T. Hashiguchi[2], N. Shigyo[2], D. Satoh[3], Y. Uozumi[2], T. Y. Song[4], C. W. Lee[4], J. W. Kim[4], S. C. Yang[4], Y. Koba[5], N. Matsufuji[5], S. Endo[1]

1 Hiroshima University, Higashi-Hiroshima, 739-8527, Japan
2 Kyushu University, Fukuoka, 819-0395, Japan
3 Japan Atomic Nuclear Agency, Tokai, 319-1195, Japan
4 Korea Atomic Nuclear Agency, Daejeon, 305-353, Korea
5 National Institute of Radiological Sciences, Chiba, 263-8555, Japan
email: kajimoto@hiroshima-u.ac.jp

We measured proton, deuteron, and triton production double differential cross sections for carbon by 290 MeV/nucleon Ar ions at the Heavy-Ion Medical Accelerator in Chiba of the National Institute of Radiological Sciences. The kinetic energy of each particle was determined with the time of flight technique. The energy region was limited from 45 to 90 MeV for protons, from 55 to 140 MeV for deuterons, and from 65 to 170 MeV for tritons due to the selection of particle identification.

1. Introduction

Neutron data is very important for shielding design of accelerators because of strong penetrating capability and generating activities. The shielding design is based on empirical formulas such as the Moyer model [1] or particle transport Monte Carlo code such as FLUKA [2], PHITS [3], GEANT4 [4], and so on. Because of the simplicity, the empirical formula has limitation of the energy range of beam particle and angular range. In contrast, these codes are not limited under a finite geometrical condition. However, the results obtained using codes should be validated with many experimental data.

The heavy ion accelerator named "RAON" is being built in KOREA [5]. RAON will provide various kinds of rare isotope beam. One of candidate of combination of accelerated ions and target materials are 300 MeV/nucleon argon ions and a carbon, respectively. A particle transport Monte Carlo code will be used for shielding design of the facility. To prove the validity of use of the code, experimental data of neutrons induced by reactions between beam particle and material such as target, a beam pipe, collimator, or beam dump was required.

290 MeV/nucleon argon incidence neutron production double differential cross sections (DDXs) for carbon target were measured and will be reported by Shigyo et al. [6]. The data is useful for shielding design for the target of the facility. For progress of the further

reliability of the code, experimental DDXs are needed for not only neutron but also other particle production.

We measured proton, deuteron, and triton production DDXs on carbon by 290 MeV/nucleon argon ions. These DDXs were obtained by reanalyzing data for neutron production DDXs by Shigyo et al. This paper mainly describes the methodology to derive proton, deuteron, and triton production DDXs with data of neutron measurement.

2. Experiment

The experiment was performed at the Heavy-Ion Medical Accelerator in Chiba (HIMAC) of the National Institute of Radiological Sciences (NIRS). The experimental set up and electronic circuit for data acquisition were almost the same as in Ref. [7].

A schematic view of the experimental arrangement is shown in Fig. 1. The beam was 290 MeV/nucleon Ar ions. Before irradiating, the spot of beam was confirmed. The spot size was about Φ10 mm. The graphite target with 5.0 mm thickness was set to be 7.1 mm length on beam line by rotating the target at 45 degrees. Argon ions were counted by a 0.5 mm thick plastic (beam pick up) scintillator located upstream of the target. Particles emitted from the target were detected by three NE213 scintillators since this experiment was for neutrons and the pulse shape discrimination of NE213 scintillator is effective for the identification between neutrons and gamma rays. The NE213 scintillators which had 127 mm thickness and 127 mm in diameter were located at 15, 30, and 45, or 60, 75, and 90 degrees with respect to the beam axis. A 2 mm thick plastic scintillator as a veto detector was set in front of each NE213 scintillator.

Data acquired event by event were time difference between signals of the beam pick up scintillator and each NE213 scintillator, pulse height of signal from each NE213 scintillator,

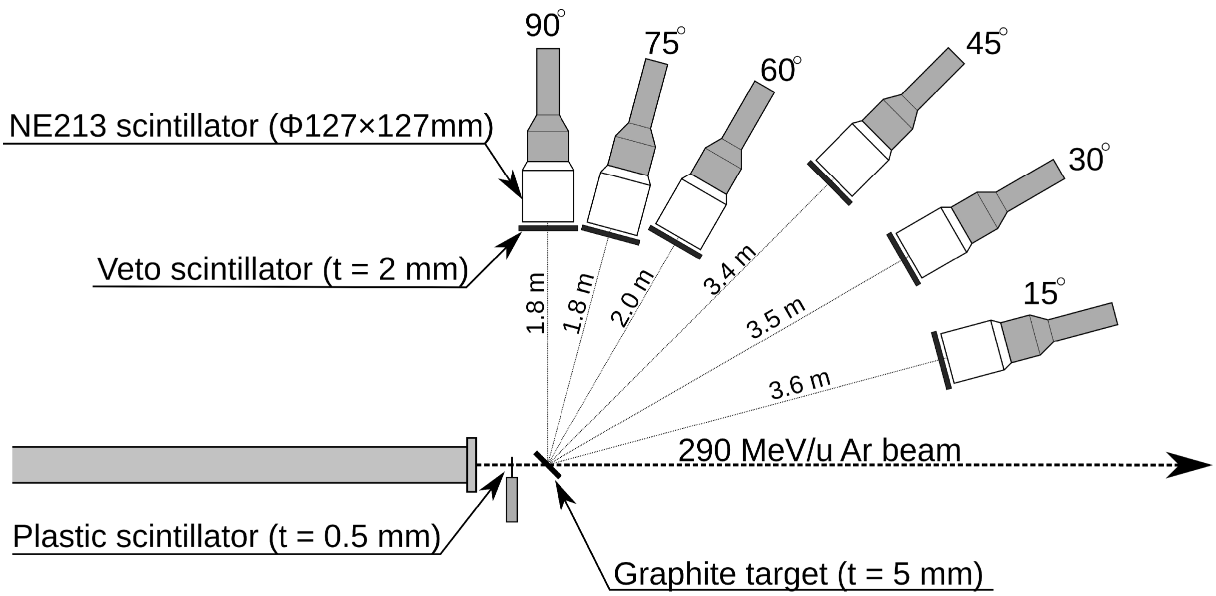

Fig. 1 Schematic view of experimental setup with beam axis, a target, a beam pick up scintillator, veto detectors, and NE213 scintillators.

pulse height of signal from each veto detector, and bit pattern of a fired NE213 scintillator. The data acquisition (DAQ) system consisted of NIM and CAMAC modules. The detail of DAQ system was mentioned in Ref. [7]. The DAQ had dead time since a trigger signal can not be accepted in data acquisition process. To correct dead events, the number of signals from the beam pick up scintillator and each NE213 scintillator were counted with NIM scaler in alive and dead time.

3. Analysis

Proton, deuteron, and triton production DDXs ($d\sigma^2/dEd\Omega$) in energy bin width of dE, centered at an energy of E, into a solid angle $d\Omega$ were derived as:

$$\frac{d^2\sigma}{dE\,d\Omega} = \frac{C(E)\,f}{\epsilon(E)\,\rho_A\,N\,\Delta E\,\Delta\Omega}\quad,$$

where $C(E)$ is energy histogram of protons, deuterons, or tritons, f is correction factor of dead events, $\varepsilon(E)$ is peak efficiency of each paticle, ρ_A is area density of the target, N is count of incident argon ions, ΔE is the energy bin width of the histogram, and $\Delta\Omega$ is the solid angle of the NE213 scintillator.

Energy histograms for proton, deuteron, and triton composed from events passing analysis procedure: selection of charged particle events, particle identification, and kinetic energy determination. Charged particle events were discriminated from uncharged particle events with pulse height distribution of each veto detector. Particle identification was performed by event selection of two scatter plots: time difference and pulse height of veto detector as shown in Fig. 2, and time difference and pulse height of NE213 scintillator as shown in Fig. 3. The selection of Fig. 2 excluded events by particles more than atomic number Z = 2. The selection of Fig. 3 identified event by each isotope of Z = 1. Bands by particles more than Z = 2 did not appear in Fig. 3 because of the selection of Fig. 2. The kinetic energy was determined with time of flight technique. A sharp peak from prompt gamma ray events on time difference distribution was adopted to the time base. The sharp peak consists of events

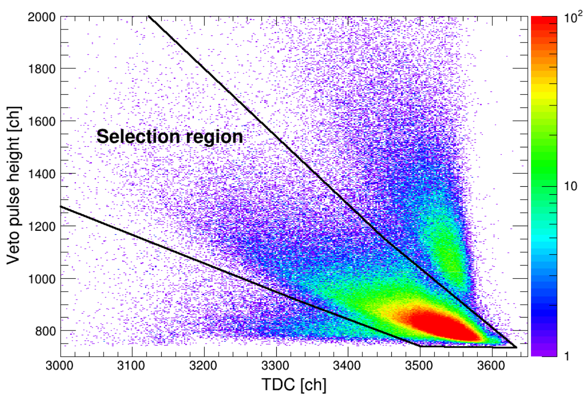

Fig. 2 Scatter plot of time difference and pulse height of veto detector. The events in selection region were extracted.

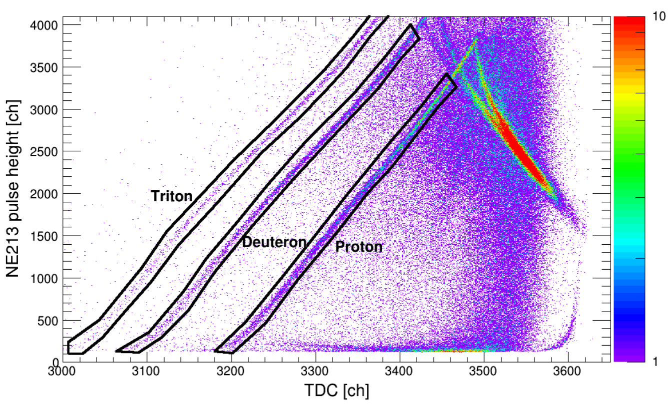

Fig. 3 Scatter plot of time difference and pulse height of NE213 scintillator. Three bands were selected as protons, deuterons, and tritons.

extracted from uncharged events with pulse shape discrimination of NE213 scintillator. The deceleration of proton, deuteron, and triton in flight from the target to the NE213 scintillator was considered with values of linear energy transfer extracted from PHITS [3][8]. The energy loss of proton, deuteron, and triton in the target was calculated by assuming that these particles produced at the center of the target. The assumption causes deterioration of energy resolution.

Calculated values were adopted to the peak efficiency. Since we extracted events for particles giving the full energy to the NE213 scintillator in the analysis, the efficiency should be obtained from the full energy peak in the deposited energy distribution for mono-energy particle incidence. The deposited energy distributions for proton, deuteron, and triton incidence were calculated in each angle with PHITS. An example of the calculated distribution were shown in Fig. 4. The distribution consists of a sharp peak and continuous region. The probability of the peak were adopted to the peak efficiency. The obtained peak efficiency was shown in Fig.5. However, the sharp peak is broaden by the energy resolution in actual experiment, determination of peak region causes an uncertainty of peak efficiency. We assumed the uncertainty of the peak efficiency to be 5 %.

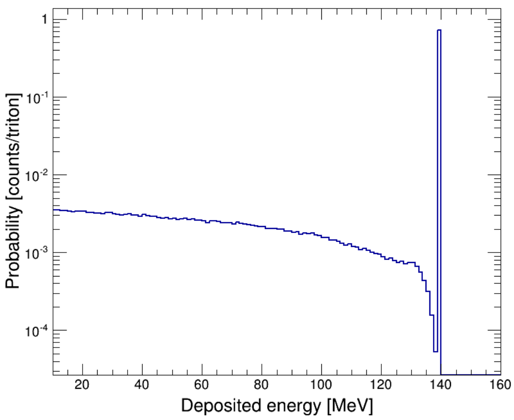

Fig. 4 Deposited energy distribution for 150 MeV triton incidence at 45 degrees. The distribution was calculated by PHITS.

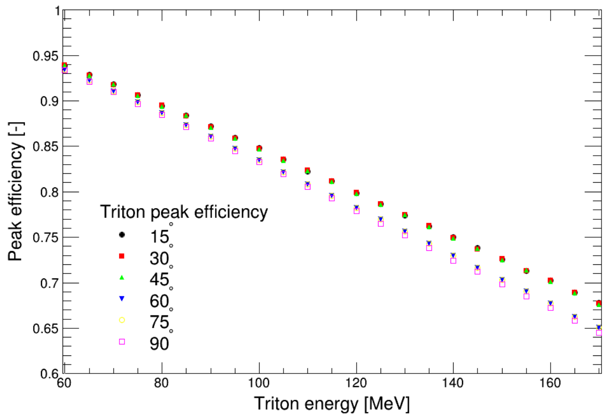

Fig. 5 Triton peak efficiency in each angle.

4. Results and discussion

Figure 6 shows proton, deuteron, and triton production double differential cross sections on carbon by 290 MeV/nucleon Ar ions. These values have uncertainty. The uncertainty is due to statistical and systematic errors. The systematic error resulted from the peak efficiency determination (5%). The energy regions were limited from 45 to 90 MeV for protons, from 55 to 140 MeV for deuterons, and from 65 to 170 MeV for tritons due to the event selection by the particle identification.

Measured DDXs are compared with values calculated by FLUKA and PHITS. The version of each code was fluka2011.2b and PHITS2.52. The RQMD [9] and JQMD [10] codes for nucleus-nucleus collision calculations were implemented in FLUKA and PHITS,

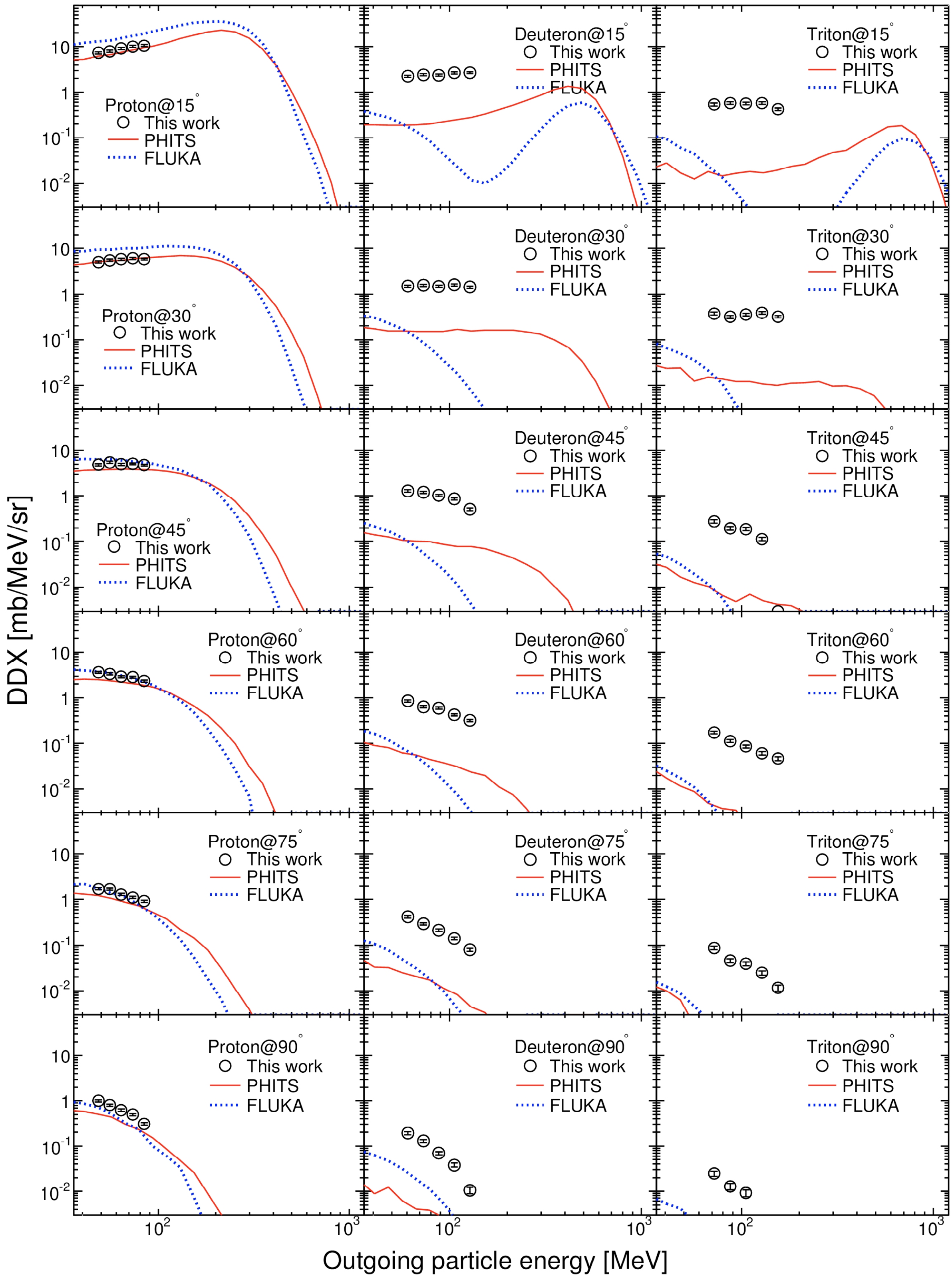

Fig. 6 Proton, deuteron, and triton production double differential cross sections for carbon by 290 MeV/nucleon argon ions. The solid and dotted lines show calculations by PHITS and FLUKA, respectively.

respectively. The proton DDXs gave agreement with both calculated values. However, large discrepancies between measured and calculated DDXs were found for deuteron and triton. The deuteron and triton DDXs by FLUKA and PHITS are different from each other in shape. Measurements of DDXs with wide energy region are required for elucidating the shape.

5. Summary

Proton, deuteron, and triton production DDXs on carbon by 290 MeV/nucleon argon ions were measured at the HIMAC. Measured DDXs were obtained by reanalyzing data for neutron production DDXs. The event selection by particle identification limited the energy region between 45-90 MeV for protons, 55-140 MeV for deuterons, and 65-170 MeV for tritons. The measured DDXs were compared with calculation values by FLUKA and PHITS. The proton DDXs gave agreement with both calculated values. However, large discrepancies between measured and calculated DDXs were found for deuteron and triton.

All the data will be useful as benchmarks in investigating the validity of Monte Carlo simulations. However, the energy region was limited for obtained DDXs. Measurements of DDXs with wide energy region are required for elucidating the DDX shape. Furthermore, experimental DDXs for particle production except for nucleon are needed to confirm differences of DDXs.

Acknowledgment

This work was performed as a part of Research Project with Heavy Ions at NIRS-HIMAC. We gratefully acknowledge financial support from JSPS KAKENHI Grant Number 22360406.

References

[1] B. J. Moyer, Proc. 1st Int. Conf. Shielding around High Energy Accelerators, Presses Universitaires de France, Paris, (1962) p.65.
[2] G. Battistoni, S. Muraro, P. R. Sala et al., Proceedings of the Hadronic Shower Simulation Workshop 2006, Fermilab 6-8 September 2006, M. Albrow, R. Raja eds., AIP Conference Proceeding 896 (2007) pp.31-49.
[3] T. Sato, K. Niita, N. Matsuda et al., J. Nucl. Sci. Technol. 50 (2013) pp.913-923.
[4] S. Agostinelli, J. Allison, K. Amako et al., Nucl. Instrum. Methods A 506 (2003) pp.250-303.
[5] K. Tshoo, Y. K. Kim, Y. K. Kwon et al., Nucl. Instrum. Methods B 317 (2013) pp.242-247.
[6] N. Shigyo, Y. Uozumi, Y. Imabayashi et al., submitted for Proceedings of the 2013 Symposium on Nuclear Data in this Proceeidngs.
[7] D. Satoh, D. Moriguchi, T. Kajimoto et al., Nucl. Instrum. Methods A 644 (2011) pp.59-67.
[8] T. W. Armstrong, K. C. Chandler, ORNL Report ORNL-4869, ORNL, Oak Ridge, TN, USA, May 1973.
[9] H. Sorge, Phys. Rev. C 52 (1995) pp.3291-3314.
[10] K. Niita, Phys. Rev. C 52 (1995) pp.2620-2635.

24. Measurement of Cross Sections and Yields of Neutron Produced by 100 MeV/u C(C,xn) Reaction

Youichi IMAHAYASHI[1], Nobuhiro SHIGYO[1], Yusuke UOZUMI[1], Yutaro ITASHIKI[1], Daiki SATOH[2], Tsuyoshi KAJIMOTO[3], Toshiya SANAMI[4], Yusuke KOBA[5], Masashi TAKADA[5] and Naruhiro MATSUFUJI[5]
1 Kyushu University, Fukuoka, 819-0395, Japan
2 Japan Atomic Energy Agency (JAEA), Tokai, 319-1195, Japan
3 Hiroshima University, Higashi-Hiroshima, 739-8527, Japan
4 High Energy Accelerator Research Organization (KEK), Tsukuba, 305-0801, Japan
5 National Institute of Radiological Sciences (NIRS), Chiba, 263-8555, Japan
e-mail: youichi@kune2a.nucl.kyushu-u.ac.jp

Neutron production double differential cross sections (DDX) and thick target neutron yields (TTNY) from reaction by 100 MeV/u carbon incidence on a carbon were measured at HIMAC of the NIRS by time-of-flight method. Neutron DDX and TTNY were obtained in a wide neutron energy region from several hundred MeV down to 0.6 MeV and the angular distribution from 15° to 90° using two sizes of NE213 neutron detectors. The experimental DDX and TTNY were compared with the calculation data by some Monte Carlo particle transport codes.

1. Introduction

Heavy ion radio therapy has a great advantage in treatment of cancer owing to the potential to reduce the damage to patients. On the other hand, it is considered as health issue that a patient is exposed to secondary particles, such as neutron and γ-ray[1, 2]. It is known that neutrons around 1 MeV region have a large effect on the human body. Then, it is essential to estimate neutrons produced from heavy ion incidence on bio elements for assessment of secondary radiation dose. In particular, the experimental data of neutron energy spectra around 1 MeV region by several hundred MeV/u heavy ion incidence which is actually employed in the therapy on bio elements (carbon, oxygen, nitrogen and so on) are insufficient. Therefore, neutron production double differential cross sections (DDX) and thick target neutron yields (TTNY) by such incidence on target are required.

Monte Carlo simulation codes are useful method to obtain the information which is hard to gain by experiments. The codes are required to predict neutron yields around 1 MeV for estimating secondary exposure of patients and developing a treatment plan.

The 290 MeV/u carbon ion radio therapy has been carried out at the Heavy Ion Medical Accelerator in Chiba (HIMAC) of the National Institute of Radiological Science (NIRS). In the previous work, the neutron DDX by 290 MeV/u carbon ion incidence on bio elements have been measured down to 0.6 MeV of neutron energy using NE213 liquid organic scintillators. Monte Carlo simulation code PHITS[3] reproduced the measured neutron spectra well[4, 5]. And in the next experiment, for investigation of neutron production by decelerated 290 MeV/u carbon ions in a human body, 100 MeV/u carbon incident neutron DDX for a carbon target have been measured in June 2012[6]. The neutron DDX below several MeV energy in forward direction have been much higher than ones in backward direction, despite the projection that the neutron in that energy region would be isotropically produced on the evaporation state.

In this study, 100 MeV/u carbon incident neutron DDX for a carbon target were again measured, and TTNY for a carbon target were obtained, down to 0.6 MeV neutron energy. The experimental data were compared with calculation results of some Monte Carlo codes.

2. Experiment

The experiment was performed at the PH2 beam line of HIMAC of the NIRS. The experimental setup is shown in **Figure 1**. The 100 MeV/u ^{12}C ions were extracted from the synchrotron. Average beam intensity was 7×10^5 ions /3.3 seconds, and the beam spot diameter was less than 10 mm.

The target was 50 mm × 50 mm × 2 mm graphite plate with natural isotopic composition. It was placed on the beam axis being rotated with 45° according to the axis. This was because the effective target thickness should have been kept almost same to all measurement direction. The 100 MeV/u carbon ions imparted 10 % energy to the target of 2.8 mm effective thickness. In order to obtain neutron yields from thick target, the measurements using a 20 mm thick graphite target were gone on. The target thickness was larger than the range of the 100 MeV/u ^{12}C ions beam in carbon.

The carbon ion beam were passed through a 0.5 mm thick NE102A plastic scintillator (beam pick up detector) to count the number of incident particles and they were bombarded with the target. Neutron produced in the target were detected by six NE213 liquid organic scintillators (neutron detector) placed from 15° to 90° to get angular distribution. Two sizes of NE213 scintillators were adopted. The large ones to cover above 5 MeV of neutron energy were 127 mm in diameter and thickness. The small scintillators had the diameter and the thickness of 50.8 mm to measure neutrons below 10 MeV. For calibration of the light outputs of the neutron detectors, γ-rays from ^{241}Am, ^{137}Cs, ^{60}Co and ^{241}Am-Be were measured. A 2 mm thick NE102A plactic scintillator was set in front of each NE213 scintillator to discriminate between charged and non-charged particles (veto detector). The beam pick up detector and each neutron detector provided the signal for the time-of-flight (TOF) measurement.

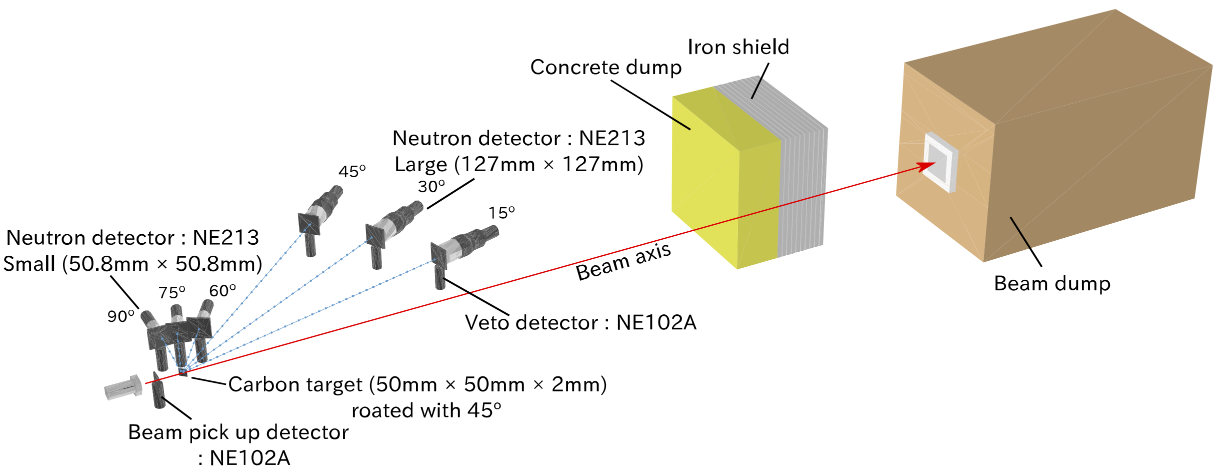

Figure 1: Experimental setup

The flight path length from the target to each neutron detector at the experiment in 2012[6] and 2013 (this experiment) is listed in **Table 1**. The large neutron DDX below several MeV in forward direction in the 2012 experiment could have been caused by background neutrons which had come from a beam dump. In this experiment, in order to improve signal to noise ratio for low energy neutrons, small neutron detector were set at shorter flight path length than the previous experiment as shown in **Table 1**.

Table 1: Flight path leangth at each angle.

Angle (deg.)	Flight path length (cm)			
	2012		2013	
	Large	Small	Large	Small
15	3.6	2.1	3.8	1.4
30	3.5	2.1	3.7	1.4
45	3.4	2.1	3.6	1.7
60	1.9	2.0	1.9	1.1
75	1.8	1.7	1.9	1.0
90	1.8	1.7	1.9	1.0

The concrete and iron shields were placed as drawn in **Figure 1** to reduce neutrons from the beam dump. The thickness of iron and concrete were 63 and 50 cm, respectively.

In this experiment, neutrons which indirectly came from the target to the NE213 detector were treated as background events. In order to evaluate background events, measurement with iron shadow bars between the target and smaller and larger NE213 scintillators were also performed. The lengths of iron shadow bars were 60 and 110 cm for smaller and larger scintillators, respectively.

Data about amount of light output of each detector and neutron flight time triggered by the beam pick up scintillator and the neutron detectors were measured by a NIM and CAMAC electronic circuit.

3. Data Analysis

Figure 2 is an example of TOF spectrum of neutrons and γ rays. The start signals were sent by the neutron detector and the stop signals were sent by the beam pick up detector, then the right side events of horizontal axis of TOF spectra are fast particle events. The sharp peak around 2400 ch is prompt γ ray. The kinetic energy of neutron E_n is obtained from the following expression,

$$E_n = m_n \left(\frac{1}{\sqrt{1 - \left(\frac{L}{ct_{\gamma-n} + L} \right)^2}} - 1 \right)$$

where, m_n is the rest mass of the neutron, L is the flight path length, c is the velocity of light, and $t_{\gamma-n}$ is difference of flight times between prompt γ ray and neutron.

Figure 3 shows light outputs of the beam pick up detector. The beam pick up detector counted the number of incident ions and sent start signals of TOF for each event. However, when two or more ions entered to the beam pick up detector simultaneously, it was unable to know which ions cause neutron reaction. Those events were designated as multiple incident events shown in **Figure 3**. The beam intensity was controlled to keep the condition that the number of the multiple incident events is 10 % or less than that of single ones. The multiple incident events were discriminated in the analysis, and the correction factor was introduced.

Charged particle events were distinguished from non-charged particle events by using the veto detector. The light outputs of the veto detector are drawn in **Figure 4**. Non-charged particles, i.e. neutrons and γ rays, less interact in the veto detector, a sharp peak by neutrons and γ rays is shown in low light output region in **Figure 4**. On the other hand, charged particle events has higher light output than non-charged particle events. Charged particle events were distinguished from non-charged particle events.

Inside an NE213 scintillator, neutrons are detected as recoiled protons by neutrons, and γ rays are done as electrons produced by Compton scattering. Because decay time of electron event is shorter than that of proton one, events of neutron and γ ray are able to be separated by using two gate width of light output integration. **Figure 5** indicates neutron and γ ray events discriminated by two gate integration method. The threshold level was determined from ^{241}Am Compton edge, the level corresponds to 0.14 MeV in neutron energy.

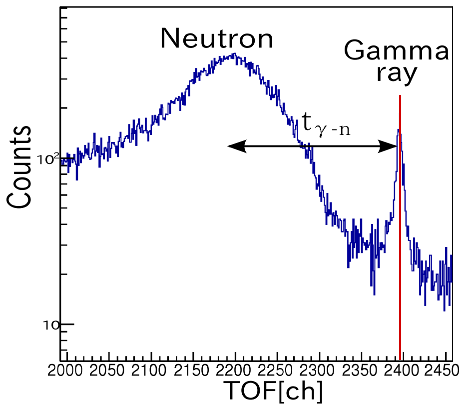

Figure 2: An example of TOF spectrum at 15°

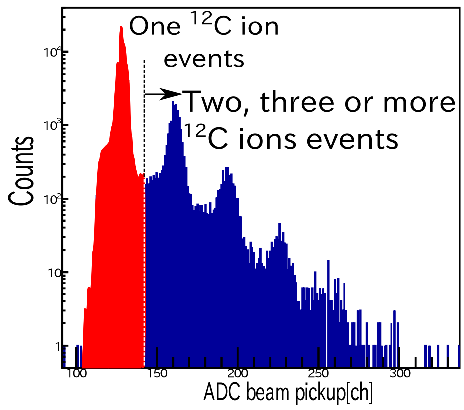

Figure 3: Light outputs of the beam pickup detector at 15°

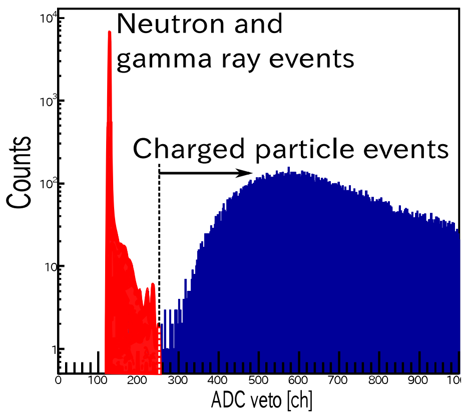

Figure 4: Light outputs of the veto detector at 15°

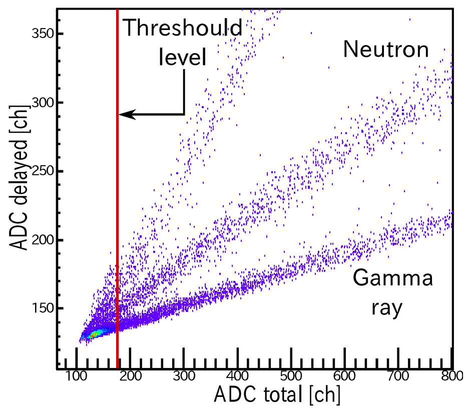

Figure 5: Discrimination of neutron and γ ray events by the two gate integration method at 15°

Neutron DDX $d^2\sigma/dEd\Omega$ was gained from the following equation,

$$\frac{d^2\sigma}{dEd\Omega} = \frac{N_n(E)F}{N_{ion}\varepsilon(E)\rho\Delta\Omega\Delta E}$$

where N_n is the number of the detected neutron, N_{ion} is the number of the incident carbon ion, ε is neutron detection efficiencies of the NE213 scintillators obtained by using SCINFUL-QMD[7], ρ is the surface density of the target, $\Delta\Omega$ is the solid angle of each neutron detector, and ΔE

is the width of the energy bin, F is the factor which contains the correction of multiple ion incidence events and detection dead time. The TTNY was also obtained in the same manner. Then, the background neutrons should be removed from the neutron yields. To obtain the DDX and the TTNY, neutron energy spectra with shadow bars were subtracted from those without shadow bars.

4. Results

The DDX at angles of 15°, 30°, 45°, 60°, 75° and 90° are presented in **Figure 6**. Red and blue circles are experimental data of this experiment (2013) and previous experiment (2012), respectively. The error bar contains only statistic errors. Two experimental results are close except for the region below several MeV at 15°.

The calculation results of three Monte Carlo simulation codes, PHITS 2.62, FLUKA 2011.2b[8] and GEANT4 9[9, 10], are compared with the experimental data. For heavy ion interaction, JQMD (JAERI Quantum Molecular Dynamics) model was used in PHITS, RQMD (Relativistic Quantum Molecular Dynamics) model and BME (Boltzmann Master Equation) model were employed in FLUKA, and INCL++ (Lie'ge Intra Nuclear Cascade) model was done in GEANT4. The best agreement calculation with experiment data is PHITS-JQMD, and the 2013 experimental data agree with PHITS better than previous experimental ones. However, PHITS and others agree poorly in several MeV neutron energy region at forward angles. The background estimation in this region might have some problems.

The TTNY of experimental and calculated data are shown in **Figure 7**. The figure indicates that PHITS calculation overestimates experimental data above 1 MeV for all directions. This could be because PHITS was not able to reproduce the neutron production by the decelerated heavy ions in the target. In that case, the neutron high energy component of DDX by lower energy heavy ion incidence could not be reproduced.

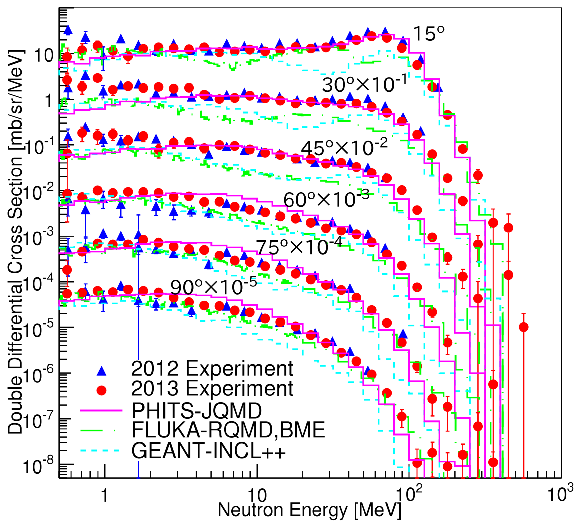

Figure 6: Neutron DDX for 100 MeV/u ^{12}C + C reaction

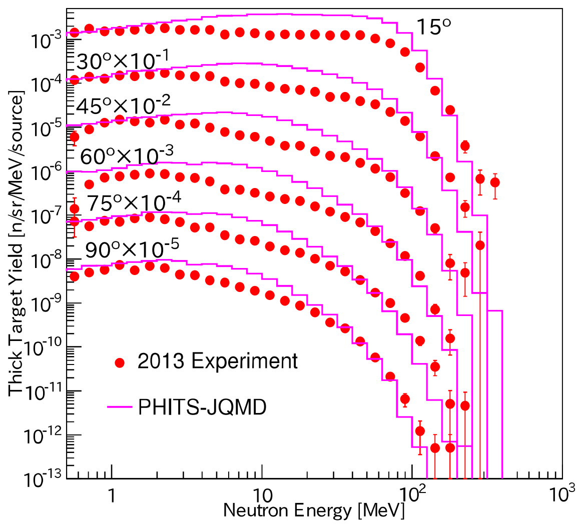

Figure 7: TTNY for 100 MeV/u ^{12}C + C reaction

5. Conclusion

For investigation of neutron production by decelerated 290 MeV/u carbon ions in a human body, neutron DDX and TTNY from 100 MeV/u carbon incident on carbon were measured by TOF method using NE213 liquid organic scintillators down to 0.6 MeV. The results were close to the previous experiment. PHITS calculation is able to reproduce the DDX above a few MeV energy region compared with other simulation codes, however overestimates TTNY.

Acknowledgement

This work is supported by grand-aid of ministry of education (KAKENHI 22360406) in Japan and was performed as a Research Project with Heavy Ions at NIRS-HIMAC.

References

[1] B. Clasie, et al., Assessment of out-of-field absorbed dose and equivalent dose in proton fields, Med. Phys. 37 (2010), pp. 311-321.

[2] E. J. Hall, Intensity-modulated radiation therapy, protons, and the risk of second cancers, Int. J.Radiat. Oncol. Biol. Phys. 65 (2006), pp. 1-7.

[3] T. Sato, K. Niita, N. Matsuda, S. Hashimoto, Y. Iwamoto, S. Noda, T. Ogawa, H. Iwase, H. Nakashima, T. Fukahori, K. Okumura, T. Kai, S. Chiba, T. Furuta and L. Sihver, Particle and Heavy Ion Transport Code System PHITS, Version 2.52, J. Nucl. Sci. Technol. (2013), pp. 913-923.

[4] D. Satoh, D. Moriguchi, T. Kajimoto, H. Uehara, N. Shigyo, M. Ueyama, M. Yoshioka, Y. Uozumi, T. Sanami, Y. Koba, M. Takada, and N Matsufuji, Measurement of neutron-production double- differential cross-sections on carbon bombarded with 290-MeV/nucleon carbon and oxygen ions, Nucl. Instrum. Meth. A644 (2011), pp. 59-67.

[5] D. Moriguchi, Y. Nakamura, T. Kajimoto, Y. Koba, M. Ueyama, M. Yoshioka, N. Shigyo, Y. Uozumi, D. Satoh, T. Sanami, M. Takada and N. Matsufuji, Measurement of Neutron-Production Cross Sections for 290 MeV/u Carbon Ion Incidence, J. Korean Phys. Soc. 59 (2011), pp. 1789-1792.

[6] N. Shigyo, Y. Uozumi, H. Uehara, T. Nishizawa, T. Mizuno, D. Satoh, T. Sanami, Y. Koba, M. Takada and N. Matsufuji, Measurement of 100 MeV/u carbon incident neutron production cross sections on a carbon target, Proceedings of the 2012 Symposium on Nuclear Data, INDC(JPN)-198, JAEA-Conf 2013-002 (2013), pp. 137-142.

[7] D. Satoh, T. Satoh, N. Shigyo and K. Ishibashi, SCINFUL-QMD: Monte Carlo Based Computer Code to Calculate Response Function and Detection Efficiency of a Liquid Organic Scintillator for Neutron Energies up to 3 GeV, JAEA-Data/Code 2006-023, Japan Atomic Energy Agency, (2006).

[8] G. Battistoni, et al., Proceedings of the Hadronic Shower Simulation Workshop 2006, Fermilab 6–8 September 2006, M. Albrow, R. Raja eds., AIP Conference Proceeding 896 (2007), pp. 31-49.

[9] S. Agostinelli, et al., Geant4 a simulation toolkit, Nucl. Instrum Meth. A506 (2003), pp.250-303.

[10] J. Allison, et al., Geant4 Developments and Application, Nucl. Sc. 53 No.1 (2006), pp.270-278.

25. Light Mass Fragment Production DDXs of 70 MeV Proton, Helium and Carbon Induced Reactions

Toshiya Sanami
Applied research laboratory, High energy accelerator research organization,
Oho 1-1, Tsukuba, Ibaraki 305-0801 JAPAN
Email: toshiya.sanami@kek.jp

Double-differential cross sections of light-mass fragment (LMF) production were measured for 70 MeV protons, helium nuclei and carbon nuclei on carbon and aluminum targets. The data clarify the dependence of LMF production on the type of incident particle in the energy range of tens of MeV. The LMFs of Li, Be, B, and C were measured using Bragg curve counters at angles of 30, 60 and 90 degrees. The results were compared with theoretical calculations. The calculation results are in fair agreement with the experimental data for the carbon target but underestimate for the aluminum target.

1. Introduction

The double-differential cross section (DDX) is important in estimating particle transportation and energy deposition. Recent progress in ion-beam application requires precise calculation and measurement for the amount of energy deposition in the region of tens of MeV. Several Monte Carlo codes have been used for this purpose with detail particle tracking for an actual three-dimensional structure. The codes treat a nuclear reaction during particle transportation in matter. Several theoretical models have been employed to describe the nuclear reactions. The applicable energy range and particle types of the models should be carefully evaluated though comparison with experimental data. Experimental data for light-mass fragment (LMF) production are required because the data are generally not sufficiently available in the region of tens of MeV.

Several experimental data have been obtained for a proton and carbon nucleus as an incident particle [1–9]. The data were employed to improve reaction models and parameters of theoretical calculation. The Monte Carlo codes switch reaction models at the early stage of a nuclear reaction depending on the incident particle type, employing an intra-nuclear cascade model for the nucleon and quantum molecular dynamics for the nucleus. Thus, LMF production data for the same energy but different particle types would help to clarify the dependency of the production on the type of incident particle.

From this viewpoint, the present study obtained experimental data of LMF production reactions induced by a proton, helium nucleus or carbon nucleus on a carbon or aluminum target with impinging energy of 70 MeV using a Bragg curve counter (BCC). Results for the fragment DDX as well as an outline of the data taking procedure and results of theoretical calculations are presented.

2. Experimental

The details of the experimental apparatus and procedure were the same as those for measurements of proton-induced reactions described in the literature [1–9]. The experiments were carried out using the NIRS 930 cyclotron at the National Institute of Radiological Science (NIRS). Figure 1 is a photograph of the experimental setup.

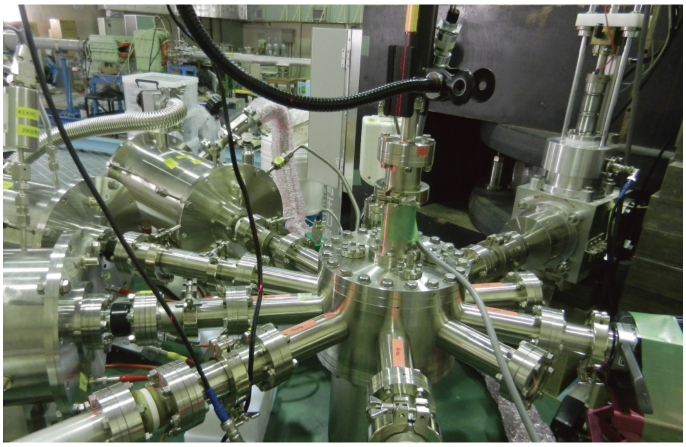

Fig. 1 Experimental setup

A projectile beam (proton beam of 70 MeV, helium beam of 70 MeV and carbon beam of 6 MeV/n (72 MeV in total)) was focused to a spot 5 mm in diameter on a target foil placed at the center of a scattering chamber. The target foils were graphite with density of 206 μg/cm^2 and Al with thickness of 0.8 μm. Fragments from the target were measured by BCCs mounted on ports of the scattering chamber at angles of 30, 60 and 90 degrees.

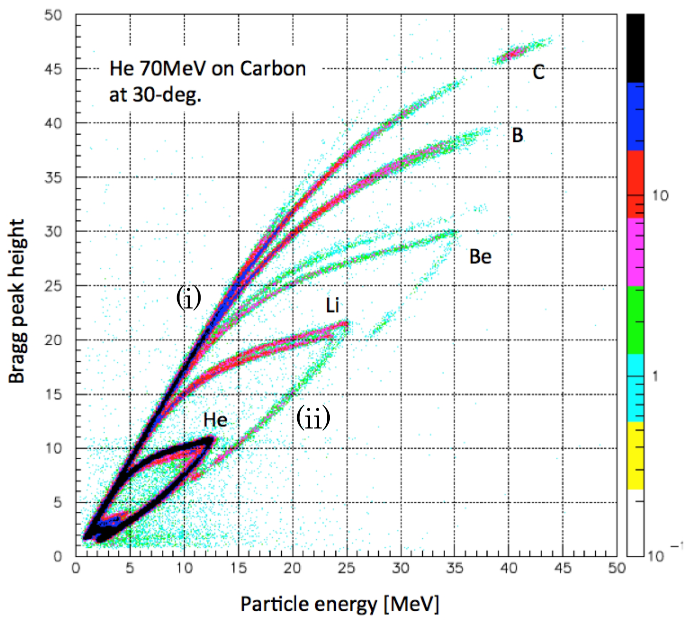

Fig. 2 Two-dimensional spectrum of the Bragg peak versus energy at a laboratory angle of 30 degrees for 70-MeV helium on a carbon target

The BCC is a parallel-plate ionization chamber with a grid. The details of the BCC, operation parameters and readout electronics have been described elsewhere [1]. Figure 2 shows the two-dimensional spectrum of the Bragg peak versus energy at a laboratory angle of 30 degrees for 70-MeV helium on the carbon target, as an example. Fragments from He to C are clearly separated in the figure. In addition, the low-energy events (i), which were too low in energy to form a Bragg peak, were separated using a range–energy plot derived from the time difference between signals from the cathode and anode [1]. The events shown in (ii) were too high in energy to stop within the BCC length. The missing energies of these events were compensated by calculation [2]. These two procedures are essential to cover the required energy range of the fragment measurement.

After identifying particles from the scatter plot, energy spectra were obtained for each fragment. The energy spectra were normalized by the number of incident particles and solid angle. The number of incident particles was obtained from a Faraday-cup measurement for each run. The solid angle was deduced analytically and confirmed by counting α-particles from a ^{241}Am check source placed instead of the target.

3. Result and discussion

Figures 3–6 show experimental results of the DDX at 30, 60 and 90 degrees and the angular differential cross section (ADX) for beryllium or carbon emission when a proton, helium nucleus or carbon nucleus on a carbon or aluminum target. Dots in the figures correspond to experimental results. Lines are the calculation results obtained using PHITS code, version 2.52, with default options; i.e., INCL and QMD codes for the incident of nucleon (proton) and nucleus (helium and carbon), respectively, in the first stage of the nuclear reaction, and GEM code for the evaporation process [10,11]. The ADX for experimental data are obtained by simply summing data points, and there is no extrapolation for missing data because of the finite low energy threshold. The low energy threshold extends below 10 MeV, which is sufficiently low to observe fragment emission suppression due to the Coulomb barrier effect for a heavy projectile.

Figures 3 and 4 show that the calculation is in good agreement with experimental results for the carbon target except for components of the direct reaction that have a peak structure in Fig. 4 for carbon emission in the case of incident carbon and helium nuclei. The components would be described by treating elastic and inelastic processes for the nucleus with information of low-lying levels. Thus, the ADX of the calculation represents the tendency of experimental data well for the carbon target. There is only large discrepancy for the proton data at large emission angles; such values are difficult to measure because of the relatively low energy.

In contrast, as shown in Figs. 5 and 6, the calculation underestimates both beryllium and carbon emission from the aluminum target for all three incident particles. This underestimation is partially due to the reason given in the case of the carbon target (i.e., a lack of elastic and inelastic processes) because the maximum energies of the emitted particles obtained by calculation are always smaller than those observed by experiment. Another factor, such as ambiguity of the total reaction cross section, must also be involved because the underestimation was observed for not only carbon but also beryllium emission. ADX results also show discrepancy between calculation and experiment.

4. Conclusion

Double-differential cross sections of light-mass fragment (LMF) production were measured for 70 MeV protons, helium nuclei and carbon nuclei on carbon and aluminum targets using Bragg curve counters at angles of 30, 60 and 90 degrees. The experimental results were compared with theoretical calculations. The calculation results are in fair agreement with the experimental data for the carbon target but underestimate for the aluminum target.

Acknowledgements

The authors wish to thank the operators and supporting crew of the NIRS cyclotron for their help in performing the beam experiment. The experiment was performed with the support of a Grant-in-Aid from the Ministry of Education "KAKENHI" (24561051, T. Sanami, KEK).

References

[1] T. Sanami, M, Hagiwara, M. Takada and M. Baba, “Measurement of fragment production DDX of 72 and 144 MeV ^{12}C beam induced reaction on carbon using Bragg Curve Counter”, *Proc. 2009 Symp. Nucl. Data*, 2010 Dec; JAEA-Conf 2010-005: pp.87-91.

[2] T. Sanami , M. Hagiwara, T. Ohishi, M. Baba, M. Takada., *Nucl. Instrm. Meth.* 2008 Feb;A589 : pp.193-201.

[3] M. Hagiwara, T. Sanami, T. Ohishi, M. Baba, M. Takada, *Nucl. Instrm. Meth*. 2008 Mar;A592 : pp.73-79.

[4] T.Sanami, M. Hagiwara, H.Iwase, " Angular distribution of light fragments for proton induced reaction at intermediate energies”, *Proc. 2011 Symp. Nucl. Data*, 2012 Jul; JAEA-Conf 2012-001: pp.189-194.

[5] T. Sanami, M. Hagiwara, M. Takada, M. Baba, “Recent progress of fragment measurement from tens of MeV proton induced reaction using Bragg Curve Counter”, *Proc. 2008 Symp. Nucl. Data,* 2009 Oct; JAEA-Conf 2009-004: pp.111-116.

[6] T. Sanami, M. Hagiwara, H. Iwase, M. Takada, D. Satoh, Y. Iwamoto, S. Kunieda, H. Yashima, A. Tamii, M. Baba, "Fragment DDX measurement of proton induced reactions on light-medium nuclei for energy range from reaction threshold to a few hundred MeV ", *Journal of Korean Physics Society* 2011 Aug; 59: pp.1805-1808.

[7] T. Sanami, M. Hagiwara, H. Iwase, M. Takada, D. Satoh, H. Yashima, T. Kajimoto, Y. Iwamoto, S. Kamada, Y. Nakane, S. Kunieda, A. Tamii, K. Hatanaka, “Experimental studies of light fragment production cross section for nucleon induced reaction at intermediate energies”, *Proc. 2010 Symp. Nucl. Data,* 2011 Sep; JAEA-Conf 2011-002: pp.59-64.

[8] M. Hagiwara, T. Sanami, T. Ohishi, M. Baba, M. Takada, "Differential cross sections on fragment ($2 \leq Z \leq 9$) production for carbon, aluminum and silicon induced by tens-of-MeV protons", *Journal of Nuclear Science and Technology*, 2012 Jun; 49(6): pp.571-587.

[9] T. Sanami, “Target Dependency of Light Mass Fragment Production DDX for 6 MeV/u Carbon Induced Reaction”, *Proc. 2012 Symp. Nucl. Data,* 2013 Oct;JAEA-Conf 2013-002:pp.185-190.

[10] T. Sato, K. Niita, N. Matsuda, S. Hashimoto, Y. Iwamoto, S. Noda, T. Ogawa, H. Iwase, H. Nakashima, T. Fukahori, K. Okumura, T. Kai, S. Chiba, T. Furuta and L. Sihver, "Particle and Heavy Ion Transport Code System PHITS", Version 2.52, *J. Nucl. Sci. Technol.* 2013 Sep; 50(9):pp. 913-923.

[11] J. Cugnon, A. Boudard, S. Leray, and D. Mancusi, "New Features of the INCL4 Model for Spallation Reactions", *J. Korean Phys. Soc.* 2011 Aug; 59: pp.955-958.

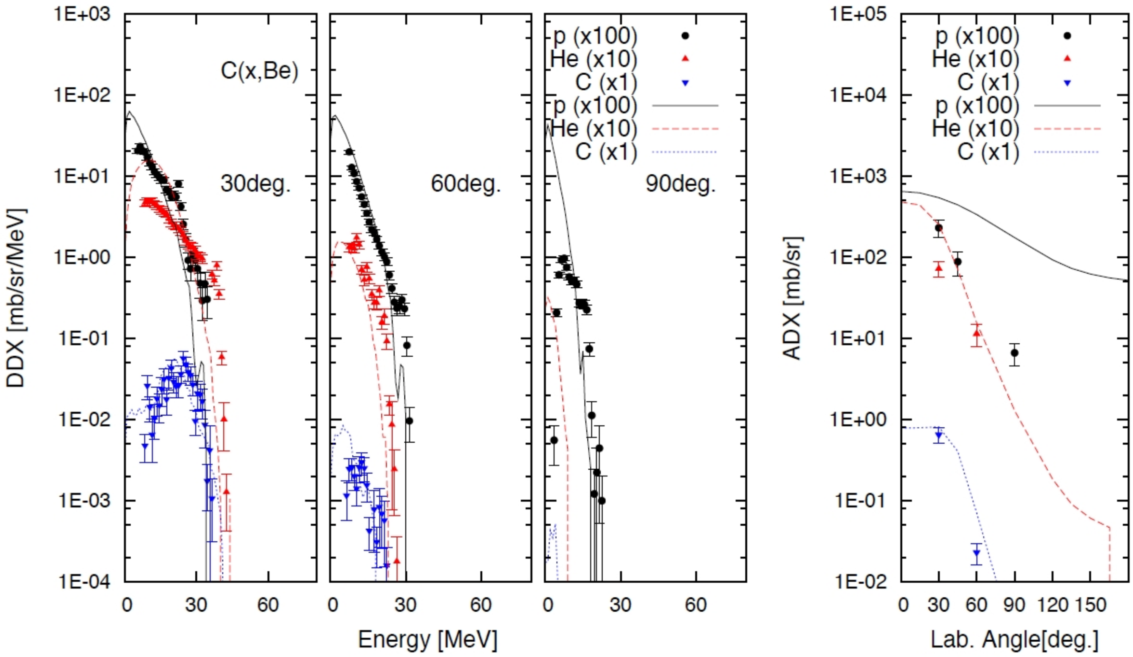

Fig. 3 DDXs and ADX of beryllium emission for various projectiles on carbon target.

Dot:Experimental data, Line:Caluculation result

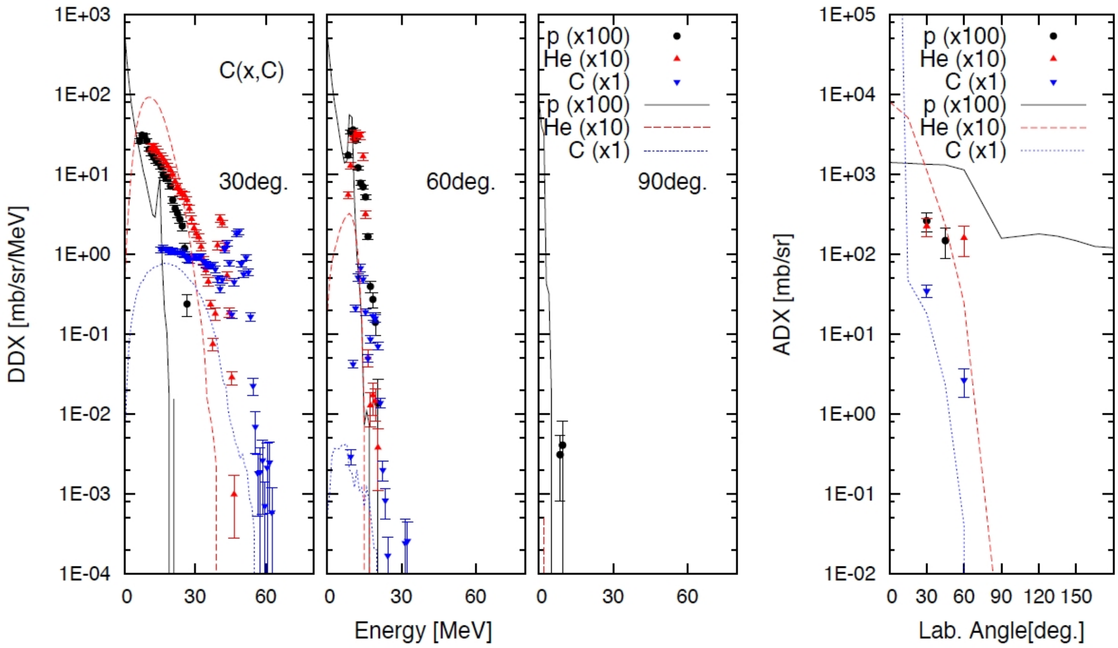

Fig. 4 DDXs and ADX of carbon emission for various projectiles on carbon target.

Dot:Experimental data, Line:Caluculation result

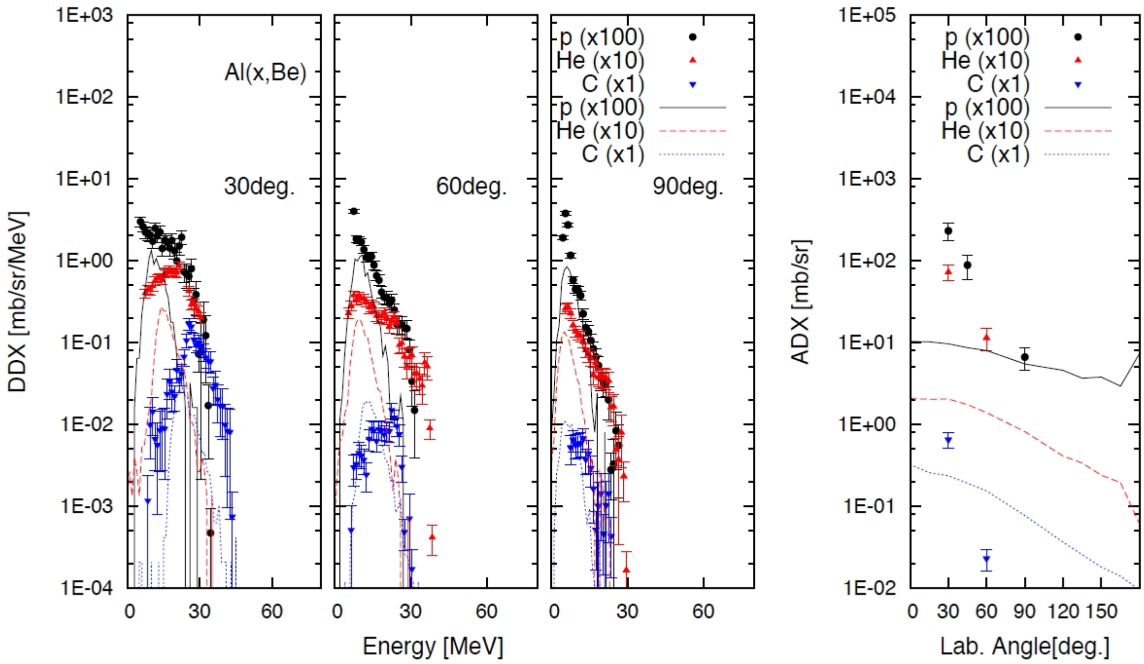

Fig. 5 DDXs and ADX of beryllium emission for various projectiles on aluminum target.
Dot:Experimental data, Line:Caluculation result

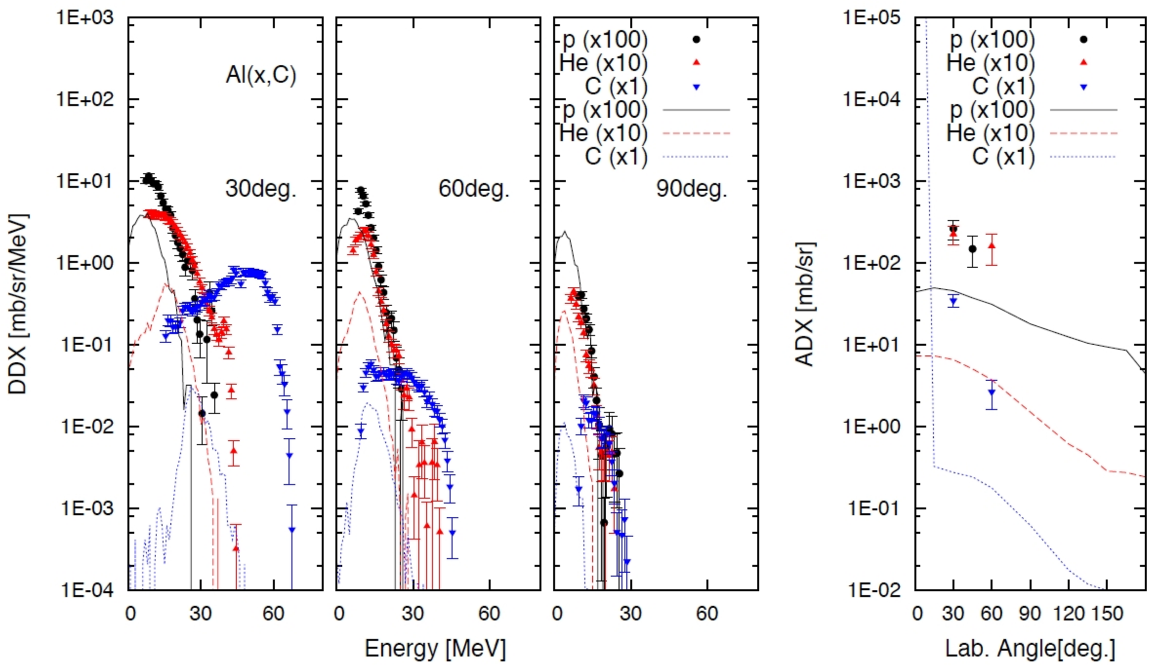

Fig. 6 DDXs and ADX of carbon emission for various projectiles on aluminum target.
Dot:Experimental data, Line:Caluculation result

26. Feasibility Study on High-dynamic-range Neutron Spectrometer with Continuously Thick-adjustable Moderator/Absorber

Shingo TAMAKI, Isao MURATA
Division of Electrical, Electronic and Information Engineering, Osaka University
2-1 Yamadaoka, Suita, Osaka 565-0871 Japan
e-mail:stamaki@ef.eie.eng.osaka-u.ac.jp

Neutron spectrum measurement is very important for various applications. However, it is very difficult to measure it in a wide energy range. In addition, there is a few ways to measure such neutron energy spectrum and it is said that their results are sometimes doubtful for practical use, for example, BNCT. In this study, we numerically examine a feasibility of a new neutron spectrometer having liquid moderator and absorber, whose thicknesses can be adjusted continuously so as to utilize a quasi-continuous response function.

At first, we compute the detector response function with MCNP-5. After that, we perform numerical tests to confirm the reproducibility of quasi-mono-energetic neutron energy spectra, using this detector model. As a result, we confirm the reproducibility of neutron energy spectra in energies between 0.01 eV and a few MeV, if the statistical error could be suppressed within 10 %.

In future, we will confirm the reproducibility of more general neutron energy spectra, for example, fission spectrum, and design the detector which has a structure to reduce the effect from room-scattering neutrons.

1. Introduction

Boron Neutron Capture Therapy (BNCT) is greatly concerned as a new treatment for cancer, which can kill only tumors suppressing damage to normal tissues. In BNCT, cases are reported only using a nuclear reactor now because of requiring strong low-energy neutron sources. Recently, accelerator based neutron sources (ABNS) which can be constructed in medical facilities such as hospitals are being developed for BNCT. However, their intensities are still weak, and patients should thus be positioned near the target. It causes difficulty to moderate neutrons enough, and the neutron energy spectrum is distorted depending on accelerators. In order to use the ABNS based neutron field for BNCT, we have to know its absolute energy spectrum accurately. In the present study, we carry out conceptual design of a new high-performance neutron spectrometer with a high-dynamic range from 0.01 eV to a few MeV and confirm its feasibility.

Bonner Sphere System (BSS) is one of the famous neutron energy spectrum measuring techniques. BSS requires moderator shells which have several fixed thicknesses. However, the number of them is limited, which means that the number of the response functions for neutron energy is limited. Nevertheless, it is generally unreal to make a lot of shells. Consequently, it causes poor energy resolution and low accuracy in the measured energy spectrum. In this study, we examined the feasibility of a new neutron spectrometer with a quasi-continuous response function. This could be realized by using liquid moderator and absorber which can be adjusted their thicknesses continuously.

2. Design of spectrometer

2.1. Theory

Radiation detector has its own response function $R(E, E')$. Here, E is incident radiation energy and E' is pulse height of detector. For example, using a commonly used liquid scintillator, NE213, we obtain a variable pulse height spectrum depending on incident neutron and γ-ray energy E. In this study, we used a ^{3}He neutron detector covered with moderator and absorber, like Bonner Sphere. In this case, the measured data will be the number of neutron counts C, which is an integral value of E'. This value can be deduced theoretically with a response function $R(E)$ defined as a probability to detect incident neutrons with energy E. We finally obtain the integral count C as $C = \int R(E)\phi(E)\, dE$, if neutrons having a spectrum $\phi(E)$, incident to the detector.

In the present spectrometer, the response function is varying because we can adjust the moderator's and absorber's thicknesses continuously. In other words, if we use many kinds of detectors having different combination of the moderator's and absorber's thicknesses, we will obtain many kinds of detector response values, which is as the same number as the number of moderator-absorber combinations. In the case we use m kinds of detectors with different moderator-absorber combinations and digitize the neutron energy into n groups, the count C is expressed as m dimensional vector $\boldsymbol{C} = \boldsymbol{R}(E) \cdot \boldsymbol{\phi}(E)$, where $\boldsymbol{R}(E)$ is a response function represented as $m \times n$ dimensional matrix and $\boldsymbol{\phi}(E)$ neutron energy spectrum as n dimensional vector. If we know detector's count $\boldsymbol{C}$ and the response function $\boldsymbol{R}(E)$, we can obtain the neutron energy spectrum $\boldsymbol{\phi}(E)$ by solving an inverse problem of this matrix equation.

Although several methods are known to solve inverse problem for radiation detection, most of them require "initial guess spectrum" containing appropriate priori information, and sometimes bring us unphysical solutions, i.e., oscillating or negative spectrum, due to statistical errors included in the measured result. In order to avoid these problems, we employed Bayesian spectrum unfolding method [1].

2.2. Detector model

In order to obtain an accurate neutron spectrum in good energy resolution with the present method, dimension m of the count vector $\boldsymbol{C}$, i.e., the number of response function, is an important factor, because generally, the larger m is, the better the accuracy of the estimated neutron spectrum is. In principle, we can increase m by changing the neutron sensitive section like neutron moderator, absorber and so on. We finally designed a conceptual model having liquid moderator and absorber. By adjusting the thickness continuously, quasi-continuously varying detector response function was successfully obtained.

The conceptual model is shown in Fig.1. In this model, a broad parallel neutron beam was employed. As shown in the figure, neutrons are incident to the spectrometer from a fixed direction. We utilized a ^{3}He proportional detector as a neutron detector, whose radius was 1 inch and gas pressure was 1.013 MPa. The absorber and moderator were arranged in front of the detector. Properties of used absorber and moderator are summarized in Table 1. These materials are selected because they are liquid in room temperature. Also we took into account how easy to handle and the response function shape.

Table 1 Materials of detector's moderator and absorber

	Material	**Thickness [mm]**	**Melting Point[K]**	**Boiling point [K]**
Absorber	$B(OCH_3)_3$	0～30	245 (-28℃)	341 (+68℃)
Moderator	C_6H_{14}	0～170	178 (-95℃)	342 (+69℃)

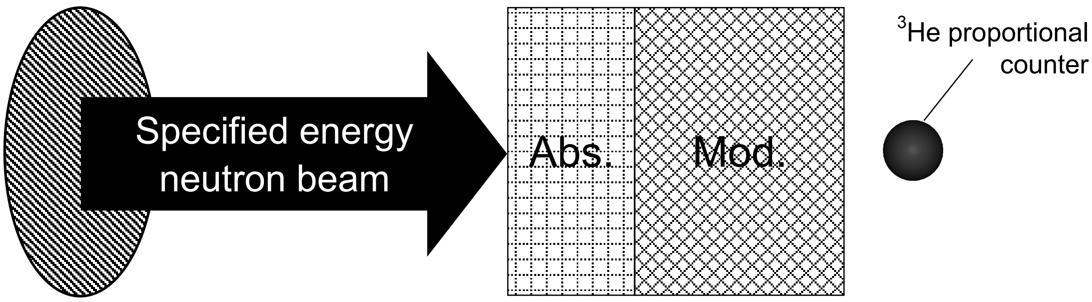

Fig. 1 Conceptual model of the present spectrometer. Emitted neutrons have a parallel broad beam shape and its energy E is $E_j < E \leq E_{j+1}$, here E_j $(j = 0,1,\cdots,n)$ is energy bin of neutron spectrum $\boldsymbol{\phi}(E)$.

2.3. Response function

The response function $\boldsymbol{R}(E)$ was evaluated with A General Monte Carlo N-Particle Transport Code, Version 5 (MCNP-5) [2]. In this study, the energy bin is set to be 10 bins per decade to realize quasi-continuous response function. For this purpose, we calculated the detector response to various absorber and moderator combinations formed by increasing their thicknesses by 1 mm. Practical energy structure shows a small bin ($\mathrm{E_j} < E \leq \mathrm{E_{j+1}}$) to calculate a mean reaction rate of ^{3}He(n,p) reaction. The response was normalized by the emitted neutron flux so as to be per 1 neutron/cm^2/sec incidence. We obtained finally 201 response functions shown in Fig. 2. It can be confirmed that the response functions are changing quasi-continuously.

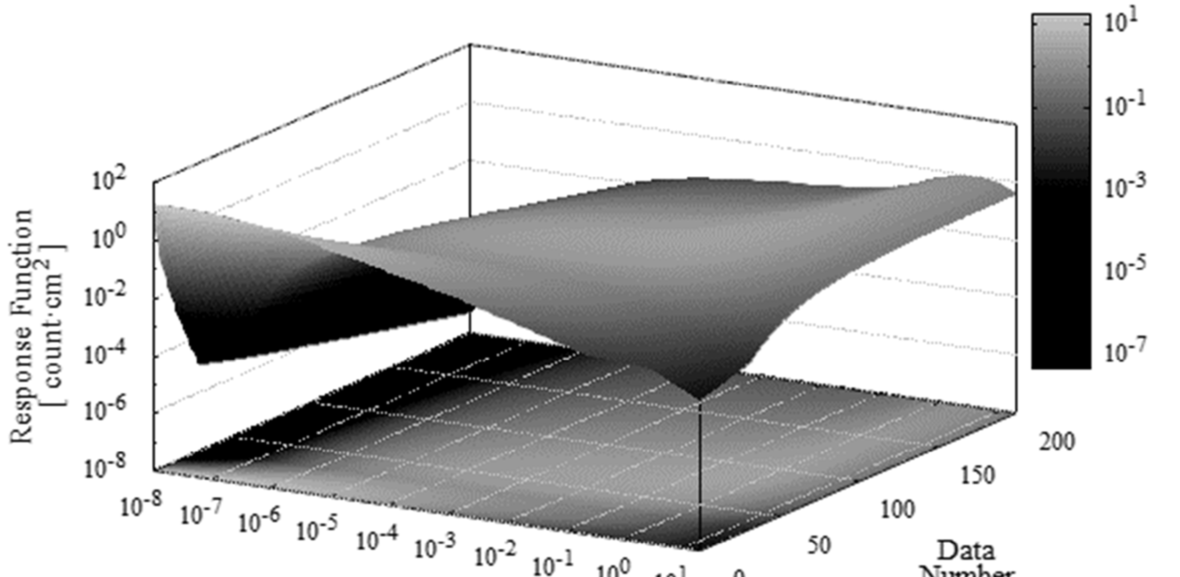

Fig. 2 Response functions of detector model. The brighter the graph color is, the larger the detector's response function value is.

3. Numerical test

As mentioned in section 2.1, if we know statistical-error free detector count $\boldsymbol{C}$ and correct response function $\boldsymbol{R}(E)$, and assuming $\boldsymbol{C} = \boldsymbol{R}(E) \cdot \boldsymbol{\phi}(E)$ is strictly met mathematically, we could obtain the exact neutron energy spectrum $\boldsymbol{\phi}(E)$ by a certain unfolding process. However, in case count $\boldsymbol{C}$ includes statistical error, obtained energy spectrum could be different from the true spectrum. We thus performed numerical tests to confirm the energy spectrum reproducibility in the case that statistical errors are included in the measured count $\boldsymbol{C}$.

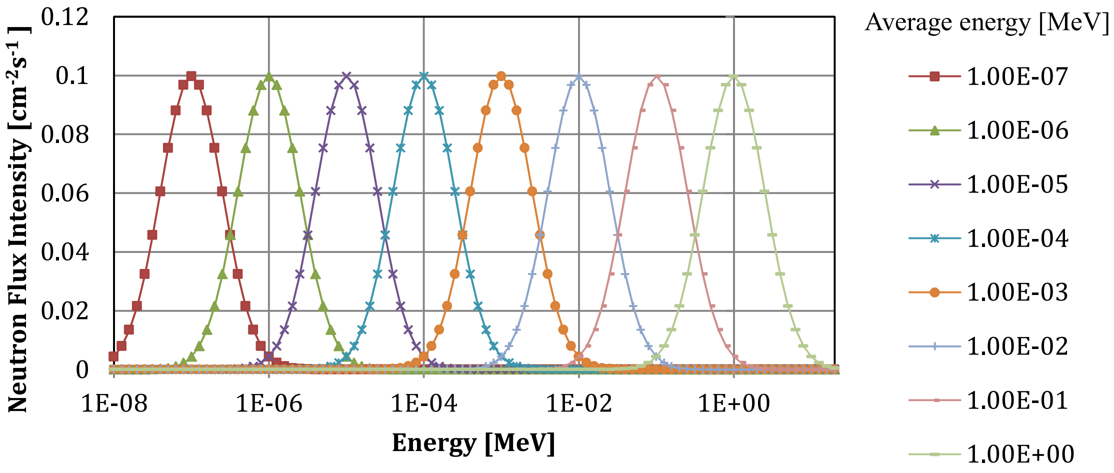

Fig. 3 True energy spectra $\boldsymbol{\phi_t}(E)$. Value in legend means the average energy of each spectrum.

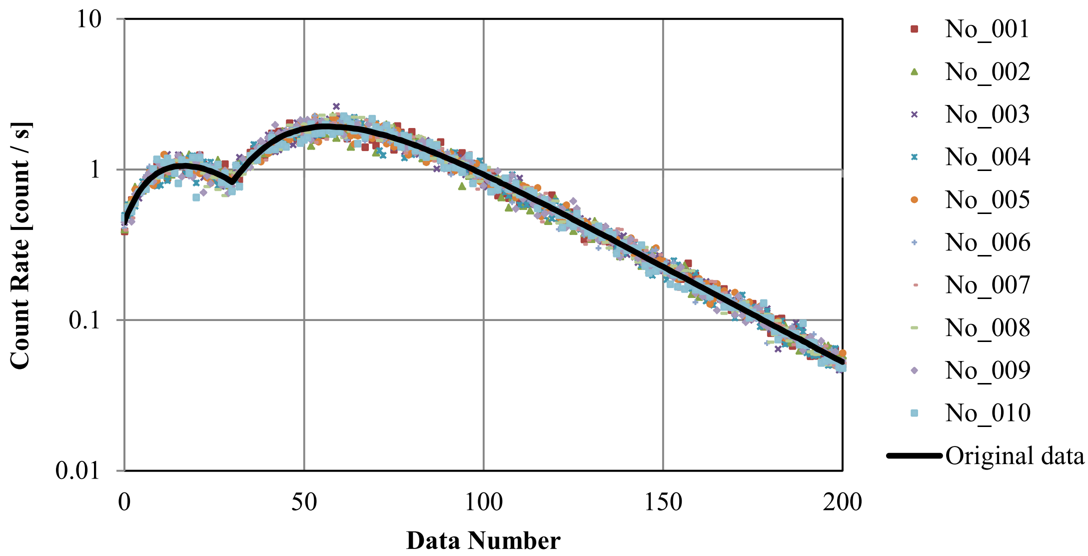

Fig. 4 Example of $\boldsymbol{C}$ as solid line and C' as other ten spectra in which statistical errors of 10% are added. The average energy of the spectrum is 1 keV as shown in Fig. 3. Each of No_001 to No_010 was made by employing a different random number sequence.

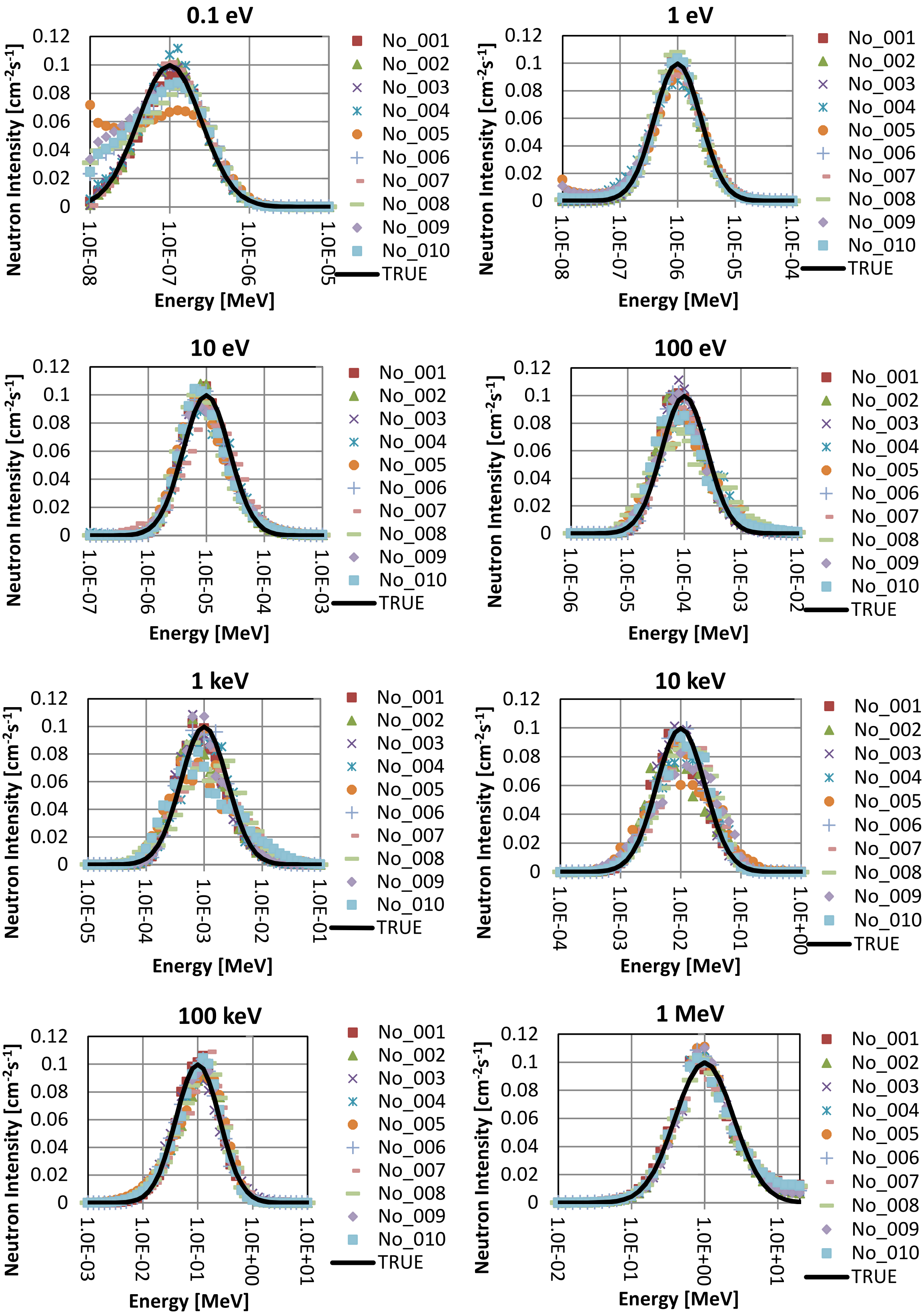

Fig. 5 Numerical test results. TRUE is a true energy spectrum shown in Fig. 3. Numbers, e.g., No_001, means $\boldsymbol{C}'$ spectra were prepared by employing different random number sequences.

At first, we assumed neutron energy spectra shown in Fig. 3 as true energy spectra $\boldsymbol{\phi_t}(E)$. The true count $\boldsymbol{C}$ to be measured is obtained by the product of $\boldsymbol{R}(E) \cdot \boldsymbol{\phi}(E)$. In this numerical test we ignored errors of $\boldsymbol{R}(E)$. After that, we added statistical error based on normal distribution to the count $\boldsymbol{C}$ and the obtained count was denoted as $\boldsymbol{C'}$. To simplify the numerical test calculation, we employed normal distribution approximately instead of Poisson distribution by assuming that the count $\boldsymbol{C'}$ would be sufficiently large. Finally, we unfolded $\boldsymbol{C'}$ with $\boldsymbol{R}(E)$ by Bayesian spectrum unfolding method. The obtained spectra $\boldsymbol{\phi_{inf}}(E)$ were compared with the initial spectra $\boldsymbol{\phi_t}(E)$ as shown in Fig. 3 in order to examine the reproducibility.

Figure 4 shows an example of $\boldsymbol{C}$ and $\boldsymbol{C'}$ in the case of neutron average energy of 1 keV, the spectrum of which is shown in Fig. 3. In this case 10 % statistical error is artificially added.

4. Results and Discussion

Numerical test result for each energy spectrum $\boldsymbol{\phi_{inf}}(E)$ is shown in Fig. 5. Comparing $\boldsymbol{\phi_t}(E)$ with $\boldsymbol{\phi_{inf}}(E)$, we confirmed the energy spectra were reproduced fairly well in energies from 0.01 eV to a few MeV. This is the case for statistical error of 10 %. We carried out other cases in which errors less than 10 % were artificially added. From the result, reproducibility was confirmed if statistical errors could be suppressed within 10 %. However, between 100 eV and 10 keV region in Fig. 5 (10 % error case), the energy resolution is sometimes a little bit poor. It would be caused by the shape of response function as follows: Due to the property of moderator and absorber shown in Table 1, the response function would not change meaningfully in the energy region, resulting in the present poor energy resolution. It is expected that this problem could be solved by examining moderators or absorbers more carefully.

5. Conclusion

In this study, we examined the feasibility of a new high-dynamic-range neutron spectrometer which has quasi-continuous response function by using liquid absorber and moderator. As a result of numerical tests using this detector model, we confirmed the energy spectrum reproducibility in the energy range between 0.01 eV and a few MeV, if the statistical error in the measured spectrum could be suppressed within 10 %. In conclusion, we could obtain neutron energy spectrum precisely in this region, by developing the presently proposed spectrometer which can adjust the thicknesses of absorber and moderator by using liquid materials.

In the next step, we are planning to examine reproducibility of more complex or general energy spectra, like fission spectrum, to confirm applicability of the present spectrometer to real cases. Hereafter, we will design and develop a proto-type spectrometer having a side moderator and absorber structure to suppress the effect from room-scattering neutrons.

Reference

[1] S. Iwasaki. A new approach for unfolding PHA problems based only on the Bayes Theorem. In Proceedings of the 9th International Symposium on Reactor Dosimetry; 1996 September 2-6; Singapore; 1998. pp. 245–252.

[2] X-5 Monte Carlo Team. MCNP –A General Monte Carlo N-Particle Transport Code, Version 5, Volume I: Overview and Theory, LA-UR-03-1987. USA: Los Alamos National Laboratory; 2003.

27. Scattering Problems in Complex Scaling Method: Scattering Cross Sections for Various Potential Systems

Myagmarjav Odsuren[1,2], Masayuki Aikawa[3], Kiyoshi Katō[3], Takayuki Myo[4,5]
[1] Meme Media Laboratory, Hokkaido University, Sapporo 060-8628, Japan
[2] Nuclear Research Center, National University of Mongolia, Ulaanbaatar 210646, Mongolia
[3] Faculty of Science, Hokkaido University, Sapporo 060-0810, Japan
[4] General Education, Faculty of Engineering, Osaka Institute of Technology, Osaka 535-8585, Japan
[5] Research Center for Nuclear Physics (RCNP), Osaka University, Ibaraki 567-0047, Japan
e-mail: odsuren@nucl.sci.hokudai.ac.jp

We investigate the total and partial scattering cross sections for various potential systems. In order to obtain the decomposition of scattering cross sections into the resonance and the residual continuum terms, the complex scaled orthogonality condition model and the extended completeness relation are used.

1. Introduction

The studies of scattering problems in the nuclear science have been developed by using various experimental techniques and theoretical methods so far. Recently, with the development of unstable nuclear beam experiments, much interest has been concentrated on many-body resonances. As a very promising method, the complex scaling method (CSM) [1] has been applied to those resonance problems. This approach seems to be very promising to unify the description of the nuclear structure, and reactions and also in nuclear data evaluations, especially, for light nuclear mass systems [2].

In this work, we study the scattering phase shifts using CSM. The scattering phase shifts have been shown to be calculated from the continuum level density (CLD) [3]. We develop the method of calculating CLD to investigate the effects of the resonant states which is related to the nuclear structures, separated from continuum states providing background contributions in the phase shifts. This new method is applied to the complex scaled orthogonality condition model [4] of several scattering systems including the n-α and α-α systems. The background phase shift is also obtained by using the residual continuum solutions in CSM. We discuss the problems of scattering in this framework, and show that this method is very useful in the investigation of the effect of the resonance in the observed scattering cross sections.

2. Evaluation and discussion

The CLD $\Delta(E)$ is given as

$$\Delta(E) = -\frac{1}{\pi}\,\mathrm{Im}\left\{Tr\left[G(E) - G_0(E)\right]\right\}, \qquad (1)$$

where $G(E)=(E-H)^{-1}$ and $G_0(E)=(E-H_0)^{-1}$ are the full and free Green's functions, respectively. In this study, the Hamiltonian H and H_0 are transformed by using the CSM.

The CLD is related to the scattering phase shifts δ and it can be expressed by following form in the single channel case [5]:

$$\Delta(E)=\frac{1}{\pi}\frac{d\delta(E)}{dE}. \tag{2}$$

Using this relation, we can obtain the phase shift as a function of the eigenvalues in the complex scaled Hamiltonian by integrating the CLD.

When we expand the wave functions in terms of the finite number N of the basis states, the discretized eigenstates are obtained with number N and the level density can be approximated [3]

$$\Delta(E)=-\frac{1}{\pi}\mathrm{Im}\left[\sum_{B=1}^{N_B}\frac{1}{E+i0-E_B}+\sum_{r=1}^{N_r^\theta}\frac{1}{E-E_r^{res}+i\Gamma_r/2}+\sum_{c=1}^{N_c^\theta}\frac{1}{E-\varepsilon_c^r+i\varepsilon_c^i}-\sum_{k=1}^{N}\frac{1}{E-\varepsilon_k^{0r}+i\varepsilon_k^{0i}}\right] \tag{3}$$

where $N=N_B+N_r^\theta+N_c^\theta$ for bound (B), resonant (r) and continuum (c) solutions. Then we can obtain the phase shift

$$\delta_N^\theta(E)=N_b\pi+\sum_{r=1}^{N_r^\theta}\left\{-\cot^{-1}\left(\frac{E-E_r^{res}}{\Gamma_r/2}\right)\right\}+\sum_{c=1}^{N_c^\theta}\left\{-\cot^{-1}\left(\frac{E-\varepsilon_c^r}{\varepsilon_c^i}\right)\right\}-\sum_{k=1}^{N}\left\{-\cot^{-1}\left(\frac{E-\varepsilon_k^{0r}}{\varepsilon_k^{0i}}\right)\right\}, \tag{4}$$

where $E>0$. When we define δ_r, δ_c and δ_k as

$$\cot\delta_r=\frac{E_r^{res}-E}{\Gamma_r/2},\ \cot\delta_c=\frac{\varepsilon_c^r-E}{\varepsilon_c^i},\ \cot\delta_k=\frac{\varepsilon_k^{0r}-E}{\varepsilon_k^{0i}} \tag{5}$$

respectively, we can write the phase shift

$$\delta_N^\theta(E)=N_b\pi+\sum_{r=1}^{N_r^\theta}\delta_r+\sum_{c=1}^{N_c^\theta}\delta_c-\sum_{k=1}^{N}\delta_k. \tag{6}$$

The geometrical indications for δ_r, δ_c and δ_k are given for two energy cases, larger or smaller than real parts of eigen-energies E_r, ε_c and ε_k, in Fig.1.

The phase shift δ_r for the resonances is the angle of the r-th resonant pole measured at the energy E on the real energy axis. At $E=E_r^{res}$, we have $\delta_r=\pi/2$ for every resonant pole. Furthermore, while $\delta_r>0$ at $E=0$, $\delta_r=\pi$ at $E=+\infty$. On the other hand, it is seen that the phase shifts from the continuum terms of the asymptotic and full Hamiltonian are lay on the 2θ line.

The cross section is described by using these phase shifts, and we can identify the contributions from every resonant pole and continuum terms. When we concentrate our interest on the contribution from a single resonant pole and other terms which are mainly described as a background phase shift, we can have the same discussion as done by Fano [6].

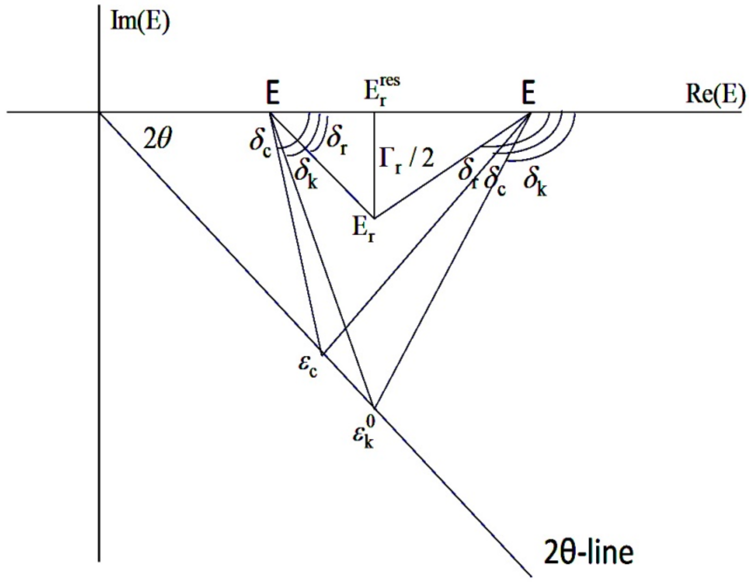

Fig. 1. The geometrical indications for phase shifts: δ_r, δ_c and δ_k

The total and partial reaction cross sections can be calculated by using the results of phase shifts decomposed into the contributions of resonance and continuum. From the results, we can investigate the contributions of resonance and continuum states in the cross sections.

The partial cross sections σ_l for the each partial wave with index l is expressed as

$$\sigma_l = \frac{4\pi}{k^2}(2l+1)\sin^2\delta_l . \tag{7}$$

where $k^2 = \frac{2E\mu}{\hbar^2}$ and μ is the reduced mass of a system. The total cross section is expressed as

$$\sigma = \sum_l^{\infty}\sigma_l . \tag{8}$$

In this work, the scattering phase shifts of two-body two systems is calculated by Eq. (4) which is derived from the CLD with the extended completeness relation. After the calculation of the decomposed scattering phase shifts, the partial cross sections of low-lying states are studied with the resonance and continuum contributions for the n-α and α-α systems, respectively.

The total cross sections of the n-α system shown in Fig. 2 are calculated in terms of the scattering phase shifts by using Eq. (8). The theoretical total cross section is in reasonable agreement with the experimental data. The present results of the scattering total cross section that is performed by theoretical formulation are displayed as the dotted line. The open circles in Fig.2 show the experimental data which were taken from Refs. [7-10[7]]. The partial cross sections, including contributions of the resonance and continuum terms, are given in Fig. 2 for j=1/2$^-$ and 3/2$^-$ waves of the n-α system, respectively. The dashed-, solid- and dotted-lines represent the partial cross section and the contributions of resonance and continuum terms, respectively.

The total cross section is given by a sum of the partial ones which are expressed as an interference of resonance and continuum contribution as discussed by Fano [6] due to the relation $\delta_\ell = \delta_r + \delta_c$ in the phase shifts given in Eq. (6). The continuum contributions of the cross section are almost the same behavior in both states of $p_{3/2}$ and $p_{1/2}$ as shown in Fig. 3. These contributions change the form of the cross section from a symmetric Breit-Wigner shape to asymmetric peaks. Although the resonant peak of the cross section can be clearly seen in the case of $p_{3/2}$, the $p_{1/2}$ results show a mild bump in the partial cross section, the peak of which is smaller than the peak in the resonance contribution.

These interference of resonance and continuum terms in the cross section are well understood from the Fano formula.

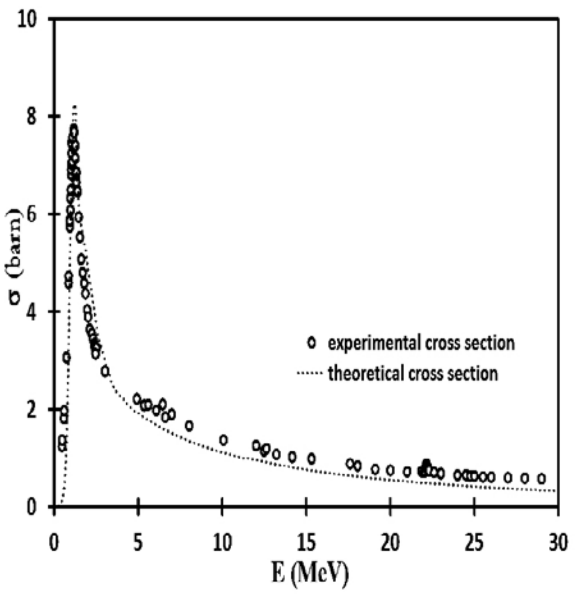

Fig. 2. Total cross section of the n-α system. The open circles display the experimental data taken fr om Ref. [7-10], and dotted lines show the p resent results

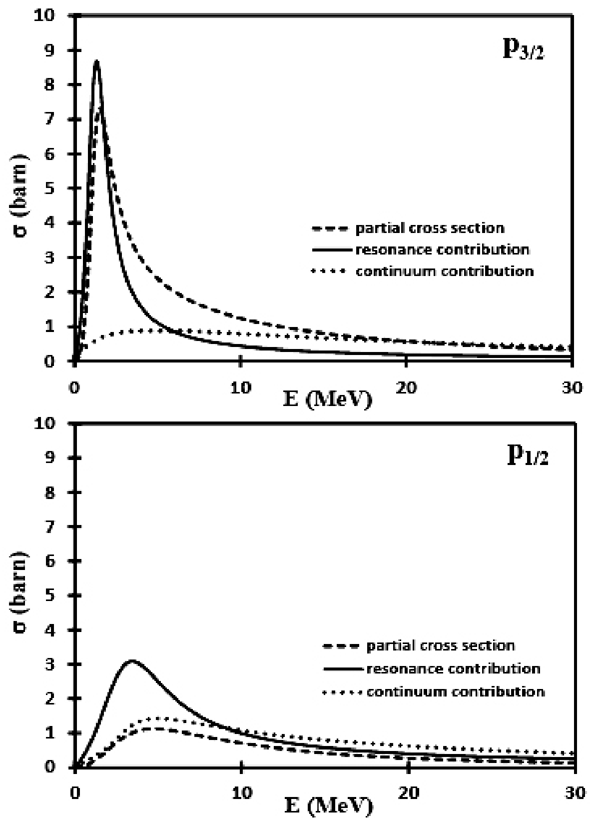

Fig. 3. The results of partial cross sections (dashed-line) and contributions from the resonance (solid line) and continuum (dotted line) terms in j=1/2$^-$ and 3/2$^-$ waves of the n-α system

Fig. 4 shows the results of cross sections of the α-α system in the relative angular momentum L = 2, 4, 8 and 10 waves, respectively.

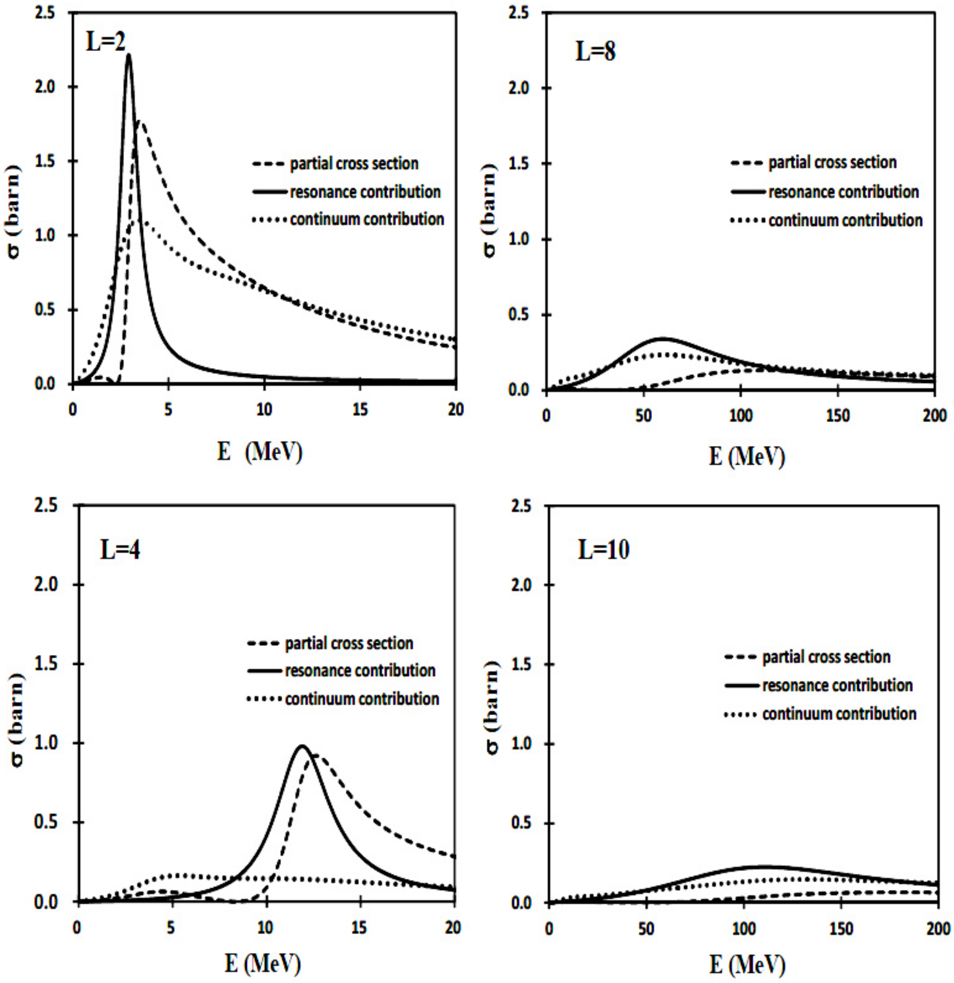

Fig. 4. The partial cross sections in L = 2, 4, 8 and 10 waves of the α-α system. The curves, dotted-lines and dashed-lines denote the results of resonance, continuum contributions of cross sections and partial cross sections, respectively.

It is interesting to see the behavior of cross sections in the relative angular momentum. From Fig. 4, it can be clearly seen in the L = 2 and 4 partial waves give a bell-shaped structure of cross section. However, a bell-shaped structure of cross sections in the L = 8 and 10 partial waves is not observed.

3. Summary

We have investigated the scattering cross sections of the various potential systems. In the present study, not only the scattering cross sections but also the contributions of the resonance and continuum states were computed for partial states of two various systems.

Acknowledgement

The authors are grateful for the support by “'R&D' Platform Formation of Nuclear Reaction Data in Asian Countries (2010-2013)”, Asia-Africa Science Platform Program, Japan Society for the Promotion of Science (JSPS).

Reference

[1] Ho Y. K. The method of complex coordinate rotation and its applications to atomic collision processes. Phys. Rep. 1983; 99: pp.1-68.

[2] Aoyama A, Myo T, Katō K, Ikeda K. The complex scaling method for many-body resonances and its applications to three-body resonances. Prog. Theor. Phys. 2006; 116: pp.1-35.

[3] Suzuki R, Kruppa A, Giraud B.G, Katō K. Continuum Level Density of a Coupled-Channel System in the Complex Scaling Method. Prog. Theor. Phys. 2008; 119: pp.949-963.

[4] Kruppa A. T, Katō K. Resonances in complex-scaled orthogonality condition model of nuclear cluster system. Prog. Theor. Phys. 1990; 84: pp.1145-1159.

[5] Shlomo S. Energy level density of nuclei. Nucl. Phys A. 1992; 539: pp.17-36.

[6] Fano U. Effects of configuration interaction on intensities and phase shifts. Phys. Rev. 1961; 124: pp.1866-1878.

[7] Austin S. M, Barschall H. H, Shamu R. E. Scattering of Neutrons by α Particle. Phys. Rev. 1962; 126: pp.1532-1539.

[8] Shamu R. E, Jenkin J. G. Neutron-Alpha Scattering in the 20-MeV Range. Phys. Rev. 1964; 135: B99-B109.

[9] Vaughn F. J, W. L. Imhof W. L, Johnson R. G, Walt M. Total Neutron Cross Sections of Helium, Neon, Argon, Krypton, and Xenon. Phys. Rev. 1960; 118: pp.683-686.

[10] Los Alamos Physics and Gryogenics Groups. Total neutron cross sections of the hydrogen and helium isotopes. Nucl. Phys. 1959; 12: pp.291-297.

28. Recent Activity of Central Asian Nuclear Reaction Database and Asian Collaboration on Nuclear Reaction Data Compilation

Meruert Takibayeva[1,2], Venera Kurmangalieva[1], Nurgali Takibayev[1], Masayuki Aikawa[3], Naoya Furutachi[3], Kiyoshi Katō[3], Ayano Makinaga[3], Vidya Devi[4], Shuichiro Ebata[4], Dagvadorj Ichinkhorloo[4], Myagmarjav Odsuren[4], Kohsuke Tsubakihara[5], Toshiyuki Katayama[6], Naohiko Otuka[7]

[1] Central Asian Nuclear Reaction Database, Almaty 050-040, Kazakhstan

[2] Graduate School of Science, Hokkaido University, Sapporo 060-0810, Japan

[3] Nuclear Reaction Data Centre (JCPRG), Faculty of Science, Hokkaido University, Sapporo 060-0810, Japan

[4] Meme Media Laboratory, Hokkaido University, Sapporo 060-8628, Japan

[5] Department of Engineering Science, Osaka Electro-Communication University, Neyagawa 572-8530, Japan

[6] School of Economics, Hokusei Gakuen University, Sapporo 004-8631, Japan

[7] Nuclear Data Section, International Atomic Energy Agency, A-1400 Wien, Austria

e-mail: aikawa@sci.hokudai.ac.jp

Central Asian countries, such as Kazakhstan and Uzbekistan, have a long history of nuclear research and have been energetic in producing a large quantity of nuclear data. In order to compile such nuclear data, a new nuclear data centre called the Central Asian Nuclear Reaction Database (CA-NRDB) was established. The establishment of the CA-NRDB was promoted in collaboration with the Hokkaido University Nuclear Reaction Data Centre (JCPRG) and the Centre for Photonuclear Experiments Data of the Moscow State University. The activity of the CA-NRDB will be valuable for researchers of nuclear data in Central Asia, as well as in the rest of the world.

1. Introduction

Nuclear reaction data are applicable in many fields, including nuclear physics, astrophysics, nuclear engineering, and radiation therapy. Many experimental works have been performed worldwide to obtain nuclear reaction data, such as cross sections and product yields. Most of these data are published in scientific journals, which may entail costs and be accessible only by researchers. In addition, nuclear reaction experiments can only be performed at enormous expense and require extreme effort of researchers. Such data, therefore, must be compiled in a database and be freely available via the Internet.

2. Nuclear Data Compilation

The compilation of nuclear data requires broad and long-term effort due to the large number and variety of experiments. One such compilation is the EXFOR database [1], which is maintained by the International Atomic Energy Agency (IAEA) and the International Network of Nuclear Reaction Data Centres (NRDC). The NRDC consists of fourteen members worldwide, and cooperates in the compilation of experimental nuclear reaction data for the EXFOR database.

In order to promote the compilation activities, international cooperation is unavoidable. Cooperation in Asian countries was supported by the Japan Society for the Promotion of Science for three years, from April 2010 to March 2013. Under their support, annual workshops called Asian Nuclear Reaction Database Development Workshops, were held to share information, to strengthen collaboration and to promote the dissemination and improvement of data compilation techniques. Even though the support had been complete since April 2013, the fourth workshop was held in October 2013 at the Al-Farabi Kazakh National University, Almaty, Kazakhstan, in order to promote compilation activity in Central Asia.

Central Asian countries, such as Kazakhstan and Uzbekistan, have a long history of nuclear research. In order to compile nuclear data obtained in Central Asia, a new nuclear data centre, called the Central Asia Nuclear Reaction Database (CA-NRDB), was established. The CA-NRDB began to compile nuclear data obtained at their domestic facilities. Two NRDC members, the Hokkaido University Nuclear Reaction Data Centre (JCPRG) and the Centre for Photonuclear Experiments Data of the Moscow State University, support the CA-NRDB.

3. Collaboration between Kazakhstan and Japan

Hokkaido University concluded an Inter-University Exchange Agreements with the Al-Farabi Kazakh National University in August 2011. Under the terms of the agreement, researchers at the two universities

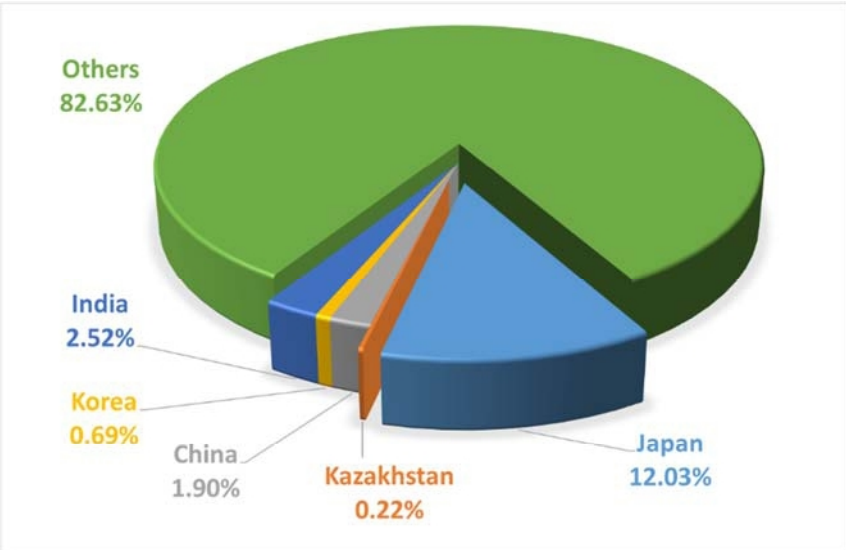

Figure 1: Asian contributions in the EXFOR database

promote collaborative research concerning nuclear data. The compilation of nuclear data obtained in Kazakhstan originated as one of these collaborative enterprises. In the EXFOR database, the contribution of facilities in which experiments were performed in Japan and Kazakhstan is 12.03% and 0.22%, respectively (Figure 1). The compilation of nuclear data performed in Central Asia is being promoted.

4. Summary

Nuclear data and its compilation are important for many fields of application. The Central Asia Nuclear Reaction Database (CA-NRDB) was established in order to compile and distribute nuclear data obtained in Central Asia. Nuclear data, such as cross sections and product yields, are compiled and transmitted to the EXFOR database, which is maintained by the International Atomic Energy Agency (IAEA) and the International Network of Nuclear Reaction Data Centres (NRDC). As one of the NRDC members, and under the Inter-University Exchange Agreements with Al-Farabi Kazakh National University, the Hokkaido University Nuclear Reaction Data Centre cooperates on compilation with the CA-NRDB. The ratio of the contribution by Kazakhstan facilities in the EXFOR database is 0.22% at present and is expected to increase with compilations from the CA-NRDB.

Acknowledgement

The authors are grateful for the support of the ITT-8 Project of the Ministry of Education and Sciences of the Republic of Kazakhstan, of the ‘R&D’ Platform Formation of the Nuclear Reaction Data in Asian Countries (2010-2013), the Asia-Africa Science Platform Program and the Grant-in-Aid for Publication of Scientific Research Results (No. 257005), the Japan Society for the Promotion of Science (JSPS), and of the Hokkaido University Support program for research exchange with inter-university foreign partners.

Reference

[1] N. Otuka et al., "Towards a More Complete and Accurate Experimental Nuclear Reaction Data Library (EXFOR): International Collaboration Between Nuclear Reaction Data Centres (NRDC)", Nucl. Data Sheets 120, 272 (2014).

29. FENDL-3.0 Benchmark Test with Shielding Experiments at JAEA/TIARA

Chikara Konno, Masayuki Ohta, Hiroo Asahara, Kentaro Ochiai, and Satoshi Sato

Fusion Research and Development Directorate, Japan Atomic Energy Agency
Tokai-mura, Naka-gun, Ibaraki-ken 319-1195 Japan
e-mail : konno.chikara@jaea.go.jp

IAEA released a new version of Evaluated Nuclear Data Library (FENDL), FENDL-3.0 in 2012 in order to extend the neutron energy range of neutron-induced reactions from 20 MeV to more than 60 MeV and to include general purpose and activation data libraries for proton- and deuteron-induced reactions up to more than 60 MeV. We already reported the benchmark tests of the general-purpose data library for neutron-induced reactions below 20 MeV in FENDL-3.0. In this symposium we will present the benchmark tests of the general-purpose data library for neutron-induced reactions in FENDL-3.0 by using iron and concrete shielding experiments with the 40 and 65 MeV neutron sources at TIARA in JAEA. As a result, it is found out that the calculations with FENDL-3.0 agree with the measured ones for the iron experiment well, while they overestimate the measured ones for the concrete experiment more for the thicker assemblies.

1. Introduction

A nuclear data library is one of the most important data that control the calculation accuracy in nuclear analyses for fusion reactor designs. IAEA compiles the best data from the evaluated nuclear data libraries in the world for each nucleus concerning fusion reactor applications. This library is Fusion Evaluated Nuclear Data Library (FENDL) and the current version is FENDL-2.1 [1]. In 2008 IAEA started a new coordinate research project to update FENDL-2.1, to extend the neutron energy range from 20 MeV to 150 MeV and to include general purpose and activation data libraries for p- and d-induced reactions up to 150 MeV. This new library is named as FENDL-3.0 [2], which was released in December, 2012. We already reported the benchmark tests of the general-purpose data library for neutron-induced reactions in FENDL-3.0 by using integral experiments with the DT neutron source at FNS in JAEA and TOF experiments with the DT neutron source at OKTAVIAN in Osaka University [3]. In this paper we describe the benchmark tests of the general-purpose data library for neutron-induced reactions in FENDL-3.0 by using iron and concrete shielding experiments [4] with the 40 and 65 MeV neutron sources at TIARA in JAEA.

2. Method

The Monte Carlo code MCNP-5 [5] and ACE file of FENDL-3.0 supplied from IAEA Nuclear Data Section were used for the benchmark test. The source of FENDL-3.0 is the followings,

- ^{1}H:ENDF/B-VII.1 [6] (<20MeV) + JENDL/HE-2007 [7] (>20MeV)
- ^{16}O, ^{27}Al, $^{28-30}$Si, ^{54}Fe, ^{57}Fe : ENDF/B-VII.0 [8]
- ^{56}Fe, ^{58}Fe : JEFF-3.1.1 [9] (<20MeV) + TENDL-2011 [10] (>20MeV)
- ^{40}Ca : JENDL-4.0 [11] (<20MeV) + JENDL/HE-2007 (>20MeV)

We also used JENDL/HE-2007, ENDF/B-VII.1 (where the ^{1}H data are replaced by those in FENDL-3.0, because the ^{1}H data in ENDF/B-VII.1 are for neutrons less than 20 MeV) and FENDL-3.0 shadow [12] (where the ^{1}H data in FENDL-3.0 are adopted, because they are not included in FENDL-3.0 shadow, and the ^{16}O data in FENDL-3.0 shadow are replaced with those in TENDL-2010 [13], because they do not include mt5 data) for comparison. The ACE files of these libraries are supplied from JAEA [14], NNDC [15] and IAEA [12], respectively.

In the TIARA shielding experiments, quasi-mono energetic 40 or 65 MeV neutrons were generated by bombarding 43 or 68 MeV proton to a ^{7}Li target and collimated ones were injected to a test assembly of 1.2 m x 1.2 m as shown in Fig. 1. The collimated neutron beam and experimental assemblies with additional shields were modeled in the analysis as shown in Fig. 2. The measured source neutron spectrum was used. Neutron spectra above 10 MeV on beam axis were obtained.

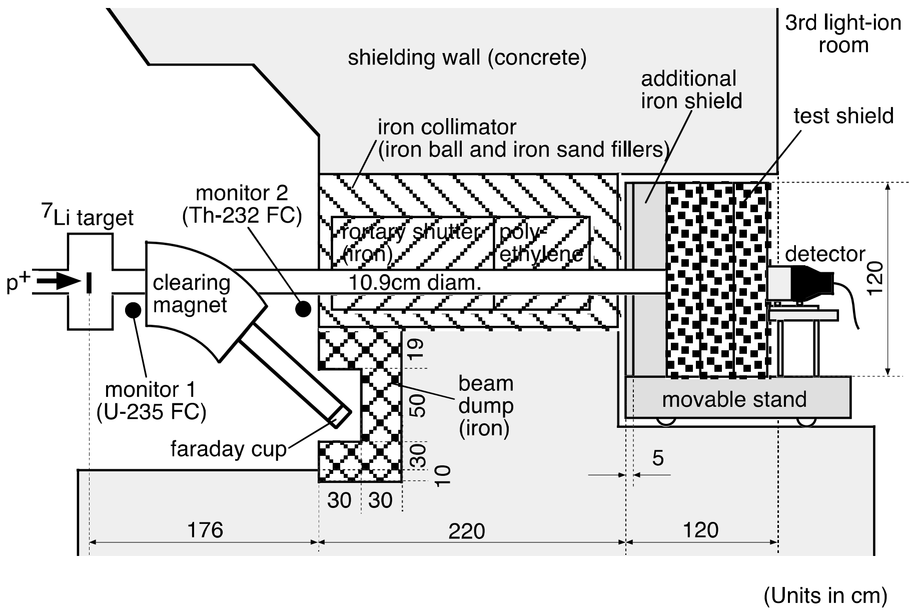

Fig. 1 Experimental configuration of TIARA shielding experiments

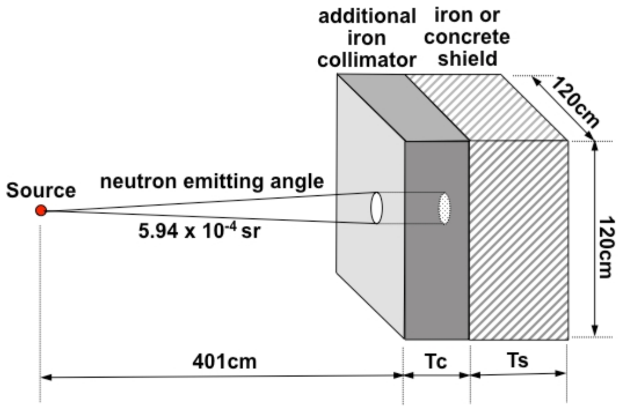

Fig. 2 Calculation model

3. Results and discussion

The typical results for the iron experiment with 40 MeV neutrons are shown in Fig. 3. Figure 3 (a) plots the measured neutron spectra with the calculated ones. Figure 3 (b) and (c) show the ratios of the calculated peak (35 - 45 MeV) and continuum (10 - 35 MeV) neutron fluxes to the measured ones, respectively. The calculation results with FENDL-3.0, JENDL/HE-2007 and FENDL-3.0 shadow agree with the measured ones well, though a strange peak appears around 20 MeV in those in FENDL-3.0 and those with FENDL-3.0 shadow overestimated the continuum neutrons more at the deeper positions. On the other hand, those with ENDF/B-VII.1 overestimate the measured neutrons with the thickness of the assemblies. The similar trend appears in the typical results for the iron experiment with 65 MeV neutrons as shown in Fig. 4. When checked closely, the calculation results with JENDL/HE-2007 tend to be smaller than those with FENDL-3.0, the overestimation for the peak neutrons in those with ENDF/B-VII.1 is smaller and those with FENDL3.0 shadow overestimate the continuum neutrons.

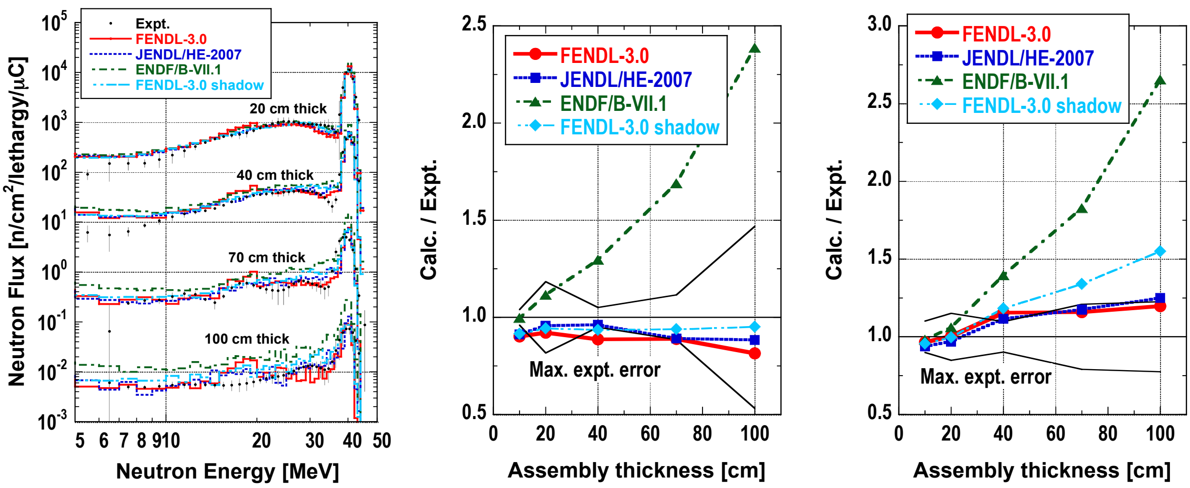

(a) Neutron spectra (b) C/E for peak neutrons (35-45MeV) (c) C/E for continuum neutrons (10-35MeV)

Fig. 3 Typical results for iron experiment with 40 MeV neutrons

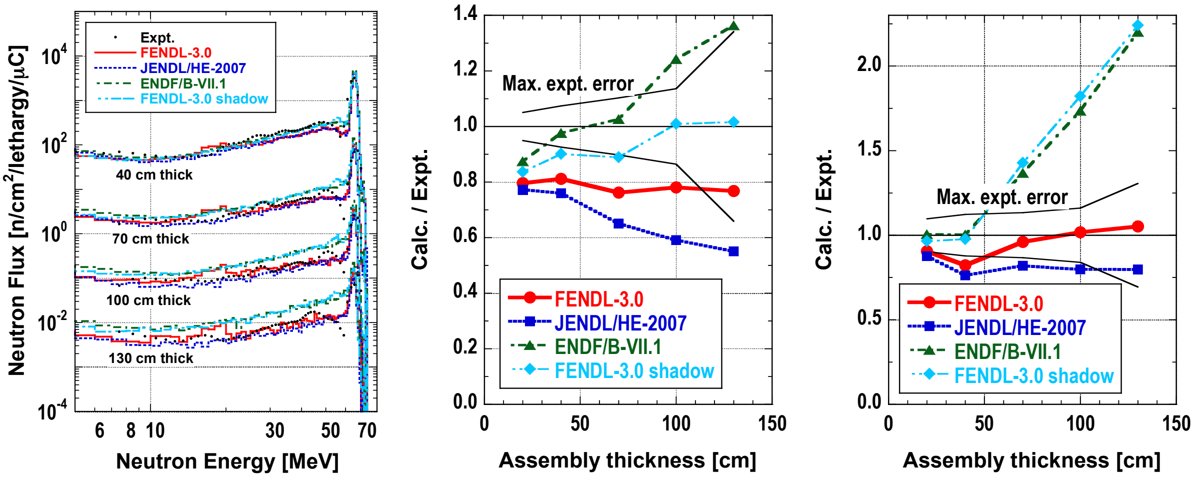

(a) Neutron spectra (b) C/E for peak neutrons (60-70MeV) (c) C/E for continuum neutrons (10-60MeV)

Fig. 4 Typical results for iron experiment with 65 MeV neutrons

Figure 5 shows the typical results for the concrete experiment with 40 MeV neutrons. The calculation results with FENDL-3.0 and ENDF/B-VII.1 are almost the same and overestimate the measured neutrons more for the thicker assemblies. The strange peak around 20 MeV disappears in those with FENDL-3.0. Those with JENDL/HE-2007 agree with the measured ones better. Those with FENDL-3.0 shadow are by 20 % smaller for neutrons from 10 to 35 MeV than those with JENDL/HE-2007. The typical results for the concrete experiment with 65 MeV neutrons are shown in Fig. 6. Those with FENDL-3.0 and ENDF/B-VII.1 overestimate the measured neutrons above 60 MeV more for the thicker assemblies, while they do not overestimate the measured neutrons from 10 to 60 MeV. Those with JENDL/HE-2007 and FENDL-3.0 shadow agree with the measured neutrons.

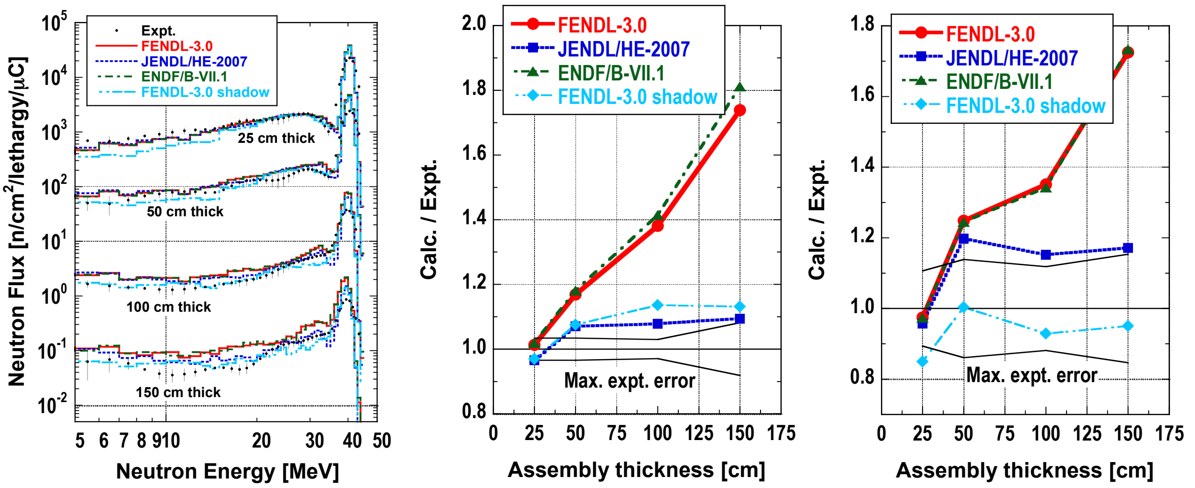

(a) Neutron spectra (b) C/E for peak neutrons (35-45MeV) (c) C/E for continuum neutrons (10-35MeV)

Fig. 5 Typical results for concrete experiment with 40 MeV neutrons

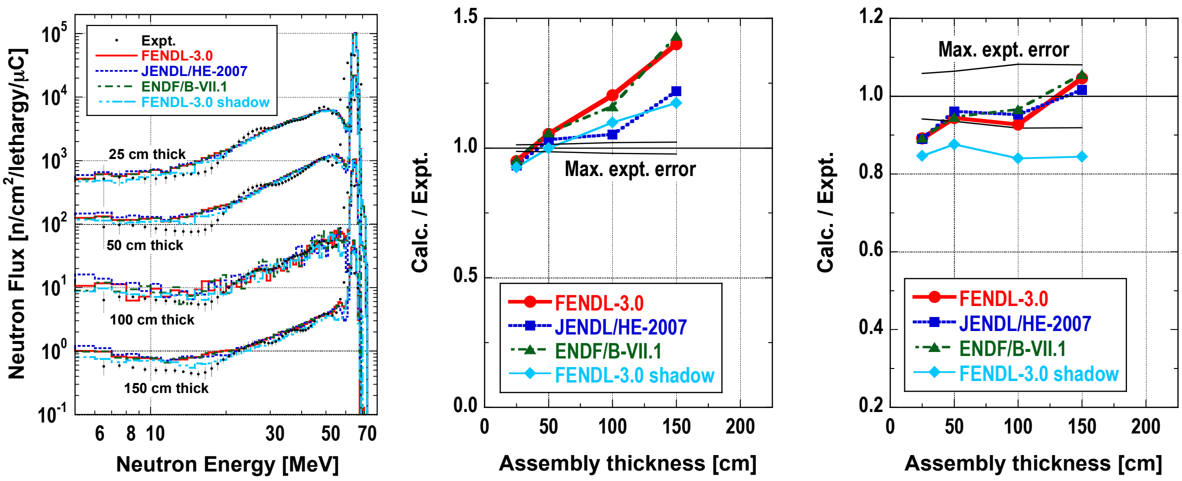

(a) Neutron spectra

(b) C/E for peak neutrons (60-70MeV)

(c) C/E for continuum neutrons (10-60MeV)

Fig. 6 Typical results for concrete experiment with 65 MeV neutrons

4. Summary

We analyzed the iron and concrete shielding experiments at JAEA/TIARA with FENDL-3.0, HENDL/HE-2007, ENDF/B-VII.1 and FENDL-3.0 shadow in order to benchmark FENDL-3.0 newly released in 2012. As a result, the followings are found.

1) The calculations with FENDL-3.0 agree with the measured ones for the iron experiment well, while they overestimate the measured ones for the concrete experiment more for the thicker assemblies.
2) The calculations with JENDL/HE-2007 fairly agree with the measured ones both for the iron and concrete experiments.
3) The calculations with ENDF/B-VII.1 overestimate the measured ones both for the iron and concrete experiments.
4) The calculations with FENDL-3.0 shadow agree with the measured ones both for the iron and concrete experiments except for the continuum neutron flux in the iron experiment with 65MeV neutrons.

We will investigate reasons of the discrepancies between the calculation and measured results hereafter.

References

[1] Aldama DL, Trkov A. FENDL-2.1: Update of an evaluated nuclear data library for fusion applications. INDC(NDS)-467. Austria: International Atomic Energy Agency; 2004.

[2] Forrest RA, Capote N, Otsuka N, Kawano T, Koning AJ, Kunieda S, Sublet J-Ch, Watanabe Y. FENDL-3 Library – Summary documentation. INDC(NDS)-0628. Austria: International Atomic Energy Agency; 2012.

[3] Konno C, Ohta M, Takakura K, Ochiai K, Sato S. FENDL-3 Benchmark Test with Neutronics Experiments related to Fusion in Japan. Submitted to Fusion Eng. Design.

[4] Nakane Y, Hayashi K, Sakamoto Y, Yoshizawa N, Nakao N, Ban S, Hirayama H, Uwamino Y, Shin K, Nakamura T. Neutron transmission benchmark problems for iron and concrete shields in low, intermediate and high energy proton accelerator facilities. JAERI-Data/Code 96-029. Japan: Japan Atomic Energy Research Institute; 1996.

[5] X-5 Monte Carlo Team. MCNP - A General Monte Carlo N-Particle Transport Code, Version 5. LA-UR-03-1987. USA: Los Alamos National Laboratory; 2005.

[6] Chadwick MB, Herman M, Oblozinsky P, Dunn ME, Danon Y, Kahler AC, Smith DL, Pritychenko B, Arbanas G, Arcilla R, Brewer R, Brown DA, Capote R, Carlson AD, Cho YS, Derrien H, Guber K, Hale GM, Hoblit S, Holloway S, Johnson TD, Kawano T, Kiedrowski BC, Kim H, Kunieda S, Larson NM, Leal L, Lestone JP, Little RC, McCutchan EA, MacFarlane RE, MacInnes M, Mattoon CM, McKnight RD, Mughabghab SF, Nobre GPA, Palmiotti G, Palumbo A, Pigni MT, Pronyaev VG, Sayer RO, Sonzogni AA, Summers NC, Talou P, Thompson IJ, Trkov A, Vogt RL, van der Marck SC, Wallner A, White MC, Wiarda D, Young PG. ENDF/B-VII.1 Nuclear Data for Science and Technology: Cross Sections, Covariances, Fission Product Yields and Decay Data. Nucl Data Sheets. 2011;112:2887–2996.

[7] Available from :”*Nuclear Data Center JENDL High Energy File 2007”*, http://wwwndc.jaea.go.jp/ftpnd/jendl/jendl-he-2007.html

[8] Chadwick MB, Oblozinsky P, Herman M, Greene NM, McKnight RD, Smith DL, Young PG, MacFarlane RE, Hale GM, Frankle SC, Kahler AC, Kawano T, Little RC, Madland DG, Moller P, Mosteller RD, Page PR, Talou P, Trellue H, White MC, Wilson WB, Arcilla R, Dunford CL, Mughabghab SF, Pritychenko B, Rochman D, Sonzogni AA, Lubitz CR, Trumbull TH, Weinman JP, Brown DA, Cullen DE, Heinrichs DP, McNabb DP, Der- rien H, Dunn ME, Larson NM, Leal LC, Carlson AD, Block RC, Briggs JB, Cheng ET, Huria HC, Zerkle ML, Kozier KS, Courcelle A, Pronyaev V, van der Marck SC. ENDF/B-VII.0: next generation evaluated nuclear data library for nuclear science and technology. Nucl Data Sheets. 2006;107:2931–3059.

[9] Santamarina A, Bernard D, Blaise P, Coste M, Courcelle A, Huynh TD, Jouanne C, Leconte P, Litaize O, Mengelle S, Noguère G, Ruggiéri J-M, Sérot O, Tommasi J, Vaglio C, Vidal J-F. The JEFF-3.1.1 Nuclear Data Library. JEFF Report 22. Paris (France) : OECD Nuclear Energy Agency; 2009.

[10] Available from: ftp://ftp.nrg.eu/pub/www/talys/tendl2011/tendl2011.html

[11] Shibata K, Iwamoto O, Nakagawa T, Iwamoto N, Ichihara A, Kunieda S, Chiba S, Furutaka K, Otuka N, Ohsawa T, Murata T, Matsunobu H, Zukeran A, Kamada S, Katakura J. JENDL-4.0: a new library for nuclear science and engineering. J Nucl Sci Technol. 2011;48: pp.1-30.

[12] Available from "*Nuclear Data Services FENDL-3.0*": https://www-nds.iaea.org/fendl30/

[13] Available from : ftp://ftp.nrg.eu/pub/www/talys/tendl2010/tendl2010.html

[14] Sasa T, Sugawara T, Kosako K, Fukahori T. Continuous Energy Cross Section Library for MCNP/MCNPX Based on JENDL High Energy File 2007 -FXJH7-. JAEA-Data/Code 2008-022. Japan; Japan Atomic Energy Agency; 2008.

30. Analysis of Integral Experiment for Th-232 (n,γ) Reaction Cross Section at KUCA

Tadafumi Sano, Yoshiyuki Takahashi, Jun-ichi Hori, Hironobu Unesaki, Ken Nakajima
Kyoto University Research Reactor Institute
1010, Asashiro-nishi-2, Kumatori-cho, Sennan-gun, Osaka, 590-0494, Japan
e-mail : t-sano@rri.kyoto-u.ac.jp

To measure integral neutronics characteristics of thorium loaded core, critical experiments had been carried out using Kyoto University Critical Assembly (KUCA). The critical experiments were performed with various neutron spectrums and thorium inventories. The thorium loaded cores has two regions which are a test zone and a driver fuel zone. The test zone consists of thorium plates and graphite plates. In order to systematically vary the neutron spectrum of the experimental neutron field, the graphite/Th-232 ratio at the test zone had been systematically varied by changing the combination of the thorium plates and the graphite plates in a unit cell.

In this study, the criticalities of thorium loaded core were analyzed by MVP2.0 with JENDL-4.0, JENDL-3.3 and ENDF/B-VII.0. In addition, sensitivity analyses were performed by SAGEP and uncertainties of the numerical results were evaluated using cross section covariance matrix.

1. Introduction

To improved Th-232 nuclear data, integral evaluations of thorium loaded cores at Kyoto University Critical Assembly (KUCA) are carried out. The critical experiments were performed with various neutron spectrums, thorium inventories and unit cell patterns. On the other hand, the results of integral evaluations, especially sample reactivity worth, have large differences[1,2] of the results between uses of JENDL-4.0[3] and JENDL-3.3[4]. Figure 1 shows large difference of Th-232 capture cross section in the neutron energy region of 0.1 – 100 eV between JENDL-4.0 and JENDL-3.3.

In this study, integral evaluations of criticalities for the thorium loaded core at KUCA are carried out. The numerical calculations of criticalities are performed by continuous energy Monte-Carlo code MVP2.0[5] with JENDL-4.0, JENDL-3.3 and ENDF/B-VII.0[6].

In addition, sensitivity analyses are performed by SAGEP[7] and uncertainties of the numerical results are evaluated using cross section covariance matrix.

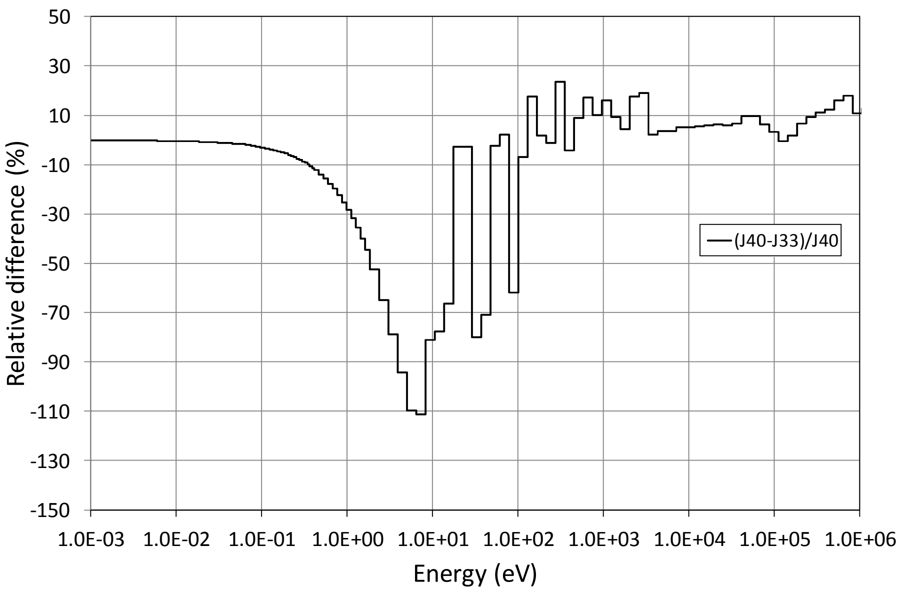

Fig.1 Difference of Th-232 capture cross section between JENDL-4.0 and JENDL-3.3

2. Experimental Geometry

KUCA solid moderated core is able to consist of enriched uranium fuel plate and various moderator plates (i.e. polyethylene and graphite). In this study, the results of the zone-type thorium-uranium core experiments are used for integral evaluations of Th-232 capture cross section as (n,γ) reaction cross section. The critical core consists of the central test zone loaded with thorium plates and graphite plates[8]. In order to systematically vary the neutron spectrum of the experimental neutron field, the Th-232/graphite ratio at the test zone had been systematically varied by changing the combination of the thorium plates and the graphite plates in a unit cell as shown in Fig.2.1. Six cores with thorium loaded test zone were constructed. The fuel elements with thorium plates are loaded into the central 3 by 3 zone, and the driver zone is constructed by enrich uranium plates and polyethylene plates. The H/U-235 ratio was approximate 316. Figure 2.3 shows the neutron spectrums in the test zones.

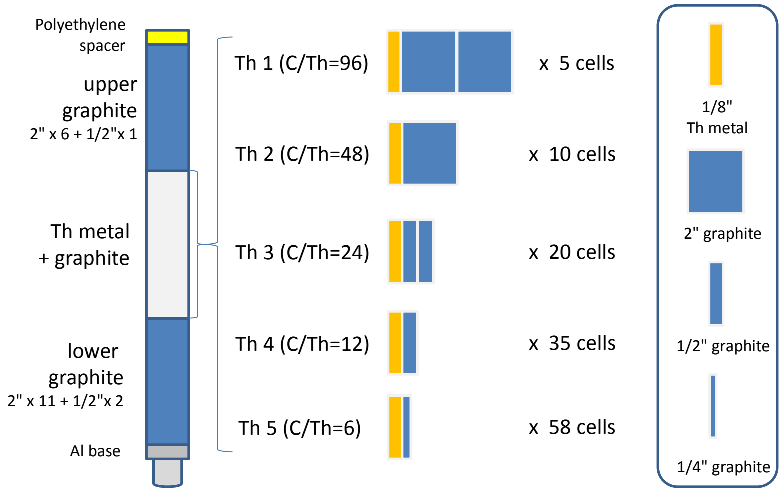

Fig.2.1 Unit cell pattern

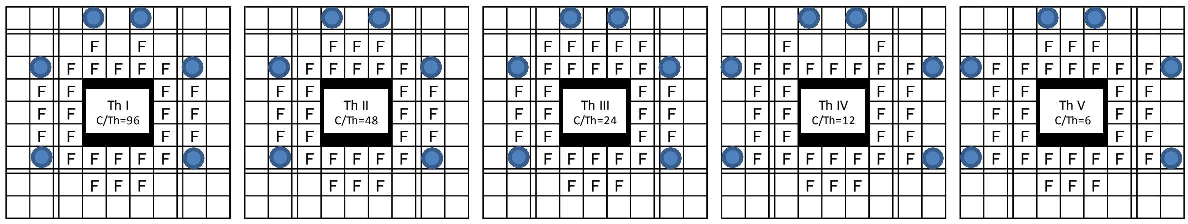

Fig.2.2 Core configuration

F :Fuel element (3/8″P36EU) ■:Test zone
:Polyethylene refrector ●:Control rod

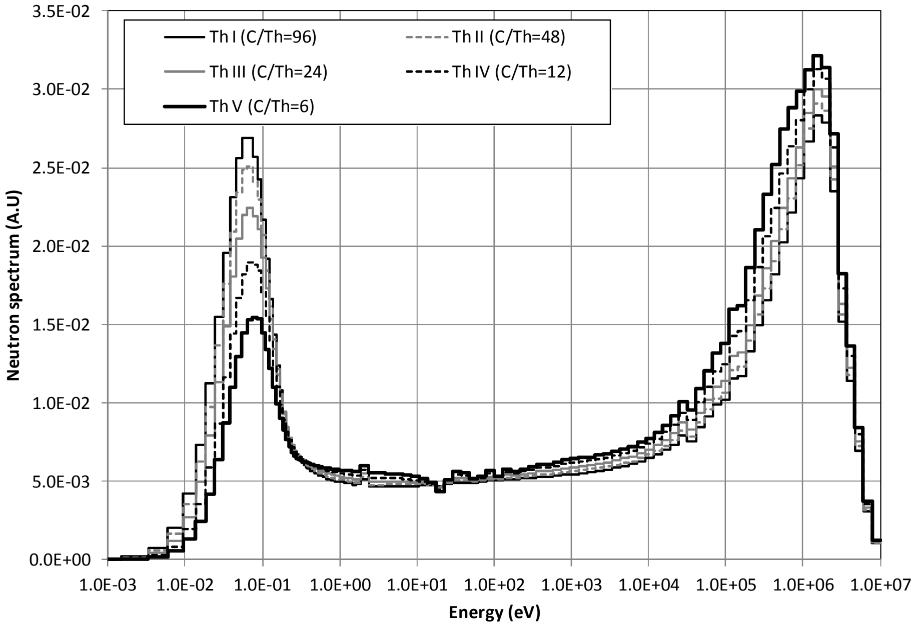

Fig.2.3 Neutron spectrums in each test zone

3. Integral Evaluation for Criticality

3.1 Calculational Model

The criticality analysis are performed by the continuous energy Monte-Carlo code MVP2.0 with the JENDL-4.0, JENDL-3.3 and ENDF/B-VII.0. In the MVP calculations, 25M neutron histories are generated to suppress the statistical error of k_{eff} to less than 0.025% (1σ) because the typical experimental error for the k_{eff} is estimated to be about 0.03%[9].

3.2 Numerical Result and Discussion

Figure 3 shows the C/E value of k_{eff} for the thorium loaded cores and enriched uranium cores without thorium (B3/8P36EU). In the case of thorium loaded core, the C/E values with JENDL-4.0 suffer from a certain pedestal of around 0.25%. Using JENDL-3.3 or ENDF/B-VII.0, the C/E values are overestimated than using JENDL-4.0. On the other hand, the no thorium core with JENDL-4.0 is good agreement with the experimental value. However, using JENDL-3.3 and ENDF/B-VII.0, the C/E values overestimate about 0.25%. This is caused by difference of U-235 capture cross section in the energy region of 450eV – 2.6keV among JENDL-4.0 and JENDL-3.3, ENDF/B-VII.0. Thus, the errors of thorium loaded core by using JENDL-4.0 are caused by the material, thorium plates or graphite plates, loaded into the test zone.

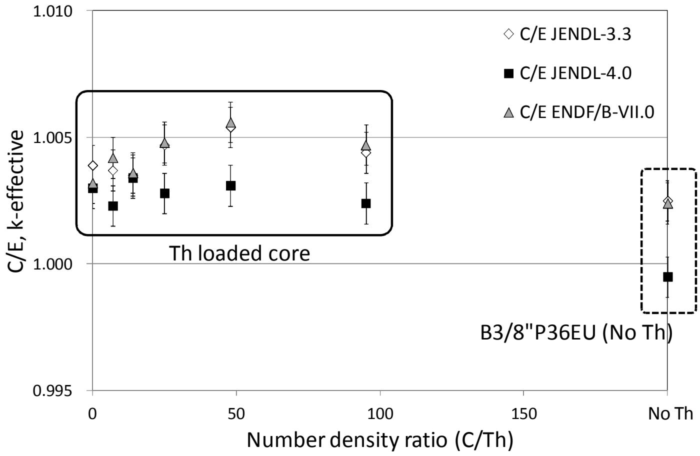

Fig.3 C/E value of k_{eff} for thorium loaded core

4. Sensitivity Analysis

4.1 Calculational Model

To calculate sensitivity coefficients, the 107-group cross section set processed by using the cell calculation code SRAC2006[10] with JENDL-4.0 and ENDF/B-VII.0 are utilized. The sensitivity coefficients are calculated using the generalized perturbation theory code SAGEP. The cross section covariance matrix was taken from JENDL-4.0 and ENDF/B-VII.0.

4.2 Numerical Result and Discussion

The sensitivity coefficients for the k_{eff} with respect to Th-232 effective capture cross section are shown in Figure 4.1. The magnitude of the sensitivity coefficient is dependent on the thorium inventory in KUCA core. Figure 4.2 shows the reactivity evaluated by the sensitivity coefficient and the effective capture cross section difference between JENDL-4.0 and JENDL-3.3. The results show cancellation of positive and negative reactivity. Thus, the

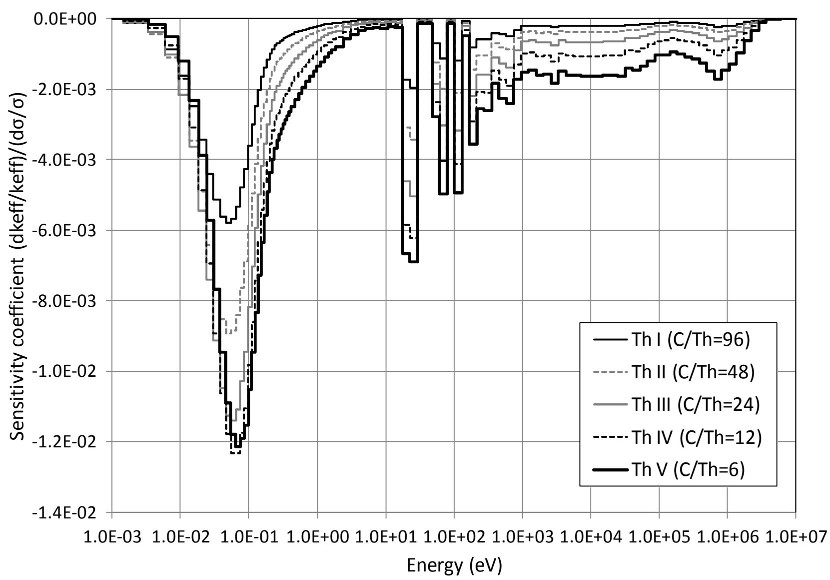

Fig.4.1. Sensitivity coefficients of k_{eff} with respect to Th-232 effective capture cross section

reactivity is less than 1×10^{-1}(%dk/k). However, the C/E values of keff have more than 1×10^{-1}(%dk/k) between JENDL-4.0 and JENDL-3.3 or ENDF/B-VII.0. So, we need to perform the sensitivity analysis for graphite plates in the test zone.

Figure 4.3 is energy dependence variance of k_{eff} for thorium loaded core (Th I). The uncertainty of k_{eff} is evaluated by the sensitivity coefficients and cross section covariance. The ENDF/B-VII.0 has small covariance in thermal region than JENDL-4.0. Thus, the uncertainty by ENDF/B-VII.0 is remarkably less than JENDL-4.0. In addition, JENDL-4.0 covariance in neutron energy of thermal region has discontinuous spectrum and large difference at the boundary.

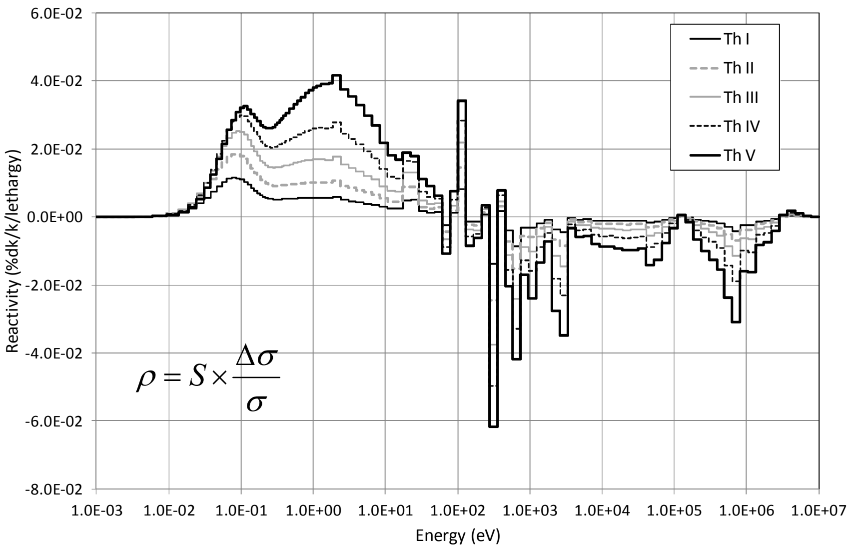

Fig.4.2 Energy dependence of reactivity component for thorium loaded core between JENDL-4.0 and JENDL-3.3

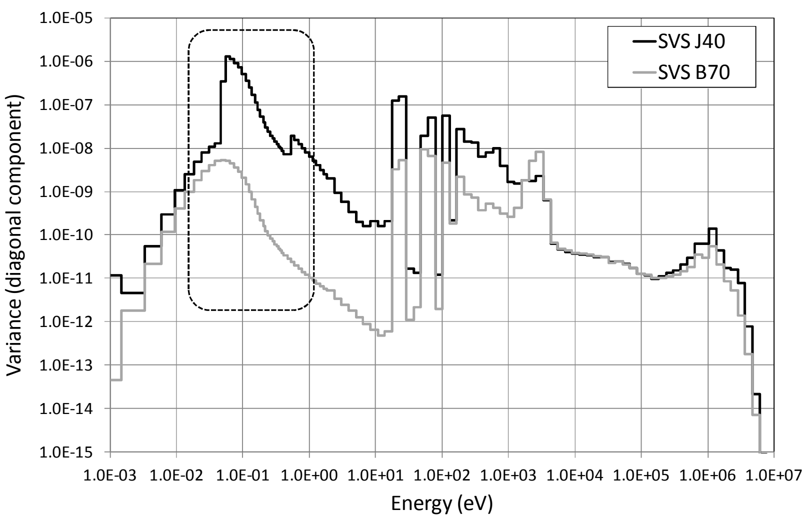

Fig.4.3 Energy dependence of variance for Th I core

5. Conclusion

The critical experiments had been carried out using Kyoto University Critical Assembly (KUCA). The critical experiments were performed with various neutron spectrums and Th inventories.

In this study, the criticalities of thorium loaded core were analyzed by MVP2.0 with JENDL-4.0, JENDL-3.3 and ENDF/B-VII.0. In addition, the sensitivity analysis and uncertainty evaluation were carried out. As the results, the reactivity between JENDL-4.0 and JENDL-3.3 is less than 1×10^{-1}(%dk/k). However, the C/E values of k_{eff} have more than 1×10^{-1}(%dk/k) between JENDL-4.0 and the other nuclear data library. Thus, we need to perform the sensitivity analysis for graphite plates in the future works.

Acknowledgment

A part of this study was supported by CHUBU Electric Power Co., Inc.

Reference

[1] Fujii T, Wada K, Mai VT, Kitada T, Yamaguchi A, Watanabe H, Takaki N Unesaki H. Critical Experiment with Thorium at KUCA. Proceeding of the 2011 Symposium on Nuclear Data; 2011 Nov.16-17; Tokai-mura, Japan: JAEA; 2012 July.

[2] Mishiro T, Kitada T, Fujii T, Kojima T. The evaluation of Thorium cross-section by the experimental analysis of Thorium replacement worth [abstract]. AESJ Fall Meeting; 2013 Sep 3-5; Hachinohe, Japan; [CD-ROM].

[3] Shibata K, Iwamoto O, Nakagawa T, N. Iwamoto N, A. Ichihara A, S. Kunieda S, S. Chiba S, Furutaka K, Otuka N, Ohsawa T, Murata T, Matsunobu H, Zukeran A, Kamada S, Katakura J. JENDL-4.0: A New Library for Nuclear Science and Engineering. J Nucl Sci Technol. 2011; 48(1):1-30.

[4] Shibata K, Kawano T, Nakagawa T, Iwamoto O, Katakura J, Fukahori T, Chiba S, Hasegawa A, Murata T, Matsunobu H, Ohsawa T, Nakajima Y, Yoshida T, Zukeran A, Kawai M, Baba M, Ishikawa M, Asami T, Watanabe T, Watanabe Y, Igashira M, Yamamuro N, Kitazawa H, Yamano N Takano H. Japanese Evaluated Nuclear Data Library Version 3 Revision-3: JENDL-3.3. J Nucl Sci Technol. 2002; 39(11):1125-1136.

[5] Nagaya Y, Okumura K,Mori T. MVP/GMVP II: General Purpose Monte Carlo Codes for Neutron and Photon Transport Calculations based on Continuous Energy and Multigroup Methods. JAERI 1348. Japan: Japan Atomic Energy Research Institute; 2005.

[6] Chadwick MB, Obložinský P, Herman M, Greene NM, McKnight RD, Smith DL, Young PG, MacFarlane RE, Hale GM, Frankle SC, Kahler AC, Kawano T, Little RC, Madland DG, Moller P, Mosteller RD, Page PR, Talou P, Trellue H, White MC, Wilson WB, Arcilla R, Dunford CL, Mughabghab SF, Pritychenko B, Rochman D, Sonzogni AA, Lubitz CR,

Trumbull TH, Weinman JP, Brown DA, Cullen DE, Heinrichs DP, McNabb DP, Derrien H, Dunn ME, Larson NM, Leal LC, Carlson AD, Block RC, Briggs JB, Cheng ET, Huria HC, Zerkle ML, Kozier KS, Courcelle A, Pronyaev V, Marck SC. ENDF/B-VII.0: Next Generation Evaluated Nuclear Data Library for Nuclear Science and Technology. Nucl. Data Sheets. 2006;107(12):2931-3060.

[7] Hara A, Takeda T, Kikuchi Y. SAGEP: Two-Dimensional Sensitivity Analysis Code Based on Generalized Perturbation Theory. JAERI-M 84-027. Japan: Japan Atomic Energy Research Institute; 1984. Japanese.

[8] Unesaki H, Shiroya S. Proceeding of International Conference on the Physics of Nuclear Science and Technology; 1998 Oct. 5-8; Long Island, New York; 1998.

[9] Unesaki H. Study on Verification of Nuclear Data for Nuclear Design of Next Generation Thermal Reactors [dissertation]. [Kyoto]: Kyoto University; 2001. 126p.

[10] Okumura K, Kugo T, Kaneko K, Tsuchihashi K. SRAC2006: A Comprehensive Neutronics Calculation Code System. JAEA-Data/Code 2007-004. Japan Atomic Energy Agency; 2007.

31. Neutron Spectrum Measurement of Am-Be Source by Multi-activation-foil Method

Ryotaro Nakamura, Isao Murata
Division of Electrical, Electronic and Information Engineering, Graduate School of Engineering,
Osaka University, Yamada-oka 2-1, Suita, Osaka 565-0871, Japan
E-mail: rnakamura@ef.eie.eng.osaka-u.ac.jp

Boron Neutron Capture Therapy (BNCT) is a promising cancer treatment. Neutrons are bombarded with cancer cells accumulating Boron-10 in advance. As a result, cancer cells are destroyed without serious damages to normal cells. For basic researches for BNCT, standard neutron fields are indispensable. In the Authors' group, Am-Be neutron sources are utilized. In this study, with multi-foil-activation method, property of Am-Be source, i.e. neutron yield and spectrum, was measured. As a result, fairly good agreement was obtained between the present experiment and previous result and literature. We plan to carry out more precise experiments to measure more accurate spectrum and absolute intensity of the Am-Be neutron source for basic researches for BNCT.

1. Introduction

Recently, a new radiation therapy named Boron Neutron Capture Therapy (BNCT) is regarded as a promising cancer therapy. This is a treatment of the next generation, i.e. accumulating ^{10}B in cancer cells in advance, and neutrons are bombarded there. As a result, cancer cells are destroyed by charged particles emitted from a nuclear reaction, $^{10}\mathrm{B} + \mathrm{n} \rightarrow [^{11}\mathrm{B}] \rightarrow \alpha + {}^{7}\mathrm{Li}$. The principle of BNCT is schematically shown in Fig.1.

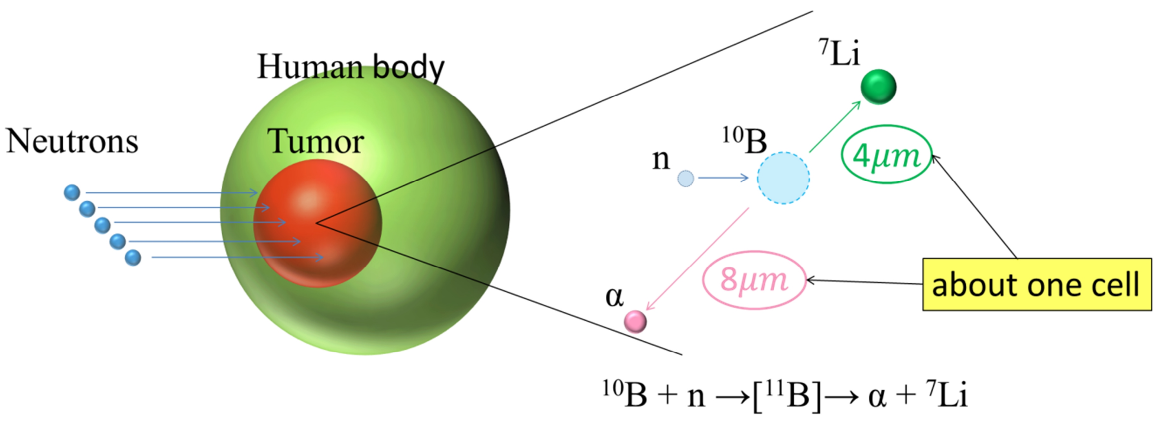

Fig. 1. Principle of BNCT.

In the authors' group, at present, developments of a new neutron spectrometer covering from thermal to epithermal energy region and a new SPECT system for BNCT to monitor the treatment effect are underway. For these studies, it is indispensable to construct neutron fields of thermal and epithermal energies which can be utilized for basic experiments for BNCT. Naturally, neutron sources are necessary to construct this standard neutron fields [1]. In Osaka University, we have four Am-Be neutron sources, the intensity of which is 4.7 GBq for each. Am-Be sources are convenient for use and the intensity is very high. Our Am-Be sources have been utilized for a long time for subcritical reactor experiments. However, it is known that the spectrum of Am-Be source varies depending on mixture ratio of Am and Be, chemical form of them and how to mix them. Consequently, it becomes necessary to measure the neutron spectrum of each source by a user himself/herself.

But, as is well known, it is difficult to measure the neutron spectrum directly because neutrons have no electrical charge. In this study, we employ the multi-foil-activation method as a convenient measuring procedure to determine the neutron spectrum of Am-Be source.

2. Multi-foil-activation method

The multi-foil-activation method is a means of determining the neutron spectrum indirectly. The principle is given briefly in the following: At first, foils are irradiated having different thresholds for activation reactions. Then, discrete γ-rays emitted from the irradiated foils are measured. They are generated after β decay. The neutron spectrum can finally be estimated by unfolding a lot of pairs of activation reaction rates and their reaction cross sections. There exist a lot of isotopes known, which emit γ-rays if activated by neutrons. If employing suitable activation foils, their emitted γ-rays can easily be measured by a Ge semiconductor detector. Because energy dependence of activation cross section shows difference among activation foils, we can obtain the spectral information of neutron source, if we select several activation foils appropriately. In this study, activation foils were selected as in the following manner:

①Possible reactions from Mg to Te were extracted from JENDL-4 [2] taking into account their cross sections above 0.1 barn and threshold energies less than 11 MeV. The reason why reactions having more than 0.1 barn were chosen is in the following:

At this stage, it is unknown whether these reactions really produce activated nuclides. However, if they were activated, the activation cross sections would show generally smaller than the reaction cross sections. And, the upper threshold energy of 11 MeV is for covering the energy range of neutrons emitted from Am-Be sources.

②Nuclides having abundance under 1 % out of the selected nuclides in ① were removed. This is because small abundance ratio causes increase of the sample size, resulting in deterioration of the measurement precision.

③reactions which are actually not activated taking into account the data of JENDL/A-96 were removed [3].

④reactions having half-life from 5 minutes to 15 hours are selected. This has two reasons. The first reason is that a reaction having a very short half-life decreases the amount of radioactivity by over-cooling. The second reason is that a reaction having a long half-life increases the irradiation time and measuring time as a result [4].

Finally, by the above procedure, we selected 9 activation foils. Table 1 shows 9 selected reactions, their half-lives, γ-ray energies and relative intensities.

Table 1 Selected reactions, their half-lives, γ-ray energies and relative intensities.

Reaction	half-life(s)	γ-ray energy(keV)	incidence of γ-ray
$^{24}Mg\ (n,p)^{24}Na$	54000	1368	1
$^{27}Al\ (n,p)^{27}Mg$	567	843.76	0.718
$^{27}Al(n,\alpha)^{24}Na$	54000	1368	1
$^{56}Fe(n,p)^{56}Mn$	9216	840	0.84
$^{59}Co(n,\alpha)^{56}Mn$	9216	840	0.99
$^{64}Zn(n,p)^{64}Cu$	45720	511	0.378
$^{111}Cd(n,n')^{m111}Cd$	2912	245.395	1
$^{113}In(n,n')^{m113}In$	5970	391.69	1
$^{115}In(n,n')^{m115}In$	16150	335	0.459

3. Experiment

Experiments were carried out in an arrangement shown in Figs. 2 and 3. The Am-Be source used in this study is a quasi-point source positioned at the center of a cylindrical casing of 6 cm in height and 3cm in diameter. The Am-Be source and a foil were set so that the distance between the two was 5cm and their heights on a wooden plate was 3cm. A circular wooden jig placed at the center of the wooden; late is to easily and firmly fix the Am-Be source as soon as it is taken from the storage container, in order to suppress unnecessary radiation exposure. By attaching a foil in advance, irradiation can be carried out correctly in the same condition for every foil even having a short time half-life. Foils were irradiated with neutrons emitted from the Am-Be source for a prescribed time theoretically calculated in advance. After irradiation, foils were cooled for 10 minutes (2min. for $^{27}Al(n,p)$ because its half-life is short), and γ-rays emitted from the foils were measured by an HpGe detector.

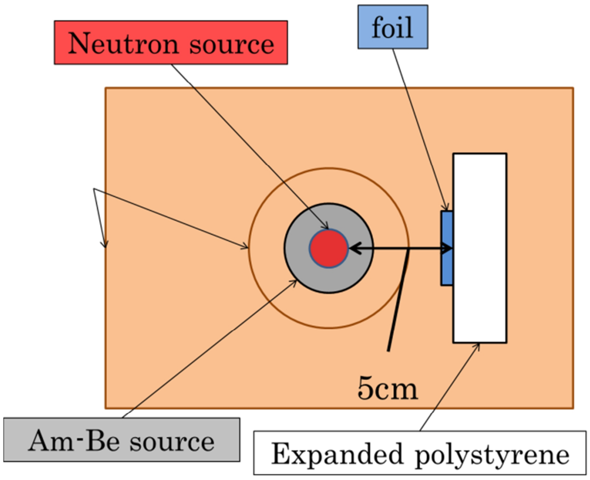

Neutron source region is around the center of the cylinder, the size of which is ∼1cm cubic.

Fig. 2. Experimental setup. Wooden board and Expanded polystyrene were chosen experimental material in order not to disturb experiment results

Fig. 3. Photo of the actual experiment

4. Results and Discussion

Measured results were analyzed by the Bayes theorem to estimate the neutron spectrum of the Am-Be source. The spectrum unfolding process based only on the Bayes theorem was first introduced by Iwasaki of Tohoku University [5]. It is a standard unfolding process in the authors' group [6]. The obtained results are shown in Fig. 4 and Table 2.

Table 2 Neutron yield of Am-Be source

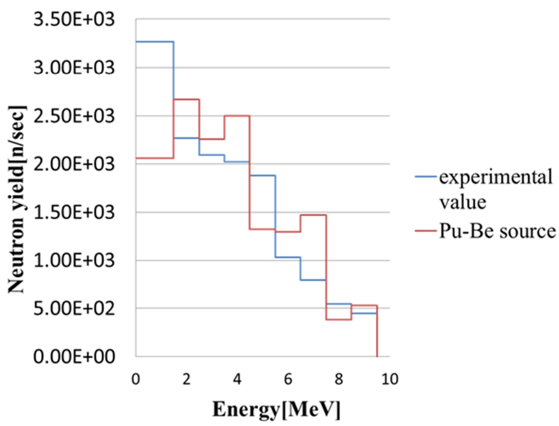

	neutron yield[n/sec]*
Am-Be source(this study)	4.5 ± 0.4 E+06
Am-Be source(previous data)**	2.4 ± 0.2 E+06
Am-Be source(calculated value)***	3.79E+06
Am-Be source(experiment value)***	3.24E+06

*per 4.71×10^{10} [Bq]
**Iehito Tsuda, Osaka university student's graduation thesis(2011)
***K.W.Geiger and L.Van der Zwan,Nucl.Instrum.Meth,131,315(1975)

Fig. 4. Measured energy spectrum of Am-Be source

The structure of the energy spectrum is slightly different from that of the literature data. There are two reasons for this discrepancy. Firstly, the energy of α particle inducing nuclear reactions is different from the energy of neutrons emitted from the Am-Be source. Am-Be neutron source is a mixture of α particle emitter (Am) and Be which are enclosed in a double-sealed stainless steel casing. The spectrum of neutron source is known to change according to the mixture ratio of Am and Be and the shape and thickness of an external stainless steel vessel. Also, molecular formula of Am and Be may change the α particle energy. Secondly, the neutron spectrum can be described coarsely because only 9 foils were used in this study. Generally speaking, the more the number of foils is, the worse the energy resolution is.

Next, obtained neutron yield is compared with the previous result by Tsuda performed in 2011 with gold foils. The neutron yield measured by Tsuda is 2.4×10^6 n/sec, which is different from the present result of 4.51×10^6 n/sec by about twice. There are two reasons about this difference. Firstly, there is some possibility of including systematic error in Tsuda's experiment. As a matter of fact, according Tsuda's article, the measured value of γ-ray disagrees with that of the neutron yield, the cause of which is not yet made clear. Secondly, we have to consider our side problem. The most possible cause is thought to be cross section errors of foils. About activation reactions used frequently, reliability of the cross sections is expected to be enough high. But, for activation reactions used not so often, precision of evaluated nuclear data may be low. This low precision may induce a substantial error seen in this study.

5. Future Work

As a result of the present study, we think of the followings to be carried out as future works. First, about neutron spectrum, we will carry out more precise spectrum measurements using more number of foils so as to confirm the complex spectral shape fixed depending on nuclear levels of Be. As for the neutron yield, disagreement with the previous data, other measuring techniques will be employed to solve above problems, i.e. increasing the number of activation foils in the multi-foil-activation method and more accurate neutron spectrum measurements with time-of-flight (TOF) technique, double scintillator measurement and pulse height spectrum unfolding with n/γ discrimination.

6. Conclusion

The purpose of this study was to measure the neutron spectrum of Am-Be source (4.7GBq) stored in OKTAVIAN facility of Osaka University, which commonly used as standard neutron field for various basic researches especially for BNCT. The neutron spectrum of the Am-Be source and the absolute intensity were measured with 9 activation foils having different threshold energies for their activation cross sections. For an Am-Be source (No.4) stored in the OKTAVIAN facility, the spectrum shape was in acceptably good agreement with the literature. However, the neutron yield was slightly larger than the previously measured value. We plan to perform more accurate and precise measurements for better researches for BNCT in the future.

Reference

[1] Kazuyuki Harada. Design and fabrication of thermal neutron column with Am-Be source. Thesis, Osaka University. 2010.

[2] K. Shibata, O. Iwamoto, T. Nakagawa, N. Iwamoto, A. Ichihara, S. Kunieda, S. Chiba, K. Furutaka, N. Otuka, T. Ohsawa, T. Murata, H. Matsunobu, A. Zukeran, S. Kamada, and J. Katakura. JENDL-4.0: A New Library for Nuclear Science and Engineering. J. Nucl. Sci. Technol. 48(1). 2011 ; 1-30.

[3] Y. Nakajima, JNDC WG on Activation Cross Section Data. JENDL Activation Cross Section File. Proc. the 1990 Symposium on Nuclear Data, JAERI-M 91-032, 1991, pp.43-57.

[4] Richard B. Firestone, Virginia S. Shirley*, Coral M. Baglin, S.Y. Frank Chu, and Jean Zipkin. Table of Isotopes. 8th ed. Hoboken(NJ) : John Wiley & Sons, Inc.: 1996.

[5] S.IWASAKI. A NEW APPROACH FOR UNFOLDING PHA PROBLEMS BASED ONLY ON THE BAYE'S THEOREM. Proc. the 9^{th} International Symposium on REACTOR DOSIMETRY, World Scientific Publishing Co. Pte. Ltd. 1998 : 23.

[6] Iehito Tsuda. Neutron and γ-ray absolute intensity measurement of Am-Be source with graphite column. Thesis, Osaka University. 2011.

32. Design Calculation of Epi-thermal Neutron Field with DT Neutron Source for Low Energy Neutron Spectrometer Developed for BNCT

Kunio Tsubouchi, Tsubasa Obata, Isao Murata
Division of Electrical, Electronic and Information Engineering, Graduate School of Engineering, Osaka University, Yamada-oka 2-1, Suita, Osaka 565-0871, Japan
E-mail: ktsubouchi@ef.eie.eng.osaka-u.ac.jp

In the present study, design result of an epi-thermal neutron column using an accelerator DT neutron source at the Intense 14 MeV Neutron Source Facility, OKTAVIAN, of Osaka University, Japan, was described. The neutron intensity of the OKTAVIAN facility is about 1×10^{11}n/sec. Design calculations were conducted with a general Monte Carlo code, MCNP5[1]. An epi-thermal neutron column was successfully designed giving an acceptably strong epi-thermal neutron flux, compared to the conventional one with an AmBe source.

In the next step, aiming at utilization of the column for basic researches of BNCT, the construction of it will start soon with the presently obtained design result.

1. Introduction

Recently, development of various radiotherapies for cancer is underway. Especially boron neutron capture therapy (BNCT) is a new promising radiation cancer therapy which can destroy selectively tumor cells, simultaneously suppressing influence against healthy cells. However, in BNCT, cases are reported only using nuclear reactors now because of requiring strong low-energy neutron sources. Nowadays in Japan, accelerator based neutron sources (ABNS) which can be constructed in medical facilities such as hospitals are thus being developed. ABNS is a very convenient neutron source in comparison with nuclear reactors. However, in the case of ABNS based BNCT, patients should be positioned very close to the accelerator target because the source strength is quite week at present. This leads to a problem that the spectrum is distorted and becomes different from the standard field obtained in nuclear reactors. Therefore we should measure the neutron spectrum and flux intensity precisely and accurately for each ABNS with a suitable low-energy neutron spectrometer.

In the author's group, a new neutron spectrometer is being developed covering from thermal to epi-thermal energies. Our previous studies showed that the epi-thermal neutron spectrum could be measured with this spectrometer using an AmBe neutron source[2]. However, since this AmBe source is not so strong, it required a very long time to complete a measurement, leading statistical deterioration of the result. The aim of the present research is to design an intense epi-thermal neutron column for fundamental experiments of BNCT.

2. Development of low-energy neutron spectrometer

We first describe the current status, including problems to be solved, the results and so on, for the low-energy neutron spectrometer which is being developed by the authors' group now. And we described the reason why we started this study.

2.1 Detection principle of the energy spectrum of keV region

The principle of the present spectrometer is in the following: A ^{3}He position-sensitive proportional counter is used as a base detector. The incident neutron spectrum is deduced from the detection depth distribution by the use of the relationship between the neutron energy and detection depth. Now we think of neutron incidence from one edge of the detector along to the detector axis. When neutrons react with BF_3 or He^3 gas, the cross-section is greatly changed by the energy, so that the depth of detection varies depending on the energy. If the energy is low, it is detected at a location close to the entrance surface, and if the energy is high, it is detected after penetrating deeply. Thus, by using a position-sensitive proportional counter, it is possible to estimate the energy spectrum of the incident neutron by measuring the detection depth distribution. Now, assuming X is neutron energy spectrum, R is response function that links the detection depth and neutron energy, and Y is detection depth distribution, by solving the inverse problem, i.e., Y = RX, the neutron spectrum can be derived by the equation, $X = R^{-1}Y$.

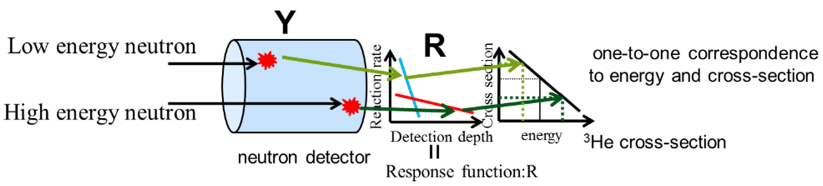

Fig. 1 Detection principle of the energy spectrum

2.2 Experimental system for measuring the neutron energy spectrum

To measure low energy neutron spectrum, an epithermal neutron column was made with an AmBe neutron source of 46 GBq as shown in **Fig. 2**. The column consists of moderator and radiation shield of AlF_3, Ti, lead, and carbon for suppressing over-moderation of neutrons and leakage to the outside. On the right side of the column, a spectrometer assembly was set up. By this assembly, neutrons can be incident to the proportional counter from one side in parallel with the detector axis in order to measure detection depth distribution.

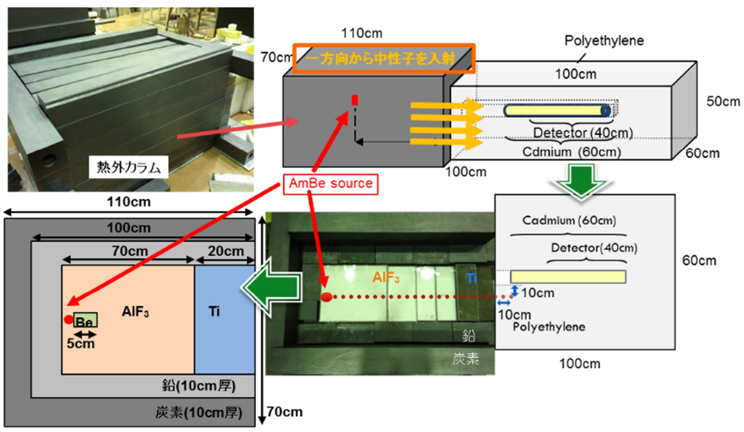

Fig. 2 Experimental system and construction of epi-thermal column using AmBe

2.3 Experimental results and discussion with the epi-thermal neutron column

On the left bottom of **Fig. 3**, the net detection depth distribution is shown. Using the response function in the left upper figure and the detection depth distribution, neutron spectrum was able to be estimated as shown in the right figure [3-4]. Compared with the result calculated by MCNP5, a fairly good agreement was seen. However, as also shown in this figure, the statistical accuracy of the detection depth distribution is low. This result is thought to be due to the fact that the used AmBe neutron source was weak, and therefore it took several days to obtain the data with an acceptable S / N ratio.

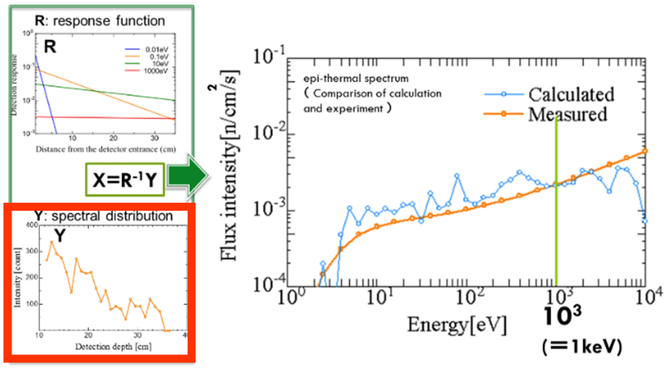

Fig. 3 Comparison of neutron spectrum measured with the epi-thermal neutron field using an AmBe source

In this study, from the above result, by making the epi-thermal neutron column with DT accelerator neutron source, researches have been started to aim at improvement of the measurement accuracy. In Osaka University, there is an accelerator DT neutron source facility, named OKTAVIAN, the neutron intensity of which is 1000 times larger than the AmBe. It may be possible to construct a strong epithermal neutron field with the DT neutron source. In the following chapters, the details of the design will be described.

3. Design of strong epi-thermal neutron field with DT neutron source

We designed a strong epithermal neutron column referring the AmBe neutron source described in Section 2.3 as a basic form, using the DT neutron source of OKTAVIAN and materials, i.e., Be, heavy water(D2O), graphite, Ti, Cd and AlF_3 [5].

The following design criteria were considered to design the present epi-thermal neutron field.

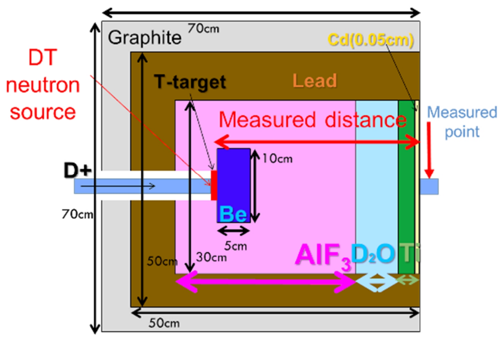

① Epi-thermal neutron intensity (φ)

$\varphi \sim 1\times10^{-4}$ n/cm^2/source

This value was estimated semi-empirically from design of the neutron field using accelerators so far. It is presumably thought that this level can ideally be achieved. In the case of OKTAVIAN facility, because the source strength is about 10^{11} n/sec, the epi-thermal neutron flux intensity is about 1×10^{7} n/cm^2/sec.

Fig. 4 Design example of epi-thermal column using DT neutron source

②Epi-thermal to fast neutron flux ratio（η）

η> 10

For the design calculations, a three-dimensional universal neutral particle Monte Carlo code, MCNP5, was used with the nuclear data library of JENDL-3.3. F2 tally was used to estimate surface averaged flux.

The following three parameters in **Fig. 4** were varied in the design.

1) AlF_3 (first moderator) thickness 2) D2O (second moderator) thickness and 3) Ti (to cut several tens keV neutrons)

In fact, it was difficult to meet conditions ① and ② at the same time. Therefore, the column design was divided into two models as follows:

○Balanced (B) source: η should be as high as possible, i.e., η > 3, called Criteria: ①.

○Pure (P) epi-thermal source: Meeting η> 10, φ should be as high as possible, i.e., φ～ 1×10^{-5} n/cm^2/source, called Criteria: ②.

In the following, columns meeting criteria ① and ② are called B-source and P-source, respectively. In this study, details of P-source and B-source column design are described.

4. Epi-thermal neutron column design results and discussion

4.1 Optimization of the length of AlF_3

Firstly, for the column of **Fig. 4**, AlF_3 was optimized. η value and epi-thermal neutron flux intensity are plotted in **Fig. 5** as a function of AlF_3 thickness. For η> 3, 40 cm or thicker one was necessary. When moderation is enhanced by addition of D2O, η value can be improved without deterioration of epi-thermal flux performance. It was found that the best η value could be obtained if the AlF_3 thickness was 33 cm. This is the design of the B-source.

On the other hand, it was necessary to increase the η value in the design of P-Source. From the figure, 60 cm or thicker one is required. By adding an appropriate thick D2O, η value can be greater than 10. As shown in **Table. 1**, the design goal was met when the D2O thickness was 10 cm and the AlF_3 layer was set to 63 cm thick.

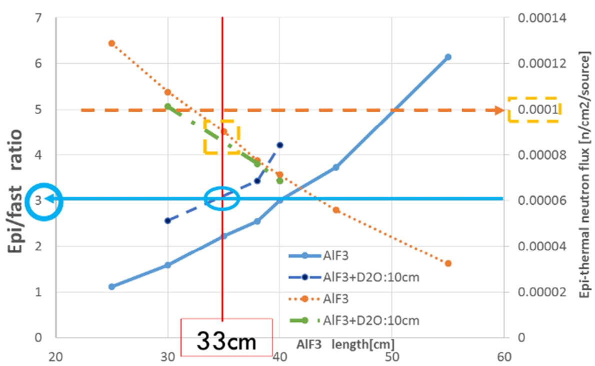

Table. 1 Result of P-source design

length [cm]	Epi/fast ratio	Epi flux [n/cm^2/sec]
AlF3:65cm	8.50	1.82E-05
AlF3:65cm + D2O:5cm	11.58	1.52E-05
AlF3:65cm + D2O:10cm	12.92	1.11E-05
AlF3:65cm + D2O:15cm	10.44	8.49E-06
AlF3:60cm + D2O:10cm	9.60	1.52E-05
AlF3:63cm + D2O:10cm	11.00	1.26E-05

Fig. 5 Graph for determining an optimum thickness of AlF_3

(line on the left shows the ratio of epi-thermal / fast , dot-line on the right shows the epi-thermal neutron flux)

Then, cadmium sheet of 0.05 cm thickness was added in front of the column to cut the thermal neutron component. For Ti layer to cut several tens keV neutrons, calculations were carried out to apply it to the P-source and B-source for 4 patterns, that is, 0cm, 1cm, 5cm, 10cm thick Ti. As a result, when employing the thicknesses of 1cm in the B-source and 5cm in P-source, the values of η and epi-thermal neutron flux showed the best. **Table. 2** summarizes the design results of P-source and B-source.

Table. 2 Design results of B and P-sources

	AlF_3	D2O	Ti	Cd	Epi/fast ratio	Epi flux [n/cm^2/sec]
B-source	33cm	10cm	1cm	0.05cm	3.07E+00	8.61E-05
P-source	63cm	10cm	5cm	0.05cm	9.27E+00	1.38E-05

4.2 Reduction of DT neutron contribution

Figure 6 shows the result of calculation for the neutron spectrum obtained for the B-source and P-source of **Table .2**. From this figure, epi-thermal neutrons have successfully been generated in energy range from 0.5eV to 10keV. However, in the present design DT neutrons were used as a neutron source. In the figure, a strong peak at 14MeV is thus seen. Especially in the B-source, the intensity of epi-thermal neutrons was lower than the peak strength of 14MeV. It means it should be necessary to reduce this contribution. The strong influence of 14MeV may arise a bad result especially in basic researches of BNCT.

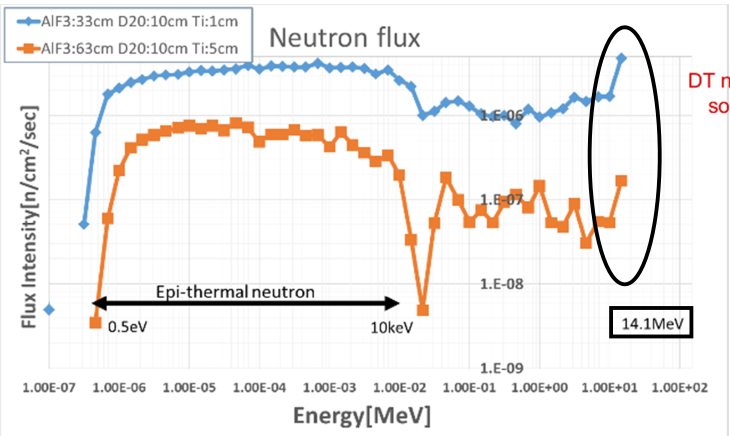

Fig. 6 Neutron flux intensity of P-source and B-source

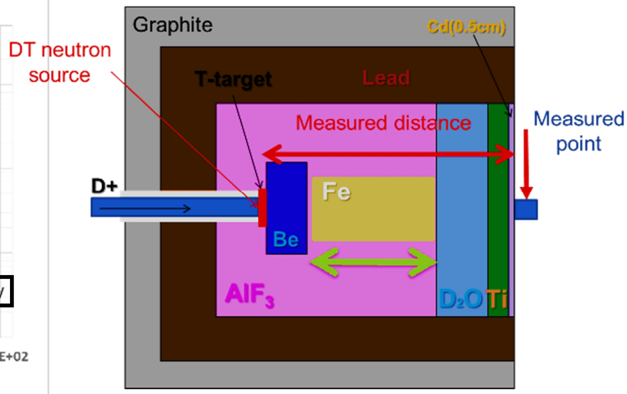

Fig. 7 Final design of the B-source with iron shield

In this study, in order to reduce direct 14MeV neutrons, calculations were carried out by adding an iron shield between Be and D2O inside the column of the B-source as shown in **Fig. 7**.

Figure 8 was the result of calculation as a function of iron thickness.

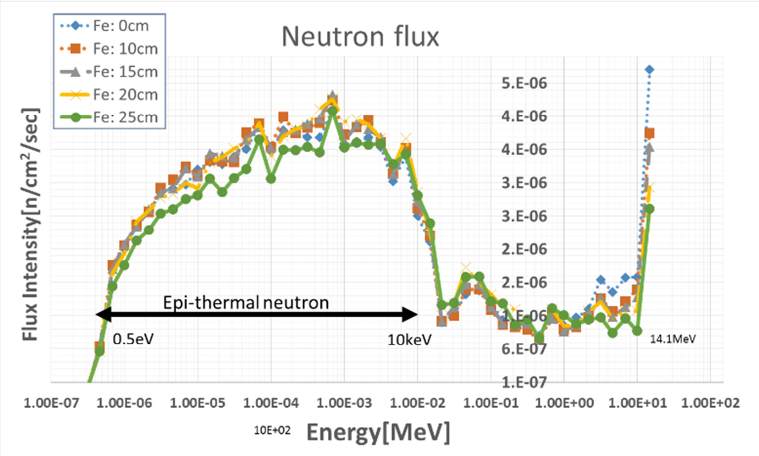

Table. 3 Each parameter when changing the length of the iron

Fe_length [cm]	Epi/Fast ratio	Epi flux [n/cm^2/sec]	14MeV_value
0	3.07	8.61E-05	4.81E-06
10	3.50	8.86E-05	3.84E-06
15	3.48	8.84E-05	3.63E-06
20	3.40	8.84E-05	3.04E-06
25	3.29	8.14E-05	2.71E-06

Fig. 8 Neutron intensity of B-source with iron to reduce the contribution of 14MeV

As shown in **Table 3** and **Figure 8**, by increasing the iron thickness from 0 cm to 25 cm, the flux intensity of 14 MeV was able to be suppressed down to about half of that without iron shield. Even though iron shield was added, the neutron performance did not deteriorate so much. Hence, physically acceptable iron thickness of 25 cm was finally employed. Final design for the B-source with iron shield was in the following:

Cd; 0.05cm, AlF3; 33cm, D2O; 10cm, Ti; 1cm, **Fe; 25cm**.

5. Conclusions and Future works

Design of an epi-thermal neutron field with a DT neutron source was carried out. Compared to the previous design with AmBe sources, the performance was really improved to be more than 3 orders of magnitude in epi-thermal neutron flux value. After contribution of gamma-rays will be examined the presently designed assembly will be constructed at the OKTAVIAN facility of Osaka University. The characteristics measurement will be carried out to compare with the simulation. Thereafter, it will be expected to be utilized for fundamental experiments of BNCT.

References

[1] X-5 Monte Carlo Team: MCNP-A General Monte Carlo N-Particle Transport Code(2003) N-particle transport code, version 5(2003).

[2] T,Obata: “Development of keV neutron spectrometer with ^{3}He position-sensitive proportional counter”, Master’s thesis, Osaka University (2013) [in Japanese].

[3] I,Murata, H.Miyamaru: “Low-energy neutron spectrometer using position sensitive proportional counter —Feasibility study based on numerical analysis”, Nuclear Instruments and methods in Physics Research A 589,445-454(2008).

[4] S.Iwasaki: “A new approach for unfolding PHA problems based only the Bayes’ Theorem”, Proc. 9th International Symposium on Rector Dosimetry, Prague, Chezk Republic, pp. 245-252 (1996).

[5] K,Harada: “Design and construction of thermal and epi-thermal neutron field for BNCT basic research using the Am-Be neutron source”, Master’s thesis, Osaka University (2012) [in Japanese].

33. Feasibility Study on Polonium-209 as Radioisotope Fuel for Space Nuclear Power

Jun NISHIYAMA
Research Laboratory for Nuclear Reactors, Tokyo Institute of Technology
2-12-1-N1-19 Ookayama, Meguro-ku, Tokyo 152-8550, Japan
E-mail:jun-nishiyama@nr.titech.ac.jp

We have investigated the performance and the production method of alternative isotopes of ^{238}Pu as a radioisotope fuel for use in space radioisotope power generators. Polonium-209 has the possibility to be an alternative material of ^{238}Pu. It has enough half-time of 102 years and the specific power of 490 W/kg. From the simulation, the beam current of 14 A with 40 MeV proton energy provides 1 kg/yr of ^{209}Po annually.

1. Introduction

Historically, plutonium-238 has been proven to be the best radioisotope for the provision of space nuclear power because of its high power density (540 W/kg), enough half-life (87.7 years), low radiation levels, and stable fuel form at high temperature. But currently there is no large-scale production of ^{238}Pu in the World [1]. Plutonium-238 produced by irradiation of ^{237}Np targets in a nuclear reactor. The ^{237}Np is derived from the production and irradiation highly enriched uranium fuel. Chemical processing is used to separate the ^{238}Pu. It was only the United States and Russia that have such reactors and processing facilities. In the U.S., the K-Reactor at the Savannah River Site in South Carolina, which was shut down in 1996, was the last reactor to produce significant quantities of ^{238}Pu. And Russia has also lost its capability to produce new ^{238}Pu. In addition, plutonium has a safeguards issue. International Atomic Energy Agency in their publication, INFIRC 153 [2], mentioned that plutonium containing 80% of ^{238}Pu or more is exempted from proliferation concerns. There is no problem if pure ^{238}Pu can be produced but ^{239}Pu is contained in actuality. Therefore, isotope ratio of ^{238}Pu would be less than 80% by its half-life eventually.

Current concerns over the limited supply and difficult treatment of ^{238}Pu have increased the need to explore alternative isotopes for space nuclear power applications. Polonium-209 has the possibility to be an alternative material of ^{238}Pu. The ^{209}Bi (p, n)^{209}Po reaction is one of production method. The purpose of this study is to evaluate the production efficiency of ^{209}Po by the proton accelerator.

2. Polonium-209 and their production method

The key factors involved in selecting the radioisotope fuel for use in radioisotope power generators are: long half-life compared to the operational mission lifetime; a high power density and high specific power [W/kg]; low radiation emissions; and a stable fuel form with a high melting point suitable for the application. Moreover cost of fuel production and cost relative to benefits must be reasonable. A simple calculation of specific power was performed to find an alternative radioisotope of ^{238}Pu. Specific power q_α [W/kg] by α decay can be expressed as

$$q_\alpha = \frac{\lambda Q_\alpha b_\alpha N_A}{M} \quad (1)$$

where λ is the decay constant[1/s], Q_α is the Q-value of α decay [J] [3], b_α is the branching ratio of α decay, N_A is the Avogadro constant [1/mole] and M is the Molar mass [kg/mole]. Assuming that all energy of charged particles is converted to heat and the decay of the daughter nuclides are ignored.

Table 1 shows the calculation results of ^{238}Pu and major nuclides which have long half-life (> 10 years) and high specific power (> 100 W/kg). Considering the production by nuclear reaction, ^{209}Po is the best alternative material of ^{238}Pu. It has an enough half-time of 102 years compared to the operational mission lifetime. In addition it does not depend on the nuclear fuel such as uranium and plutonium. ^{147}Gd also has good performance but there is no production path from natural element by one or two nuclear reaction. For ^{209}Po, the ^{209}Bi (p, n)^{209}Po reaction is a promising production path from natural element.

Figure 1 shows the measurements [4-8] and evaluations [9, 10] of ^{209}Bi (p,n)^{209}Po reaction cross section. The threshold energy of this reaction is 2.69 MeV. Above the threshold energy the cross section has a peak around 12 MeV because (n, 2n) reaction channel is opened at 9.69 MeV. It means that using high energy proton produces Po isotopes. Po isotopes other than ^{209}Po have shorter half-life than ^{209}Po, for example ^{208}Po is 2.898 y, ^{210}Po is 138.4 d. It requires enough cooling time. For this reason, it is better that the Po isotopes production is smaller.

Table 1. Specific power of major α decay nuclides

Nuclide	Specific power [W/kg]	Half-life [year]
^{238}Pu	567.5	87.7
^{147}Gd	660.9	70.9
^{209}Po	492.5	102.0
^{232}U	717.5	68.9
^{241}Am	114.5	432.6
^{243}Cm	1842.4	29.1
^{244}Cm	2830.2	18.1
^{249}Cf	152.5	351.1
^{250}Cf	3965.7	13.1

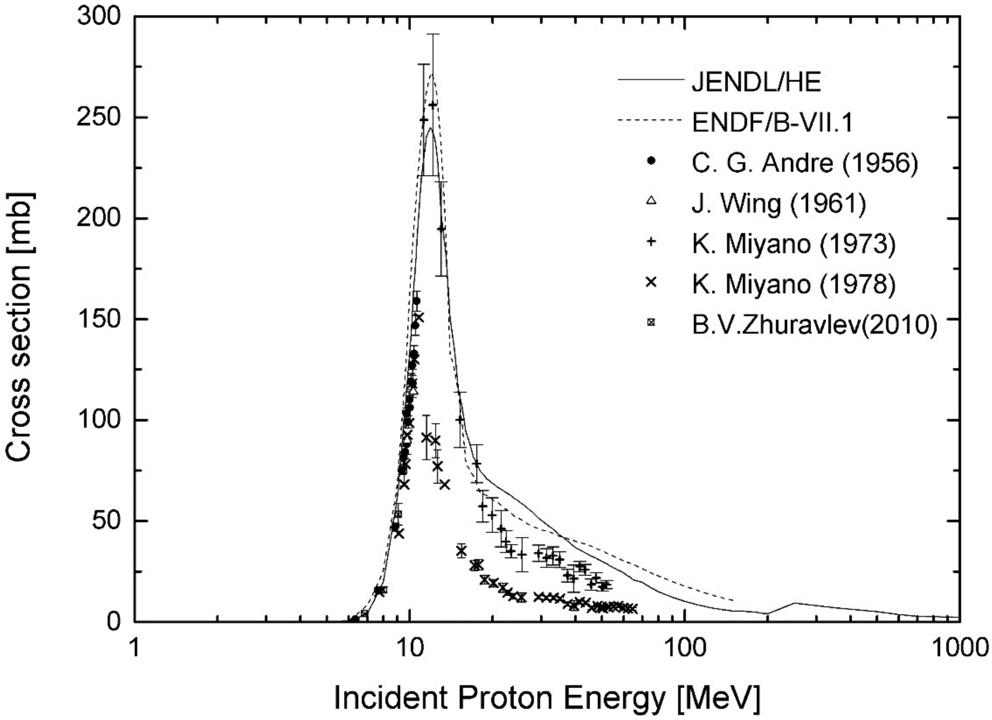

Figure 1. Cross section of ^{208}Bi(p,n)^{209}Po reaction

3. Calculation results

Simulations for the production rate of Po isotopes were performed using the PHTIS code [11] with a simple geometry. In this calculation, INCL (Intra-Nuclear Cascade of Liege) [12] was used as nuclear reaction model for nucleons induced reactions. The target was natural Bi (metallic form of ^{209}Bi) and was thick enough that all protons stopped completely. It was assumed that the target composition does not change with irradiation. The calculation results of Po isotope production rate are shown in **Figure 2** and the ratio of ^{209}Po is shown in **Figure 3**. The production rate of ^{209}Po rapidly increases as the incident proton energy increases around the threshold energy. Above 10 MeV, its increase was moderate. Additionally, the ^{208}Po is generated and the ratio of ^{209}Pu/($^{208+209}$Pu) was constant of about 0.2 above 20 MeV. Using these results, requirement for the proton beam were obtained. **Figure 4** and **5** are show the beam requirement of current and power for annual production of 1 kg ^{209}Po, respectively. The incident proton energy of 40 MeV is the most efficient regarding beam power. But it requires large beam current of 14 A to product 1 kg ^{209}Po per year. This requirement for accelerator is quite large in comparison with the current accelerator technology.

The reaction of ^{209}Bi (n, γ)^{210}Bi (β decay) ^{210}Po (n, 2n)^{209}Po is another production path. This reaction may be possible in a system to use nuclear reactor and accelerator such as the ADS with Lead-Bismuth target. For evaluating the production rate using this system, transport calculation of proton and neutron and burnup calculation of Pb-Bi target are needed.

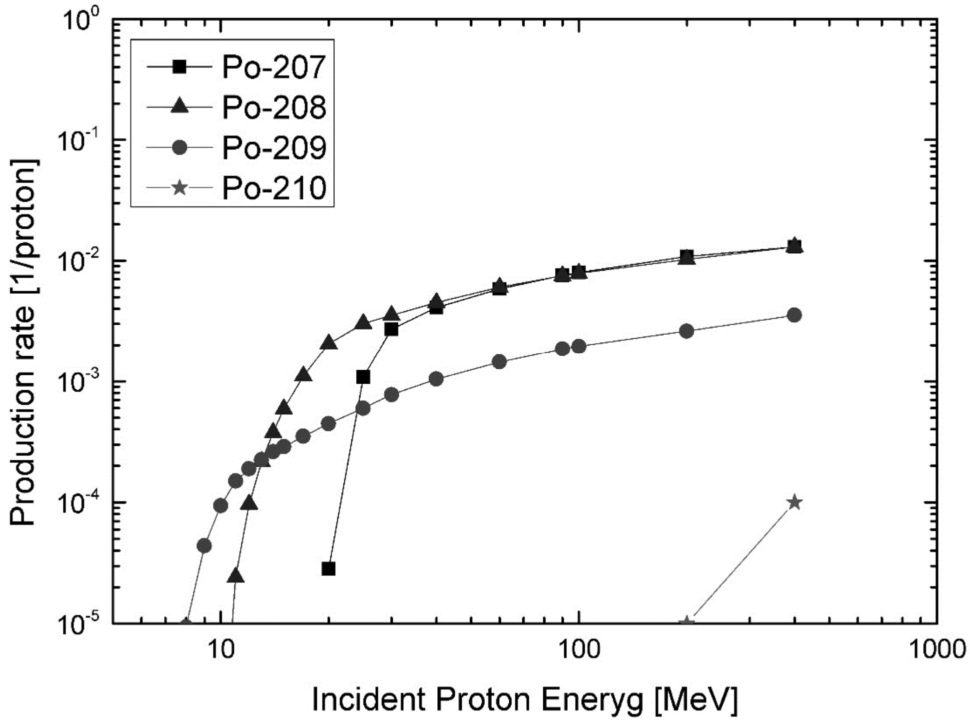

Figure 2. Production rate of Po isotopes

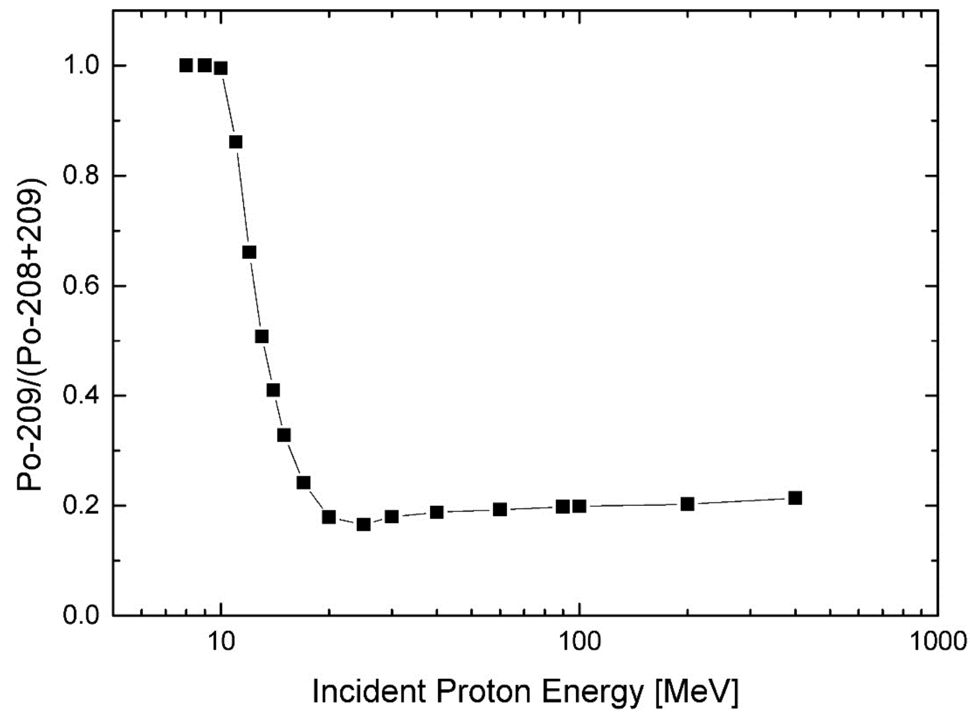

Figure 3. Ratio of ^{209}Po/($^{208+209}$Po)

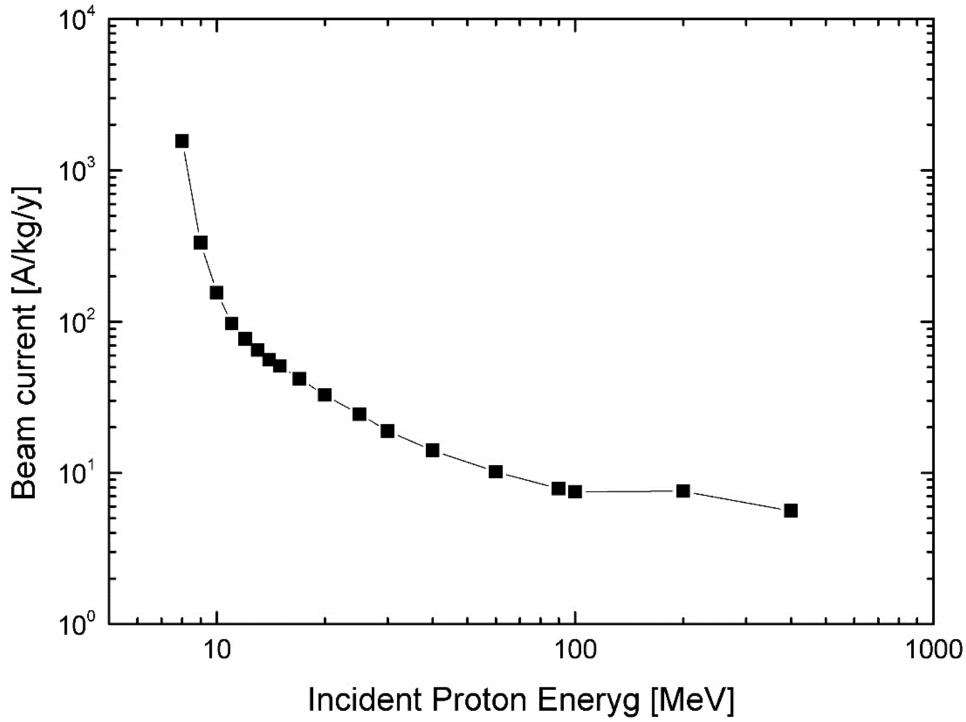

Figure 4. Beam current requirement for annual production of 1 kg ^{209}Po

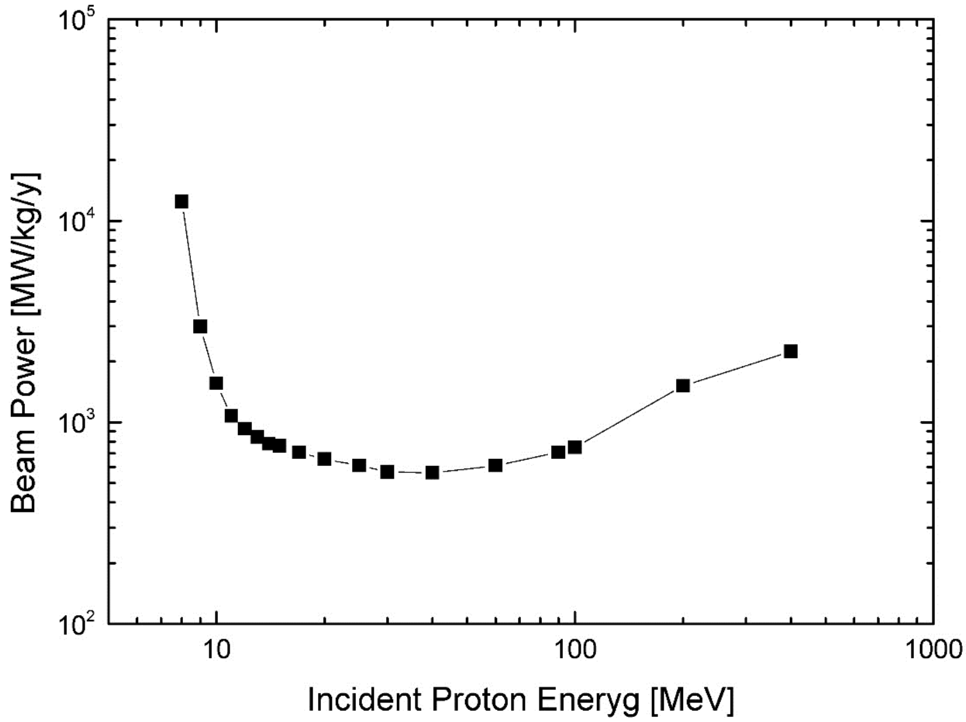

Figure 5. Beam power requirement for annual production of 1 kg ^{209}Po

4. Summary

The performance and the production method of ^{209}Po were investigated as a radioisotope fuel for use in space radioisotope power generators. The ^{209}Po has the possibility to be an alternative material of ^{238}Pu. It has an enough half-time of 102 years compared to the operational mission lifetime. The production by ^{209}Bi(p, n)^{209}Po reaction with the proton accelerator is the method which is independent of nuclear fuel. The beam current of 14 A with 40 MeV proton provides 1 kg/yr of ^{209}Po annually. However, the requirement for accelerator is quite large in comparison with the current accelerator technology.

Acknowledgements

I would like to thank Mr. Yohei Ishizu and Mr. Tomohiro Imai. They gave me the opportunity to begin this study and the information about space nuclear systems.

References

[1] Draft Environmental Impact Statement for the Proposed Consolidation of Nuclear Operations Related to Production of Radioisotope Power Systems. DOE/EIS-0373D, U.S. DOE; 2005.
[2] Information Circular INFCIRC/153. International Atomic Energy Agency; 1972.
[3] Audi G, Wapstra AH, and Thibault C, The AME2003 atomic mass evaluation (II). Tables, graphs, and references. Nucl. Phys. 2003;A729:337-676.
[4] Andre CG, Huizenga JR, Mech JF, Ramler WJ, Rauh EG, Roclin SR, Proton cross section of ^{209}Bi. Phys. Rev. 1956;101:645-651.
[5] Wing J, Huizenga JR. (p,n) Cross Sections of V51, Cr52, Cu63, Cu65, Ag107, Ag109, Cd111, Cd114, and La139 from 5 to 10.5 MeV. Phys. Rev. 1956;128:280-290.
[6] Miyano K, Nakahara H, The cross section and the recoil range study of the ^{209}Bi(p,n) and (p,2n) reactions. J. Phys. Soc. Jpn. 1973;35:953-956.
[7] Miyano K, Ando T, Kudo H, Yanokura M, Nakahara H. The (p,n) reaction on Bi-209 and pre-compound process. J. Phys. Soc. Jpn. 1978;45:1071-1075.
[8] Zhuravlev BV, Lychagin AA, Titarenko NN, Demenkov VG, Trykova VI. Nuclear level densities in Bi-208 and Po-209 from the neutron spectra in the (p,n) reactions on Pb-208 and Bi-209 nuclei. Phys. Atom. Nucl. 2010;73:1111-1115.
[9] Shibata K, Nakagawa T, Fukahori T, Iwamoto O, Ichihara A, Iwamoto N, Kunieda S, Otuka N, Katakura J, Watanabe Y, Kosako K. Recent advances in the JENDL project. Proc. Int. Conf. on Nucl. Data for Sci. and Technol; 2007 Apr 22-27; Nice. France; 2008:727–732.
[10] Chadwick MB, Herman M, Oblozinsky P, Dunn ME, Danon Y, Kahler AC, et al. ENDF/B-VII.1 Nuclear Data for Science and Technology: Cross Sections, Covariances, Fission Product Yields and Decay Data. Nuclear Data Sheets. 2011;112:2887-996.
[11] Sato T, Niita K, Matsuda N, Hashimoto S, Iwamoto Y, Noda S, Ogawa T, Iwase H, Nakashima H, Fukahori T, Okumura K, Kai T, Chiba S, Furuta T, Sihver L. Particle and Heavy Ion Transport Code System PHITS, Version 2.52. J. Nucl. Sci. Technol. 2013;50:913-923.
[12] Boudard A, Cugnon J, David JC, Leray S, Mancusi D. New potentialities of the Liège intranuclear cascade model for reactions induced by nucleons and light charged particles Phys. Rev. 2013;C87:014606.

34. Study on Fluid Temperature Measurements using an AmBe Neutron Source

Hideya Ito, Isao Murata
Division of Electrical, Electronic and Information Engineering, Osaka University Yamada-oka 2-1, Suita, Osaka, 565-0871 Japan
e-mail:hito@ef.eie.eng.osaka-u.ac.jp

Neutrons attract scientist's attention as an important probe to see material because it can easily transmit through matter and it has appropriate reaction cross section for most nuclides. In particular, researches are underway in fields such as mine exploration, neutron CT, visualization of coolant flow. In the authors' group, study on visualization of coolant is carried out with a DT neutron source. As a part of these efforts, there is a study of temperature measurements of fluid using slow neutrons. In this study, the possibility of temperature measurements of fluid by using an AmBe neutron source is examined. The principle is quite simple, that is, the peak of the Maxwellian distribution is shifted by temperature change. As a result, the reaction rate of (n, γ) reactions is changed by it. In this time, because we confirm the principle verification, we examine a water sample, which is most-frequently used out of coolants. Varying the temperature of the water, we measured hydrogen capture γ-rays emitted from the sample. As a result of measurements, the feasibility was confirmed experimentally by checking the intensity change of discrete peaks of capture γ-rays of hydrogen. By this technique, temperature measurements can be performed non-destructively and safely inside machines and at places difficult in entering and/or approaching.

1. Introduction

The authors' group has carried out studies on visualization of the coolant, such as an automobile engine by using a DT neutron source. Recently, as a part of these efforts, researches on non-destructive measurements of the fluid temperature has been advanced with slow neutrons. In the case of visualization of water flow, DT neutrons are necessary because beta decay of the ^{16}N reaction produced by ^{16}O(n, p) reactions is utilized. In the case of the temperature measurement, as described in detail in the following chapter, it uses neutron capture reactions. It is thus not necessary to use the DT neutron. An AmBe neutron source is very easy to use compared to the DT neutron. In this study, thermal neutrons are created using the AmBe neutron source, in order to investigate the possibility of temperature measurements of the fluid experimentally. By this study it can be expected to be possible to safely measure the temperature nondestructively in a machine, even in a difficult place to enter.

2. Principle

For most nuclides, as shown in an example of hydrogen in Fig. 1, the cross section of neutron capture depicts a shape that is inversely proportional to the velocity of neutrons.

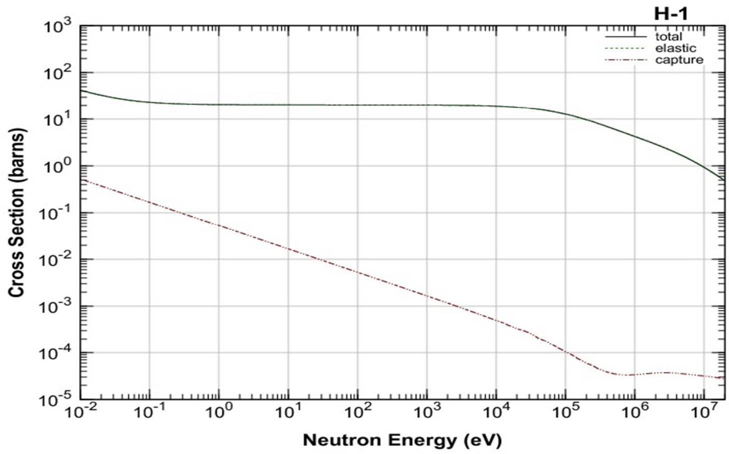

Fig 1 Cross section of $^1H(n,\gamma)^2H$.[1]

When the substance reaches its equilibrium state in a room, the neutron spectrum in the substance varies depending on the kind of the composition and its temperature. It shows the Maxwellian distribution as shown in Fig. 2 schematically. The peak position of the distribution is determined by the material temperature.

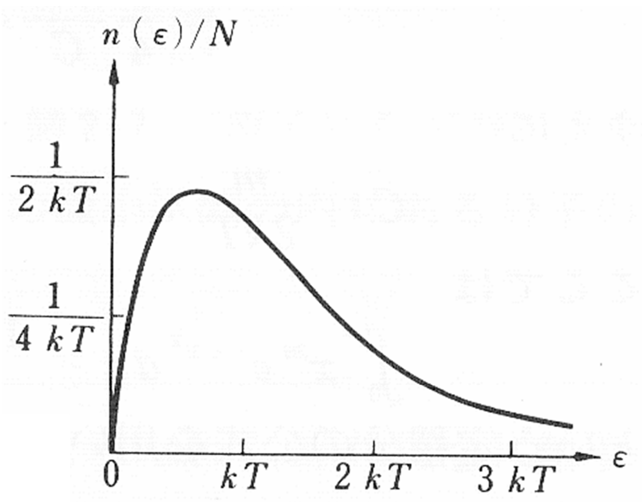

Fig. 2 The Maxwellian distribution at the temperature T, where k is Boltzmann's constant and $n(\varepsilon)/N$ is the relative particle number density distribution.[2]

The reaction rate, $N\sigma\varphi$, for the (n, γ) reaction, can be calculated by the energy integral of $\sigma\varphi$. When the temperature rises, the distribution of φ shifts to the high energy side. Because σ decreases with increase of neutron energy, the reaction rate decreases accordingly. By measuring the decrease, it is possible to estimate the fluid temperature.

3. Experiment and results

In this study, in order to perform proof-of-principle of temperature measurements, water that is most commonly used as a coolant was selected as the sample. Capture cross sections of ^{1}H contained in water are large. Monochromatic γ rays of 2.22MeV are thus emitted via this reaction. In addition, we use an AmBe source (185 GBq), because it is easy to use as a neutron source. As shown in Figs. 3 and 4, the source was placed on the side surface of water in a constant temperature bath. By adjusting the temperature of the bath, the average energy of the hydrogen can be controlled through the water temperature. It is verified how much change is seen in the measured intensity of the neutron capture gamma rays.

The 2.22MeV gamma-rays emitted by ^{1}H (n, γ) capture reactions were measured by an HpGe semiconductor detector shielded heavily, which was arranged to view only the water sample.

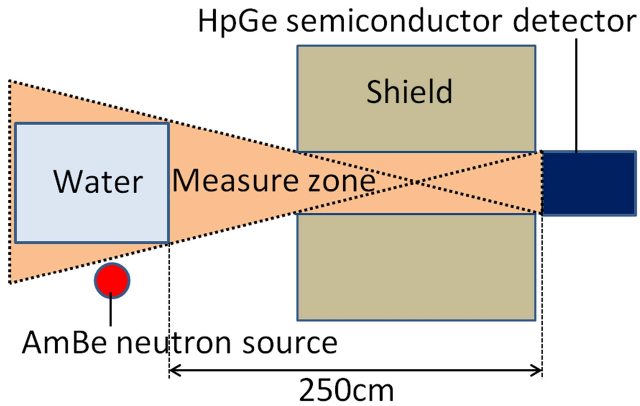

Fig. 3 Horizontal cross section of the experimental arrangement

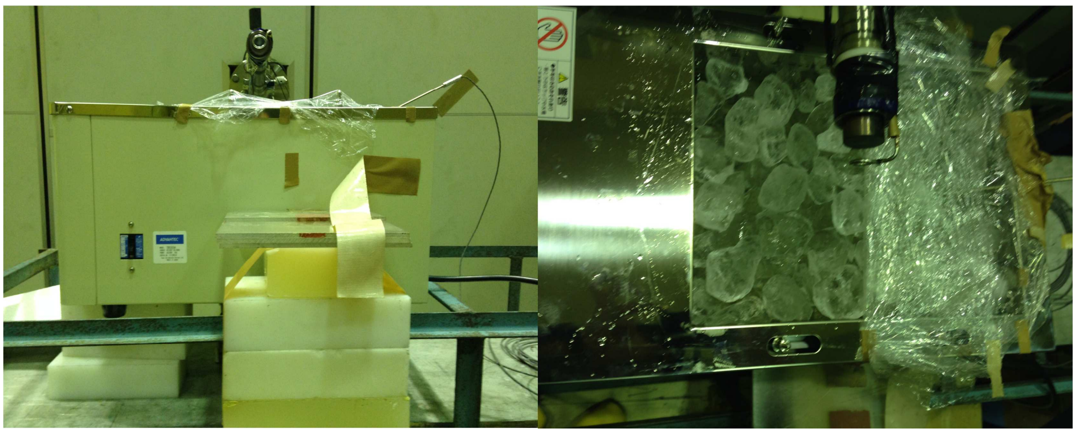

Fig. 4 Photos of experimental equipments; side view (left) and top view (right)

Two kinds of experiments were carried out as follows:

○Experiment 1: 11 L water measured at temperatures, 22.6℃, 53.1℃, and 77.6℃.

○Experiment 2: 7.5 L ice and 3 L water measured at temperatures, 1.2℃ and 53.2℃.

In each measurement, gamma-rays of 2.22MeV emitted by the capture reaction from water were measured. From the latter measurement, the data of 0℃ can be obtained by normalizing the value at 53.2℃. Figure 5 shows an example of the spectrum measured at 22.6℃ (room temperature). In order to accurately measure the small changes due to the small temperature difference, measurement was continued so that the net area counts of 2.22 MeV gamma rays (shown as a ROI in Fig. 5) reached more than 10000 counts.

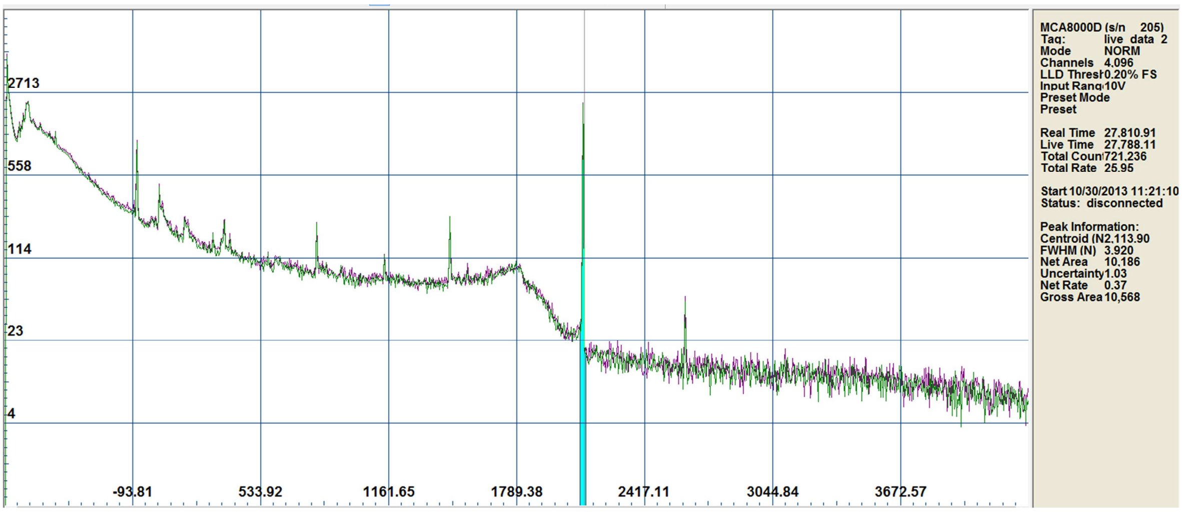

Fig. 5 Gamma-ray pulse height spectrum for water sample at 22.6 ℃

Figure 6 shows the measured net area count divided by the measurement time (CPS). Measured values are summarized in Table 1. For experimental values in the figure, after plotting three-point data of Experiment 1, the data of 1.2℃ was plotted which was evaluated by normalizing the data of Experiment 2 at 50℃ with three data of Experiment 1. This is because the measurement conditions are different in Experiments 1 and 2. Lines in Fig. 6 were obtained by a least-squares fitting of points. A red dotted line shows the fitted analytical calculation result performed with MCNP5[3] under the following conditions. A computational model was made by simulating the real system precisely in three dimensions as shown in Figs 3 and 4. As a detector, the F2 tally was used to measure gamma-rays. In addition, in order to accurately evaluate the difference by neutron temperature, was used S(α, β) of the light water. Temperature points are 300K, 400K and 500K. The results of the three points are shown in the figure together with the experimental values.

Table 1 Reaction rate change due to temperature change

Temperature(℃)	Net area	Gross area	Total area	Live time(sec)	Net area/Live time	Normalized**
22.6	9915	10272	633263	22780.72	0.435236	-
53.1	31724	32769	2112404	75296.33	0.421322	-
77.6	25275	26176	1746282	62507.69	0.404350	-
1.2	10011	10427	694032	25829.02	0.387587	0.443496
53.2	10186	10568	721236	27788.11	0.366560	0.419435
27*	-	-	-	-	-	0.434
127*	-	-	-	-	-	0.377
227*	-	-	-	-	-	0.326

*: MCNP calculation, **: Normalized to Experiment 1 at 50℃

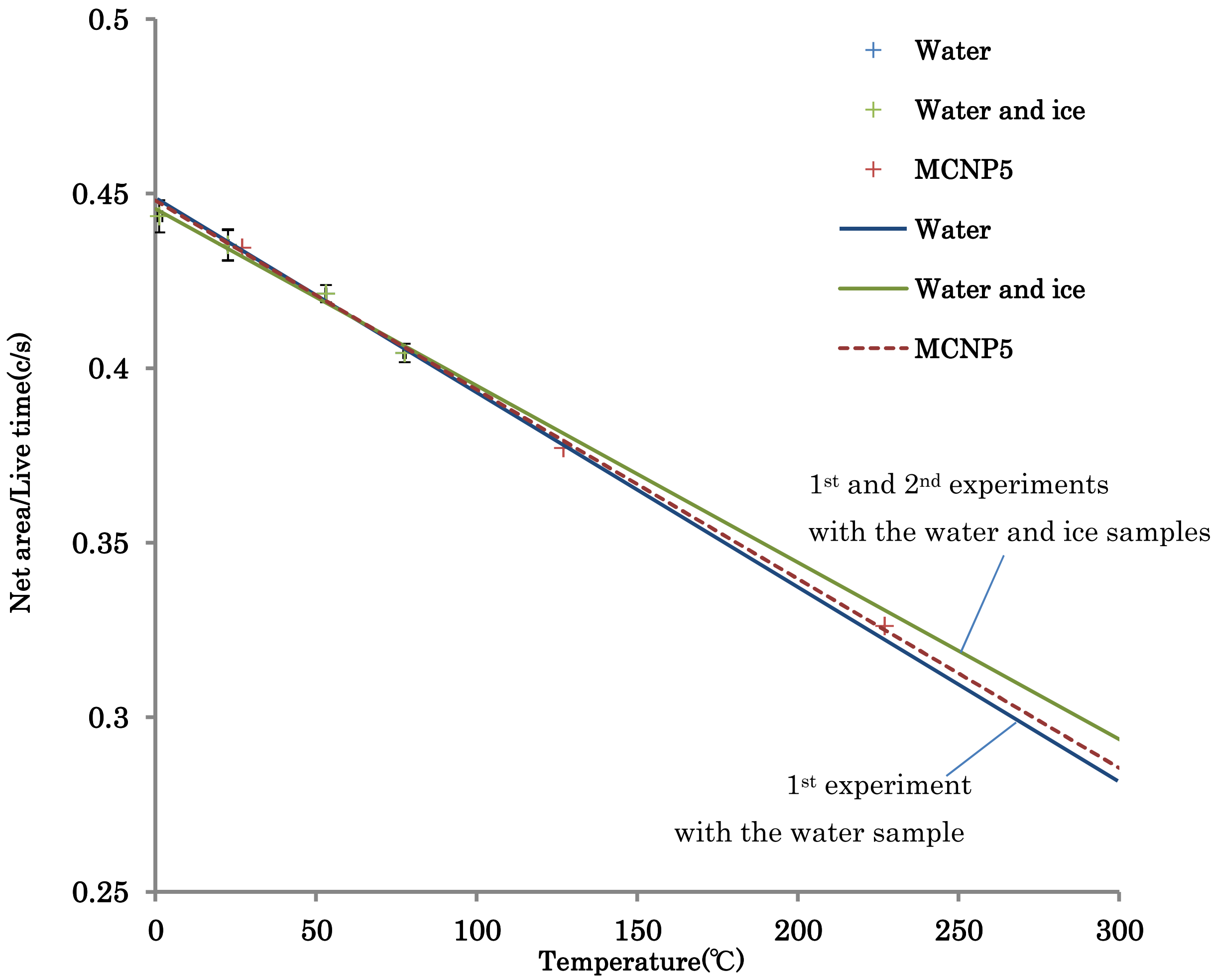

Fig. 6 Experimental values and calculation results.

4. Discussion and conclusion

In Fig. 6, a clear change is experimentally observed in reaction rates through the difference in the water temperature. However, in order to obtain accurate data, i.e., with statistical errors of 1-2%, using a strong AmBe neutron source of 185 GBq, it took necessarily several hours to complete the measurement for the water sample of about 10L. The quantity of fluid seems to give not so large influence to the results. However, since it is difficult to utilize neutron sources stronger than the present case, there is still a severe issue that the measurement time is too long. On the other hand, the theoretical values evaluated with the MCNP5 code were in good agreement with the measured values. As a result, it can be expected that applications with the presently proposed technique can be designed and predicted by theoretical calculatiion. However, in the case of water, it seemed to be possible to estimate the temperature difference by using the evaluated S(α, β). As for other materials, if S(α, β) is not evaluated particularly, it may be difficult to estimate the accurate effect. It should be noted that when a Ge detector is used for measuring γ rays, because it is set in a very large background neutron field, it is seriously irradiated. In this point, we should pay great attention to take an extreme care for radiation shielding.

From the result, it was confirmed that it is in principle possible to perform temperature measurements nondestructively. However, we think of the following problems to be solved in the future:

-Examination of the experimental conditions

More detailed discussions about conditions for practical applications should be necessarily carried out for amount of sample, measurement time, AmBe strength, experimental arrangement, performance of the detector and so on.

- It is necessary to evaluate how the minimum temperature difference can be measured in acceptable accuracy for each material.
- Finally, feasibility studies should be carried out for other material, e.g., Li, F, Na, Hg, Pb and so on.

References

[1] K. Shibata, O. Iwamoto, T. Nakagawa, N. Iwamoto, A. Ichihara, S. Kunieda, S. Chiba, K. Furutaka, N. Otuka, T. Ohsawa, T. Murata, H. Matsunobu, A. Zukeran, S. Kamada, and J. Katakura: "JENDL-4.0: A New Library for Nuclear Science and Engineering," *J. Nucl. Sci. Technol.* **48**(1), 1-30 (2011).

[2] S, Shirato, “Atomic Physics I”, Nihon Riko Syuppankai, ISBN4-89019-010-4 (1995).

[3] X-5 Monte Carlo Team, "MCNP5_RSICC_1.30", LA-UR-04-5921 (2004).

35. Present Status of BNCT-SPECT Development with CdTe Detector

Masanobu Manabe*, Soichiro Nakamura, Isao Murata,
Division of Electrical, Electronic and Information Engineering,
Graduate School of Engineering, Osaka University,
Yamada-oka 2-1, Suita, Osaka 565-0871, Japan
*E-mail: mmanabe@ef.eie.eng.osaka-u.ac.jp

BNCT is a new radiation therapy which can destroy only tumor cells and will not damage healthy cells.This therapy is not yet established to be a usually utilized treatment at the present time, because it has some very serious unsolved problems. One of them is that the treatment effect cannot be known during BNCT in real time. We are now developing a SPECT system to measure the treatment effect in real time. In this paper, we describe the present status of BNCT-SPECT development.

1. Introduction

Recently, boron neutron capture therapy (BNCT) attracts medical field as a new radiation therapy. BNCT can destroy tumor cells by alpha particles(α) and lithium nuclei (^{7}Li) emitted by the reaction of thermal neutron or epithermal neutron with boron (^{10}B). Ranges of emitted α and ^{7}Li particles are as long as the same size as a human bodye cell. If ^{10}B would be accumulated only in tumor cells, it would be expected that only the tumor cells would be killed without damage of healthy cells. Also, BNCT has an advantage that drugs containing boron compounds have already been developed which could be accumulated only in tumor cells.

However, this therapy was not yet established as a usually utilized therapy at the present time. The reason is that there are some very serious problems unsolved. One of them is that the treatment effect cannot be known during BNCT in real time. In the present study, we have been developing BNCT with a SPECT technology, named BNCT-SPECT, as a gamma-ray measuring device in real time in order to solve the problem mentioned above. The BNCT treatment effect can be estimated by measuring 478keV gamma-rays emitted from the exited state of ^{7}Li nucleus created by ^{10}B(n,α)^{7}Li reaction by the SPECT technology. However, it is known to be very difficult to measure 478keV gamma-rays, because capture gamma-rays of 2.22MeV produced by ^{1}H(n,γ)^{2}H reaction and annihilation gamma-rays of 511keV to be detected just adjacent to 478keV gamma-rays become a large and critical background.

In this paper, we explain present status of BNCT-SPECT development.

2. BNCT-SPECT

At first, the principle of BNCT–SPECT is given in this chapter. ^{10}B(n,α)^{7}Li reaction is expressed by the next two nuclear reactions:

$$\begin{aligned} ^{10}\mathrm{B} + \mathrm{n} &\rightarrow \alpha + {}^{7}\mathrm{Li} + 2.79\ \mathrm{MeV}\ (6.1\%) \\ &\rightarrow \alpha + {}^{7}\mathrm{Li}^{*} + 2.31\mathrm{MeV} + \gamma(478\mathrm{keV})(93.9\%) \end{aligned} \quad (1)$$

94 % of ^{7}Li is in the first excited state, i.e., ^{7}Li*. ^{7}Li*decays in its half-life of 10^{-14} sec to emit a 478keV gamma-ray via transition from the first excited state to the ground state. If the intensity distribution of 478keV gamma-rays can be measured, we can obtain the distribution of ^{10}B(n,α)^{7}Li reaction rate in the tumor. Also, the attenuation coefficient of this photon in tissues is about 0.1 cm^{-1}. The 478keV gamma-rays can escape from a human body to a large extent. The result of the measurement can be regarded as the treatment effect of BNCT. A BNCT-SPECT device is used to measure the emission position and intensity of the 478keV gamma-rays as shown in Fig.1

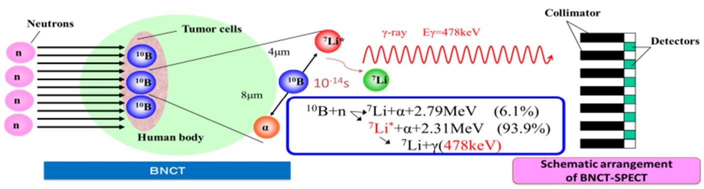

Fig.1 Principle of BNCT–SPECT

BNCT-SPECT is composed of a collimator and a multiple γ-ray detector (arrayed γ-ray detector).Emitted 478keV gamma-rays are collimated by this collimator, and measured by this array detector. The BNCT treatment effect (local tumor dose) can be estimated from an obtained three dimensional image of the gamma-rays.

However, the 478keV gamma-rays must be measured in a very high neutron field. The point is that many secondary neutrons and gamma-rays emitted by primary neutrons form a very high background field. It is thus quite difficult to accurately measure only 478keV gamma-rays out of such various unwanted radiations.

3. Design requirements for BNCT-SPECT

As mentioned in the previous chapter, BNCT-SPECT should be so designed that 478keV gamma-rays have to be measured in a very high background field. Also, actual medical site must be considered. Considering the above condition, we set four design conditions as follows.

① The spatial resolution should be about several mm in the obtained SPECT image from the viewpoint of medical treatment.

② It is necessary to complete a measurement in about 60 minutes, because the treatment time of BNCT is normally less than one hour.

③ The number of counts per unit detector should be more than 1000 counts so that the statistical accuracy can be kept to be less than several percent.

④ The energy resolution, full width at half maximum (FWHM), should be less than 33keV (511keV－478keV) so as to measure annihilation gamma-rays and 478keV prompt gamma-rays separately.

To meet requirement ①, an elemental gamma-ray detector should be downsized to be as large as the spatial resolution. However, to meet requirement ② being contrary to requirement ①, a gamma-ray detector having an enough high counting efficiency for 478keV gamma-rays should be selected. In addition, the detector should have a good energy resolution for requirement ④. Finally, we decided using a CdTe device with the following reasons[1]: a CdTe crystal is not necessarily enclosed with a casing, so that the area of radiation incidence can be kept to be small enough to easily improve the spatial resolution. Recently, a larger wafer can be produced and a high counting efficiency can be obtained so as to clear requirements ② and ③. Also, a Schottky type CdTe crystal was introduced. The energy resolution can thus be improved in order to meet requirement ④.

Next, the present status of BNCT-SPECT Development using a CdTe detector is described.

4. Present Status of BNCT-SPECT Development

Size and productivity of a CdTe element were investigated to meet design requirements(①～③) mentioned in the previous chapter. According to theoretical calculations, necessary efficiency of the CdTe element was fixed. Then, the thickness of it was determined to keep the incident surface small to some extent by the spatial resolution limit.[2,3] Consequently, thickness of over 30 mm is necessary in case of assuming that the incident surface is 2×1.5mm.[4]

Thereafter, the CdTe element was produced and the basic performance was confirmed experimentally.[5,6]The efficiency and energy resolution of the CdTe element are shown in Figs.2 and 3, respectively.

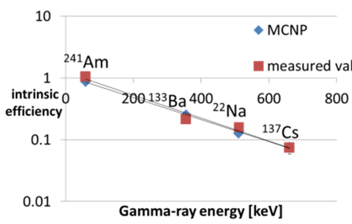

Fig2. Intrinsic efficiency of the CdTe detector

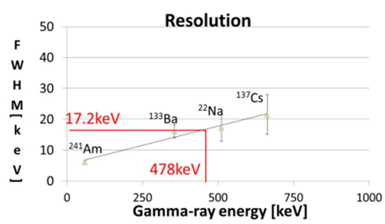

Fig3. Energy resolution of the CdTe detector

We successfully confirmed feasibility of the BNCT-SPECT, because a larger wafer of around 40 mm was able to be produced by the currently proven technology. Then a precise design of the BNCT-SPECT was started.

(1) Separate measurement of 478keV and annihilation gamma-rays[7]

We have measured a pulse height spectrum with the produced CdTe element and confirmed possibility of separate measurement of 478keV and annihilation gamma-rays (requirement ④) in a real BNCT case. Figures 4 and 5 show the produced trial CdTe elemental detector (2×1.5×30mm) and electronic circuit.

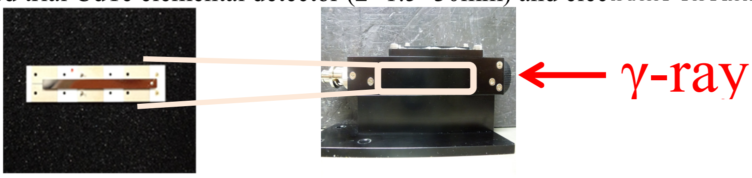

(a)CdTe element (2×1.5×30mm).　(b)CdTe detector.

Fig.4　Produced trial CdTe elemental detector

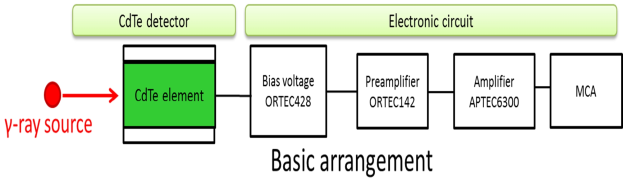

Fig.5 Experimental scheme of the energy resolution measurement with standard gamma-ray sources

The experimental procedure consists of the following three processes. First, 478keV gamma-rays were measured by the CdTe detector, using boric acid (300g) and an AmBe neutron source set in a graphite column. (Fig.6(a)) Next, 511keV gamma-rays were measured using a ^{22}Na gamma-ray source set just beside the CdTe detector.(Fig.6(b)) Figure 7 shows photos of experimental arrangements and used CdTe detector.

(a)Measurement of prompt gamma-rays of 478keV　(b)Measurement of annihilation gamma-rays of 0.511MeV

Fig.6 Schematic experimental arrangements of 478keV and 511keV gamma-rays measurements by the CdTe detector

(a)Experimental setup.　(b)CdTe detector.

Fig.7 Photos of experimental arrangement and CdTe detector

Finally, the measured two spectra were synthesized by using the intensity ratio observed in an actual BNCT scene.[8] The synthesized spectrum is shown in the Fig. 8 together with pulse height spectra for 478 keV and 511keV gamma-rays in the left side of the figure. It was confirmed according to a preliminary experiment with a HpGe detector carried out before the present experiment that the Doppler broadening of 478keV gamma-rays was surely appearing.[6] Then, it became clear that the 478keV gamma-ray peak was expanded due to the Doppler broadening from Fig. 8. FWHMs of 478 and 511keV were 17.7 and 16.9keV respectively. We finally confirmed experimentally that both gamma-rays could be measured separately even if considering statistical errors of the measurements and the Doppler broadening of 478keV gamma-rays as shown in Eq. (2).

$$\text{Measured resolution}=(17.7\pm11.3+16.9\pm3.66)/2=9.8\sim24.8<33\text{keV} \qquad (2)$$

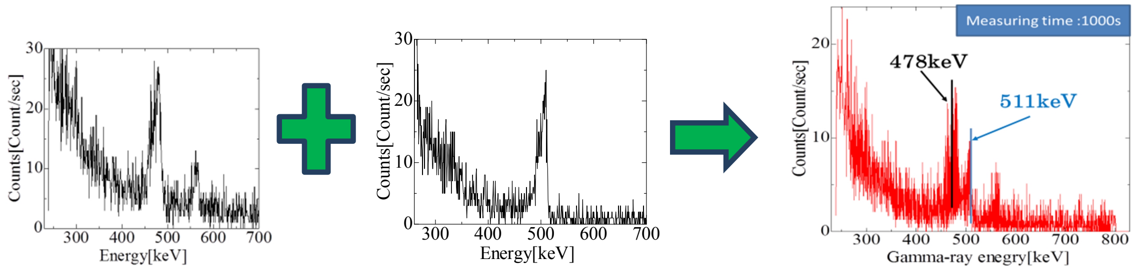

Fig.8 Synthesized pulse height spectrum of 478keV and 511keV gamma-rays to be observed in the real BNCT scene. Left upper and lower figures are for 478keV and 511keV gamma-rays, respectively.

(2)Collimator design for array type CdTe detector[9]

Next, we designed a collimator for an array type CdTe detector for requirements ② and ③.
In the present collimator design pulse height spectra to be measured at the actual BNCT spot were calculated by using MCNP5(Three-dimensional Monte Carlo N-Particle Transport Code).Design goals are as follows: The number of peak net counts at 478keV is greater than 1000 for one hour and supplementary the signal to noise (S/N) ratio at the 478keV peak is larger than unity. As for a neutron source condition, a 10 keV broad parallel neutron beam was used. We employed F4, F5 and F8 tallies to estimate reaction rate, flux and pulse height spectrum, respectively. The CdTe detector size is assumed to be the achievable maximum dimensions(2×2.5×40mm) at present in Japan. Collimator diameter and number of holes were decided considering this CdTe detector dimensions. Figure 9 shows finally obtained model of BNCT-SPECT.

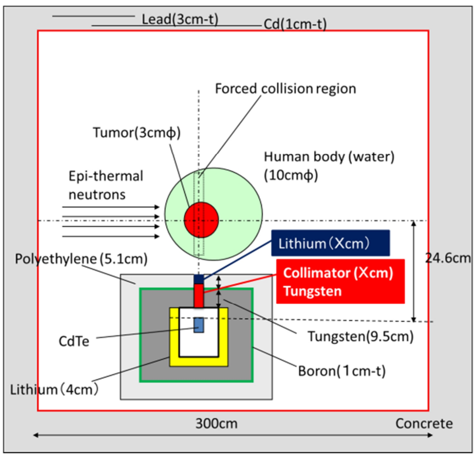

Fig.9 Final calculation model of BNCT-SPECT taking into account even irradiation room

The calculation model is composed of an irradiation room, detector assembly and human body phantom. As shown in the figure, the CdTe detector is mainly shielded with polyethylene, tungsten, boron and lithium. Also, the CdTe detector is heavily shielded with tungsten and lithium especially in the forward direction, because there are collimator holes in the direction. The thicknesses of the tungsten and lithium are parameters to be used in the design calculations later.

The results of calculations are shown in Figs.10 and 11. Figure 10 is a pulse height spectrum at 478keV nearby From this result, it was confirmed that a peak of 478keV gamma rays from ^{10}B(n,α)^{7}Li reaction is distorted greatly by noises due to gamma-rays other than 478keV gamma-rays. Among them, highly-influential cause is a created Compton continuum by 2.22MeV gamma rays emitted from ^{1}H(n,γ)^{2}H reaction. According to the calculation results, 2.22MeV gamma-rays, the contribution ratio of which is 72%, have a bad influence. Figure 11 shows the S/N ratio and net count rate at 478 keV as a function of Li and W thicknesses in front of the collimator.

From the figure, we decided the optimum thicknesses of tungsten and lithium to be 14 cm and 1.5 cm, respectively. The count rate of 478keV is 1159 counts per 60 minutes, which is larger than the target value. On the other hand, the S/N ratio is 0.21 being less than the supplementary reference value.

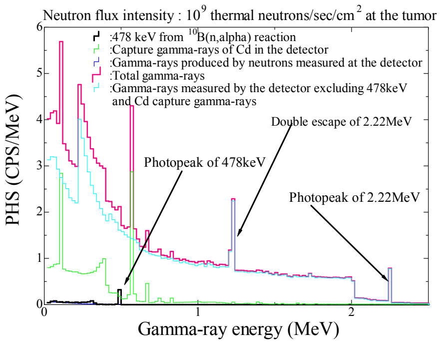

Fig.10 Calculated PHS at 478keV nearby

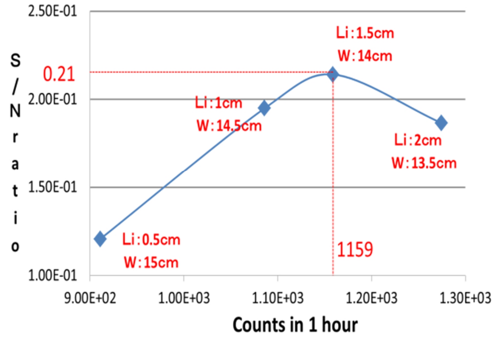

Fig11. S/N ratio and count rate at 478 keV as a function of Li and W thicknesses

Next, we started to improve the S/N ratio. As described earlier, deterioration of the S/N ratio is caused by the influence of Compton scattering. We then examined whether anti-Compton measurement in the arrayed CdTe crystals could decrease the noise due to Compton scatterings.The calculation was carried out with MCNP5. Figure 12 shows a calculation model example, that is, a case of nine elemental detector crystals. In calculations, firstly, assuming 2.22MeV gamma-rays are incident only to the center detector. Compton continuum at 478keV is formed when the energy of Compton scattering gamma-ray of 2.22MeV gamma-ray is 1.742 MeV. By F1 tally was calculated the leakage rate of the gamma-rays, a, escaping to an outside sphere model without detection of 8 surrounding CdTe detectors. It means that the amount of 1.742 MeV gamma-rays detected by the surrounded CdTe detectors is $1-a$. Through the above simple calculation, the percentage of anti-coincidence detection so as to reduce the Compton base part at 478 keV can be obtained without “event mode” by the next equation.

$$\eta(1-a)*100\% \tag{3}$$

Actually, η, which is a correction factor for the angular distribution, is required for this calculation, because the angular distribution of emitted Compton scattering gamma-rays is not taken into consideration. However, this effect is known to be not so large, as high as 0.9 from the precise calculation. Figure 13 shows the result of anti-coincidence decreasing rate as a function of the number of detectors surrounding the central detector. The vertical axis is anti-coincidence decreasing rate, and horizontal axis is reciprocal of the total number of detectors. We calculated several cases for the total number of detectors, i.e., 9, 25, 49 and so on. The anti-coincidence decreasing rate is estimated to be 46 % by extrapolation to the actual case, in which there are 4096 detectors, that is, a 64 by 64 array detector case. The S/N ratio would be doubled, that is improved to be 0.42.

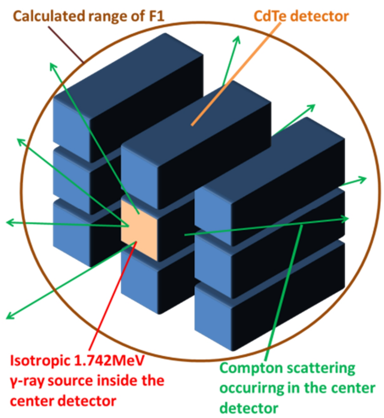

Fig.12 Anti-coincidence calculation model

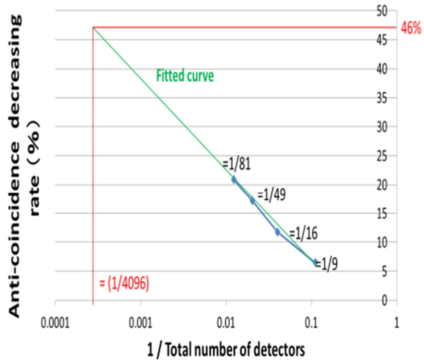

Fig.13 Anti-coincidence decreasing rate

5.Future Work

As a future work, we are planning to carry out measurement of actual anti-coincidence detection ratio by using a two-element CdTe detector. For this purpose, we already produced a first-trial two-element CdTe detector this year. Figure 14 shows a photo of the two-element CdTe detector. Furthermore, to reduce the Compton base at 478keV more substantially, a scintillation detector is set just behind the CdTe detector as shown Fig. 15.

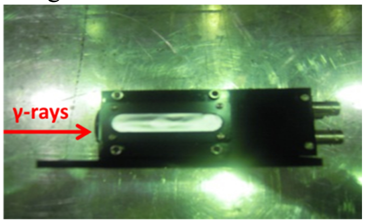

Fig.14 Photo of the two-element CdTe detector.

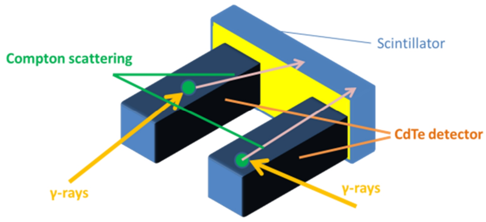

Fig.15 Schematic view of anti-coincidence detection.

6.Conclusion

To realize a SPECT system to estimate the treatment effect of BNCT in real time, we have been developing the so-called BNCT-SPECT in Osaka University. After basic theoretical examination for the elemental device, we produced a CdTe elemental detector by which we carried out the characterization measurement. We thereafter confirmed possibility of separate measurement of 478keV and 511keV annihilation gamma-rays experimentally with the developed CdTe detector by synthesizing their spectra measured separately.

We then designed a collimator for BNCT-SPECT, and the best result was obtained when using a combination of 14 cm thick tungsten shield and neutron shield of 1.5 cm thick lithium. As a result, the count rate was 1159 counts per 60minutes, but the S/N ratio was 0.21 due to influence of Compton scattering of 2.22 MeV hydrogen capture gamma-rays mainly. By considering the arrangement of an array type CdTe detector to be implemented to the real BNCT-SPECT, the anti-coincidence decreasing rate of the Compton scattering of 2.22MeV at 478 keV can be reduced by about 46%, that is, the S/N ratio of 0.42.

After testing the two-element CdTe detector, we will start designing of the real BNCT-SPECT soon.

Reference

[1] I. Murata, T. Mukai, M. Ito, H. Miyamaru, S.Yoshida, Feasibility study on BNCT-SPECT using a CdTe detector,*Progress in Nucl. Sci. Technol.*1 (2011), pp. 267-270.

[2] T. Mukai, I. Murata, M. Ito, H. Miyamaru, Development of CdTe detector for BNCT-SPECT, *Proceedings of the 2009 Annual Symposium on Nucl. Data, RICOTTI, Tokai-mura, Ibaraki-ken, Japan*,26-27 Nov. 2009, JAEA-Conf 2010-005 (2010), pp.75-80.

[3] I. Murata, T. Mukai, S. Nakamura, H. Miyamaru, I. Kato, Development of A Thick CdTe Detector for BNCT-SPECT, *Appl. Radiat. Isotopes.*69 (2011), pp. 1706-1709.

[4] S.Nakamura, T.Mukai, M.Manabe, I.Murata, Characterization Test of CdTe Detector Element Designed and Developed for BNCT-SPECT, *Proceedings of the 2011 Annual Symposium on Nucl. Data*, RICOTTI, Tokai-mura, Ibaraki-ken, Japan ,16-17 Nov.2011, JAEA-Conf 2012-001 (2012), pp.165-170.

[5] S.Nakamura, T.Mukai, M.Manabe, I.Murata, Precise Numerical Simulation of Gamma-ray Pulse Height Spectrum Measured with a CdTe Detector Designed for BNCT-SPECT, *Progress in Nucl. Sci. Technol.* 3, (2012), pp. 52-55.

[6] I.Murata, S.Nakamura, M.Manabe,H.Miyamaru, I. Kato, *Characterization Measurement of A Thick CdTe Detector for BNCT-SPECT - Detection Efficiency and Energy Resolution -* , presented in 15th International Congress on NeutronCaptureTherapy(ICNCT-15), Tsukuba,Japan,10-14Sept., 2012.

[7] M.Manabe, S.Nakamura, I.Murata, *Separate measurement of 478keV and annihilation gamma-rays by CdTe detector for BNCT-SPECT*, presented in 7th International Symposium on Radiation Safety and Detection Technology(ISORD-7), Sanya,China,15-18Jun., 2013.

[8] T. Kobayashi, Y. Sakurai, A noninvasive dose estimation system for clinical BNCT based on PG-SPECT－Conceptual study and fundamental experiments using HPGe and CdTe semiconductor Detectors, *Med.Phys.*27(9),(2000), pp.2124-2132.

[9] M.Manabe, S.Nakamura, I.Murata,*Study on Measuring Device Arrangement of Array-type CdTe Detector for BNCT-SPECT*, presented in 7th Young Researchers' Boron Neutron Capture Therapy (7YBNCT), Granada,Spain, 22-26 September,2013.

36. Study on the Validity of Thorium-232 Cross-section in JENDL-4.0

Takuji MISHIRO, Takanori KITADA, Takashi FUJII, Tatsuya KOJIMA
Osaka University, 2-1 Yamadaoka, Suita-shi, Osaka, Japan, 565-0871
t-mishiro@ne.see.eng.osaka-u.ac.jp

The object of this study is to clarify the validity of Thorium cross-section in JENDL-4.0[1] through the analysis of Thorium replacement worth experiments measured at Kyoto University Critical Assembly (KUCA). The analysis results of Thorium experiment worth underestimate the experimental results. The sensitivity analysis was carried out to clarify the cause of the underestimation and it is suggested that the underestimation is caused by the smaller estimation of Thorium capture cross-section at energy range of 0.0542 eV-0.532 eV and 22.6 eV-4.31 keV.

1. Introduction

Recently, Thorium fuel has been re-focussed because of its potentials. However, the accuracy of Thorium cross-section remains lower than other major actinides such as Uranium, Plutonium etc. The objective of this study is to clarify the validity of Thorium cross-sections and covariances of JENDL-4.0, and to suggest the desirable reaction types and energy range in order to enhance the validity of the cross-section data.

2. Experiment and Analysis

Thorium replacement worths were measured at KUCA during 2011-2013 as the collaboration work among Osaka University, Tokai University (later Tokyo City University) and Kyoto University. In this campaign, the worths were measured at several cores with different spectrum field by changing the arrangement of unit fuel where H/U (Hydrogen to Uranium-235 Ratio) =50, 140 and 210. Figure 1 shows neutron spectrum of several cores measured worths. For measurement of Thorium replacement worth, the excess reactivity of two core types were measured. One was replaced no Thorium plate, the other was replaced four Thorium plates with Aluminium plates in central fuel rod. After measurement the excess reactivity of each core, Equation 1 was used to evaluate Thorium replacement worths. The experimental results were summarized in Table 1 with experimental error.

$$\text{Thorium replacement worth} = \rho' - \rho \qquad (1)$$

where ρ is the excess reactivity before replacement and ρ' is the excess reactivity after replacement.

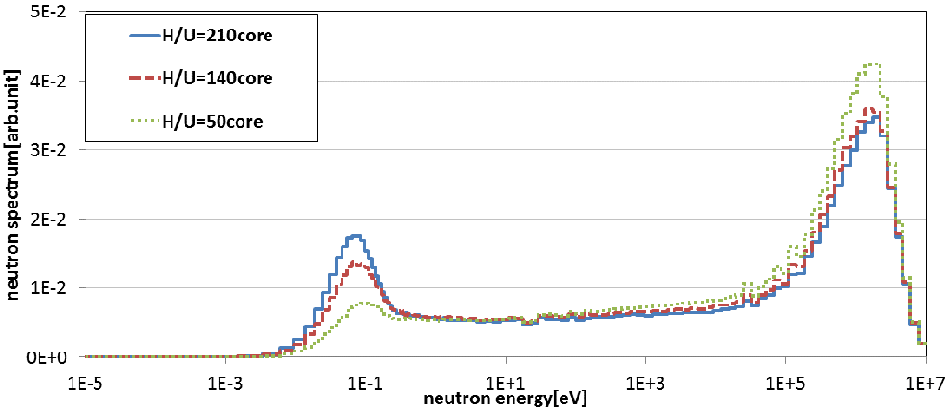

Figure 1 Neutron spectrum of H/U=50,140 and 210 core

Table 1 Experimental results of excess reactivity and Thorium replacement worth

Core H/U	Excess reactivity [%Δk/k]		Thorium replacement worth
	before replacement	after replacement	
50	0.1157±0.0037	0.3379±0.0029	0.2222±0.0047
140	0.0435±0.0003	0.2438±0.0011	0.2003±0.0012
210	0.0492±0.0004	0.3029±0.0010	0.2537±0.0011

The analysis of the worths was performed by continuous energy Monte Carlo code MVP[2] with JENDL-4.0, 1 billion history. The analysis results of Thorium replacement worth were summarized in Figure 2 with one standard deviation of experimental error and statistical (Monte Carlo) error. The analysis results show the underestimation of 5-10 %.

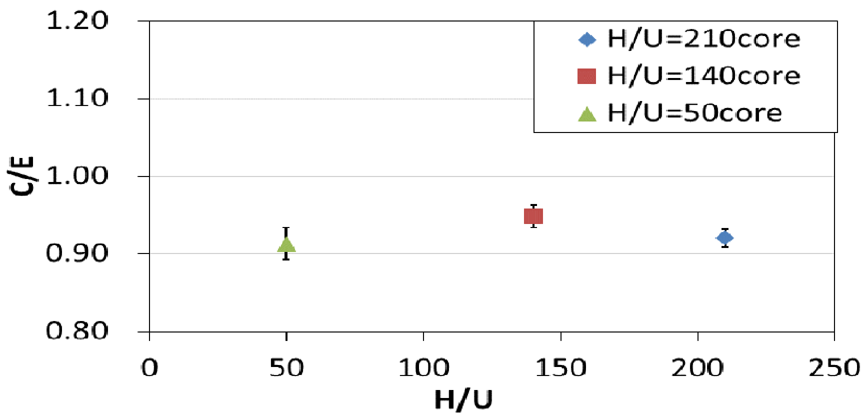

Figure 2 C/E of Thorium replacement worth at H/U=50,140,210 core

3. Uncertainty Analysis with covariance data

Sensitivity analysis was carried out by SAGEP[3] so as to clarify the detail of the underestimation of C/E by considering cross-section covariances. Cross-section covariances were evaluated by using the ERRORR module of NJOY99.364[4]. The following equations were used to calculate the sensitivity of the worth and uncertainty of worth.

$$S_w = -\frac{\left(\frac{S_k}{k} - \frac{S_{k'}}{k'}\right)}{\left(\frac{1}{k} - \frac{1}{k'}\right)} \qquad (2)$$

$$\delta\mathrm{E} = \sqrt{S_w{}^T V S_w} \qquad (3)$$

where S_k is the sensitivity coefficient of effective multiplication factor before replacement, $S_{k'}$ is the sensitivity coefficient of effective multiplication factor after replacement, k is effective multiplication factor before replacement, k' is effective multiplication factor after replacement, S_w is the sensitivity coefficient of worth, $S_w{}^T$ is the transposed matrix of the sensitivity coefficient of worth, V is cross-section covariance matrix, $\delta\mathrm{E}$ is the uncertainty of worth.

Figure 3 shows the uncertainty of C/E considering the uncertainty of cross-section. This figure reveals that all cores cover C/E=1 within one standard deviation. Figure 4 shows the breakdown of the uncertainty of C/E evaluated by nuclides. This figure reveals that Thorium cross section has a remarkable contribution to the uncertainty. Figure 5 shows the breakdown of the uncertainty of C/E evaluated by Thorium cross-section covariances of several reaction types; capture, fission, elastic, inelastic, (n,2n) scattering. This figure reveals that the capture reaction has a remarkable contribution to the uncertainty of C/E.

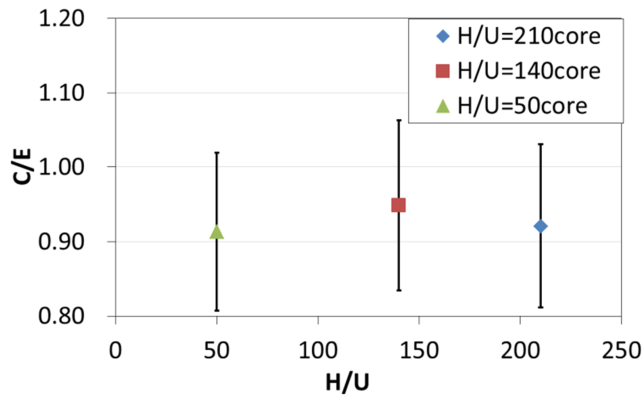

Figure 3 C/E of worth considering the uncertainty of cross-section

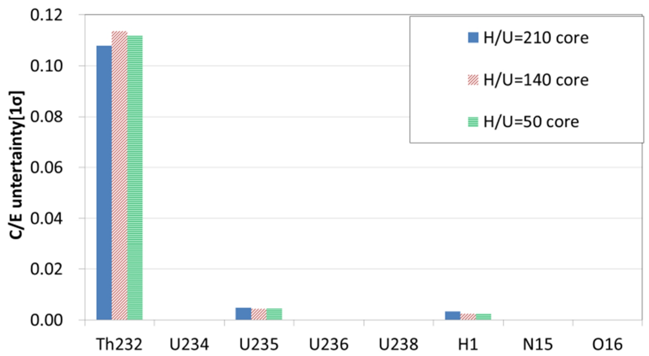

Figure 4 Breakdown of uncertainty of C/E by nuclide

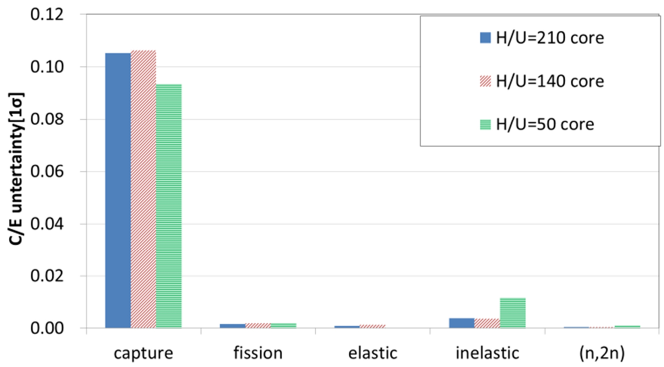

Figure 5 Breakdown of uncertainty of C/E by reaction

Energy regions were decomposed based on capture cross-section covariance matrix so as to clarify the contribution of each energy range to the uncertainty of C/E. Figure 6 shows the sensitivity coefficient of worth by capture reaction, capture cross-section. Table 2 show the contribution to the uncertainty of C/E by the capture cross-section decomposed into several energy ranges. The main contribution to the uncertainty comes from 0.0542 eV–0.532 eV and 22.6 eV–4.31 keV where one standard deviation of capture reaction covers the underestimation shown in Figure 2.

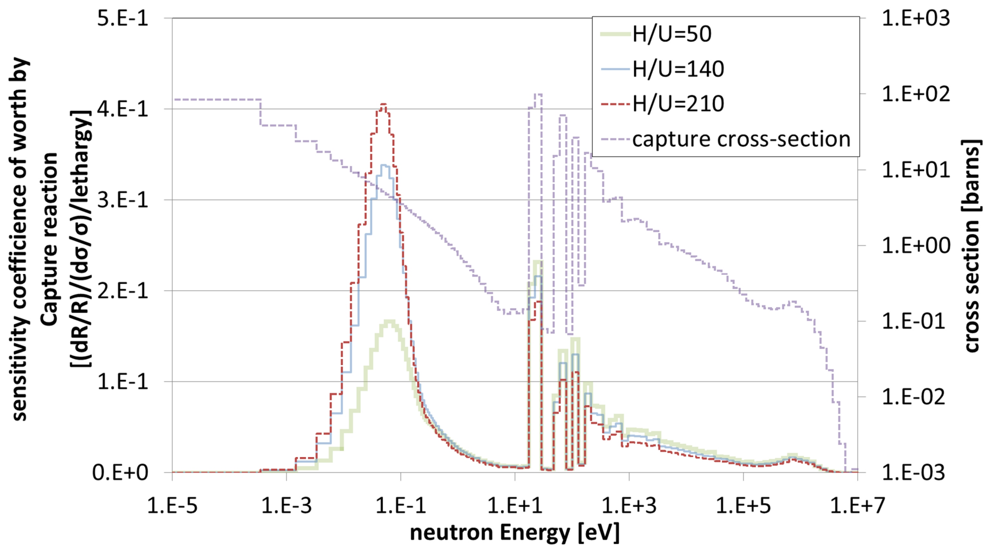

Figure 6 Sensitivity coefficient of worth by capture reaction, capture cross-section

Table 2 Uncertainty of C/E by energy range

core H/U	energy range[eV]						
	1.00E−5～ 1.47E−3	1.47E−3～ 5.42E−2	5.42E−2～ 5.32E−1	5.32E−1～ 2.26E+1	2.26E+1～ 4.31E+3	4.31E+3～ 1.00E+7	total
210	0.012	0.021	0.086	0.033	0.059	0.014	0.108
140	0.015	0.022	0.089	0.037	0.075	0.018	0.116
50	0.021	0.024	0.065	0.042	0.087	0.024	0.106

Figure 7 shows C/E for the case of changing capture cross-section at certain energy range so as to be unity of C/E at H/U=50 core. About 26 % of capture cross-section at energy range of 0.0542 eV–0.532 eV and about 20 % of capture cross-section at energy range of 22.6 eV–4.31 keV are changed in Figure 7.This figure reveals that C/E for the case of changing capture cross-section at energy range of 22.6 eV–4.31 keV is smaller effect on the difference between neutron spectrum of each core than C/E for the case of changing capture cross-section at energy range of 22.6 eV–4.31keV. It is concluded that Thorium capture cross-section at energy range of 22.6 eV-4.31 keV is more likely to be underestimation than that of 0.0542 eV-0.532 eV.

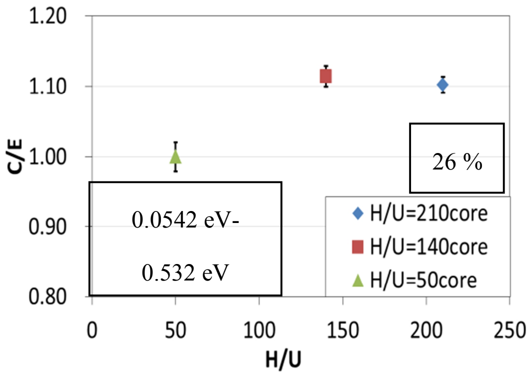

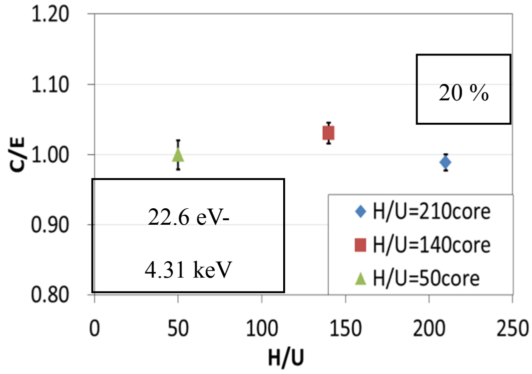

Figure 7 C/E of worth after changing capture cross-section at each energy range

4. Conclusion

The validity Thorium cross-section in JENDL-4.0 was evaluated through the experimental analysis and the sensitivity analysis of Thorium replacement worth. The analysis results show that Thorium cross-section is likely to be underestimation of about 20 % at energy region of 0.0542 eV–0.532 eV and 22.6 eV–4.31 keV. Considering the difference between neutron spectrum of each core, Thorium capture cross-section at energy range of 22.6 eV–4.31 keV is more likely to be underestimation than that of 0.0542 eV–0.532 eV.

Acknowledgements

The authors send gratitude of Prof. Takaki of Tokyo City University, and Prof. Unesaki of Kyoto University Research Reactor Institute for their helpful support of the experiment and advice of the analysis.

References

[1]K. Shibata, O. Iwamoto, T. Nakagawa, N. Iwamoto, A. Ichihara, S. Kunieda, S. Chiba, K. Furutaka, N. Otuka, T. Ohsawa, T. Murata, H. Matsunobu, A. Zukeran, S. Kamada, and J. Katakura: "JENDL-4.0: A New Library for Nuclear Science and Engineering," J. Nucl. Sci. Technol. 48(1), 1-30 *(2011).*

[2]Y. Nagaya, K. Okumura, T. Mori et al., MVP/GMVP Version 2 : General Purpose Monte Carlo Codes for Neutron and Photon Transport Calculations based on Continuous Energy and Multigroup Methods,

JAERI 1348 (2005).
[3]A. Hara, T. Takeda, Y. Kikuchi, “SAGEP : Two-dimensional sensitivity analysis code based on generalized perturbation theory,” JAERI-M 84-027, Japan Atomic Energy Research Institute (JAERI) (1984).
[4]R. E. MacFarlane, D. W. Muir, R. M. Boicourt, “The NJOY nuclear data processing system, Volume I: User’s manual”, LA-9303-M (ENDF-324) (1982).

This is a blank page.

国際単位系（SI）

表１．SI 基本単位

基本量	SI 基本単位	
	名称	記号
長さ	メートル	m
質量	キログラム	kg
時間	秒	s
電流	アンペア	A
熱力学温度	ケルビン	K
物質量	モル	mol
光度	カンデラ	cd

表２．基本単位を用いて表されるSI組立単位の例

組立量	SI 基本単位	
	名称	記号
面積	平方メートル	m^2
体積	立法メートル	m^3
速さ，速度	メートル毎秒	m/s
加速度	メートル毎秒毎秒	m/s^2
波数	毎メートル	m^{-1}
密度，質量密度	キログラム毎立方メートル	kg/m^3
面積密度	キログラム毎平方メートル	kg/m^2
比体積	立方メートル毎キログラム	m^3/kg
電流密度	アンペア毎平方メートル	A/m^2
磁界の強さ	アンペア毎メートル	A/m
量濃度 (a)，濃度	モル毎立方メートル	mol/m^3
質量濃度	キログラム毎立法メートル	kg/m^3
輝度	カンデラ毎平方メートル	cd/m^2
屈折率 (b)	（数字の）　1	1
比透磁率 (b)	（数字の）　1	1

(a) 量濃度（amount concentration）は臨床化学の分野では物質濃度（substance concentration）ともよばれる。
(b) これらは無次元量あるいは次元１をもつ量であるが、そのことを表す単位記号である数字の１は通常は表記しない。

表３．固有の名称と記号で表されるSI組立単位

組立量	SI 組立単位			
	名称	記号	他のSI単位による表し方	SI基本単位による表し方
平面角	ラジアン(b)	rad	1 (b)	m/m
立体角	ステラジアン(b)	sr(c)	1 (b)	m^2/m^2
周波数	ヘルツ (d)	Hz		s^{-1}
力	ニュートン	N		$m\ kg\ s^{-2}$
圧力，応力	パスカル	Pa	N/m^2	$m^{-1}\ kg\ s^{-2}$
エネルギー，仕事，熱量	ジュール	J	N m	$m^2\ kg\ s^{-2}$
仕事率，工率，放射束	ワット	W	J/s	$m^2\ kg\ s^{-3}$
電荷，電気量	クーロン	C		s A
電位差（電圧），起電力	ボルト	V	W/A	$m^2\ kg\ s^{-3}\ A^{-1}$
静電容量	ファラド	F	C/V	$m^{-2}\ kg^{-1}\ s^4\ A^2$
電気抵抗	オーム	Ω	V/A	$m^2\ kg\ s^{-3}\ A^{-2}$
コンダクタンス	ジーメンス	S	A/V	$m^{-2}\ kg^{-1}\ s^3\ A^2$
磁束	ウエーバ	Wb	Vs	$m^2\ kg\ s^{-2}\ A^{-1}$
磁束密度	テスラ	T	Wb/m^2	$kg\ s^{-2}\ A^{-1}$
インダクタンス	ヘンリー	H	Wb/A	$m^2\ kg\ s^{-2}\ A^{-2}$
セルシウス温度	セルシウス度(e)	℃		K
光束	ルーメン	lm	cd sr(c)	cd
照度	ルクス	lx	lm/m^2	m^{-2} cd
放射性核種の放射能 (f)	ベクレル (d)	Bq		s^{-1}
吸収線量, 比エネルギー分与, カーマ	グレイ	Gy	J/kg	$m^2\ s^{-2}$
線量当量, 周辺線量当量, 方向性線量当量, 個人線量当量	シーベルト (g)	Sv	J/kg	$m^2\ s^{-2}$
酸素活性	カタール	kat		s^{-1} mol

(a)SI接頭語は固有の名称と記号を持つ組立単位と組み合わせても使用できる。しかし接頭語を付した単位はもはやコヒーレントではない。
(b)ラジアンとステラジアンは数字の１に対する単位の特別な名称で、量についての情報をつたえるために使われる。実際には、使用する時には記号rad及びsrが用いられるが、習慣として組立単位としての記号である数字の１は明示されない。
(c)測光学ではステラジアンという名称と記号srを単位の表し方の中に、そのまま維持している。
(d)ヘルツは周期現象についてのみ、ベクレルは放射性核種の統計的過程についてのみ使用される。
(e)セルシウス度はケルビンの特別な名称で、セルシウス温度を表すために使用される。セルシウス度とケルビンの単位の大きさは同一である。したがって、温度差や温度間隔を表す数値はどちらの単位で表しても同じである。
(f)放射性核種の放射能（activity referred to a radionuclide）は、しばしば誤った用語で"radioactivity"と記される。
(g)単位シーベルト（PV,2002,70,205）についてはCIPM勧告2（CI-2002）を参照。

表４．単位の中に固有の名称と記号を含むSI組立単位の例

組立量	SI 組立単位		
	名称	記号	SI 基本単位による表し方
粘度	パスカル秒	Pa s	$m^{-1}\ kg\ s^{-1}$
力のモーメント	ニュートンメートル	N m	$m^2\ kg\ s^{-2}$
表面張力	ニュートン毎メートル	N/m	$kg\ s^{-2}$
角速度	ラジアン毎秒	rad/s	$m\ m^{-1}\ s^{-1}=s^{-1}$
角加速度	ラジアン毎秒毎秒	rad/s^2	$m\ m^{-1}\ s^{-2}=s^{-2}$
熱流密度，放射照度	ワット毎平方メートル	W/m^2	$kg\ s^{-3}$
熱容量，エントロピー	ジュール毎ケルビン	J/K	$m^2\ kg\ s^{-2}\ K^{-1}$
比熱容量，比エントロピー	ジュール毎キログラム毎ケルビン	J/(kg K)	$m^2\ s^{-2}\ K^{-1}$
比エネルギー	ジュール毎キログラム	J/kg	$m^2\ s^{-2}$
熱伝導率	ワット毎メートル毎ケルビン	W/(m K)	$m\ kg\ s^{-3}\ K^{-1}$
体積エネルギー	ジュール毎立方メートル	J/m^3	$m^{-1}\ kg\ s^{-2}$
電界の強さ	ボルト毎メートル	V/m	$m\ kg\ s^{-3}\ A^{-1}$
電荷密度	クーロン毎立方メートル	C/m^3	m^{-3} sA
表面電荷	クーロン毎平方メートル	C/m^2	m^{-2} sA
電束密度，電気変位	クーロン毎平方メートル	C/m^2	m^{-2} sA
誘電率	ファラド毎メートル	F/m	$m^{-3}\ kg^{-1}\ s^4\ A^2$
透磁率	ヘンリー毎メートル	H/m	$m\ kg\ s^{-2}\ A^{-2}$
モルエネルギー	ジュール毎モル	J/mol	$m^2\ kg\ s^{-2}\ mol^{-1}$
モルエントロピー, モル熱容量	ジュール毎モル毎ケルビン	J/(mol K)	$m^2\ kg\ s^{-2}\ K^{-1}\ mol^{-1}$
照射線量（Ｘ線及びγ線）	クーロン毎キログラム	C/kg	kg^{-1} sA
吸収線量率	グレイ毎秒	Gy/s	$m^2\ s^{-3}$
放射強度	ワット毎ステラジアン	W/sr	$m^4\ m^{-2}\ kg\ s^{-3}=m^2\ kg\ s^{-3}$
放射輝度	ワット毎平方メートル毎ステラジアン	$W/(m^2\ sr)$	$m^2\ m^{-2}\ kg\ s^{-3}=kg\ s^{-3}$
酵素活性濃度	カタール毎立方メートル	kat/m^3	$m^{-3}\ s^{-1}$ mol

表５．SI 接頭語

乗数	接頭語	記号	乗数	接頭語	記号
10^{24}	ヨタ	Y	10^{-1}	デシ	d
10^{21}	ゼタ	Z	10^{-2}	センチ	c
10^{18}	エクサ	E	10^{-3}	ミリ	m
10^{15}	ペタ	P	10^{-6}	マイクロ	µ
10^{12}	テラ	T	10^{-9}	ナノ	n
10^{9}	ギガ	G	10^{-12}	ピコ	p
10^{6}	メガ	M	10^{-15}	フェムト	f
10^{3}	キロ	k	10^{-18}	アト	a
10^{2}	ヘクト	h	10^{-21}	ゼプト	z
10^{1}	デカ	da	10^{-24}	ヨクト	y

表６．SIに属さないが、SIと併用される単位

名称	記号	SI 単位による値
分	min	1 min=60s
時	h	1h =60 min=3600 s
日	d	1 d=24 h=86 400 s
度	°	1°=(π/180) rad
分	’	1’=(1/60)°=(π/10800) rad
秒	”	1”=(1/60)’=(π/648000) rad
ヘクタール	ha	$1ha=1hm^2=10^4m^2$
リットル	L，l	$1L=1l=1dm^3=10^3cm^3=10^{-3}m^3$
トン	t	$1t=10^3$ kg

表７．SIに属さないが、SIと併用される単位で、SI単位で表される数値が実験的に得られるもの

名称	記号	SI 単位で表される数値
電子ボルト	eV	$1eV=1.602\ 176\ 53(14)\times10^{-19}J$
ダルトン	Da	$1Da=1.660\ 538\ 86(28)\times10^{-27}kg$
統一原子質量単位	u	1u=1 Da
天文単位	ua	$1ua=1.495\ 978\ 706\ 91(6)\times10^{11}m$

表８．SIに属さないが、SIと併用されるその他の単位

名称	記号	SI 単位で表される数値
バール	bar	$1\ bar=0.1MPa=100kPa=10^5Pa$
水銀柱ミリメートル	mmHg	1mmHg=133.322Pa
オングストローム	Å	$1\ Å=0.1nm=100pm=10^{-10}m$
海里	M	1 M=1852m
バーン	b	$1\ b=100fm^2=(10^{-12}cm)2=10^{-28}m^2$
ノット	kn	1 kn=(1852/3600)m/s
ネーパ	Np	SI単位との数値的な関係は、対数量の定義に依存。
ベル	B	
デジベル	dB	

表９．固有の名称をもつCGS組立単位

名称	記号	SI 単位で表される数値
エルグ	erg	$1\ erg=10^{-7}$ J
ダイン	dyn	$1\ dyn=10^{-5}N$
ポアズ	P	$1\ P=1\ dyn\ s\ cm^{-2}=0.1Pa\ s$
ストークス	St	$1\ St=1cm^2\ s^{-1}=10^{-4}m^2\ s^{-1}$
スチルブ	sb	$1\ sb=1cd\ cm^{-2}=10^4cd\ m^{-2}$
フォト	ph	$1\ ph=1cd\ sr\ cm^{-2}\ 10^4lx$
ガル	Gal	$1\ Gal=1cm\ s^{-2}=10^{-2}ms^{-2}$
マクスウェル	Mx	$1\ Mx=1G\ cm^2=10^{-8}Wb$
ガウス	G	$1\ G=1Mx\ cm^{-2}=10^{-4}T$
エルステッド (c)	Oe	$1\ Oe \triangleq (10^3/4\pi)A\ m^{-1}$

(c) ３元系のCGS単位系とSIでは直接比較できないため、等号「 ≙ 」は対応関係を示すものである。

表10．SIに属さないその他の単位の例

名称	記号	SI 単位で表される数値
キュリー	Ci	$1\ Ci=3.7\times10^{10}Bq$
レントゲン	R	$1\ R=2.58\times10^{-4}C/kg$
ラド	rad	$1\ rad=1cGy=10^{-2}Gy$
レム	rem	$1\ rem=1\ cSv=10^{-2}Sv$
ガンマ	γ	1 γ=1 nT=10-9T
フェルミ		1フェルミ=1 fm=10-15m
メートル系カラット		1メートル系カラット = 200 mg = 2×10-4g
トル	Torr	1 Torr = (101 325/760) Pa
標準大気圧	atm	1 atm = 101 325 Pa
カロリー	cal	1cal=4.1858J（「15℃」カロリー），4.1868J（「IT」カロリー）4.184J（「熱化学」カロリー）
ミクロン	µ	$1\ \mu=1\mu m=10^{-6}m$

（第8版，2006年改訂）